PEPTIDE NANOFIBERS FOR

ENGINEERING TISSUES AND IMMUNE SYSTEM

A DISSERTATION SUBMITTED TO

MATERIALS SCIENCE AND NANOTECHNOLOGY PROGRAM

OF THE GRADUATE SCHOOL OF ENGINEERING AND SCIENCE

OF BILKENT UNIVERSITY

IN PARTIAL FULFILLMENT OF THE REQUIREMENTS

FOR THE DEGREE OF

DOCTOR OF PHILOSOPHY

By

RASHAD MAMMADOV

February, 2014

I certify that I have read this thesis and that in my opinion it is fully adequate, in scope and in quality, as a thesis of the degree of Doctor of Philosophy.

…….

Assoc. Prof. Dr. Ayşe Begüm Tekinay (Principal Advisor)

I certify that I have read this thesis and that in my opinion it is fully adequate, in scope and in quality, as a thesis of the degree of Doctor of Philosophy.

…….

Assoc. Prof. Dr. Mustafa Özgür Güler (Co-advisor)

I certify that I have read this thesis and that in my opinion it is fully adequate, in scope and in quality, as a thesis of the degree of Doctor of Philosophy.

…….

Prof. Dr. Mahinur Akkaya

I certify that I have read this thesis and that in my opinion it is fully adequate, in scope and in quality, as a thesis of the degree of Doctor of Philosophy.

…….

Assoc. Prof. Dr. Bahri Aydın

I certify that I have read this thesis and that in my opinion it is fully adequate, in scope and in quality, as a thesis of the degree of Doctor of Philosophy.

…….

Assist. Prof. Dr. Aykutlu Dâna

I certify that I have read this thesis and that in my opinion it is fully adequate, in scope and in quality, as a thesis of the degree of Doctor of Philosophy.

…….

Assist. Prof. Dr. Emrah Özensoy

Approved for the Graduate School of Engineering and Science:

…….

Prof. Dr. Levent Onural

Director of the Graduate School

ABSTRACT
PEPTIDE NANOFIBERS FOR ENGINEERING TISSUES AND IMMUNE SYSTEM

Rashad Mammadov
PhD in Materials Science and Nanotechnology
Supervisor: Assoc. Prof. Dr. Ayşe Begüm Tekinay
Co-supervisor: Assoc. Prof. Dr. Mustafa Özgür Güler
February, 2014

Interdisciplinary work at the interface of biology and materials science is important for finding cures to complex diseases. Achievements in materials science allow us to control materials at nanoscale and design them according to specific therapeutic purposes. This includes incorporating biophysical and biochemical signals into materials to make them biologically functional. These signals are sensed by cells in normal or pathological cases and influence their decision-making process, which eventually alters cellular behavior. However, cellular environment is so complex in terms of these signals that recapitulating it with synthetic materials is unattainable considering our limited resources. Therefore, we need to distinguish those signals that are structurally simple, but at the same time biologically critical, that would drive cellular behavior to desired outcome.

In this thesis, I will describe peptide nanofiber systems for tissue engineering and vaccinology applications. First system is inspired from heparan sulfate (HS) – a natural polymer in extracellular matrix – that bind to growth factors and regulate their functioning, therefore central for induction of various physiological processes. Peptide nanofibers with right composition of bioactive chemical functional groups from HS showed specific interaction with growth factors and induced endothelial cells to form blood vessels similar to natural matrices carrying HS. Considering mentioned features, these peptide nanofibers could be useful for effective regeneration of tissues. Secondly, the peptide nanofiber system carrying pathogenic DNA motives, which is an infection signal, was developed. While non-immunogenic by itself, these nanofibers shifted immune response against pathogenic DNA towards a context that is useful for fighting intracellular pathogens and cancer.

Overall, this thesis demonstrates that structurally simple but appropriate biophysical and biochemical signals could be synergistic for inducing desired biological processes at the nanoscale.

Keywords: peptide amphiphiles, nanofibers, biomaterials, tissue engineering, drug delivery, immunomodulation.

ÖZET
DOKU VE İMMÜN SİSTEMDE MÜHENDİSLİK İÇİN PEPTİT NANOFİBERLER

Rashad Mammadov
Malzeme Bilimi ve Nanoteknoloji, Doktora
Tez danışmanı: Assoc. Prof. Dr. Ayşe Begüm Tekinay
Eş Danışman: Assoc. Prof. Dr. Mustafa Özgür Güler
Şubat, 2014

Biyoloji ve malzeme biliminin disiplinlerarası çalışması kompleks hastalıklara çare bulunması için önemlidir. Malzeme biliminin geldiği nokta bize malzemeleri nanoölçekte kontrol etmemizi ve onları spesifik tıbbi amaçlara yönelik tasarlamamızı mümkün kılıyor. Bu biofiziksel ve biyokimyasal sinyalleri malzemelere onları biyolojik olarak fonksiyonel yapmak için ekleyebilmemizi içeriyor. Bu sinyaller normal veya hastalık durumunda hücreler tarafından algılanarak onların karar verme süreçlerini etkiliyor ve sonunda hücre davranışında değişikliğe yol açıyorlar. Ancak hücre ortamı bu sinyaller açısından o kadar karmaşıktır ki sentetik malzemelerle bunları taklit etmemiz – kaynaklarımızın sınırlılığını göze alınca – ulaşılabilir değildir. Bu yüzden yapısal olarak sade fakat aynı zamanda biyolojik olarak kritik ve hücre davranışını arzu edilen yöne doğru çekecek sinyalleri ayırt etmemiz gerekiyor.

Bu tezde doku mühendisliği ve bağışıklık uygulamaları için peptit nanofiber sistemler açıklanmıştır. İlk sistem hücrelerarası matrisde büyüme faktörlerine bağlanan ve onların fonksiyonlarını düzenleyen, bu yüzden fizyolojik süreçlerin çalıştırılması için merkezi olan polimerden – heparan sülfattan (HS) esinlenilmiştir. HS'tan doğru kimyasal fonksiyonel grupları taşıyan peptit nanofiberler büyüme faktörlerine karşı spesifik etkileşim göstermiş ve HS içeren doğal matrisler gibi endotel hücreleri damar oluştumaya yönlendirmiştir. Bu özellikleri göz önünde bulundurduğumuzda bu peptit nanofiberler dokuların efektif rejenerasyonu için faydalı olabilir. İkinci olarak bir enfeksiyon sinyali olan patojenik DNA'dan motifler taşıyan peptit nanofiberler sistemler geliştirilmiştir. Kendi başına immünojenik olmamasına rağmen, bu nanofiberler patojenik DNA'ya karşı immün tepkiyi hücreiçi patojenler ve kansere karşı savaşmasına yararlı olabilecek bir kontekste yönlendirmiştir.

Bütünlükte, bu tez yapısal olarak sade fakat uygun biyofiziksel ve biyokimyasal sinyallerin arzuedilen biyolojik süreçleri çalıştırabilmemiz için sinerji oluşturabileceğini gösteriyor.

Anahtar kelimeler: peptit amfifil, nanofiber, biyomalzeme, doku mühendisliği, ilaç taşıma, immünomodülasyon.

Babam Nizam'a…

(1933-2013)

ACKNOWLEDGEMENTS

This thesis became a possibility due to support of my supervisors. Since accepting my request to perform PhD dissertation work under their supervision, Prof. Tekinay and Prof. Guler opened lab opportunities to me, supported me to participate in symposiums and enrolled me in interesting projects from which I learned many. I would like to acknowledge these and their patience to let me grow.

I acknowledge Dr. Aykutlu Dana for assisting me in AFM studies, as well as his evaluating me as a member of thesis progress committee regularly. Special thanks also to Dr. Mahinur Akkaya, member of thesis progress committee, whose joy and cheerfulness smoothened process. I appreciate Dr. Bahri Aydın for his collaboration in corneal angiogenesis assay and Dr. Handan Kayhan for flow cytometry work.

I performed most of my dissertation work by using UNAM facilities. I would like to thank to everyone contributed to the making and working of UNAM. Operators (engineers) of facilities are indispensable for the working of UNAM and contributed to this thesis much also. I would like to express my gratitudes, especially to Zeynep Erdoğan and Mustafa Güler for their contributions.

TÜBİTAK deserves great portion of acknowledgements due to its financial support. I received my stipend from TÜBİTAK BİDEB 2215 - PhD fellowship programme during PhD period. Also, our experimental work was supported by TÜBİTAK projects 110M355 and 112T042.

NBT (Prof. Tekinay's group) and BML (Prof. Guler's group) lab members were there when I needed them. Certain parts of my dissertation work are fruits of collaborations with lab members like Büşra, Göksu, Şehmus, Sıla, Ahmet Emin and Melis. I would like to thank for their kindness and contributions to this thesis.

I appreciate my old friends Seymur, Ruslan and Tural who were a great consolation for me during this period.

In UNAM, I also met with Dr. Mecit Yaman, to whom I feel extremely grateful especially for the friendship he provided me. The books he recommended me to read became a way of communication between us after all. Now, I would like to remind "Bununla beraber hayatımın bir safhasında ufak bir eser yazmaya muvaffak oldum.".

My grandfather would have been happy, had he seen my finished dissertation. My early imaginations and ideas about science came from him, who was a physics professor.

I understood my parents after my daughter Gülnare was born. I understood that what you owe to them cannot be paid. I appreciate their and my sister Arzu's constant support, which boosted my psychology from time to time. I have also special thanks to my parents-in-law, who were equally supportive and encouraging.

At last, one was constantly with me in good days and bad days. I have very very special gratitudes to my wife Büşra who carried our rose and gave birth to her this year.

TABLE OF CONTENTS

LIST OF ABBREVIATIONS

AFM	**:**	Atomic Force Microscope
BMP	**:**	Bone Morphogenic Protein
BrdU	**:**	Bromodeoxyuridine
CD	**:**	Circular Dichroism
CS	**:**	Chondroitin sulfate
FACS	**:**	Fluorescence Activated Cell Sorter
FGF	**:**	Fibroblast Growth Factor
GAG	**:**	Glycosaminoglycan
GF	**:**	Growth Factor
HGF	**:**	Hepatocyte Growth Factor
HM-PA	**:**	Heparin Mimetic Peptide Amphiphile
HS	**:**	Heparan Sulfate
HSPG	**:**	Heparan Sulfate Proteoglycan
HUVEC	**:**	Human Umbilical Vein Endothelial Cell
ITC	**:**	Isothermal Titration Calorimetry
MHC	**:**	Major Histocompatibility Complex
NGF	**:**	Nerve Growth Factor
ODN	**:**	Oligodeoxynucleotide
PA	**:**	Peptide Amphiphile
PAGE	**:**	Polyacrylamide Gel Electrophoresis
SEM	**:**	Scanning Electron Microscope
TCP	**:**	Tissue Culture Plate
TEM	**:**	Transmission Electron Microscope

TLR	**:**	Toll-like receptor
VEGF	**:**	Vascular Endothelial Growth Factor

LIST OF FIGURES

LIST OF TABLES

CHAPTER 1

INTRODUCTION

1. INTRODUCTION

Biomaterials could provide solutions to various health problems. Today, as a result of economic and technological development, people live longer; communication and transportation are in unprecedented levels. However, increased life expectancy brought elevated incidence rate of chronic and degenerative diseases such as organ failures, cancer, neurodegenerative diseases, and chronic wounds, which cause extensive tissue damage. Also, enhanced communication and transportation cause pathogens to breach barriers against their intercontinental spread, increasing risk of pandemics. To find cures to these diseases, we need a paradigm shift in our approach. Interdisciplinary work of biology and materials science is promising in this regard. Recent achievements in materials science allow us to design materials with the purpose of curing pathophysiologies. Materials relevant to biology can be controlled, functionalized and characterized at nanoscale. Nanofibrous hydrogels for supporting cell adhesion and survival in damaged areas can be obtained with fiber sizes of a few nanometers. Drug delivery vehicles from polymeric nanoparticles and liposomes to gold nanoparticles can be obtained with different sizes and functionalized depending on specific purposes. In this thesis, we used self-assembling peptide amphiphile systems to design novel materials for tissue engineering and modulating immune response.

1.1. Self-assembling peptide amphiphile molecules

Peptide amphiphile molecules are composed of a hydrophilic peptide part and a hydrophobic alkyl tail covalently bound to each other (Figure 1.1a).[1] Charged aminoacids are included in peptide part, which besides increasing solubility of molecule, allows controlling the self-assembly process. Upon neutralization of these charges with oppositely charged ions, pH change, macromolecules or another peptide amphiphile, they self-assemble into higher order nanostructures such as nanofibers and nanospheres through collapse of hydrophobic part inward and peptide part outward (Figure 1.1b).[2] Nanofibers produced by this way are typically 5-15 nm in

diameter, which is fairly similar in size to fibers comprising natural extracellular matrices (ECM), therefore important to mimick ECM for regenerative medicine (Figure 1.1d.).

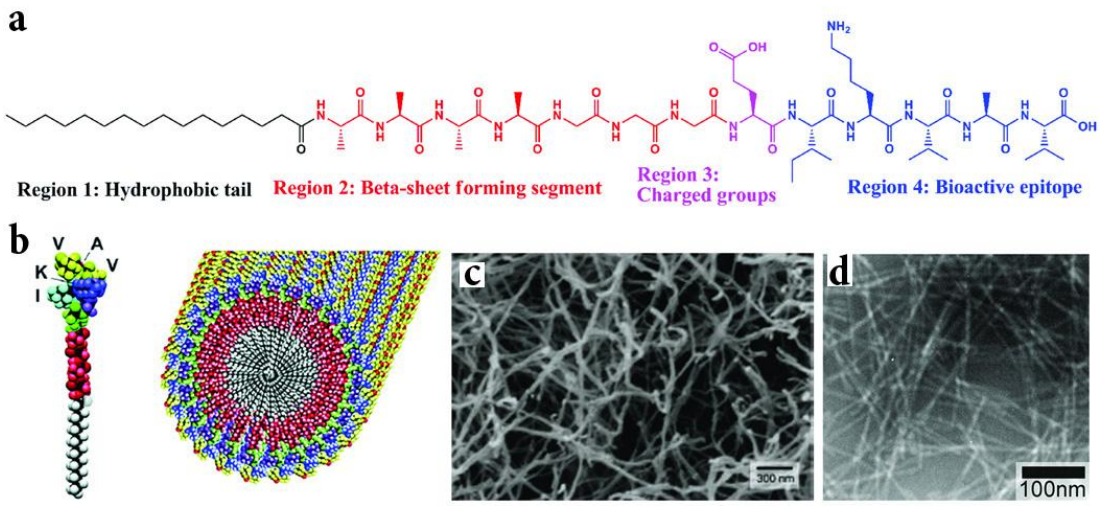

Figure 1.1. A peptide amphiphile structure. **a.** Chemical structure of a representative PA with four rationally designed modules. **b.** Molecular graphics illustration of a PA molecule with a bioactive epitope and its self-assembly into nanofibers. Note that bioactive epitopes are exposed to surrounding media in aqueous solution. **c.** Scanning electron micrograph of the PA nanofiber network formed by adding cell media (DMEM) to the PA aqueous solution. **d.** Transmission electron micrograph of the PA nanofibers. (Reproduced with permission from ref. 3, copyright © 2010 John Wiley & Sons, Inc.).[3]

Peptide nanostructures are versatile materials that are amiable to engineering for presenting biofunctional ligands (Figure 1.1a). Nanoscale structure of fibers provide high surface area to volume ratio that allows them carry epitopes (biofunctional ligands) with high density due and make them more suitable for guiding cellular physiology. Entanglements of these nanofibers emerge as macroscopic self-supporting gels at adequate concentrations (Figure 1.1c, 1.2). Gel formation can be controlled via neutralization of charges via pH change or mixing with oppositely charged molecules. This makes PA gels suitable for encapsulation of cells, growth factors or small molecules in 3D environment for *in vitro* and *in vivo* applications.

Since gel formation can be controlled externally, they can be applied also as an injectable matrix to replace native extracellular matrix in damaged tissues via less invasive methods. Besides serving as scaffolds, these nanofibers provide an environment to cells invading into matrix where they can be manipulated with peptide signals exposed to aqueous solution from nanofibers, such as shown in Figure 1.1b.

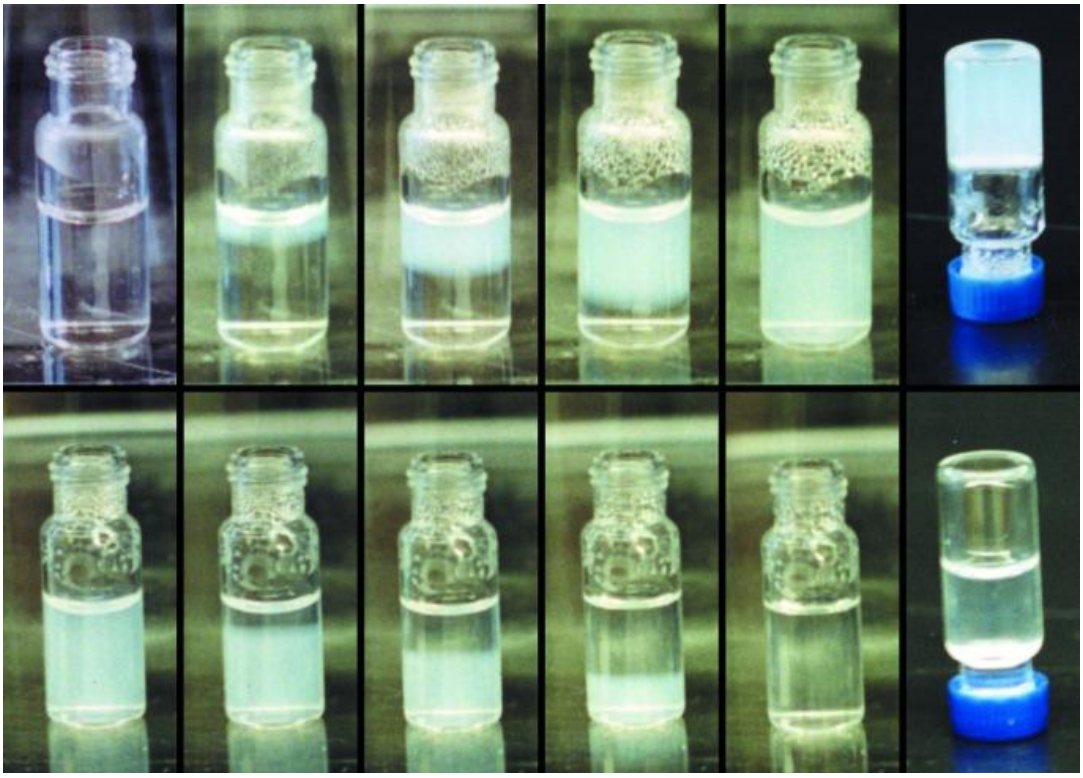

Figure 1.2. Time-dependent PA gel formation and reversion of process via changing pH. In upper part of figure, PA molecule is dissolved in water at a concentration of 0.5% by weight at pH 8 and is exposed to HCl vapor. As the acid diffused into the solution a gel phase is formed, which self-supports upon inversion (far right). In lower part of figure, the same gel is treated with NH_4OH vapor, which increases the pH and disassembles the gel, returning it to a fully dissolved solution (Reproduced with permission from ref. 2, copyright © 2002 National Academy of Sciences, U.S.A.).[2]

Peptide part can be engineered to carry epitopes from active domains of proteins such as growth factors and ECM proteins or to bind high molecular weight molecules such as heparin to generate functional nanofibers. All these properties make them very powerful tools for drug delivery and regenerative medicine. Peptide amphiphiles with heparin binding epitopes has been previously shown to exhibit strong binding to heparin.[4-5] Heparin binding conferred these nanofibers a strong affinity to angiogenic growth factors. Probably due to the mentioned feature, these nanofiber gels induced *in vitro* and *in vivo* vascularization better than control PA gels and standard scaffolds such as collagen (Figure 1.3).[4-5]

PA nanofibers with laminin-derived epitope (IKVAV) induced neuronal differentiation of NSCs better than laminin, probably due to increased density of bioactive epitope on nanofibers.[6] PAs carrying epitopes for TGF-β (transforming growth factor) binding derived from phage display library induced *in vivo* cartilage regeneration.[7] In addition, several studies for tissue regeneration and drug delivery by using PA molecules were published in recent years making PA nanostructures a promising platform for regenerative medicine applications.

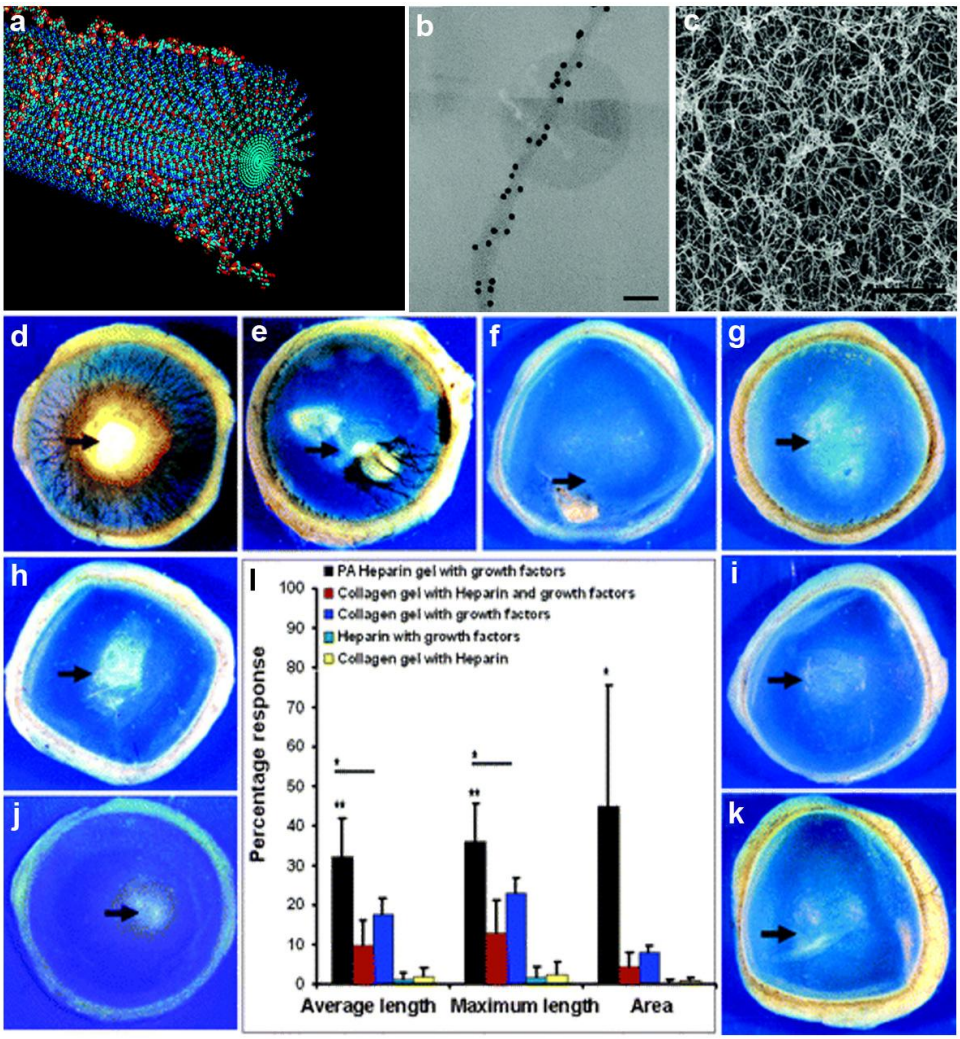

Figure 1.3. Heparin-binding peptide amphiphile. **a.** Illustration of nanofibers formed by mixing heparin and PA. Heparin is presented by nanofibers into aqueous solution **b.** TEM image showing bundle of nanofibers bound to heparin-gold nanoparticles (black dots) (scale bar = 40 nm) **c.** SEM image of nanofiber network formed by heparin and PA (scale bar = 2 μm). **d-k.** *In vivo* angiogenesis assay. Rat cornea photographs 10 days after the placement of various materials at the site indicated by the black arrow. **d.** Heparin/PA nanofiber networks with growth factors induced extensive neovascularization. Collagen with heparin and growth factors (**e**) and collagen with growth factors (**f**) show some neovascularization. Heparin with growth factors (**g**), collagen with heparin (**h**), PA with growth factors (I), Heparin/PA without growth factors (**j**) and growth factors alone (**k**) showed little to no neovascularization. The bar graph (l) contains values for the average and maximum length of new blood vessels and the area of corneal neovascularization. A 100% value in the area measurement indicates that the cornea is completely covered, and a 100% value in the length parameters indicates that the new vessels are as long as the diameter of the cornea (bars are 95% confidence levels, * $p < 0.05$ when Heparin/PA gel was compared to collagen gel with growth factors, ** $p < 0.005$ when Heparin/PA gel with growth factors was compared to all of the other controls). (Reproduced with permission from ref. 5, copyright © 2006 ACS).[5]

1.2. Materials for tissue engineering

Organ failures and tissue damages require organ and tissue replacement, however organ donors are in scarcity. Another way is to unleash regenerative potential of our body, which naturally occurs during development of fetus. This requires the understanding of type of signals that are sensed by cells in their extracellular matrix and coax them into regenerative pathway. While biology provides us with this type of knowledge, regenerative medicine aims to find ways for presenting these cues to cells in an appropriate way. Tissue engineers exploit biomaterials decorated with these signals to direct cells to proliferate, differentiate or organize into desired tissue structures such as inducing endothelial cells to form blood vessels. Extracellular matrix (ECM) of cells has long been deemed as support material for cells, so main features sought in biomaterial scaffolds were mechanical properties.[8] Physical properties such as porosity and stiffness have been emphasized extensively in material design for tissue engineering in the infancy of field. Moreover, these materials were expected to be `inert` - having minimal toxicity and immunogenicity.[9] However, lacking necessary biochemical cues for instructing cells, effect of these materials in tissue engineering were limited. Aim of material design for tissue engineering in the current paradigm is to recapitulate biophysical and biochemical features of extracellular matrix, where cells live in their natural environment, to achieve instructing cells for specific destiny.[10] However, financial considerations limit to project all complexity in ECM to designed biomaterial.[11] Natural macromolecules in ECM are used extensively as biomaterials for tissue engineering since biological cues are inherent in them.[10] However, these materials have also inherent problems regarding pathogen transmission, immunogenicity and purification. Thus, there is a need to design materials with similar functional sophistication as ECM but with simpler structural complexity. Growing understanding of principles of how cells recognize biophysical and biochemical signals in their environment, integrate them at the level of gene expression and make appropriate decisions (Figure 1.4) will pave the way to design synthetic – thus more defined - materials for tissue engineering.

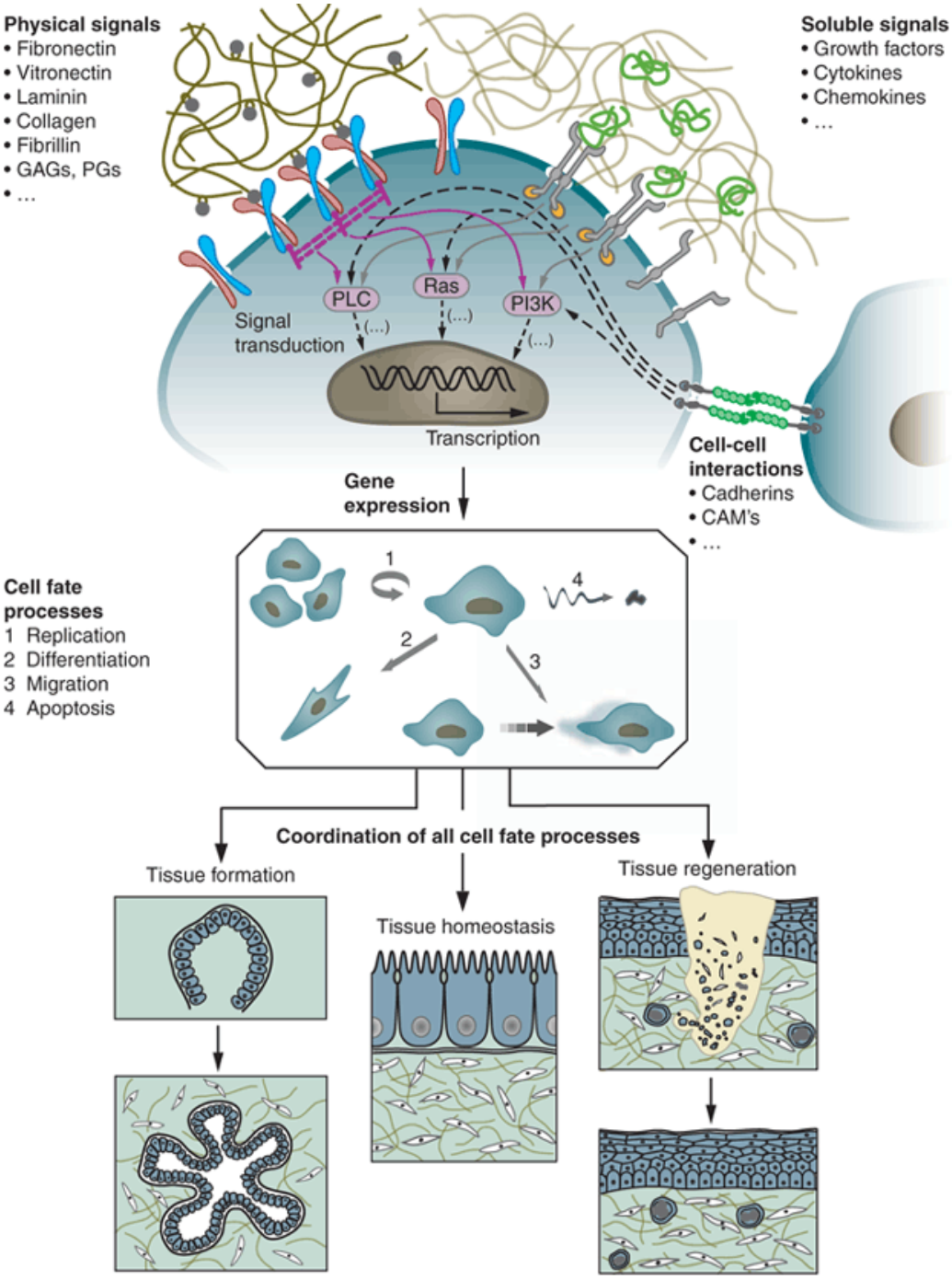

Figure 1.4. Coordination of complex physiological processes via signals sensed by cells. Cells recognize various physical and chemical signals in their environment through receptors on their membrane. This recognition is converted into signaling pathways, which eventually ends up with expression of different genes. Concerted actions of these genes influence cellular fate and induce various processes such as replication, migration or apoptosis. These cellular performances determine physiological processes at tissue level (Reproduced with permission from ref. 10, copyright © 2005 Macmillan Publishers Ltd.).[10]

What are those principles? Which distinguishable aspects of extracellular matrix are sensed by cells and what type of behavioral alterations in cells are observed as we change them? Immense amount of studies were published explaining how cells respond to biophysical signals such as stiffness, topography and size of individual fibers in ECM-like network. Stiffness of environment have shown to be a determining factor for mesenchymal stem cell (MSC) differentiation: with the increasing order of stiffness, MSCs were committed to neurogenic, myogenic and osteogenic pathways.[12] Size of fibers forming scaffolds is another cue affecting cellular behavior. Natural ECM is formed by network collagen fibrils of size at nanoscale (50-500 nm).[13-14] Smaller fiber size has larger surface area which might act synergistically with ligands carried on fibers. Endothelial cells showed more elongated phenotype, migration and capillary-like structures on micro/nano-fiber scaffold than one without nanofiber network.[15] Nanofibers allowed stretching of endothelial cells between microfibers, which is known to be critical for their responsiveness to growth factors. Neural stem cells differentiated into different lineages according to size of fibers of scaffold they were cultured on.[16] Considering available knowledge, scaffold stiffness, fiber size, porosity and topography can be adjusted according to purpose.

Recapitulating biochemical signals of natural ECM is incomparably difficult and expensive, when one considers complexity of network of these signals in ECM. Activation and performance of physiological mechanisms such as angiogenesis or neural regeneration depend on concerted act of numerous biological signals. Among these signals there are growth factors, cytokines, signaling epitopes on various structural proteins such as laminin and fibronectin, and glycosaminoglycans which bind and regulate activity of growth factors. Besides mere existence, their spatial and temporal presentation is also critical for effective regeneration. Since introducing all these ingredients into biomaterial scaffold and regulating their release from scaffolds spatiotemporally is an unattainable task, tissue engineers aim to identify critical elements in this network of biochemical signals, perturbations of which will induce regenerative pathway or desired bioactivity. In this context, conjugating integrin-binding epitopes of structural proteins, such RGD or IKVAV peptides, promote cell

adhesion to matrix.[17-20] Another strategy is delivering critical growth factors in biomaterial scaffolds. Dose of growth factors sensed by cells is a critical issue, since higher doses of growth factors might cause unwanted effects.[21] Physical encapsulation of growth factors may not be enough for slowing their release adequately, so they are conjugated to scaffolds via either non-covalent or covalent bonds. For this purpose, heparin (a highly sulfated glycoasminoglycan) has been conjugated to scaffolds, such as alginate and collagen, for binding to growth factors non-covalently and enhance their bioactivity.[22-23] This binding slowed growth factor release from scaffold and improved potency of scaffold to induce angiogenesis. Other polymers carrying sulfate groups as heparin or affinity binding peptides also exhibited increased growth factor binding and performance regarding bioactivity.[24-27] Chemical functional groups as biochemical signals are probably an irreducible form of complexity in extracellular matrix. Amazingly, it seems that they were enough to induce mesenchymal stem cell differentiation and by changing functional groups researchers were able to control cell fate.[28] These functional groups are inspired from chemical structure of extracellular matrix of various tissues. Although exact mechanism was not clear, each functional group induced stem cell differentiation into the same tissue it was inspired from. For example, phosphates (from hydroxyapatites in bone matrix) induced differentiation into osteocytes.

Both biochemical signals and biophysical signals work in the context of each other in nature. Number of ligands bound by integrins was observed to be a function of matrix stiffness in 3d scaffolds.[29] Optimal integrin binding by RGD ligands was responsible actually for induction of osteogenesis in mesenchymal stem cells at optimal stiffness. This shows that rather than focusing on biochemical signals or biophysical ones, using the right combination of simple signals from both might work synergistically and have tremendous effects on cellular behavior.

In Chapter 3 and 4 of this thesis, scaffold materials formed from networks of entangled nanofibers are described. We rendered building blocks of these nanofibers to carry chemical functional groups, which also exist on sulfated glycosaminoglycans (GAG) (please look to 1.2.1.). These building blocks are peptide amphiphile

molecules which form nanofibers when mixed with oppositely charged molecules via self-assembly. Nanofibers formed this way present chemical functional groups into environment just as GAG polymers. In chapter 3, I demonstrate that right composition of functional groups - sulfonate, hydroxyl and carboxylate together - render nanofibers avid to vascular endothelial growth factor (VEGF) and effective at inducing angiogenesis – new blood vessel formation. There, I also show that when this combination of functional groups lack one or two of these groups, functionality is severely impaired. In chapter 4, study on interaction of these nanofibers with growth factors is described. Functional groups on nanofibers made them affine to many growth factors such as VEGF, HGF and FGF-2, when compared to control nanofibers, which don't have the same composition of chemical groups. Also, interestingly, they showed affinity to the same domain of growth factors where heparin binds, which is important for bioactivity of growth factors.

1.2.1. Heparin and heparan sulfate glycosaminoglycans.

Glycosaminoglycans (GAGs) are polymers of disaccharides, carrying chemical functional groups on them (Figure 1.5). Biological roles of GAGs are not completely identified, however, it is obvious that most of them is related with their remarkable capability to bind to many proteins.[30] Heparin and heparan sulfates are members of GAGs, which has been studied extensively for their property of binding various proteins and modulate their activity. Heparin is found in mast cell and basophilic granules and serve as anti-coagulant.[30] It has the highest negative charge density of any known biological macromolecule, thanks to the sulfate and carboxylic acid groups found in its structure.[31] Average number of sulfates per disaccharide is 2.7 (Figure 1.5).[30] Heparan sulfates have similar structure but less negative charge density (average sulfate groups per disaccharide is less than 1).[30] However, disaccharide units are more variable in heparan sulfates, making them more heteregenous than heparin in terms of domains.[31] Different domains in heparan sulfates show different levels of sulfation probably allowing them to perform more complex functions (Figure 1.5). Highly sulfated domains are assumed to take role in

protein binding. Heparan sulfates are found in extracellular matrix and membrane of cells. They bind to growth factors there and protect them from enzymatic degradation, provide a reservoir of growth factors to cells and assist growth factors in their interaction with cognate receptors. Heparin is extensively used in tissue engineering because of high degree of sulfation of its monomers, which increase ability of scaffolds with heparin to bind to growth factors.

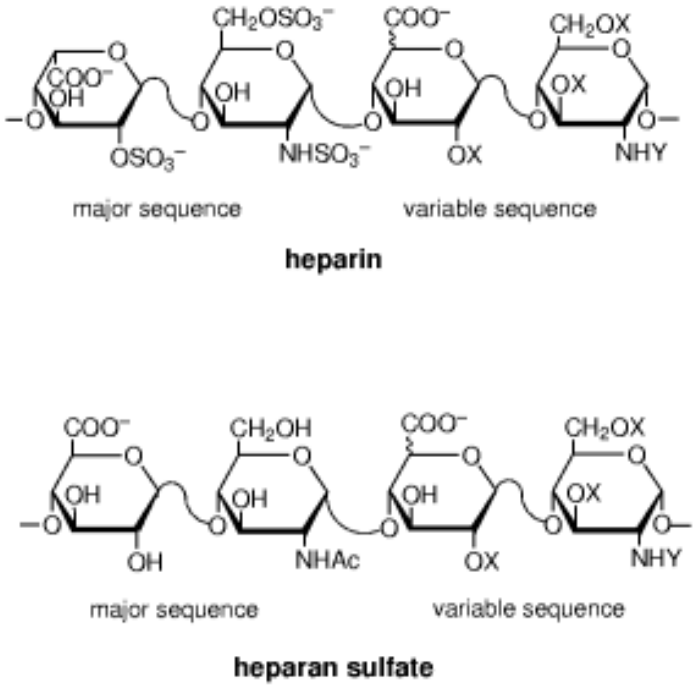

Figure 1.5. Chemical structure of heparin and heparan sulfates showing major and minor disaccharide repeating units. (X=H or SO_3^-, Y=Ac, SO_3^-, or H) (Reproduced with permission from ref. 31, copyright © 2002 John Wiley & Sons, Inc.)[31].

1.3. Materials for engineering immune response

Last part of this thesis is about materials for directing immune activity and developing vaccines against infectious diseases. Conventional vaccinology relies on introducing inactivated or live-attenuated form of pathogens into patients in an attempt to educate immune system about how to fight with the active pathogen. Basics of this strategy are fairly unchanged since invention of vaccination ("vacca"

in Latin means cow) by remarkable observation of Edward Jenner that infection with cowpox provides immunity against smallpox, in 1796. Although this strategy generates successful immune response against pathogens, it has several disadvantages. First of all, in cases of pandemic, mass production could be hampered by low growth of pathogens or scarcity of resources. Second but not least, using pathogen itself is not a defined formulation, so brings unwanted side effects and risk of becoming virulent of pathogen. For this reason, we need rational design of vaccines, which will drive immune response towards desired context (considering type of cytokines and costimulatory molecules expressed, type of cells activated) and induce long-lasting immune response, without compromising safety.[32] However, this is challenging because our knowledge of these two subjects is not sufficient.[33]

1.3.1. Pathogen-specific immune context

One question is which type of immune response is required to protect an individual from each pathogen. Immune system has evolved to protect organism against diverse pathogens, while being tolerant to self. Having a similar level of sophistication allows immune system to solve this problem (Figure 1.6). Pathogens that are able to pass first-line barriers such as skin (e.g. in cases of tissue damage) encounter with innate immune system. Innate immune system cells inspect pathogen entry sites of body such as skin or mucosal surfaces and destroy pathogens through phagocytosis or secreting antimicrobial substances upon recognition.

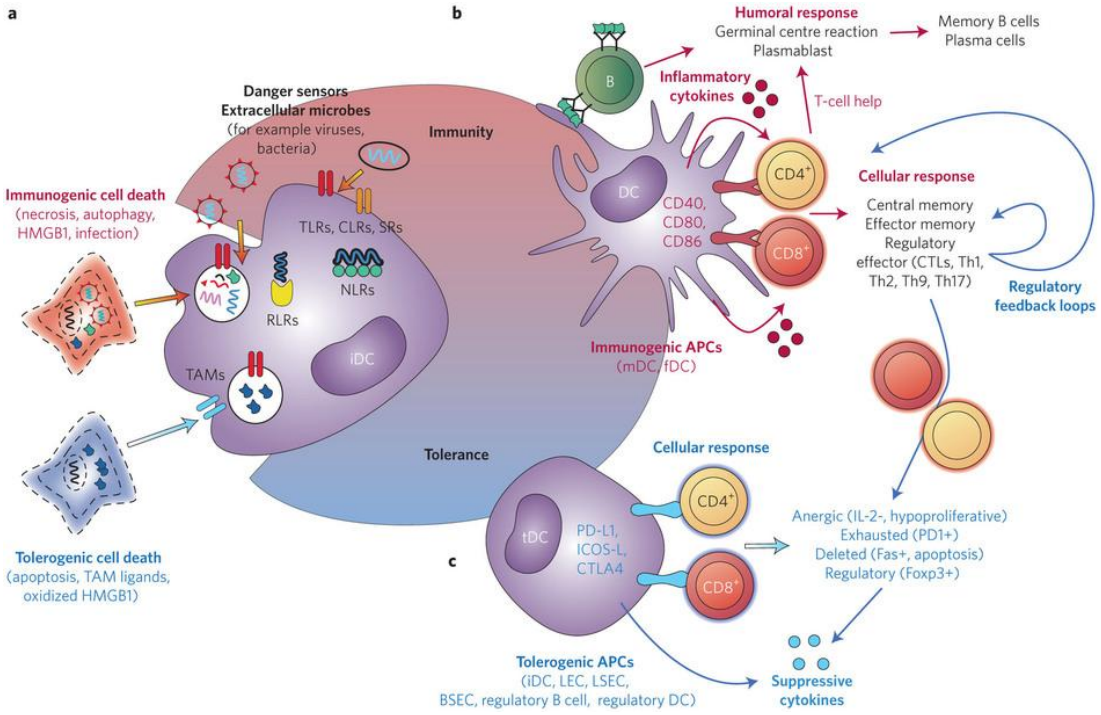

Figure 1.6. Complexity of immune system, which is evolved to distinguish pathogen from self and to provide immune context relevant to nature of pathogens. Dendritic cells (DC) distinguishes between foreign and self antigens according to microenvironmental signals. Along with other innate immune cells, their response to these signals determines the outcome of antigen recognition by T and B cells. **a.** Dendritic cells recognize immunogenic signals from infected or immunized, dying cells through danger receptors on them (TLRs, CLRs, NLRs, RLRs, SRs) and tolerogenic signals from dying self-cells or cellular debris generated by homeostatic turnover; these produce a continuous spectrum of output responses ranging from strong induction of effector-phase immunity to strong induction of tolerance, with the exact outcome determined by the integration of inputs by the dendritic cell. In response to these 'danger' or tolerizing signals, dendritic cells (and other innate cells) create the immunological context for antigen recognition by secreting cytokines, expressing diverse adhesive, co-stimulatory or regulatory receptors that provide cues to responding lymphocytes. **b.** According to mentioned cues, B cells can undergo somatic hypermutation, become short-lived plasmablasts, or differentiate into long-lived memory B cells or plasma cells while T cells can differentiate into effector cells or memory cells with distinct homing and functional capacities; effector cells can have diverse functions (Th1, Th2, Th17 and so on) depending on the context set by dendritic cells. Regulatory feedback loops are engaged even in highly inflammatory contexts, as part of the natural control system regulating immunity, and primed effector cells can be driven to anergic/exhausted states similar to tolerance at later stages of an immune response. **c.** Peripheral tolerance is maintained by a distinct set of signals: In tolerogenic contexts, T cells are driven into several different states of non-responsiveness that prevent effector responses against self or harmless environmental antigens. (Reproduced with permission from ref. 33, copyright © 2013 Macmillan Publishers Ltd.).[33]

Pathogen recognition by innate immune cells is maintained by germ-line encoded receptors, which do not change during the lifetime of organism, differing from adaptive immune cells. These receptors, collectively known as pattern recognition receptors (PRR), recognize certain common patterns from pathogens, such as peptidoglycan molecules in bacterial cell wall or unmethylated CpG (or CG, denoting cytosine and guanine) motives from viral/bacterial DNA.[34-35] PRRs include several family of secreted (mannose-binding lectin), transmembrane or cytosolic receptors.[36] Most studied and known receptor family among PRRs are Toll-like receptors (TLR). Toll-like receptors can be at cell-membrane (those recognizing surface features such as peptidoglycan or LPS layer of bacterial cell wall and membrane) or endosomal membrane (those recognizing microbial nucleic acids).

Binding of pathogenic patterns to PRRs shape adaptive immune responses.[36] This happens through activation of various signaling pathways which end up with expression of cytokines and surface receptors called as co-stimulatory molecules. Cytokines are protein molecules binding to their receptors on target cells and induce signalling pathway. Co-stimulatory molecules are expressed by antigen-presenting cells and required for activation of adaptive immune cells specific for antigen. Although these signals are necessary, neither of them is sufficient to induce adaptive immune response. However, TLR-induction is known to be sufficient to provide all factors for initiation of robust adaptive immune response.[36] Thus, besides forming another line of defense to clear infection, innate immune cells also controls the activation, types and duration of the adaptive immune response.[36]

Adaptive immune system fights with infections with two main types of immune cells – B cells and T cells. Both of cell populations have vast repertoire of antigen receptors for almost every possible antigen in the environment. These receptors are generated through random arrangement of genes, which gives rise to receptor for specific antigen on every cell. Adaptive immune response also provides memory formation about pathogens after clearing infection, through memory cells. These cells re-induce adaptive immune response after encountering antigens later. Antigen-presenting cells (APC), which are mainly dendritic cells, form link between innate

and adaptive immune system. They process and present antigens, which they recognized as foreign, on their surface to T-cells. Cytokines and co-stimulatory molecules expressed by APCs accompany to presentation of antigen at immunological synapse (Figure 1.7.).[37] T-cells integrate these signals and decide on nature of ensuing immune response.[33]

B-cells are activated by T-cells and accompanying cytokine signals. They secrete antibodies – receptors on their surface formed by combinatorial mechanism, as an effector function. These antibodies detect antigens in body fluid, so this type of response is called humoral response (Figure 1.6). Antibody binding renders toxins ineffective, and pathogens vulnerable to phagocytosis by macrophages. This is why this type of immune response is especially effective on extracellular pathogens. However, some pathogens such as viruses or mycobacterium reside in cells. Cell-mediated immune response is required to clear this type of infections. Effector function of cell-mediated immune response is activated by CD8+ cytotoxic T-cells, which induce death mechanism in cells expressing particular antigen. T-cell receptors, contrasting to B-cell ones, are not secreted, but interact with MHC molecules presented by antigen-presenting cells – mainly dendritic cells.

To summarize, adaptive immune response is antigen-specific immune response against pathogens, providing effective clearance from and memory formation about pathogens. Nature of adaptive immune response to antigen is determined by cytokines, co-stimulatory molecules and possibly other factors expressed by antigen-presenting cells (Figure 1.7).[33] These molecules are expressed according interaction of pathogen with innate immune cells through binding of pathogen-associated molecular patterns – LPS layer, CpG DNA - to pathogen recognition receptors such as TLRs.[32-33] Understanding these mechanisms might allow us to trigger them upon purpose with synthetic and defined formulations, rather than pathogen itself.

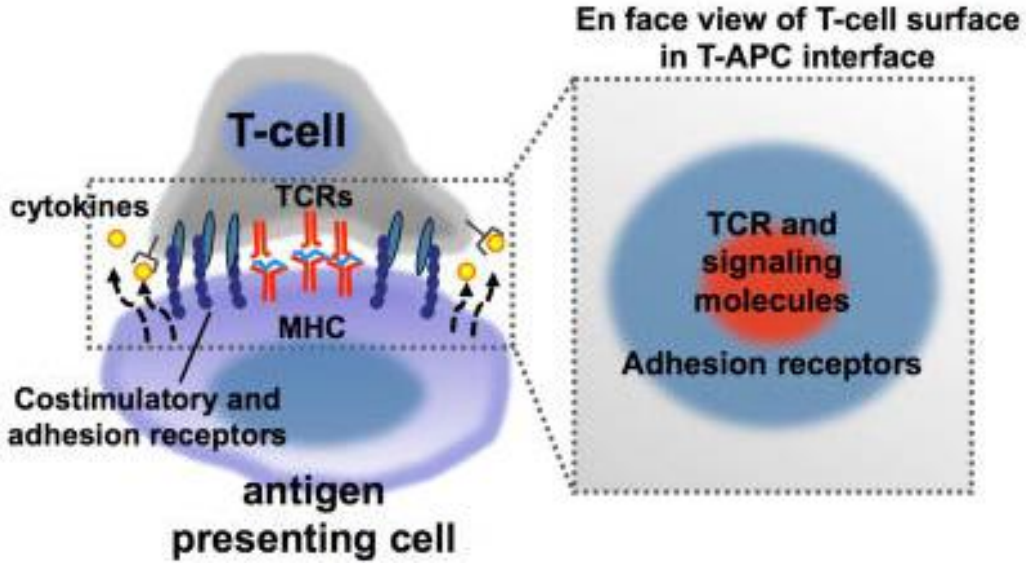

Figure 1.7. Illustration of key receptor-ligand interactions at the immunological synapse formed between an antigen presenting cell and a T-cell during T-cell activation. Profile of cytokines and co-stimulatory molecules binding to their target receptors educate adaptive immune system about nature of infection, which allows adaptive immune cells to elicit an appropriate immune response. (Reproduced with permission from ref. 37, copyright © 2012 John Wiley & Sons, Inc.)[37]

1.3.2. How to drive immune response to desired context?

Another barrier to rationalize vaccine design is our insufficient understanding of how we can drive immune response to desired context such as balance between effector/memory cells, or cell-mediated or humoral immunity.[33] Antigens themselves do not generate immune response, so molecules called adjuvants are added into vaccine formulations, which trigger immune system against antigen. Success of these adjuvants are based largely on antibodies made by B-cells.[38] This type of immune response is not competent against intracellular pathogens (e.g. tuberculosis), which can be cleared by the action of T-cells and macrophages (cell-mediated immunity). We need tools that would allow us to tune activity, magnitude and duration of various modules of immune system, such as cytotoxic T-cell activity or antibody secretion by B-cells. These tools could be found among signatures of pathogens that are recognized by immune system. Mentioned signatures can be classified as

chemical ones, which are known in literature as pathogen-associated molecular patterns (PAMP), and physical ones such as size and shape of pathogen.

PAMPs that bind PRRs (Pathogen Recognition Receptors) are promising as vaccine adjuvants, since they induce innate immune cells, which eventually shape adaptive immune response. Existence of TLR ligands in phagocytosed antigenic cargo is necessary for presentation of antigens with MHCII on the surface of dendritic cells.[39] Besides inducing antigen-presentation, profile of cytokines and co-stimulatory molecules induced by different PAMPs shape immune response according to pathogen to be destroyed.

In this context, CpG ODNs have been shown to act as safe adjuvants and drive immune response to cell-mediated immunity (Table 1.1). These are oligodeoxynucleotides with cytosine-guanine motives, where cytosine is unmethylated.[40] These motives are less frequent in vertebrate DNA than bacterial DNA, also higly methylated.[40] Mammalian immune system recognizes bacterial/viral DNA or CpG ODNs in endosomes of certain immune cells like B-cells and plasmacytoid dendritic cells via TLR9 receptor.[41] Binding of CpG ODN to TLR9 induce signaling pathways which end up with synthesis of pro-inflammatory cytokines, interferons and co-stimulatory molecules and maturation of dendritic cells.

Interactions of the immune system with pathogens are shaped not only by danger signals, but also by the physical nature of microbes, which are biological microparticles and nanoparticles.[33] Soluble exogenous antigens are not displayed by cross-presentation (MHCI), while pathogenic or particlulate antigens can be displayed.[37] Designing materials presenting these signatures to immune system on the same physical entity as pathogens, would allow us to exploit synergism between chemical and physical signals. Understanding effect of each signal on immune system will allow us to shape immune response by rationally changing concentration of each signal. While biochemical signals on pathogens are studied deeply, there is a lack of knowledge on how these perform in the context of physical signals such as size and shape. In Chapter 4, we studied how pathogenic CpG DNA signal acts in the context of shape of carrier. Our findings show that shape alters immune response to

CpG DNA, where nanofiber delivery is more relevant to induce cell-mediated immunity.

Table 1.1. Effect of "K/B" and "D/A" ODN on the Immunogenicity of Engerix B.

Normal recipients	Immunization		
	1^o	2^o	3^o
Vaccine alone	<30 (60)	4300 (100)	9200 (100)
Vaccine + D/A ODN	940 (100)	8400 (100)	21,700 (100)
Vaccine + K/B ODN	120 (80)	10,600 (100)	20,500 (100)
SIV-infected recipients (viral load < 10^7)	Immunization		
	1^o	2^o	3^o
Vaccine alone	< 10 (0)	<10 (20)	<10 (20)
Vaccine + D/A ODN	< 10 (0)	320 (100)	430 (100)
Vaccine + K/B ODN	220 (80)	400 (100)	740 (100)

Rhesus macaques (5–6/group) were immunized with 500 μl of Engerix B vaccine plus 300 μg of "K/B" or "D/A" ODN in alum. Serum anti-HepB Ab titers were monitored by ELISA. Average titers, and percent of animals with protective titers (in parenthesis) are shown. Note that the average response after both primary and secondary immunization was significantly higher in groups immunized with CpG ODN plus Engerix B vs. vaccine alone (Reproduced with permission from ref.42, copyright © 2009 Elsevier).[42]

CHAPTER 2

2. DESIGN OF HEPARIN-MIMETIC PEPTIDE NANOFIBERS FOR INDUCTION OF ANGIOGENESIS.

This work is partially described in the following publication:

Mammadov R., Mammadov B., Toksoz S., Aydin B., Yagci R., Tekinay A.B. and Guler M.O. *Biomacromolecules*, 2011, (10), pp 3508–3519.[43]

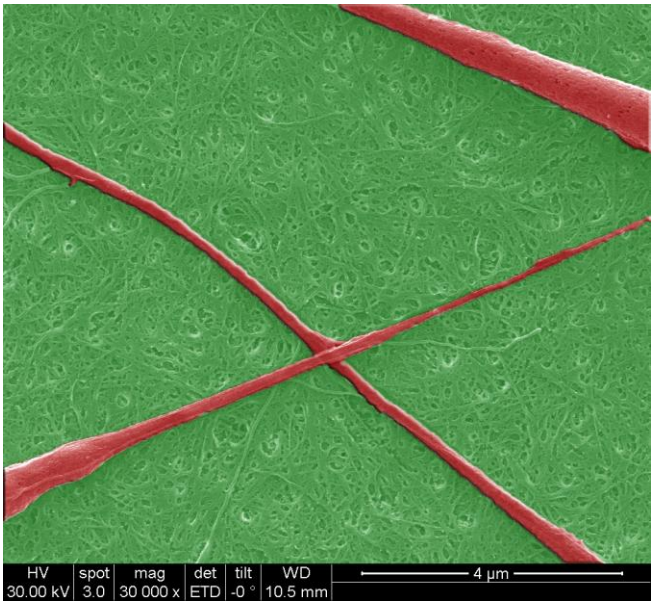

2.1. Objective

Regeneration of tissues after damage requires formation of blood vessels for survival and performance of cells migrating into damaged area. Designing materials decorated with biological signals for induction of angiogenesis would be useful for tissue engineering purposes. However, recapitulating all the signals regulating blood vessel formation is not feasible. Simpler and still effective approaches in mimicking microenvironment of angiogenesis (new blood vessel formation) are required. Sulfated glycosaminoglycans (GAG), which are an essential part of basement membrane, a specialized extracellular matrix of endothelial cells, bind to growth factors critical for angiogenesis and regulate their activity. Chemical functional groups and their distribution on GAGs, especially on heparan sulfates, are known to be critical for growth factor binding and induction of angiogenesis. In this study, our objective was to design scaffold material with similar fiber size to natural ECM and GAG-mimicking chemical functional groups on fibers. We aimed to identify appropriate composition of simple functional groups on nanoscale fibers that would be sufficient to induce angiogenesis.

2.2. Introduction

Regenerative medicine studies offer promising therapeutic approaches for the repair of damaged tissues. Induction of angiogenesis is an important mechanism for tissue repair.[10] The capillaries can only deliver oxygen and nutrients to the cells that are located at a distance of up to 200 μm, and thus angiogenesis is required for cells further away during new tissue formation.[44] Angiogenesis is triggered by the integration of various neovascularization signals by endothelial cells, which in turn differentiate to form new capillaries. Structural proteins of the extracellular matrix (ECM) (laminin, collagen, etc.), growth factors (VEGF, FGF-2, etc.), and glycosaminoglycans (heparan sulfate, etc.) make up a framework of neovascularization signals for endothelial cells.[45] Understanding the interactions between these biomolecules and endothelial cells and their roles in the regulation of

angiogenic processes paves the way to design effective synthetic biomaterials for induction of new blood vessel formation. Conventional tissue engineering strategies utilized some of the biological molecules mentioned above to provide bioactivity for promoting angiogenesis[46] because synthetic biomolecules that have been produced so far lacked the ability to mimic the functions of all of these biological components. The main motivation for developing new synthetic ECM mimicking biomaterials is to minimize utilization of the above-mentioned natural biomacromolecules exogenously with the aim of reducing cost, preventing batch-to-batch variation, and avoiding biological contamination. Therefore, designing smart biomaterials that can harness endogenous factors for desired bioactivity is essential.

Among the basic components of the signaling framework for endothelial cells, heparan-sulfate proteoglycans (HSPGs) bind to angiogenesis promoting growth factors and their receptors through heparan sulfate chains and induce growth factor signaling (Figure 2.1.).[47-50] Mice lacking heparan sulfate chain on HSPG molecule reveal defective angiogenesis and wound healing.[51] Binding of growth factors to HSPGs, which strictly depends on the distribution of functional groups, such as sulfate, hydroxyl and carboxyl groups, on heparan sulfate chains, protects growth factors from degradation, increases local concentration of growth factors, and enhances growth factor-receptor interactions, which are important for long-term stimulation of signaling pathways in endothelial cells.[8, 50, 52-53] Using glycosaminoglycans (e.g., heparin) within tissue engineering scaffolds has been shown to enhance angiogenesis significantly while reducing the need for exogenous growth factors at *in vivo* studies.[5] A peptide amphiphile (PA) scaffold for angiogenesis was previously developed by mixing heparin-binding PA molecule and heparin.[5] Heparin-binding PA molecule allowed growth factor binding and helped formation of various functional tissues.[5, 54-55] However, being an animal-derived product, utilization of heparin in tissue engineering systems might have potential side effects (e.g., immune reactions).[56] Designing heparin mimetic biomaterials will have high impacts in cellular therapy and regenerative medicine because they will enable us to avoid the use of heparin while minimizing the use of exogenous growth factors. Recent research efforts have focused on developing new scaffold materials with

proper functional groups that are sufficient to induce the desired physiological response *in vitro* without any need for growth factors or any other supplements.[28]

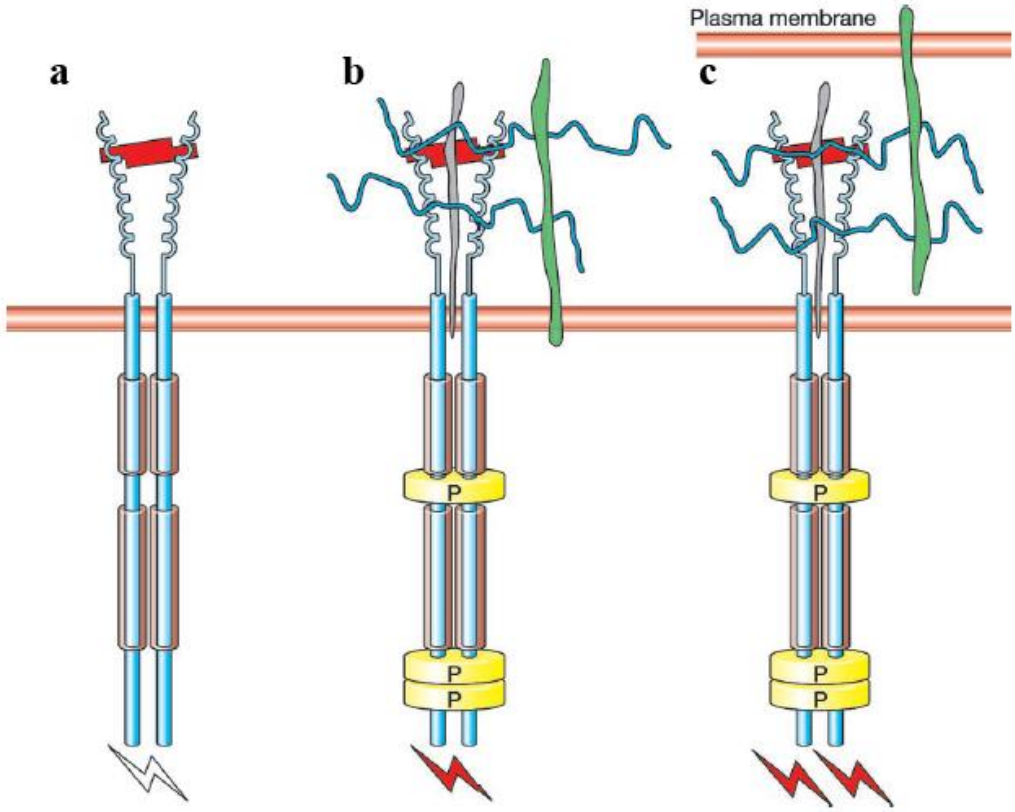

Figure 2.1. Co-receptor function of HSPG in VEGF signalling. **a.** VEGF receptor – VEGFR2 is unable for signal transduction when cells lack HSPG. **b.** HSPG (GAG side chains are shown in blue and protein part in green) expressed on endothelial cells are engaged in the VEGF/VEGFR signaling complex and may affect signaling quantitatively (by stabilizing the complex) and qualitatively (by allowing transduction of signaling pathway not induced in the absence of coreceptors. **c.** Presentation of HSPGs in trans (i.e. by another cell) leads to further stabilization of the VEGF/VEGFR signaling complex, and prolonged signal transduction (red activity arrows) (Reproduced with permission from ref. 57, copyright © 2008 Springer Science+Business Media, LLC).[57]

The addition of functional groups inspired by heparin on peptide sequences and polymers has also been previously shown to enhance growth factor binding capacity.[24, 26, 58-60] For example, sulfated alginate polymers gained growth factor binding capability and induced *in vivo* angiogenesis significantly better than

nonsulfated alginate in the presence of growth factors.[24-25] Considering these findings, we hypothesized that chemical functional groups from heparan sulfates on peptide nanofibers, will recapitulate their function. As a result, heparin-mimetic PA nanofiber gel would bring together two distinct signal in ECM – biophysical signal of nanofiber network mimicking nanofibrous matrix of ECM and biochemical signal of chemical functional groups on heparan sulfates. Heparin-mimetic PA molecule functionalized with bioactive groups was designed and synthesized for mimicking functionality of heparan sulfates in ECM. The heparin-mimetic PA molecules self-assemble to form nanofibers with ability to bind to growth factors and to promote angiogenesis without the need for addition of exogenous heparin or growth factors. This chapter demonstrates that nanostructures with bioactive chemical groups inspired from biological macromolecules can be used to activate biological machinery for regenerative medicine applications.[11, 28]

2.3. Results and Discussion

To mimic natural extracellular environment that induces angiogenesis, we designed PA molecules which carry chemical features of heparan sulfate molecules in ECM to enable enhanced functioning of the growth factors that are crucial for angiogenesis. Heparan sulfates are sugar polymers with chemical functional groups on these sugar units. Key functional groups in heparan sulfate polymer chain are highlighted in Figure 2.2 for heparin – clinically used glycosaminoglycan molecule with similar structure to heparan sulfate. These functional groups are carboxylic acid (-COOH), hydroxyl (-OH), sulfate ($-SO_4$), sulfonate and sulfamate or N-linked sulfonate ($-N-SO_3$). To assess the importance of these functional groups during angiogenesis process, several PA molecules were designed that carry from three to zero of these functional groups (Figure 2.2). Heparin-mimetic PA (HM-PA after here) molecule is decorated with carboxylic acid, hydroxyl, and sulfonate groups. Carboxylic acid and hydroxyl groups are added through coupling aspartic acid/glutamic acid and serine amino acids (side chains of these amino acids), respectively. Sulfonate group is added through coupling sulfobenzoic acid to side chain of lysine amino acid.

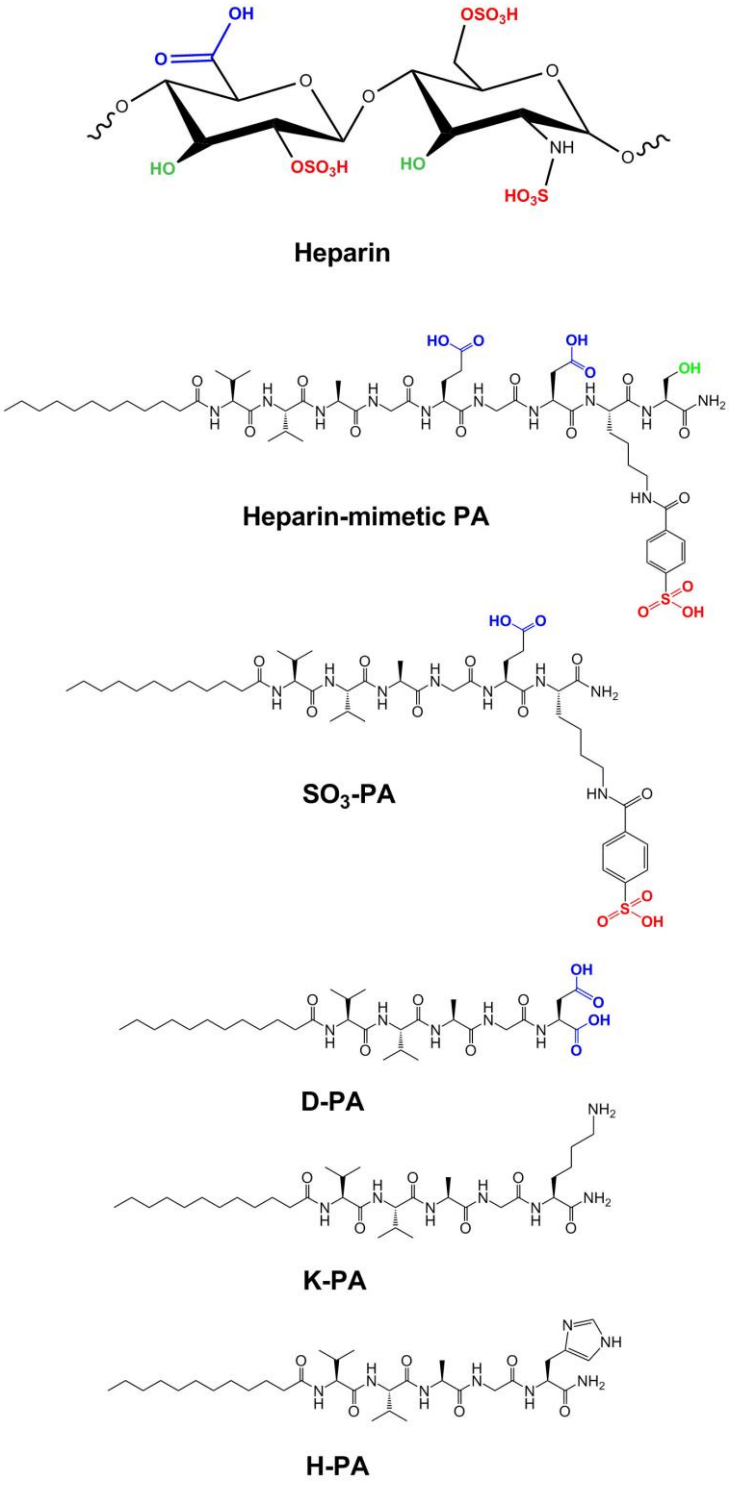

Figure 2.2. Chemical structures of heparin and designed peptide amphiphiles. Functional groups inspired from heparin are colored. Heparin-mimetic PA molecule SO_3-PA, D-PA and H-PA carries 3, 2, 1 and 0 functional groups from heparin, respectively. K-PA is used to induce nanofiber formation with (-) charged PAs.

The other molecules have less functional groups than HM-PA: SO_3-PA, has sulfonate and carboxylic acid groups, D-PA only carboxylic acid groups and H-PA no functional groups from heparin. H-PA was designed to neutralize and self-assemble into nanofibers at physiological pH to control the effect of a nonbioactive PA gel during angiogenesis. Heparin was mixed with K-PA (K-PA/Heparin) to observe the effect of heparin on bioactivity of the PA gel.

All synthesized PA molecules were purified with High-Performance Liquid Chromatography (HPLC) and analyzed with liquid chromatography-mass spectrometry (LC-MS). In LC analysis, molecules were passed from hydrophobic stationary phase (c18 alkyl tails covalently bound to silica particles), which interacts with alkyl tails of PA molecules. By running gradient from an aqueous phase (water) to organic phase (acetonitrile), PA molecules were eluded according to hydrophilicity and detected with UV detector (at 220 nm wavelength). Indeed, elution time points given in LC chromatograms (Figures 2.3b – 2.7b) were consistent with hydrophilicity of molecules. More hydrophilic ones are eluded at earlier time point, such as HM-PA with the highest number of charged groups eluded at the earliest time point, while K-PA with the lowest number of charged group eluded at the latest time point. Mass spectra of peaks obtained in LC chromatograms indicated that all synthesized PA molecules have similar masses to the expected ones (Figures 2.3c – 2.7c). These purified molecules were used in further studies.

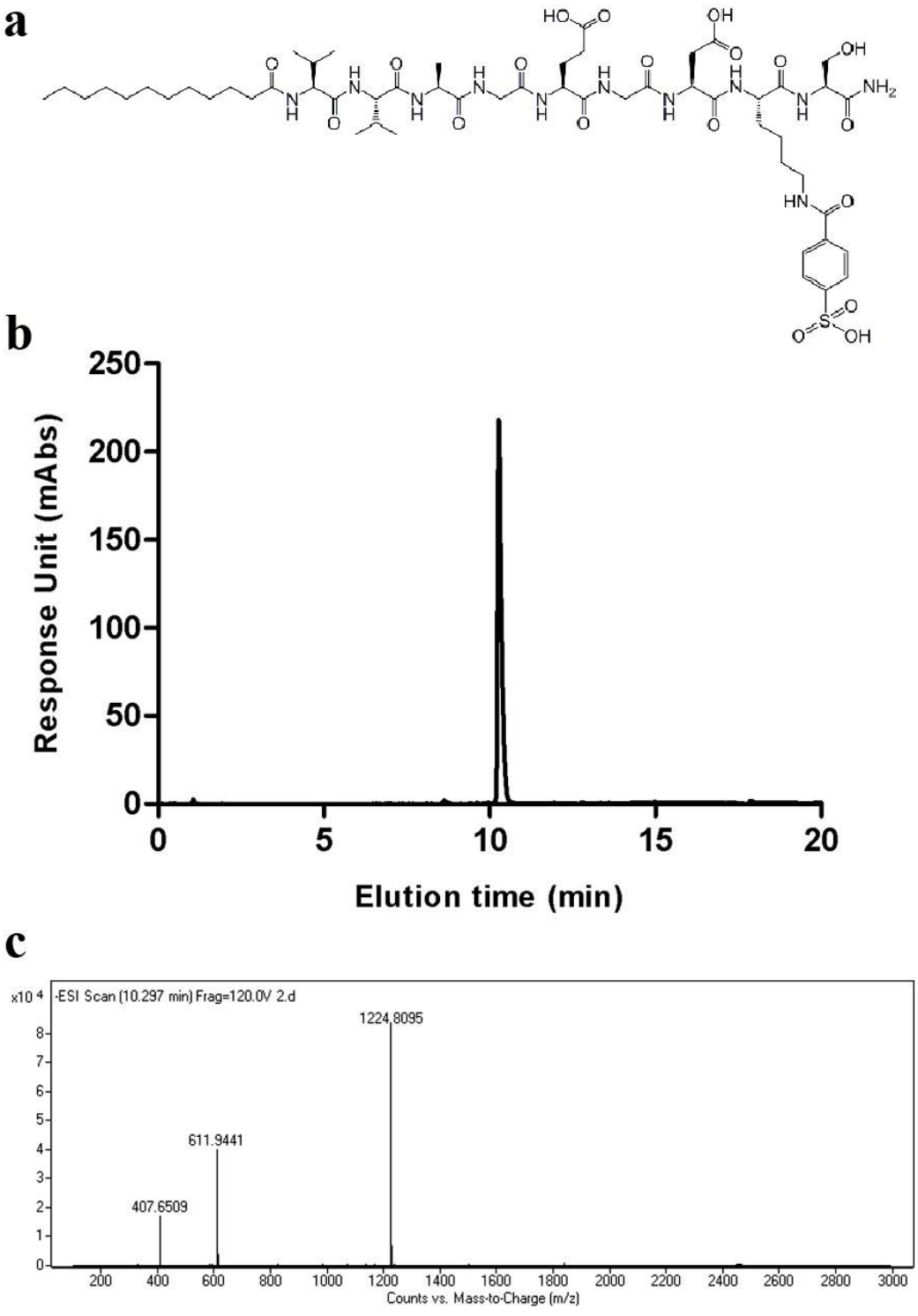

Figure 2.3. LC-MS analysis of synthesized Heparin-mimetic PA (HM-PA) molecule. **a.** Chemical structure of HM-PA molecule. **b.** LC chromatogram of purified HM-PA molecules at 220 nm indicates high purity of molecule. **c.** Mass spectrometric analysis of peak in HM-PA LC chromatogram. $[M-H]^-$ (calculated)=1225.4, $[M-H]^-$((observed)=1224.8.

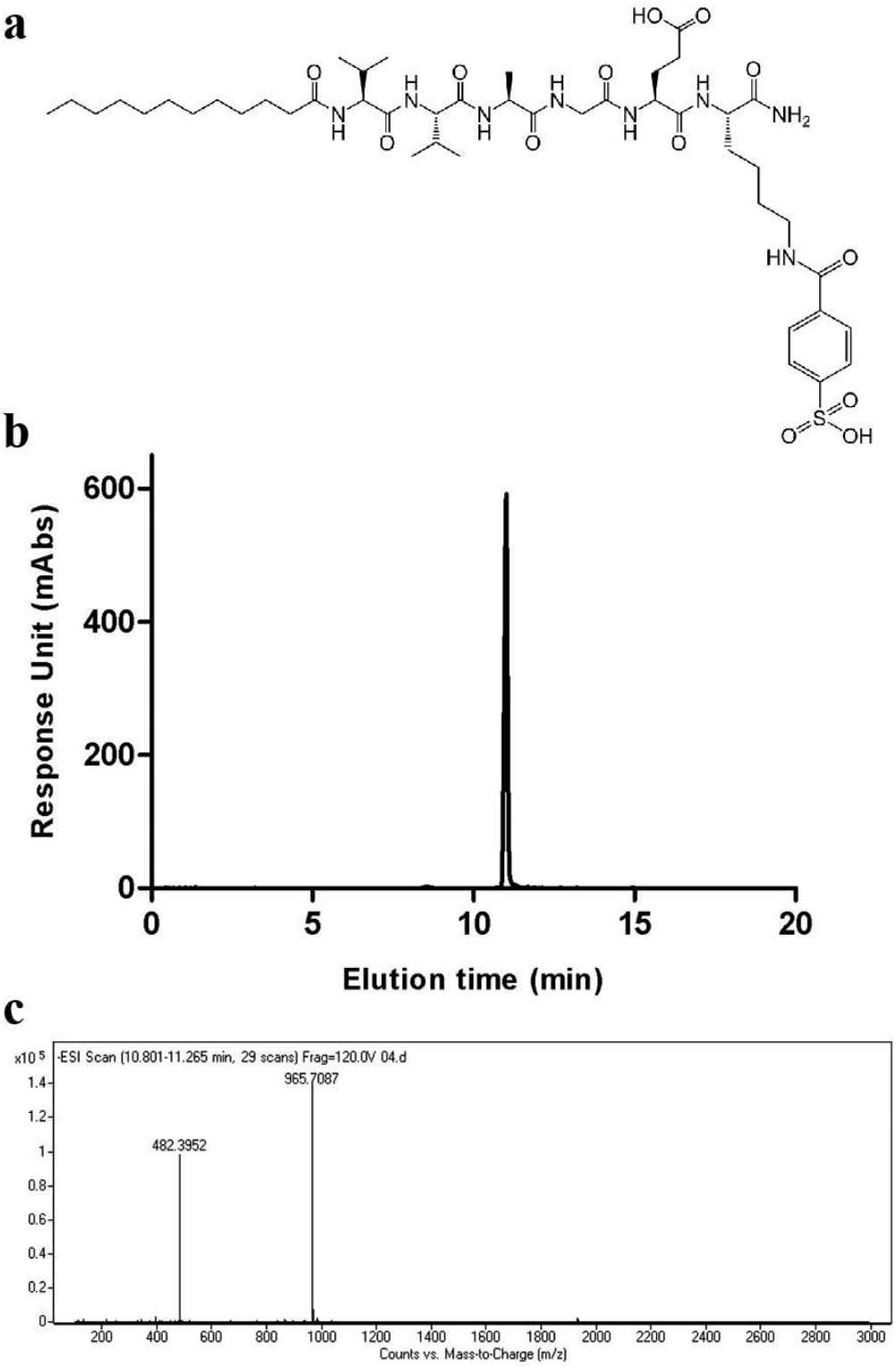

Figure 2.4. LC-MS analysis of synthesized SO_3-PA molecule. **a.** Chemical structure of SO_3-PA molecule. **b.** LC chromatogram of purified SO_3-PA molecules at 220 nm indicates high purity of molecule. **c.** Mass spectrometric analysis of peak in SO_3-PA LC chromatogram. $[M-H]^-$(calculated)=966.2, $[M-H]^-$((observed)=965.7.

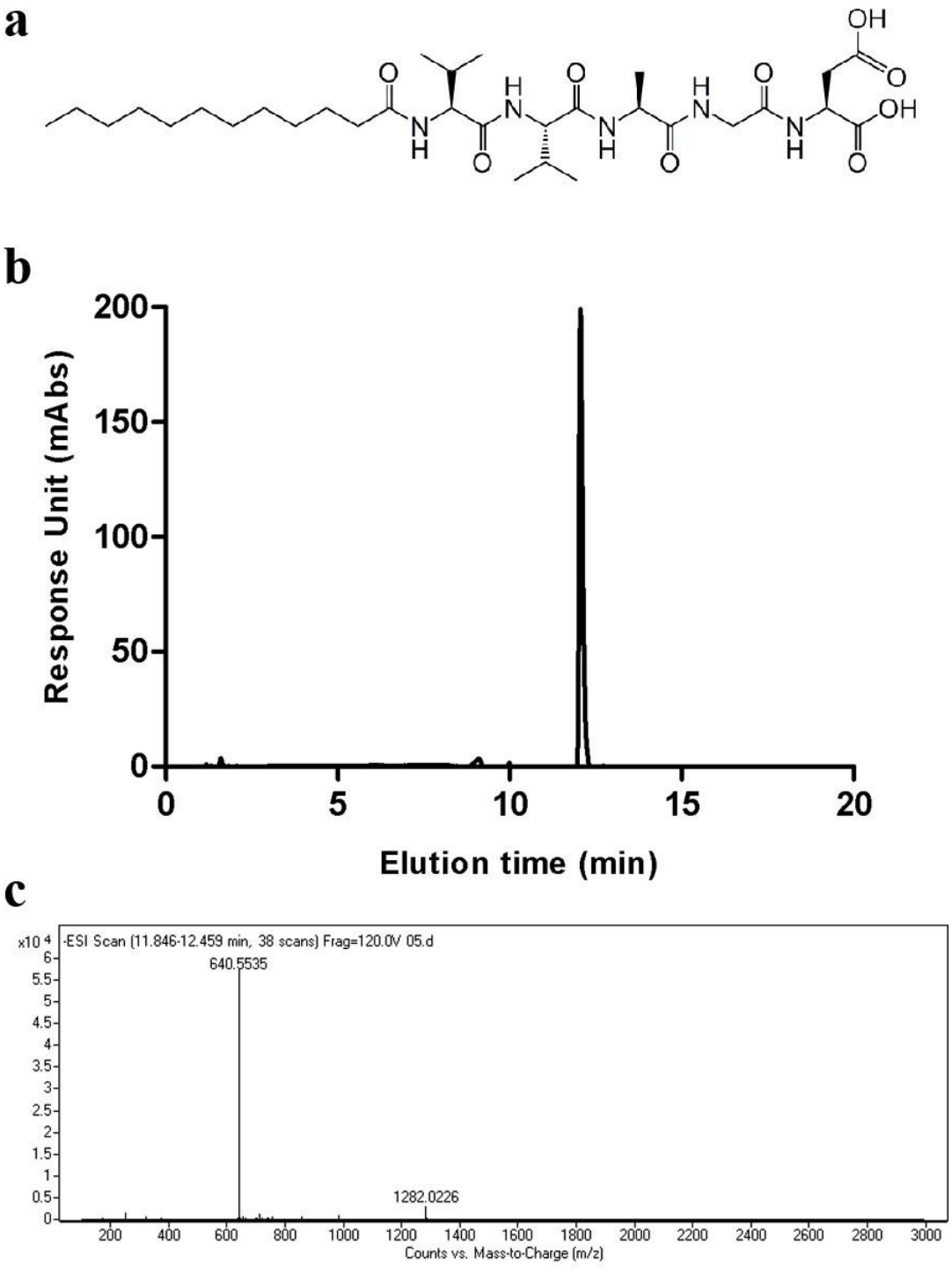

Figure 2.5. LC-MS analysis of synthesized D-PA molecule. **a.** Chemical structure of D-PA molecule. **b.** LC chromatogram of purified D-PA molecules at 220 nm indicates high purity of molecule. **c.** Mass spectrometric analysis of peak in D-PA LC chromatogram. $[M-H]^-$(calculated)=640.8, $[M-H]^-$(observed)=640.6.

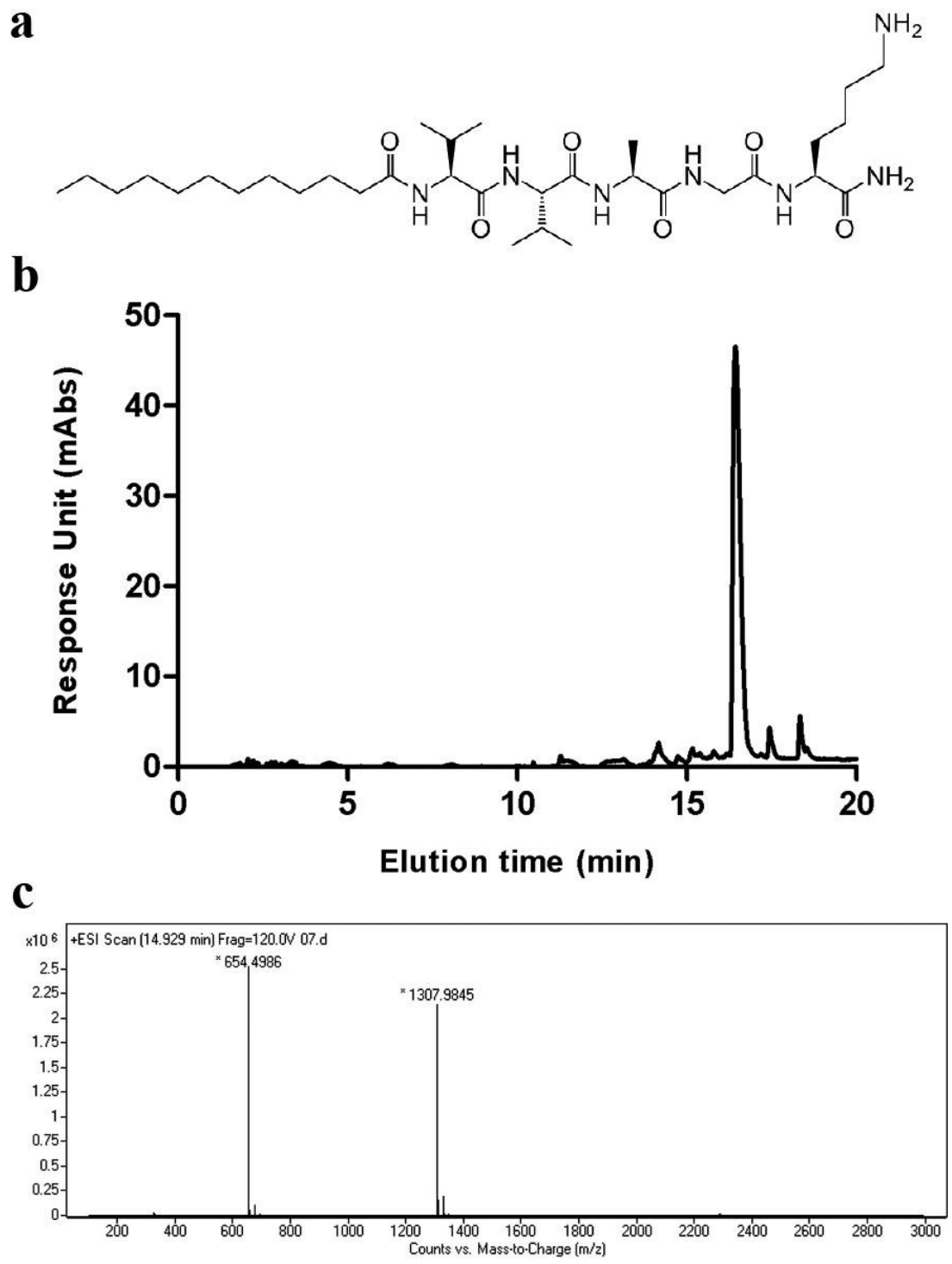

Figure 2.6. LC-MS analysis of synthesized K-PA molecule. **a.** Chemical structure of K-PA molecule. **b.** LC chromatogram of purified K-PA molecules at 220 nm indicates high purity of molecule. **c.** Mass spectrometric analysis of peak in K-PA LC chromatogram. $[M+H]^+$(calculated)=654.9, $[M+H]^+$(observed)=654.5**.**

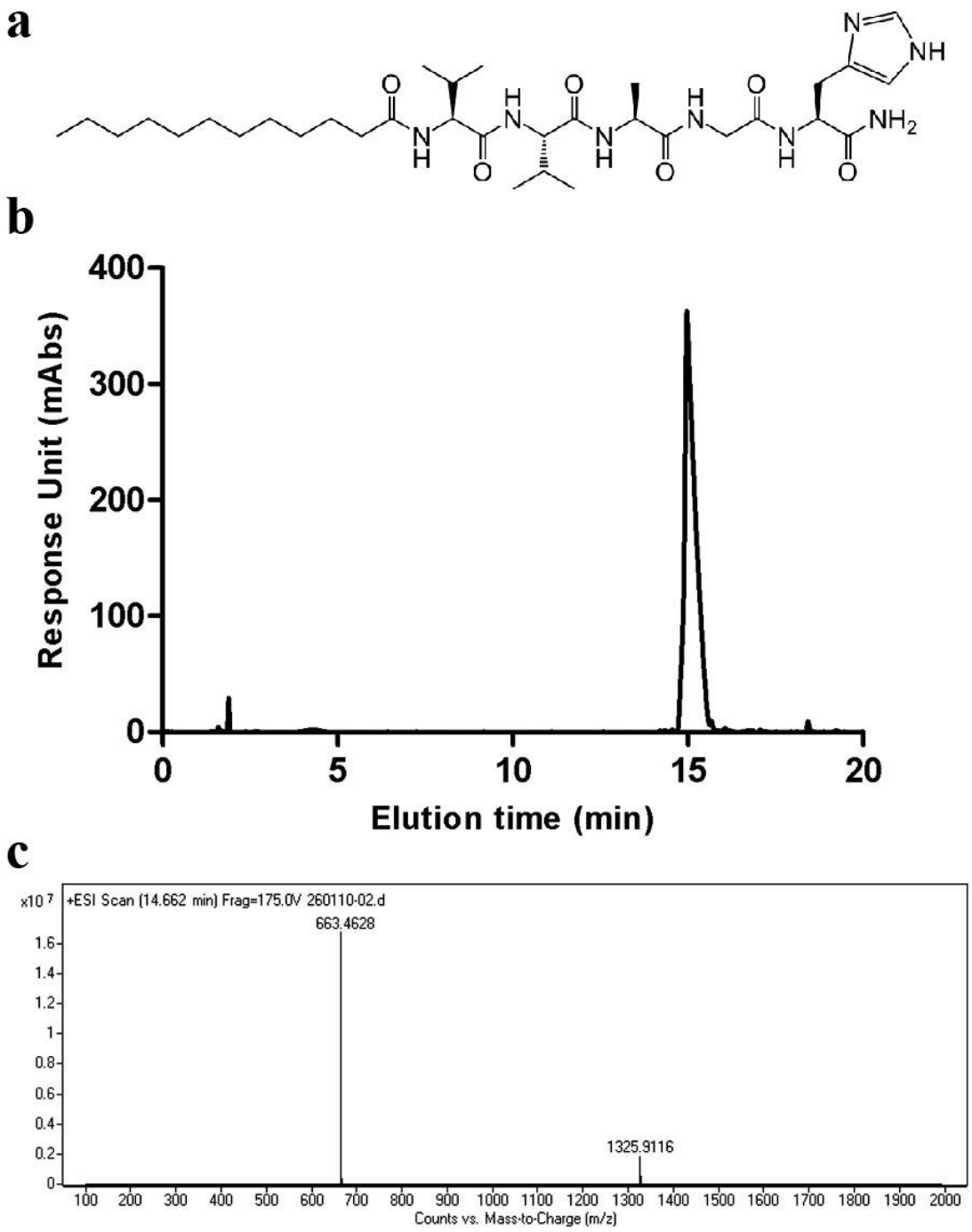

Figure 2.7. LC-MS analysis of synthesized H-PA molecule. **a.** Chemical structure of H-PA molecule. **b.** LC chromatogram of purified H-PA molecules at 220 nm indicates high purity of molecule. **c.** Mass spectrometric analysis of peak in H-PA LC chromatogram. $[M+H]^+$(calculated)= 663.9, $[M+H]^+$(observed)=663.5.

2.3.1. Structural characterization of peptide nanostructures

The abilities of these molecules to form a fibrous network, that can mimic the morphology of natural ECM,[61-62] were analyzed by Scanning Electron Microscope (SEM) imaging. Five different PA gels were prepared with final pH of 7.4 in order to render them suitable for physiological conditions. HM-PA, SO_3-PA and D-PA gels were formed by mixing negatively charged HM-PA, SO_3-PA and D-PA with positively charged K-PA at pH=7, respectively. Negatively charged heparin was mixed with positively charged K-PA to get K-PA/heparin gel. H-PA can be neutralized at pH=7 due to only histidine amino acid as a charged residue (pKa of histidine side chain is 6.0), which allows self-assembly to occur without help of another molecule at pH=7. PA gels were dehydrated by using critical point dryer to preserve 3D structure. Dehydrated 3D networks were coated with Au-Pd and analyzed by SEM imaging. All PA molecules that were analyzed exhibited similar nanofibrous network that is suitable for providing the necessary mechanical support for cells (Figure 2.8a-2.8e), similar to natural collagen matrix (Figure 2.8f). Nanofibrous matrix also allows communication between cells through pores via sprouting of cells or diffusion of soluble molecules. Thus, cells can form integrated tissue-like structures in these PA matrices, similar to natural ECM.

We further diluted these PA gels to visualize individual units forming nanofibrous networks by using and Transmission Electron Microscopy (TEM) and Atomic Force Microscopy (AFM). These images revealed that investigated PA formulations form high-aspect ratio nanofibers (Figures 2.9 to 2.13). Nanofiber diameter is critical, since it determines density of functional groups presented to cells or growth factors, therefore might be critical for bioactivity. For this reason, we compared nanofiber diameters between different PA combinations that were measured based on TEM images (Table 2.1). These measurements revealed that nanofiber diameters for HM-PA/K-PA, SO_3-PA/K-PA, D-PA/K-PA, K--PA/heparin, and H-PA samples do not differ significantly. This indicates that density of functional groups presented by different type of nanofibers is similar.

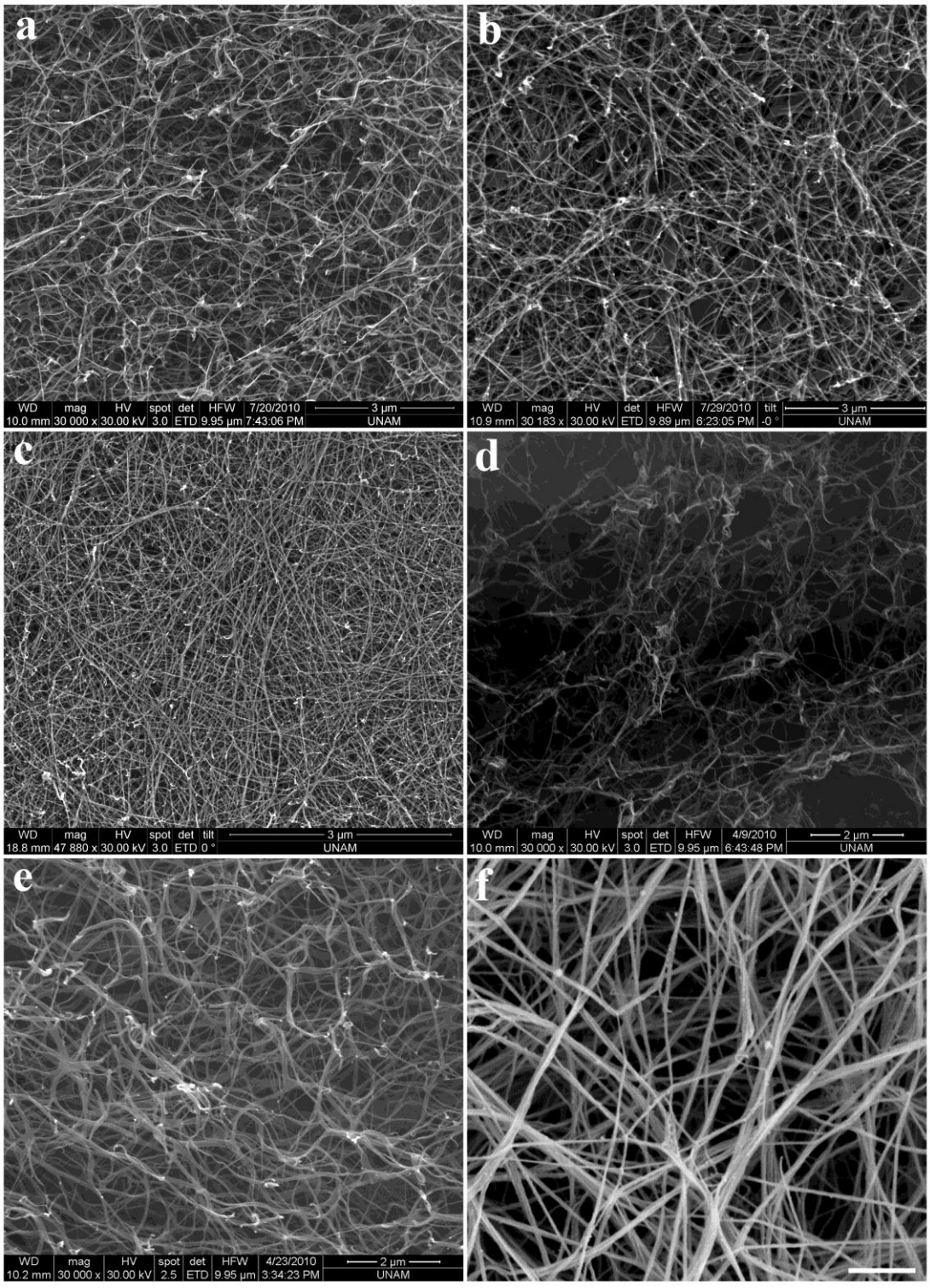

Figure 2.8. Scanning Electron Microscopy (SEM) imaging of dehydrated PA gels and collagen matrix. HM-PA/K-PA **(a**), D-PA/K-PA **(b)**, SO_3-PA/K-PA **(c)**, K-PA/Heparin **(d)**, and H-PA **(e)** gels show nanofibrous networks similar to collagen matrix (**f**; reproduced with permission from ref. 62, copyright © 2006 The Company of Biologist Limited)[62].

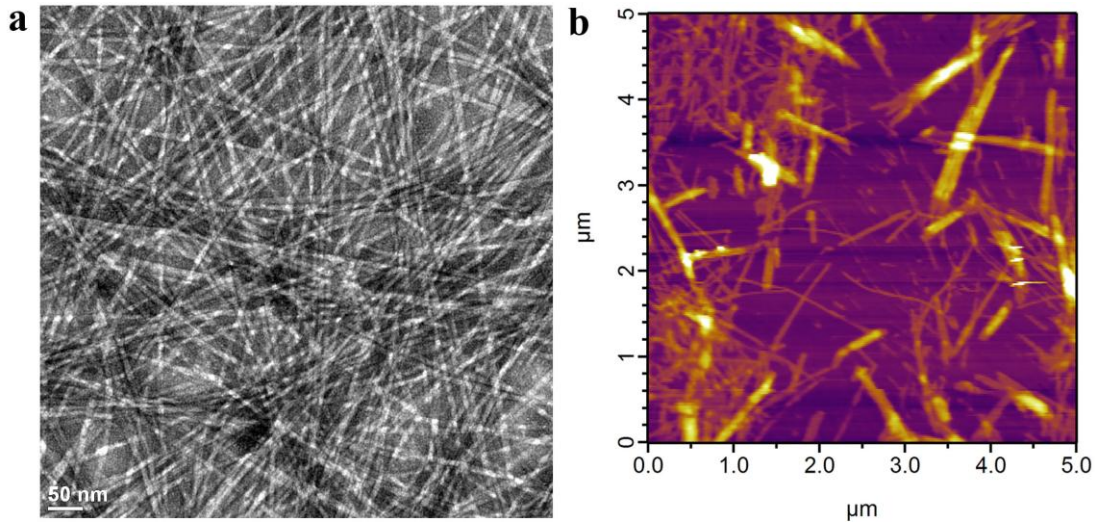

Figure 2.9. Transmission Electron Microscopy (TEM) and Atomic Force Microscopy (AFM) imaging of surfaces coated with HM-PA/K-PA formulation. **a.** TEM image reveals formation of nanofibers with 5-10 nm diameter. **b.** AFM image shows bundles of nanofibers along with single nanofibers.

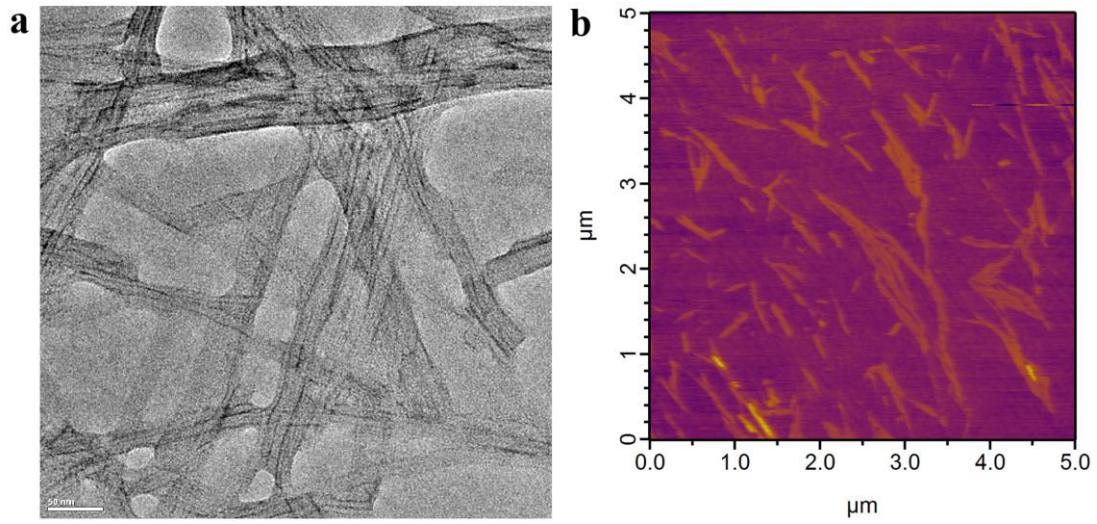

Figure 2.10. Transmission Electron Microscopy (TEM) and Atomic Force Microscopy (AFM) imaging of surfaces coated with SO_3-PA/K-PA formulation. **a.** TEM image revealed formation of nanofibers with 5-10 nm diameter and their bundling. **b.** AFM image shows mainly bundles of nanofibers.

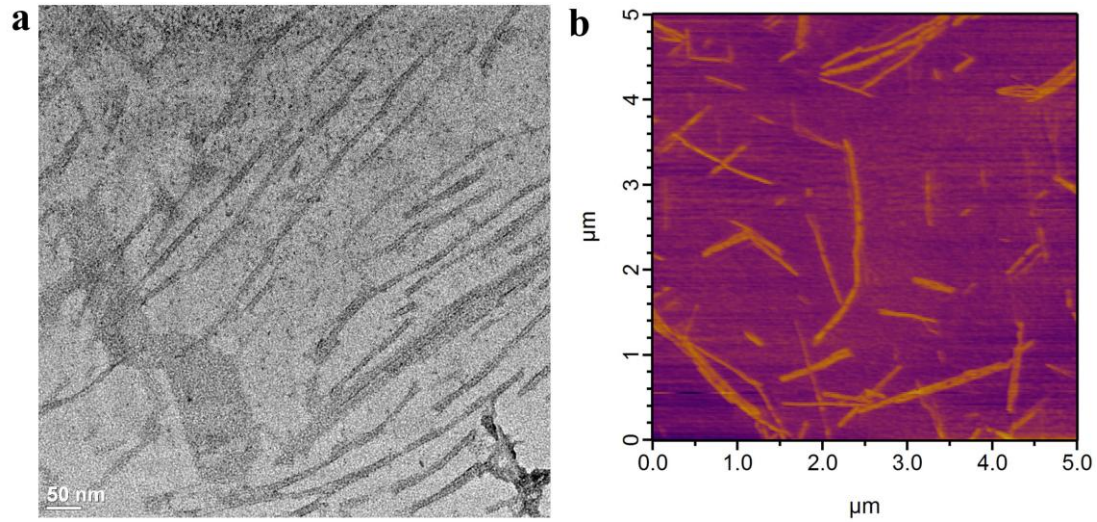

Figure 2.11. Transmission Electron Microscopy (TEM) and Atomic Force Microscopy (AFM) imaging of surfaces coated with D-PA/K-PA formulation. **a.** TEM image revealed formation of nanofibers with 5-10 nm diameter. **b.** AFM image shows mainly bundles of nanofibers.

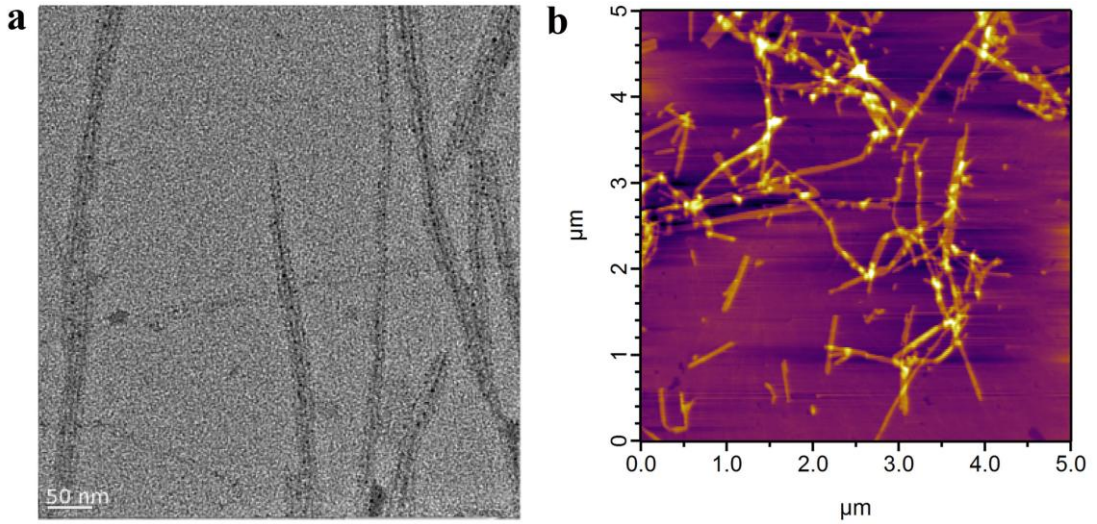

Figure 2.12. Transmission Electron Microscopy (TEM) and Atomic Force Microscopy (AFM) imaging of surfaces coated with K-PA/Heparin formulation. **a.** TEM image revealed formation of nanofibers with 5-10 nm diameter. **b.** AFM image shows mainly bundles of nanofibers.

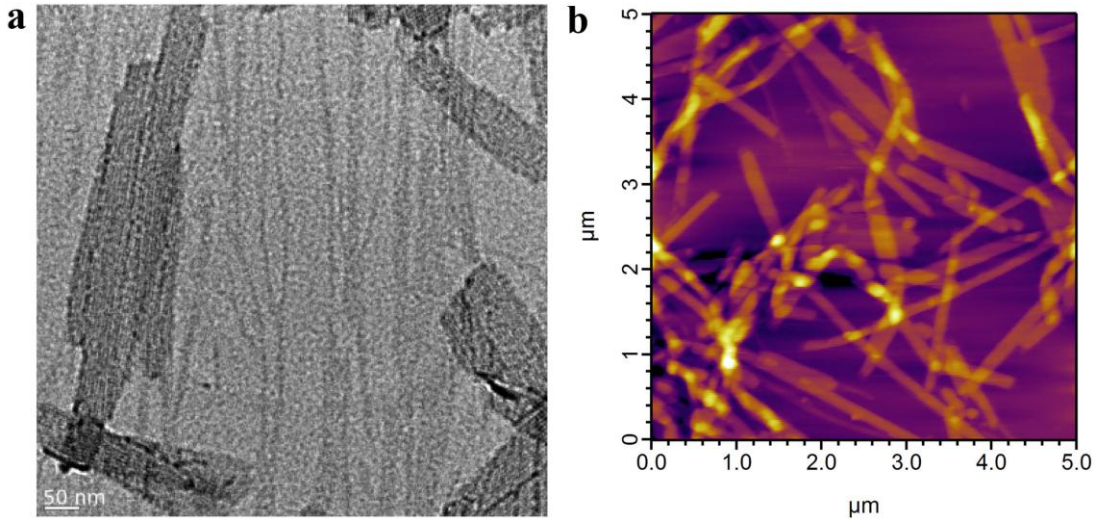

Figure 2.13. Transmission Electron Microscopy (TEM) and Atomic Force Microscopy (AFM) imaging of surfaces coated with H-PA pH=7 formulation. **a.** TEM image revealed formation of nanofibers with 5-10 nm diameter. **b.** AFM image shows mainly bundles of several nanofibers.

Table 2.1. Nanofiber size measurements of PA gels.

PA nanofiber type	Size (nm)
HM-PA/K-PA	7.5 ± 1.6
SO_3-PA/Lys-PA	7.0 ± 1.5
D-PA/K-PA	7.1 ± 0.7
K-PA/Heparin	7.1 + 1.1
H-PA pH=7	6.3 ± 0.7

Nanofiber diameters are measured by using TEM images for each formulation. Averages of nanofiber sizes between different formulations were proved to be similar.

Driving force for nanofiber formation was proposed to be hydrogen bonding between peptide molecules with β-sheet secondary structure that cause their densely packing within nanofibers.[63-64] In order to assess secondary structure character of PA

combinations, we obtained their circular dichroic (CD) spectra. Strong negative peak at 218-19 nm and positive peak around 195-200 nm for HM-PA/K-PA, SO_3-PA/K-PA and D-PA/K-PA indicates formation of β-sheet secondary structure (Figure 2.14). These results further confirm that β-sheet character of peptide amphiphiles might stabilize formation of cylindrical nanostructures.

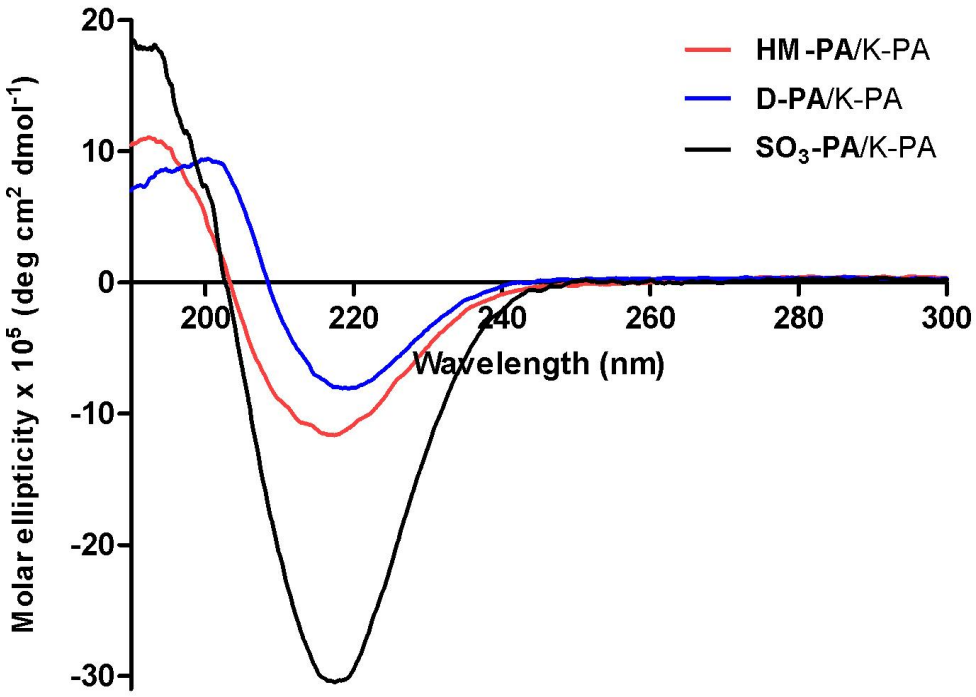

Figure 2.14. Circular dichroism analysis of heparin-mimetic and control PA molecules. Circular dichroic spectra of Heparin-mimetic PA, SO_3-PA or D-PA molecules mixed with K-PA show characteristic signals for β-sheet structure.

Mechanical properties of the extracellular environment are crucial for determining cell fate and behavior,[12, 65] and thus we compared viscoelastic properties of PA gels. For this we used oscillatory rheology to characterize viscoelastic properties of different PA gels (Figure 2.15). In oscillatory rheology stress response of gels to applied strain is measured by storage modulus (G`) and loss modulus (G``). Storage modulus measure stored energy after strain applied and represent contributions from elastic component of material. Loss modulus measure dissipated energy and represent contributions from viscous component of material. If G` is higher than G``,

material has more elastic, solid/gel-like behavior; while if G` is lower than G``, material has more viscous-like character. Each of the gels (HM-PA/K-PA, $SO_3$-PA/K-PA, D-PA/K-PA and K-PA/Heparin gel) had storage moduli (G`) higher than loss moduli (G``), indicating gel formation (Figure 2.15). Storage moduli (G`), indicating stiffness of the gels, were in the same order of magnitude for all gels designed for this study. Furthermore, loss tangents (tan δ = G``/G`) of all materials were compared, which provides information about elastic character of the gels and their gelation properties.[66-67] These values were found to be comparable for all of the PA gels tested here (Table 2.2), indicating that all materials used here has similar gelation and elastic properties. Overall, rheology measurements suggest that differences in mechanical properties of gels are not significant enough to modulate bioactivity.

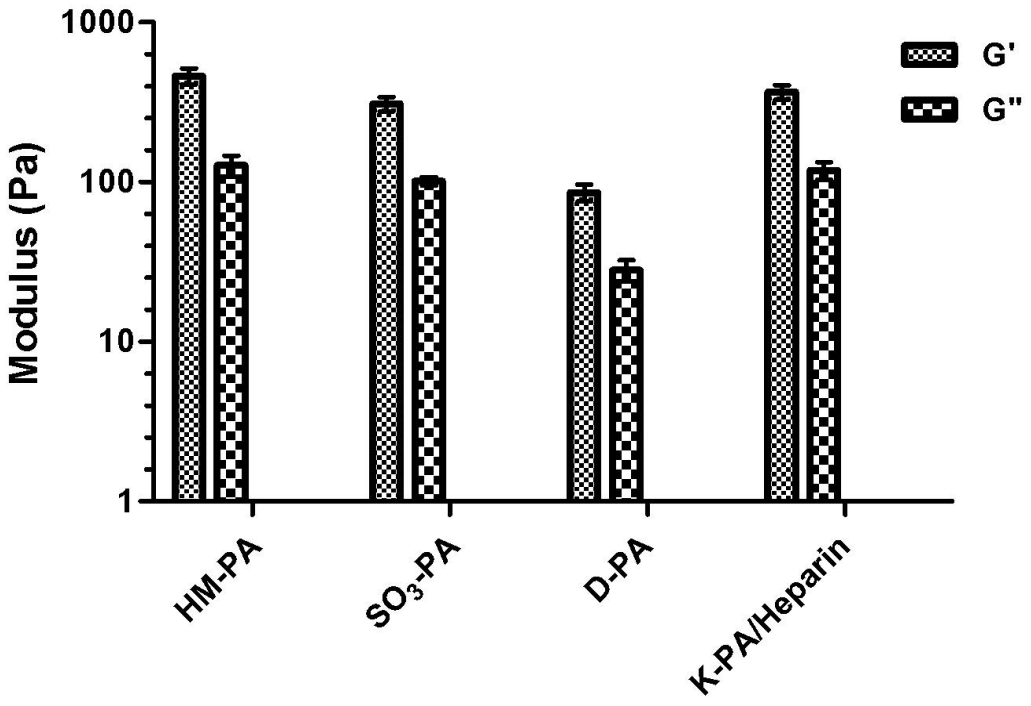

Figure 2.15. Oscillatory rheology measurements of different PA gels. Storage (G`) moduli of equimolar PA formulations were higher than loss moduli (G``) for all tested formulations, indicating gel formation. Storage moduli of HM-PA, SO_3-PA and K-PA/Heparin are similar, while difference of D-PA from others is lower than order of magnitude (n=3; Error bars are standard error mean).

Table 2.2. Loss tangents of PA gels (G''/ G').

PA gel	G''/ G'
HM- PA/K-PA	0.194
SO_3-PA/K-PA	0.177
D-PA/K-PA	0.214
K-PA/Heparin	0.180

Loss tangents give information about elastic character of gels. Similar values for all tested gels are a sign for similarity between elastic character of PA gels.

2.3.2. Evaluation of *in vitro* angiogenic potential of peptide nanofibers

Endothelial cells are known to form capillary-like tubes on different materials derived from natural ECM, when angiogenic signals are available.[68-71] We performed similar *in vitro* angiogenesis assay in order to understand whether functional groups from heparin on nanofibers confer advantage for inducing angiogenesis. For this purpose, human umbilical cord vein cells (HUVEC) were cultured on surfaces coated with PA gel and cellular morphologies were followed with light microscope. Similarly, we cultured HUVECs on Matrigel™ - basement membrane gel, which consists of natural ECM proteins as well as various growth factors, as a positive control. We observed that cells coalesce to form capillary-like structures, which emerged as polygonal network, on Matrigel™, as it is reported in the literature (Figure 2.16a, b).[68] Interestingly, cells cultured on Heparin-mimetic PA (HM-PA) matrix also formed capillary-like structures and polygonal network (Figure 2.16c, d and e), although this matrix is synthetic and does not contain any growth factors or GAG molecules. The most potent of other matrices, D-PA, induced only formation of a few tubes and lower cell migration than HM-PA matrix (Figure 2.16f). Including all the necessary functional groups from heparin might be the explanation for potency of HM-PA nanofiber gel system to induce angiogenic phenotype on endothelial cells.

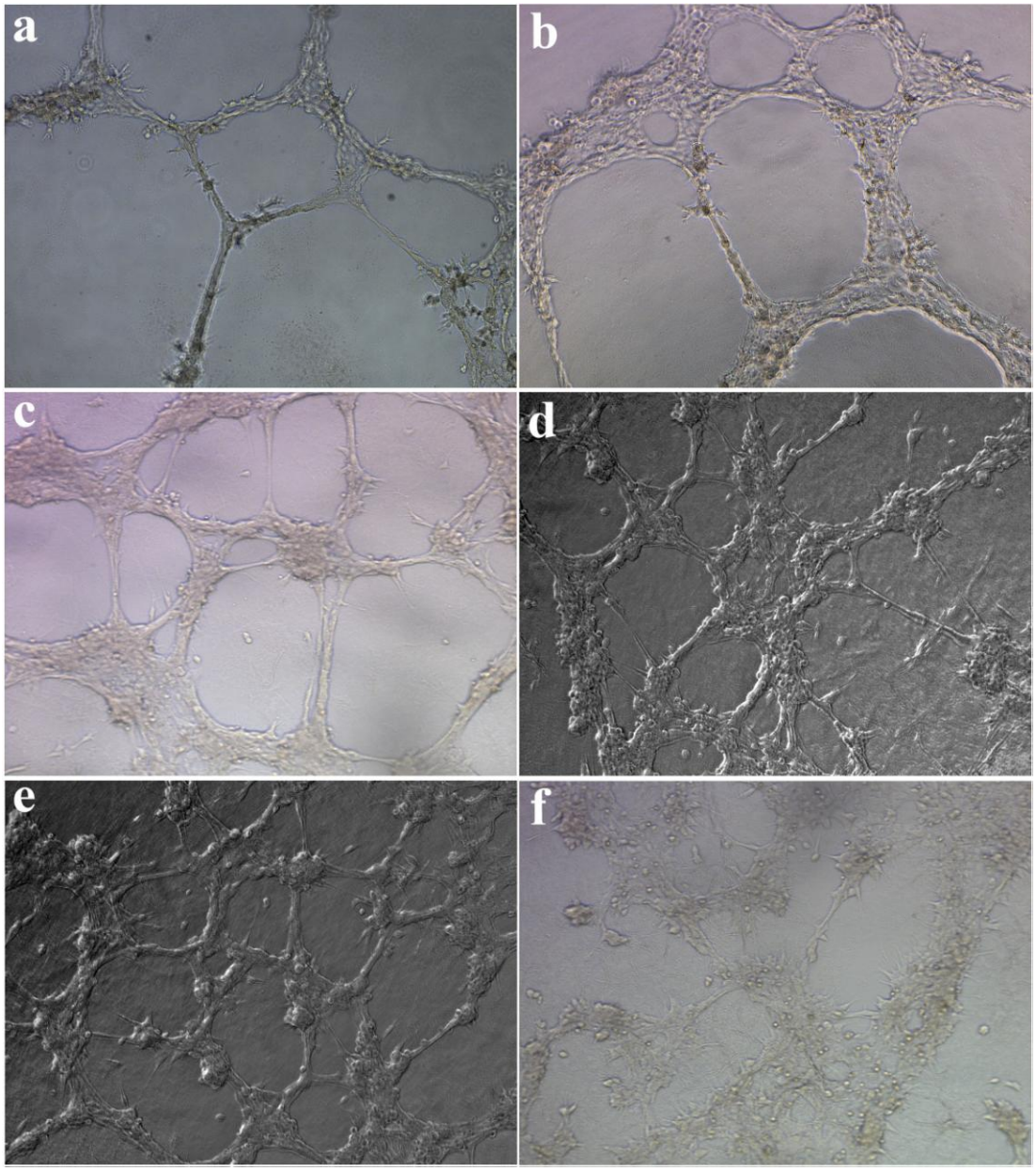

Figure 2.16. *In vitro* angiogenesis assay - Matrigel, HM-PA and D-PA. HUVECs were cultured on Matrigel **(a, b)**, HM-PA nanofiber matrix **(c, d and e)** and D-PA nanofiber matrix **(f)**; then followed for 48 h to evaluate migration and tube formation. Cells formed capillary-like tubes on Matrigel, as well as HM-PA nanofibers. However, on control D-PA nanofibers endothelial cells showed only a few tubes and cell migration. All images are bright-field and taken at 100x magnification (n = 3 for all conditions; representative images are shown).

SO_3-PA nanofiber matrix induced lower number of tubes and migration than D-PA (Figure 2.17a and 2.16f), even though SO_3-PA nanofibers have both sulfonate and carboxylic acid groups, but D-PA has only carboxylic acid groups (Figure 2.2). This suggests that factors (other than variety of functional groups) such as number of functional groups (two carboxylic acids are included on D-PA), position of these functional groups on PA molecule or proximity of functional groups on PA molecule might affect bioactivity of nanofiber matrix. H-PA, which included no functional groups from heparin, induced no angiogenic phenotype in endothelial cells, similar to bare tissue culture plate (Figure 2.17c, d).

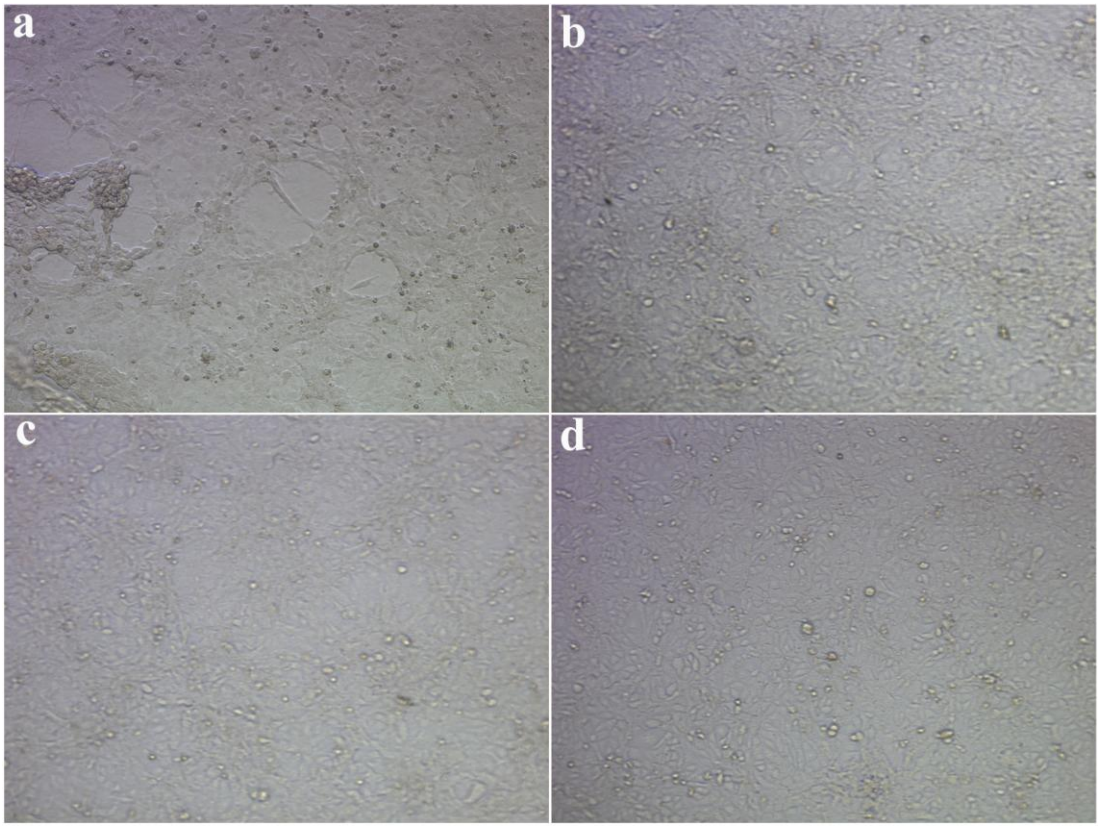

Figure 2.17. *In vitro* angiogenesis assay - SO_3-PA, K-PA/heparin, H-PA and TCP. HUVECs were cultured on SO_3-PA **(a)**, K-PA/heparin **(b)**, H-PA **(c)** nanofiber matrices and bare tissue culture plate **(d)**; then followed for 48 h to evaluate migration and tube formation. Cells show a few tubes and a little migratory phenotype on SO_3-PA matrices. On other surfaces, no sign of angiogenesis can be observed. All images are bright-field and taken at 100x magnification (n = 3 for all conditions; representative images are shown).

Overall, these data strongly suggest that proper composition of functional groups from heparin on PA nanofiber matrix induce angiogenic phenotype in endothelial cells. Also, lack of this necessary composition of functional groups severely impairs potency of nanofiber matrix.

Surprisingly, heparin carrying nanofibers (K-PA/heparin) also seemed to be incapable to induce angiogenesis, in that they were not different from tissue culture plate (Figure 2.17 b and d). Although K-PA and heparin formed a self-supporting gel with similar mechanical properties with HM-PA/K-PA gel, heparin chains probably are not stabilized by K-PA molecules and optimal presentation of heparin is not achieved by nanofibers. Previously, Rajangam et al. reported a difference between a heparin-binding PA and its scrambled sequence regarding interaction with heparin.[52] Scrambled PA sequence with basic residues at the end, similar to K-PA, bound to heparin with strong affinity and formed nanofiber gel.[4] However, binding mechanism there allowed higher dissociation rate of heparin from nanofiber system and probably its suboptimal presentation to growth factors and cells, resulting in lower tubule formation at *in vitro* by endothelial cells than heparin-binding PA.[4] To understand whether K-PA – heparin interaction is also driven by similar mechanism, that is through electrostatic interactions, we measured thermodynamic parameters such as change in enthalpy and entropy by using Isothermal Titration Calorimetry (ITC). We observed that although K-PA bound strongly to heparin (Ka ~ 2 x 10^8), interaction was driven through electrostatic interactions, as indicated by high enthalpic change (ΔH = -7.2 x 10^5 +/- 5.1 x 10^4) (Figure 2.18). High enthalpy change was also observed by Rajangam et al. when heparin and scrambled form of heparin-binding PA interacts.[52] These data collectively suggest that proper presentation of heparin to extracellular environment by PA nanofibers is critical, which cannot be achieved by K-PA/Heparin nanofibers here.

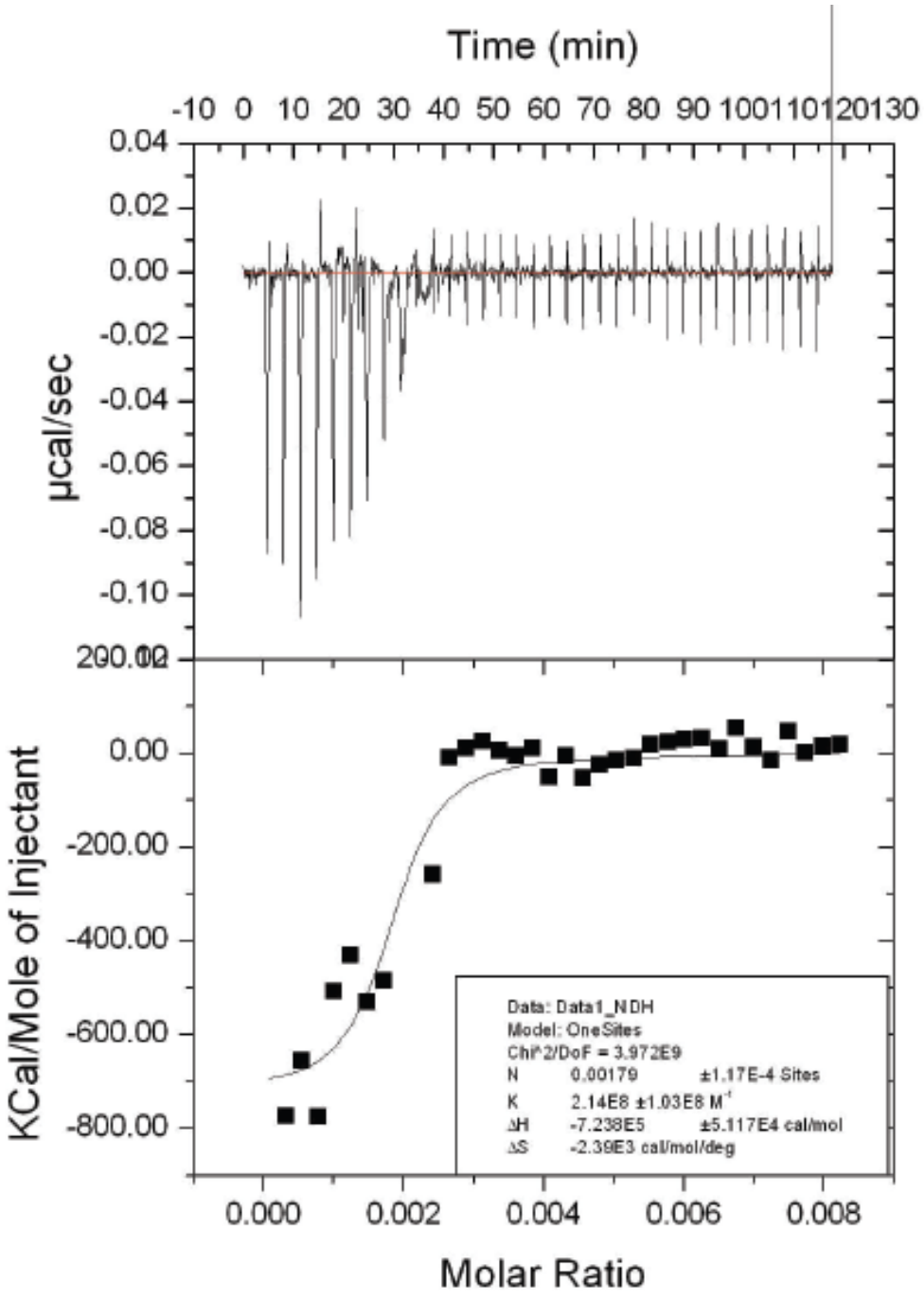

Figure 2.18. Measurement of binding constant and thermodynamic parameters in K-PA and heparin interaction by using ITC. The top graph shows heat change per unit time during heparin titration into K-PA solution and the bottom graph displays the integrated data (filled squares) and the best fit to a nonlinear function assuming one set of binding sites. K-PA and heparin showed high affinity to each other (K_a=2.14+/- 1.03 x 10^8).

Quantification of total length of the capillary-like formations per cell culture plate well revealed that HM-PA matrix is the most effective matrix when compared to basement membrane gel (Matrigel^{TM}) and other controls. Among the two most potent PA matrices - HM-PA and D-PA - HM-PA enhanced tube formation capability of HUVECs nearly four times more than D-PA (Figure 2.19a). The other PA nanofibers also demonstrated poor angiogenesis activity, likely because of the deficiency of right composition of functional groups.

Also interestingly, addition of further growth factors didn`t contribute to further tube formation on HM-PA or D-PA matrices, in terms of tube length (Figure 2.19b). In HM-PA matrices, we can claim that maximal tube formation is achieved with 'no growth factor' group, which can be deduced from existence of tubes and minimal cell aggregates on every part of the surface of the HM-PA nanofiber matrix. Probably signals inducing tube formation had already been at saturation and addition of further growth factors didn`t have any contributions to tube formation. However, surprisingly, growth factor addition was not effective to change tube formation potential of D-PA nanofiber matrix also. This might be due to several reasons. One is D-PA nanofibers can not bind optimally to growth factors and cannot present them to cells, which is important for heparin-binding growth factors such as VEGF and FGF-2 used in this study. Presence of heparan sulfate in environment is required for proper presentation of growth factors to their receptors on cell surfaces and effective signaling to occur.[47, 57] Rajangam et al. reported that PA nanofiber matrix that is not optimal for presentation of heparin showed similarly deficient *in vitro* angiogenesis in the presence or absence of growth factors, emphasizing the importance of proper presentation of heparin by nanofiber system and its interaction with growth factors.[4] Another is mentioned growth factor cocktail (VEGF/FGF-2) might be insufficient to induce angiogenic pathway themselves, therefore we didn`t observe their contributory effect to angiogenesis on control PA matrix.

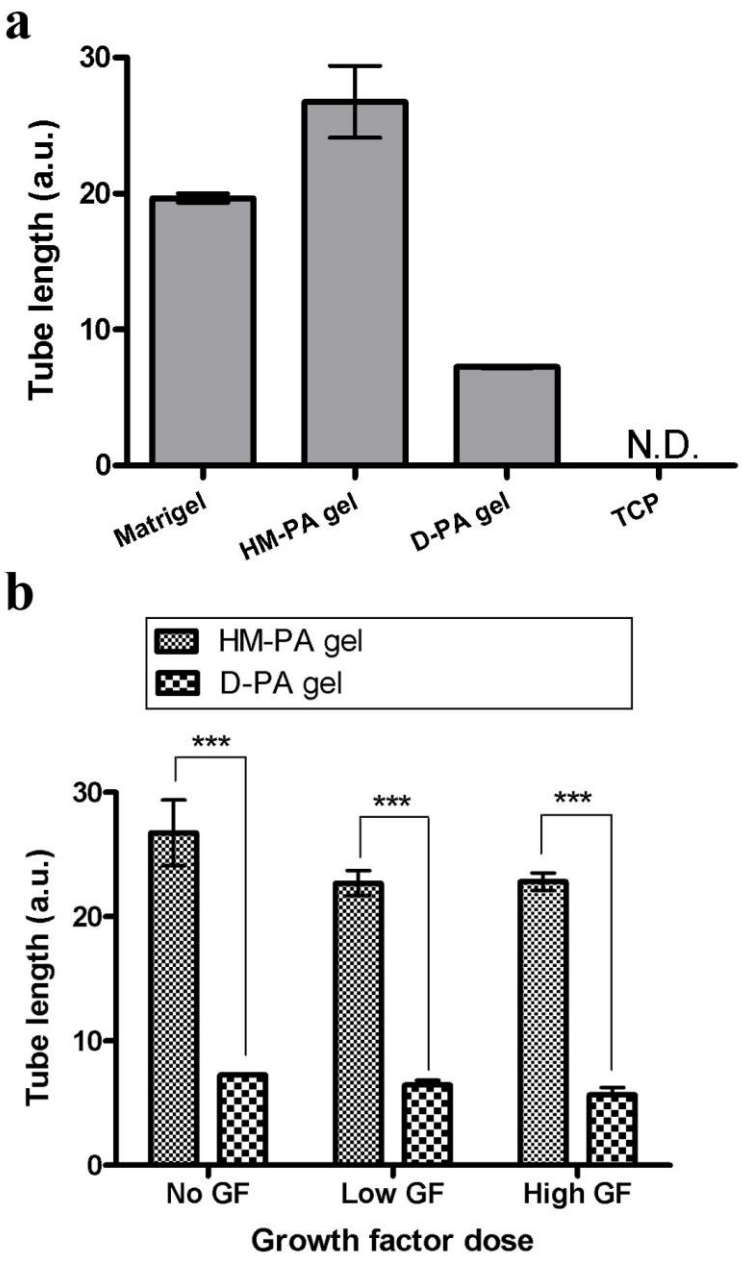

Figure 2.19. Quantification of lengths of tubes formed by endothelial cells (HUVECs). **a.** Quantification of tube lengths by HUVECs cultured on Matrigel, HM-PA gel, D-PA gel, or tissue culture plate (TCP) (a.u. is arbitrary unit). Statistical differences between groups were analyzed by one-way ANOVA test. Bonferroni's multiple comparison test was used as posthoc analysis. $p < 0.001$ between Heparin-mimetic PA (HM-PA) gel and D-PA gel or TCP. $p < 0.05$ between HM-PA gel and Matrigel. **b.** Graph illustrates quantification of tube lengths for different growth factor treatment conditions (most potent two scaffolds are shown). Low dose: 10 ng/mL VEGF/FGF-2, high dose: 50 ng/mL VEGF/FGF-2. $p < 0.001$ between HM-PA and D-PA scaffolds (analyzed by two-way ANOVA) ($n = 3$ for all conditions) Error bars indicate standard error mean.

One might address viability issue of cells on matrices and claim that cells respond to toxicity of matrices in this way – through aggregating (which we percept as tube formation). In order to understand whether endothelial cells are viable on PA nanofiber matrices, we treated cells them with Calcein AM, a chemical which is degraded in metabolically active cells and producing fluorescence. Thus, in viable cells, we should observe green fluorescence. This assay revealed that the cells cultured on HM-PA nanofiber matrices, as well as on basement membrane, control PA gels, and tissue culture plate were metabolically active (Figure 2.20). Individual cells, cellular aggregates and tubes all showed fluorescence, precluding toxicity issue of nanofiber matrices to endothelial cells.

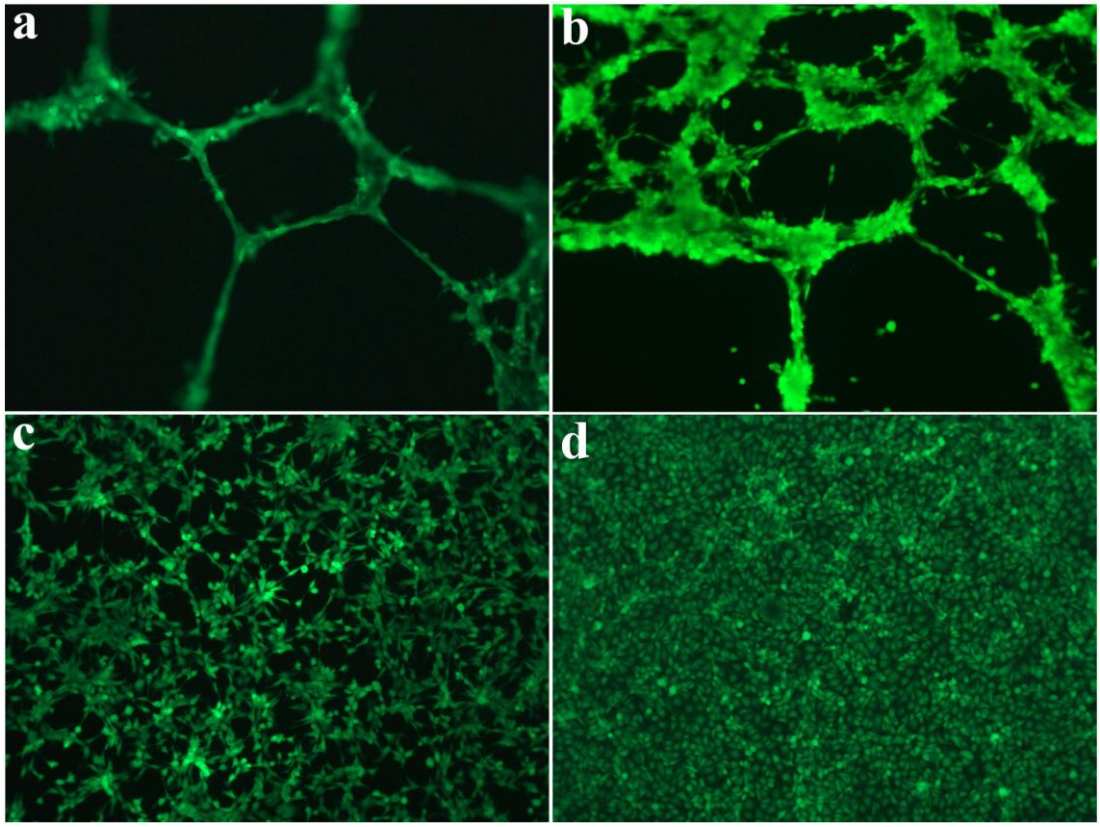

Figure 2.20. Viability of cells cultured on PA nanofiber matrices. Calcein staining revealed that HUVECs grown on these matrices are metabolically active: **a.** Matrigel^{TM} **b.** Heparin-mimetic PA nanofiber matrix **c.** D-PA nanofiber matrix **d.** All images were taken at 100x magnification. (n = 3 for all conditions; representative images are shown).

In vitro tube formation potential of HM-PA nanofiber matrix was further investigated by using H5V cell line (mouse endothelial cell line).[72] Similar to HUVECs, H5V cells also migrated and aggregated extensively and formed capillary-like tubes as well as polygonal structures on HM-PA matrices (Figure 2.21a). Although these cells were aggregated and migrated on D-PA matrix also, tube formation was ineffective and polygonal structures didn`t form (Figure 2.21b). On $SO_3$- PA matrices, both migration and aggregation was lower than HM-PA and D-PA matrices, as well as formation of tubes and polygonal lattice was impaired (Figure 2.21c). Cells didn`t show any angiogenic phenotype when seeded on bare tissue culture plate (Figure 2.21d). These results further confirm that functional group architecture of Heparin-mimetic PA has inductive effect on endothelial cells towards angiogenesis.

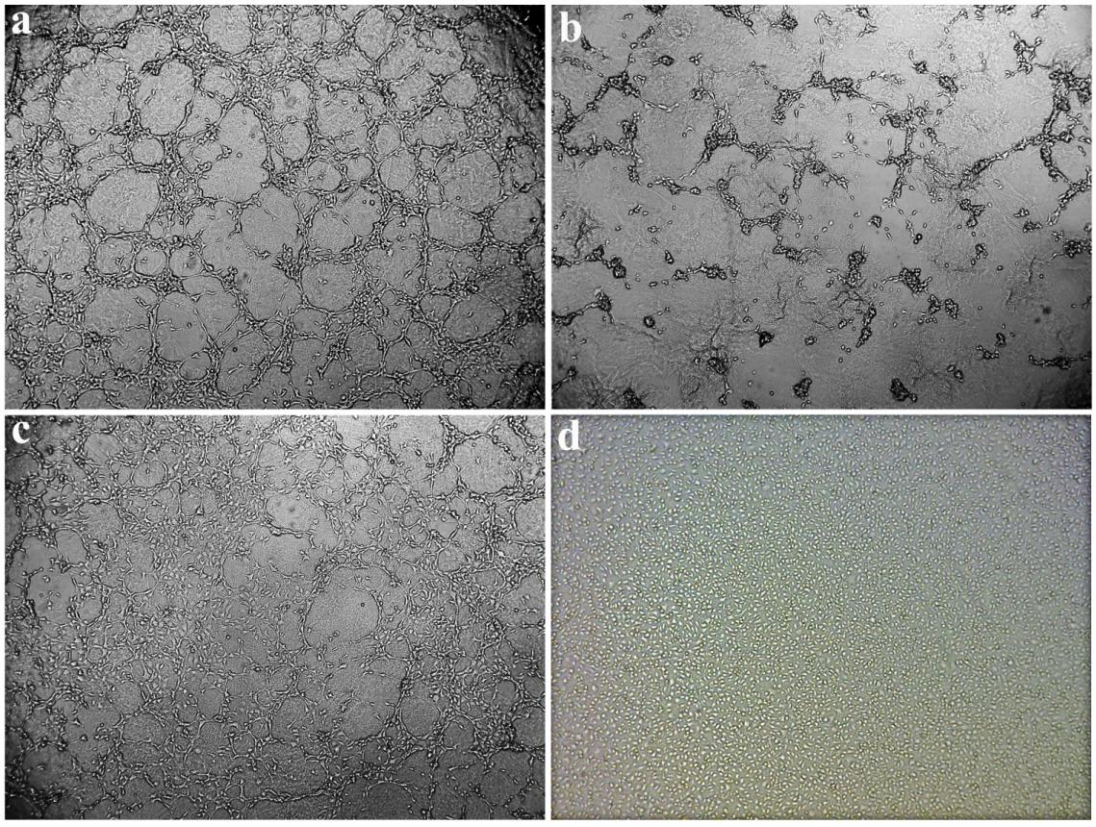

Figure 2.21. *In vitro* angiogenic performances of H5V (mouse endothelial cell line) cells on different PA nanofiber matrices. a. Heparin-mimetic PA, b. SO_3-PA, c. D-PA , d. Tissue culture plate. Extensive formation of tubes and polygonal network of tubes was observed only on HM-PA nanofiber matrix.

Proliferation of endothelial cells is one of the hallmarks of angiogenesis besides endothelial cell activation, migration, sprouting and tubule formation.[73] In order to analyze whether Heparin-mimetic PA had any effect on proliferation of endothelial cells, BrdU-based proliferation assay was used. This assay relies on incorporation of BrdU into replicating DNA, thus gives information about proliferation status of given cell population. The results exhibited that all of the PA nanofibers utilized in this study exerted similar effects on the proliferation rates of endothelial cells, which was also similar to that of bare tissue culture plate (Figure 2.22). Therefore, it can be concluded that proliferation is not among the angiogenic processes induced by Heparin-mimetic PA nanofibers in endothelial cells.

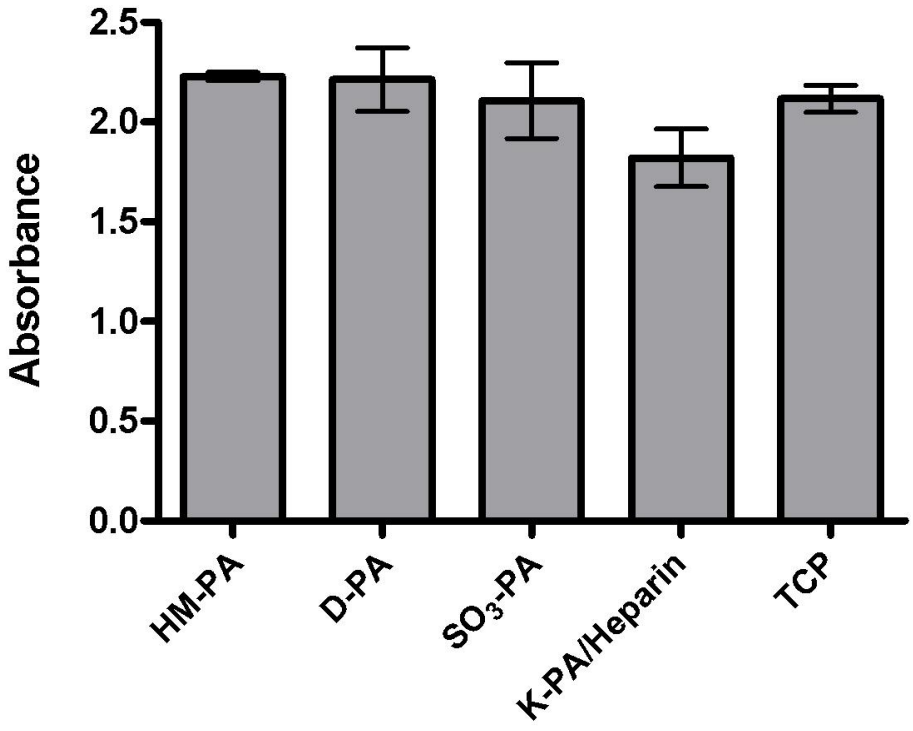

Figure 2.22. Proliferation of endothelial cells on different PA nanofiber matrices and tissue culture plate (TCP). Absorbance values indicate relative BrdU staining between different treatments given at X-axis. Differences between means are not significant according to one-way ANOVA analysis (n=3; p=0.2822;). This indicates that HM-PA or other nanofibers has no further proliferative or anti-proliferative effect on endothelial cells than TCP. Error bars indicate standard error mean.

In order to observe effects of HM-PA nanofiber matrix on endothelial cells and interaction of cells with nanofiber matrix with higher resolution, we obtained images of the cells (Figure 2.23) and their sprouts (Figure 2.24) on PA scaffold coated onto coverslip over TCP or on bare coverslip over TCP by SEM. The Heparin-mimetic PA matrix was observed to facilitate cell spreading and extensive sprouting (Figure 2.23a-d) when compared with cells grown on tissue culture plate (Figure 2.23e, f).[74] On tissue culture plate cells showed almost no sprouting with suboptimal spreading character and limited attachment sites (Figure 2.23 e, f). Multiple attachment sites of spreaded endothelial cell on HM-PA nanofiber matrix can be observed (Figure 2.23 a). Cells interact with each other and matrix via their sproutings and extensions (Figure 2.23b). Multiple sproutings per cell, their length and branching phenotype indicate angiogenic phenotype and suitability of HM-PA nanofiber matrix for this purpose (Figure 2.23 c, d).

Moreover, tubules with more than 4 μm diameter can be observed on Heparin-mimetic PA matrix (Figure 2.24a).[75] Sprouts are lengthy and varying in their diameter (Figure 2.24b, c). Vessel-like hollowness of sprouting is discernible from broken sprout in Figure 2.24c. Sprouts interact with 3d matrix and probably can grow in inside the nanofiber matrix (Figure 2.24 d-f). Overall, SEM images of endothelial cells on HM-PA nanofiber matrix and coverslips, demonstrate angiogenic phenotype gained by endothelial cells selectively on HM-PA nanofiber matrix.

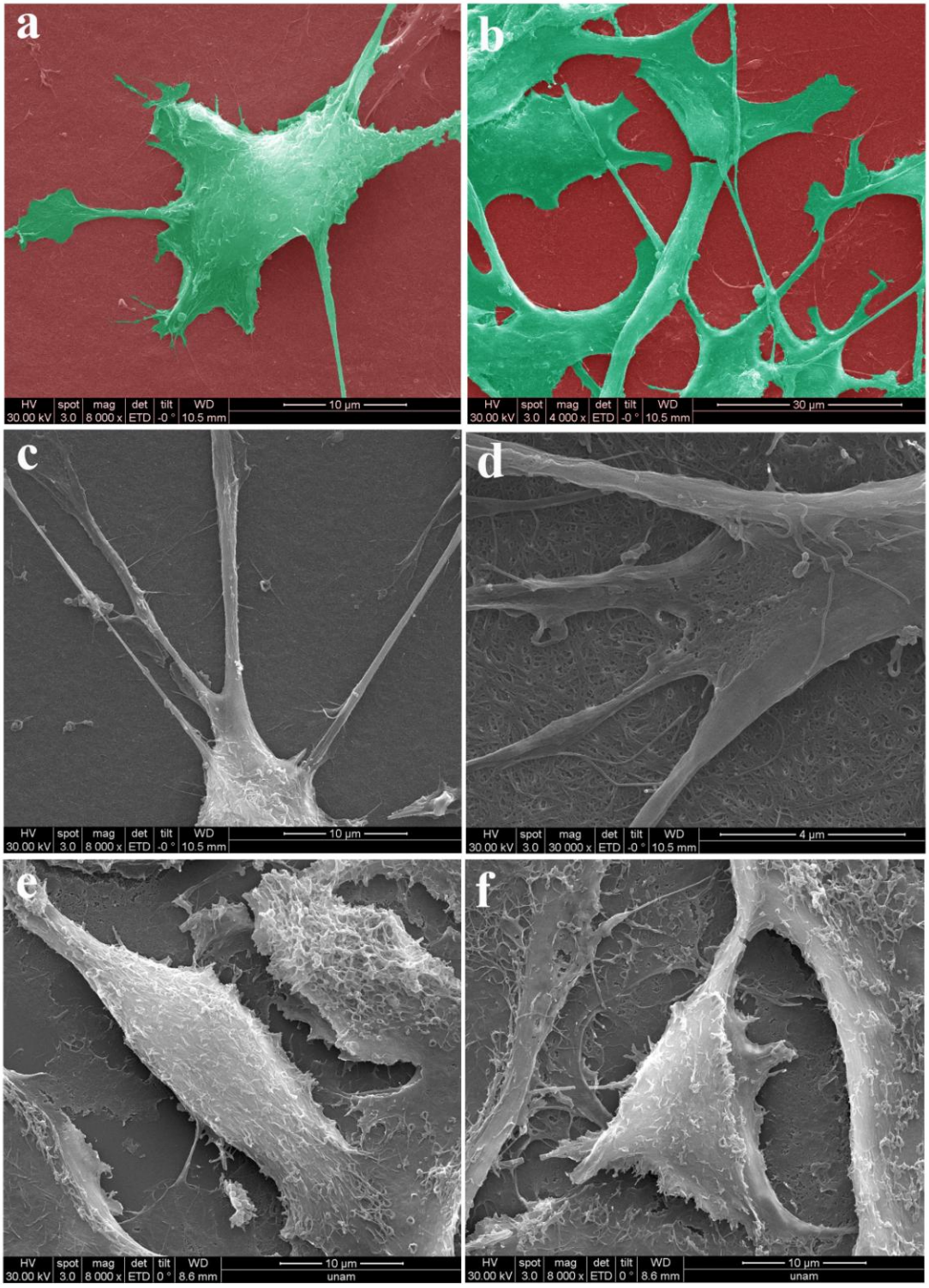

Figure 2.23. Electron micrographs of endothelial cells on HM-PA nanofiber scaffolds **(a-d)** and coverslip **(e, f)**. Endothelial cells exhibit heavily sprouting phenotype – multiple sprouts per cell and branching sprouts – on HM-PA matrices a-d, while almost no sprout on tissue culture plate (e, f) (Images a and b are artificially colored).

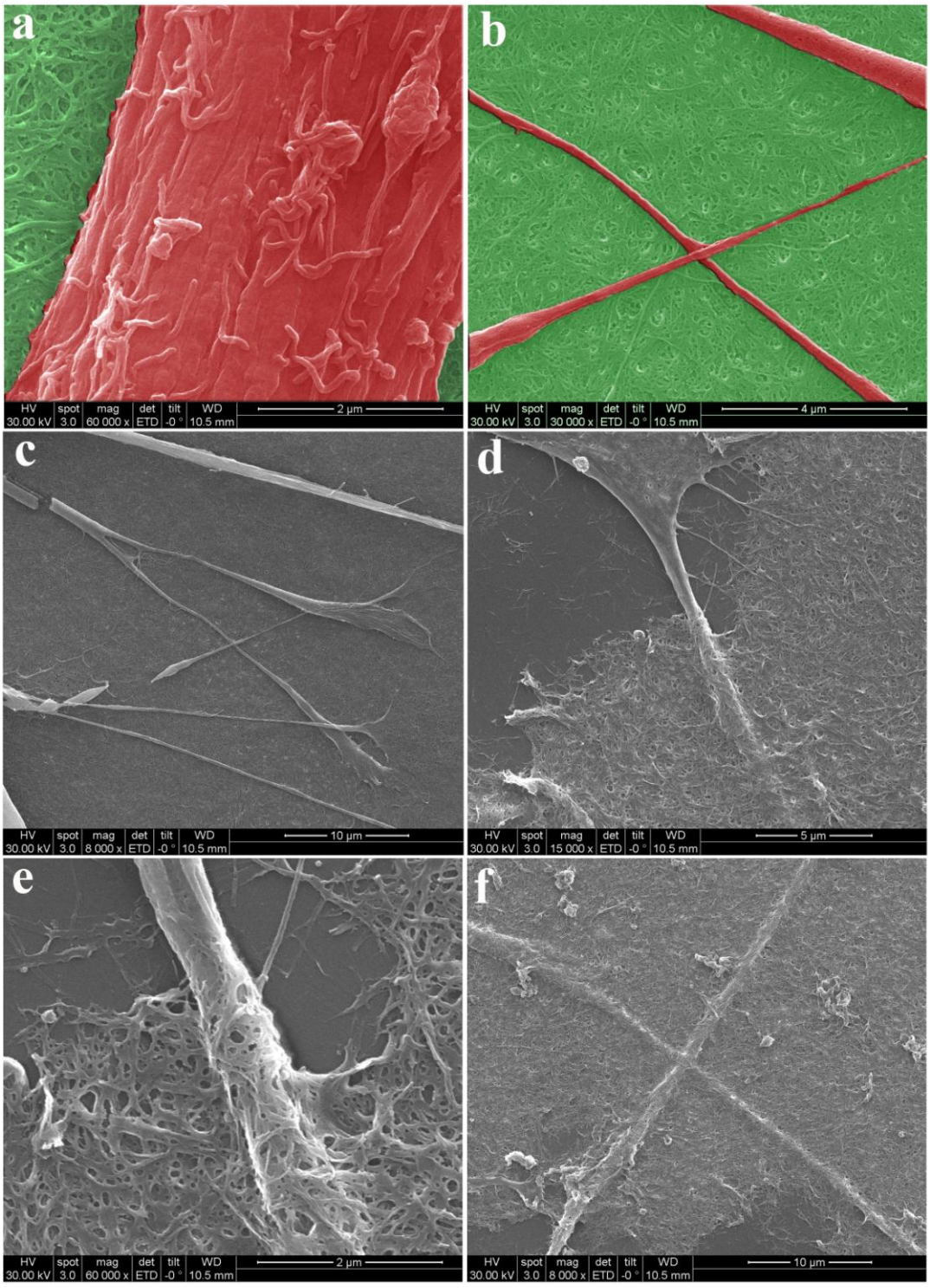

Figure 2.24. Electron micrographs of sprouts formed by endothelial cells on HM-PA nanofiber scaffolds. **a.** Tubule formed by endothelial cells with more than 4 µm diameter. **b.** Sprouts on nanofiber matrix (a and b are artificially colored). **c.** Long sprouts and hollow tube-like interior can be discerned from broken sprout. **d-f.** Cellular sprouts interact with fibrous matrix and can elongate inside the matrix.

2.3.3. Interaction of VEGF with PA nanofibers

As previously mentioned, glycosaminoglycans regulate growth factor-receptor interactions in the natural cellular environment. For example, VEGF cannot induce endothelial cells when there is no glycosaminoglycan in the microenvironment.[49, 52] Therefore, induction of angiogenesis by Heparin-mimetic PA nanofibers is possibly caused by their ability to bind to and present the growth factors that are secreted by the endothelial cells, which is critical for long-lasting angiogenic signaling to occur.[52] Specific growth factor binding to HM-PA nanofibers was investigated by isothermal titration calorimetry (ITC), which measure heat change after titrating VEGF molecules into the PA solutions (Figure 2.25 and 2.26). The binding constants between VEGF and both solution and nanofiber forms of HM-PA and D-PA were calculated by ITC (Figure 2.25, 2.26 and Table 2.3). As a result of this experiment, binding constant between HM-PA and D-PA molecules in nanofiber (mixed with K-PA) or in solution form and VEGF was found to be similar to the binding constant between heparin and VEGF, which confirms high affinity of both molecules to VEGF at given concentration.[76]

Interestingly, binding constants of solution forms of PAs with VEGF were higher than nanofiber forms with VEGF (5 fold for HM-PA and more than 2 fold for D-PA) (Table 2.3). These data suggest that bindings may be driven by charge-charge interactions, since the nanofiber forms are prepared by mixing K-PA into the solution form which neutralizes some of the negative charges on HM-PA and D-PA. Also, HM-PA molecules are mixed with 2 moles of K-PA, while D-PA molecules are mixed with 1 mole of K-PA to make final theoretical charge of the system similar. This might explain why we observed bigger difference between solution and nanofiber forms of HM-PA than D-PA (Table 2.3).

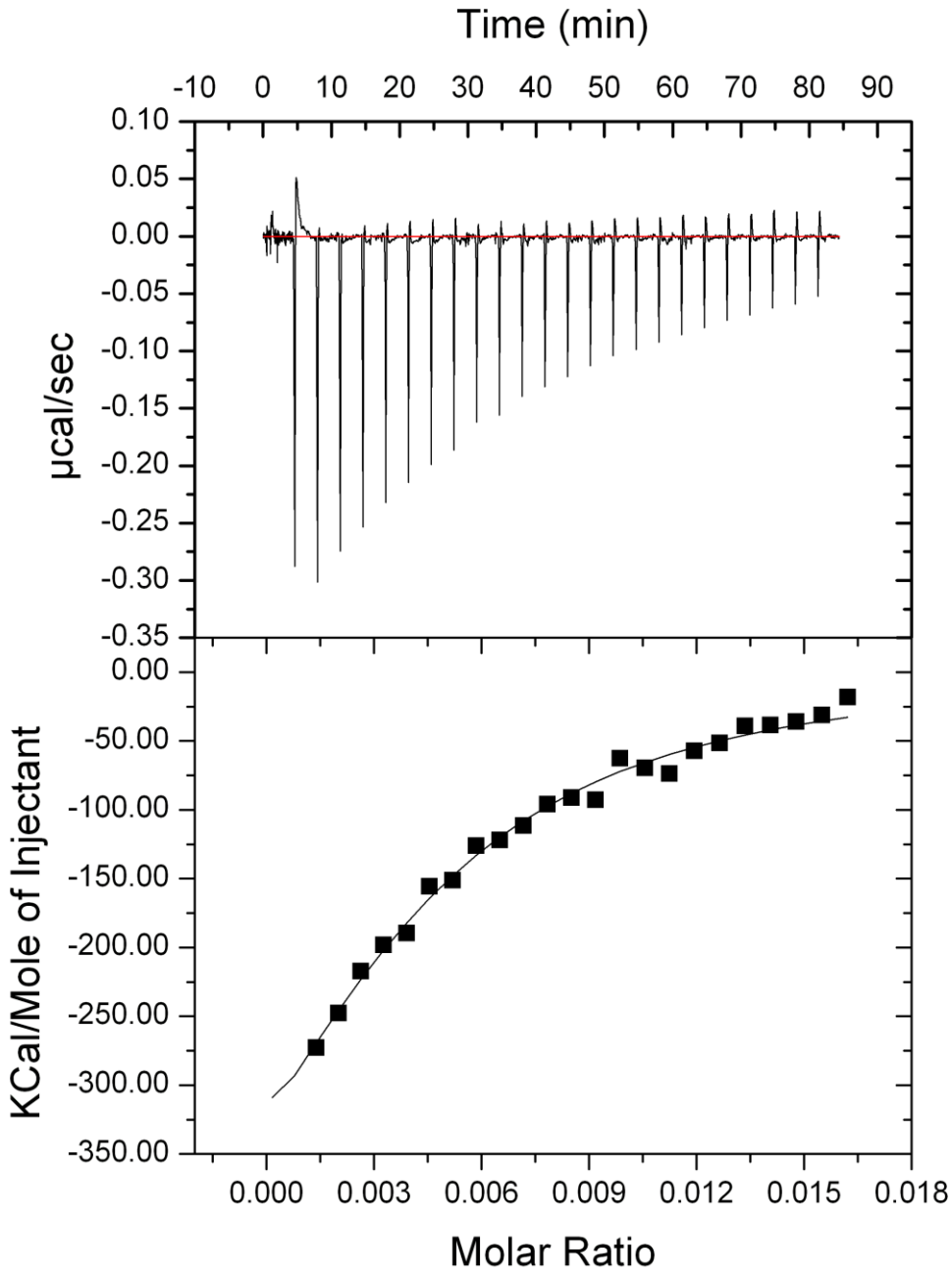

Figure 2.25. Isothermal Titration Calorimetry (ITC) graphs for titration of Heparin-mimetic PA molecules in solution form with VEGF. The top graph shows heat change per unit time during VEGF titration into Heparin-mimetic PA solution, and the bottom graph displays the integrated data (filled squares) and the best fit to a nonlinear function assuming one set of binding sites. Data indicates strong affinity between HM-PA molecules and VEGF (Ka calculated = $2.93 \times 10^{6} \pm 5.12 \times 10^{5}\ M^{-1}$).

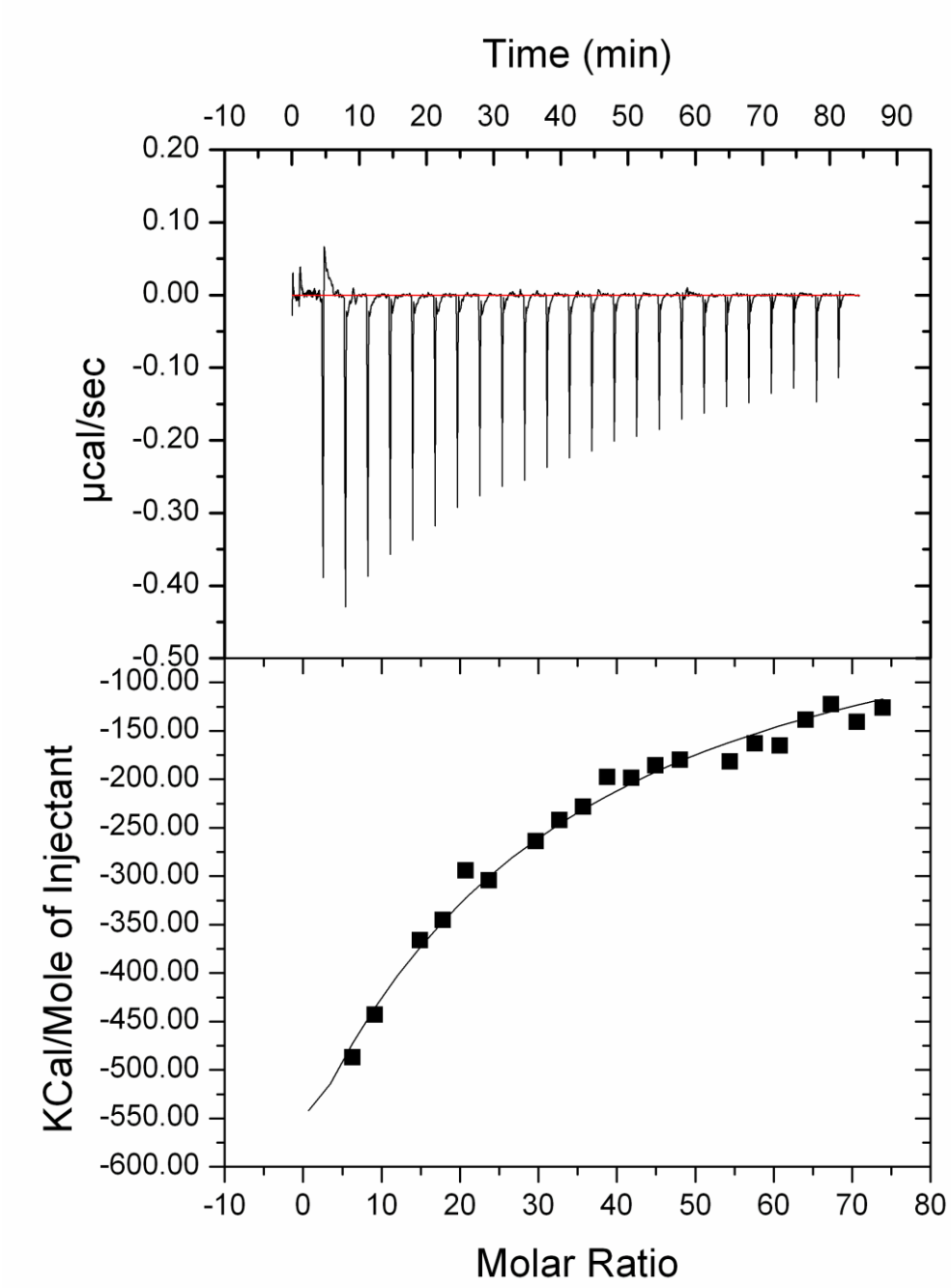

Figure 2.26. Isothermal Titration Calorimetry (ITC) graphs for titration of Heparin-mimetic PA (HM-PA) molecules in nanofiber form – mixed with K-PA – with VEGF. The top graph shows heat change per unit time during VEGF titration into Heparin-mimetic PA nanofiber solution, and the bottom graph displays the integrated data (filled squares) and the best fit to a nonlinear function assuming one set of binding sites. Data indicates strong affinity between HM-PA nanofibers and VEGF (Ka calculated $=7.37 \times 10^{5} \pm 5.1 \times 10^{4}\ M^{-1}$).

Since at higher concentrations aggregation of PA molecules and gel formation are observed, in this experiment we used low concentration of both PA molecules to make an experimental measurement possible. Both HM-PA and D-PA molecules revealed similar binding affinity to VEGF. This suggests that VEGF-PA interaction at this concentration was supported mainly by opposite charges between VEGF and PA molecules but not specific functional group architecture on nanofiber. Moreover, VEGF binding was driven by large enthalpic changes, which further support that electrostatic interactions have taken a role in the VEGF-PA binding (Table 2.3).[77] The decrease in entropy indicates the loss of conformational freedom for interacting molecules and the formation of more ordered complex structures (Figure 2.13 and Table 2.3).[78]

Table 2.3. Binding constants of VEGF – PA interaction at 30 °C measured by ITC.

Peptide Amphiphile	**Binding constant (K_a) (M^{-1})**	**Enthalpy change (ΔH) (cal/mol)**	**Entropy change (ΔS) (cal/mol/deg)**
Heparin-mimetic PA*	$2.93x10^6 \pm 5.12x10^5$	$-6.163x10^5 \pm 1.130x10^5$	$-2x10^3$
Heparin-mimetic PA**	$7.37x10^5 \pm 5.1x10^4$	$-4.122x10^7 \pm 1.79x10^6$	$-1.82x10^4$
D-PA*	$3.02x10^6 \pm 1.43x10^6$	$-9.312x10^5 \pm 6.723x10^5$	$-3.04x10^3$
D-PA**	$1.40x10^6 \pm 8.4x10^4$	$-3.870x10^7 \pm 1.24x10^6$	$-1.48x10^4$

* PA used in solution form
**PA used in nanofiber form (PA was mixed with K-PA before titration)

We further investigated the interaction of VEGF with PA nanofibers, but this time with nanofiber network formed by PA molecules. For this, we designed a growth factor release assay by encapsulating VEGF into gels formed by the PA nanofibers. VEGF release from HM-PA, D-PA, and K-PA/Heparin gels were monitored for 7 days to analyze the release rate. We observed burst release of growth factors from D-PA and heparin gels at 2 h, whereas the release rate was significantly lower for HM-PA gels (Figure 2.27). At the end of 7 days, only ~5% of the encapsulated VEGF was released from HM-PA gel, whereas this ratio was nearly 40% for heparin gel and

33% for D-PA gel. Because gelation and structural properties of the PA molecules revealed no significant differences, as analyzed by SEM, AFM, rheology, and CD; the possibility of physical release causing difference in release rate between Heparin-mimetic PA gel and other gels was eliminated. We concluded that VEGF binds to Heparin-mimetic PA nanofibers more strongly than D-PA and K-PA/heparin nanofibers. Although ITC results revealed similar binding affinities for both HM-PA and D-PA molecules to VEGF (Table 2.3), when these molecules are used in very dilute amounts ($\sim 10^{-4}$ M), the release rates of the VEGF from the corresponding gels, which are composed of densely packed nanofibers, was significantly different (Figure 2.27). According to the results of the release assay, it can be suggested that HM-PA nanofibers provide more specific binding sites for VEGF compared with D-PA nanofibers. The release profile of VEGF from K-PA/Heparin gel further demonstrates inappropriate presentation of heparin in this gel, impairing its growth factor binding capacity, which we have previously suggested according to the results of the *in vitro* angiogenesis assay and ITC measurement of interaction of K-PA and heparin (Figure 2.17b and 2.18). Importantly, slow release rate of VEGF from Heparin-mimetic PA gel is a significant finding because the formation of robust vessels requires long-term release of growth factors at low concentrations.[11, 21] Growth factor concentrations above the microenvironmental threshold (therapeutic range) cause vessel malformation with leaky and aberrant character.[11, 21, 79] HM-PA gel was observed to release VEGF within the narrow therapeutic range, which is important for clinical applications.

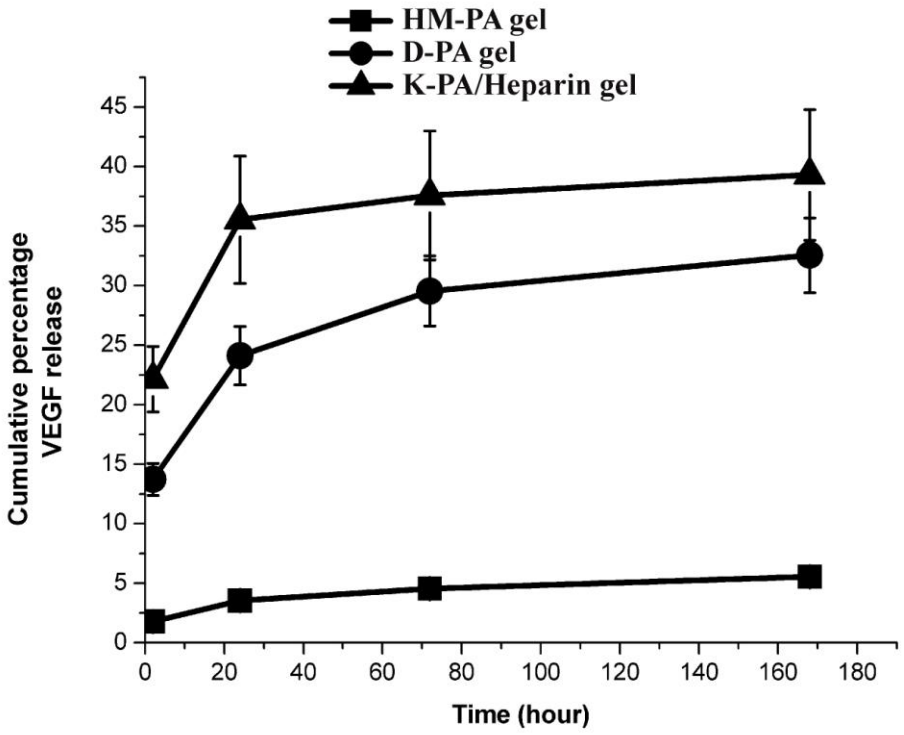

Figure 2.27. Release profile of vascular endothelial growth factor (VEGF) from various PA gels. Release of VEGF from 3 different PA gels was followed for 7 days. VEGF concentration in release buffer was measured by ELISA method. HM-PA gels released VEGF considerably slower than D-PA and K-PA/Heparin gels (n = 5 for Heparin-mimetic PA; n = 3 for D-PA and K-PA/heparin) Error bars indicate standard error mean.

Charges of these peptide nanofiber systems are important since they can give information about how growth factor binding to PA nanofiber systems depends on charge. Zeta potentials of PA solutions and nanofibers (with K-PA) were measured to understand the charge of the peptide systems (Figure 2.28). All carboxylate and sulfonate functionalized PAs and heparin revealed high negative potentials. When K-PA with a positive potential was added to the aforementioned solutions, negative charge in all solutions decreased. While HM-PA and SO_3-PA had zeta potentials of ~-90 and -70 mV, HM-PA/K-PA and SO_3-PA/K-PA combinations had potentials of nearly -30 mV (Figure 2.28). We observed a similar trend in heparin and K-PA mixture, when potential of heparin solution increased decreased from -60 to -45 mV. Whereas, D-PA potential increased to -5 mV from -60 mV after addition of K-PA

(Figure 2.28). Since bioactivity of heparan sulfates (i.e. growth factor binding) is related to their high negative charges caused by functional groups, we adjusted molar ratios of these mixtures for all experiments so that the net theoretical charge of the system will be negative (-1). However, zeta potential data indicated that charge density on PA complexes was not the same. This observation can be related to the presence of sulfonate ($-SO_3$) group in Heparin-mimetic PA and SO_3-PA, as well as heparin. Sulfonate group's pKa (~1) is lower than carboxylate group's pKa (~5), making charge neutralization of D-PA easier than that of sulfonate-bearing PAs. Therefore, the presence of sulfonate group increases the negative charge density on PA nanofibers, which might have an activatory role in growth factor binding. However, SO_3-PA nanofibers and heparin/K-PA did not as much reveal bioactivity compared with Heparin-mimetic PA nanofibers, as discussed above (Figure 2.16 and 2.17). Therefore, bioactivity of PA nanofibers is not only related to the charge of the system. Moreover, growth factor release rates from K-PA/Heparin gel shown in Figure 2.27 were significantly faster than those from HM-PA gel and D-PA gel, although charge of K-PA/Heparin system was more negative than HM-PA and D-PA. Picture drawn by all of these data suggests that growth factor interaction with PA nanofiber system is not an entirely function of charge of the system. Rather proper presentation of functional groups (or heparin in case of K-PA/Heparin) by nanofibers determines interaction of vascular endothelial growth factor with nanofiber scaffold and induction of angiogenic processes in endothelial cells.

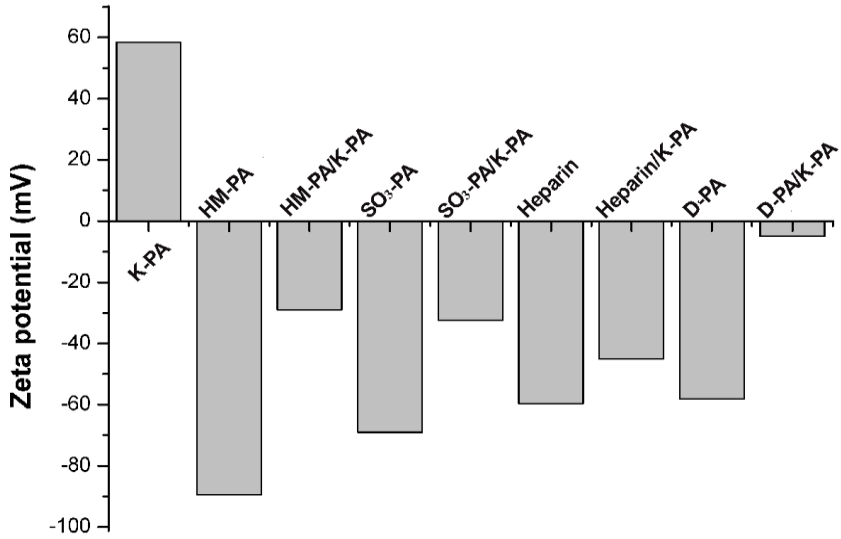

Figure 2.28. Zeta-potential measurements of PA combinations. K-PA is a positively charged peptide at physiological pH and showed positive zeta potential, while negatively charged PAs and their mixtures with K-PA had negative zeta potentials. Negative charge of D-PA neutralized very sharply upon mixing with K-PA, while heparin, HM-PA and SO_3-PA retained their negative charge considerably better.

2.3.4. Gene expression analysis of angiogenic switch in endothelial cells

Angiogenesis is initiated and maintained through distinct regulatory mechanisms that take place inside the endothelial cells. Toward this purpose, phases of endothelial cell activation and proliferation, followed by cellular migration and finally stabilization of tubular structures are required. Expressions of several genes are strictly regulated during these phases. To investigate further the mechanism of angiogenic switch in endothelial cells caused by Heparin-mimetic PA nanofibers, we analyzed the expression of genes involved in angiogenesis at mRNA level. Six different genes were selected from three different stages of angiogenesis. VEGF and FGF-2 are mainly involved in endothelial cell activation and proliferation; integrin α5 (IA5), integrin αv (IAV), and integrin β3 (IB3) take roles in cellular migration, and angiopoietin-1 (Ang-1) induces stabilization of vascular tubes.[80] Endothelial

cells were cultured on PA matrices for three different durations (6 h, 24 h, and 48 h) to simulate sequential activation of angiogenic stages in natural environment. We expected that, during the natural course of angiogenesis, VEGF and FGF-2 are upregulated at 6 h, integrins at 24 h, and Ang-1 at 48 h. Table 2.4 shows time-dependent expression of each gene, where each PA treatment was compared with the tissue culture plate. We observed that Heparin-mimetic PA scaffold enhanced the expression of genes for the aforementioned three stages of angiogenesis at expected time points (VEGF at 6 h, IA5 and IB3 at 24 h, whereas Ang-1 at 48 h; Table 2.4, Figure 2.29). FGF-2 levels were lower than VEGF, indicating that angiogenic switch was mainly driven by VEGF. The D-PA scaffold upregulated genes involved in endothelial cell activation and migration (VEGF, IA5, IB3, and IA5), whereas it downregulated Ang-1 (Figure 2.29). This observation is consistent with *in vitro* tube formation results (Figure 2.16, 2.21), where D-PA scaffold failed to form a stable tubular network, which is mainly maintained by Ang-1. Moreover, Heparin-mimetic PA nanofibers were more potent than D-PA regarding the expression of VEGF, IA5, IB3, and Ang-1, which indicates that Heparin-mimetic PA scaffold actively triggers endothelial cells to enter into angiogenic route.

Table 2.4. Gene expression profiles in endothelial cells cultured on PA nanofibers.

Gene	Time point	PA nanofiber	% change in expression
Integrin α5	6 h	D-PA	4% upregulated
		HM-PA	27% upregulated
	24 h	**D-PA**	**29%** upregulated
		HM-PA	**75%** upregulated
	48 h	D-PA	20% upregulated
		HM-PA	19% upregulated
Integrin αV	6 h	D-PA	10% downregulated
		HM-PA	16% upregulated
	24 h	**D-PA**	**7%** upregulated
		HM-PA	**15%** downregulated
	48 h	D-PA	31% downregulated
		HM-PA	39% downregulated
Integrin β3	6 h	D-PA	15% upregulated
		HM-PA	19% upregulated
	24 h	D-PA	**42% upregulated**
		HM-PA	**39% upregulated**
	48 h	D-PA	5% downregulated
		HM-PA	4% downregulated
VEGF	**6 h**	**D-PA**	**47% upregulated**
		HM-PA	**123% upregulated**
	24 h	D-PA	29% upregulated
		HM-PA	66% upregulated
	48 h	D-PA	21% upregulated
		HM-PA	21% upregulated
FGF2	6 h	**D-PA**	5% upregulated
		HM-PA	9% upregulated
	24 h	D-PA	**17% upregulated**
		HM-PA	**55% downregulated**
Ang1	24 h	D-PA	19% upregulated
		HM-PA	52% downregulated
	48 h	**D-PA**	**27% downregulated**
		HM-PA	**42% upregulated**

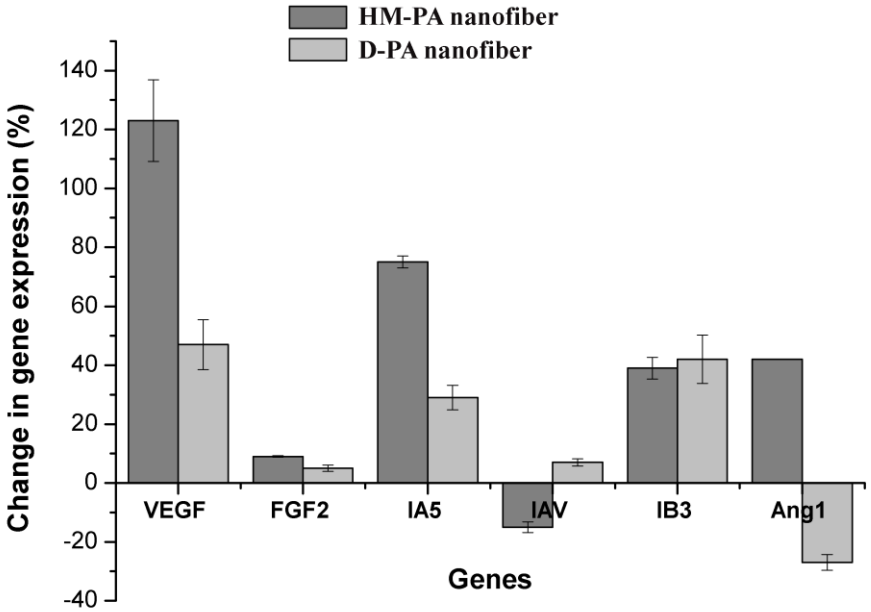

Figure 2.29. Investigation of expression profiles of angiogenic genes in endothelial cells (HUVEC) cultured on PA nanofiber matrices or tissue culture plate. Expression profiles of genes involved in different angiogenic stages were investigated at different time points by qRT-PCR. Activities of PA matrices tested here were compared with tissue culture plate, and results are illustrated as change in gene expression (%). Peak time point was selected for each gene and shown in this figure (n = 3 for all experiments). Error bars indicate standard error mean.

Since gene expression analysis in HUVECs revealed elevated expression of VEGF mRNA in endothelial cells cultured on HM-PA nanofibers and because capillary-like formations by endothelial cells can be triggered without any addition of exogenous VEGF by using these nanofibers, we asked whether VEGF secretion from HUVECs was also altered when cultured on HM-PA nanofibers. We checked VEGF secretion from HUVECs, cultured on HM-PA or D-PA nanofiber matrices or tissue culture plate, by using ELISA. ELISA results revealed that time-dependent VEGF secretion from HUVECs on HM-PA matrices increased exponentially as a function of time (Figure 2.30). At the end of 48 h, HM-PA induced four times more VEGF secretion than bare tissue culture plate and nearly two times more than D-PA. These results suggest that besides elevated expression of VEGF, the induction of VEGF secretion

is in effect. This might be due to autocrine signaling, where released VEGF molecules from cells are possibly entrapped and presented to the cells better with the HM-PA matrix, inducing the VEGF signaling pathways more robustly than the D-PA matrix and bare tissue culture plate.

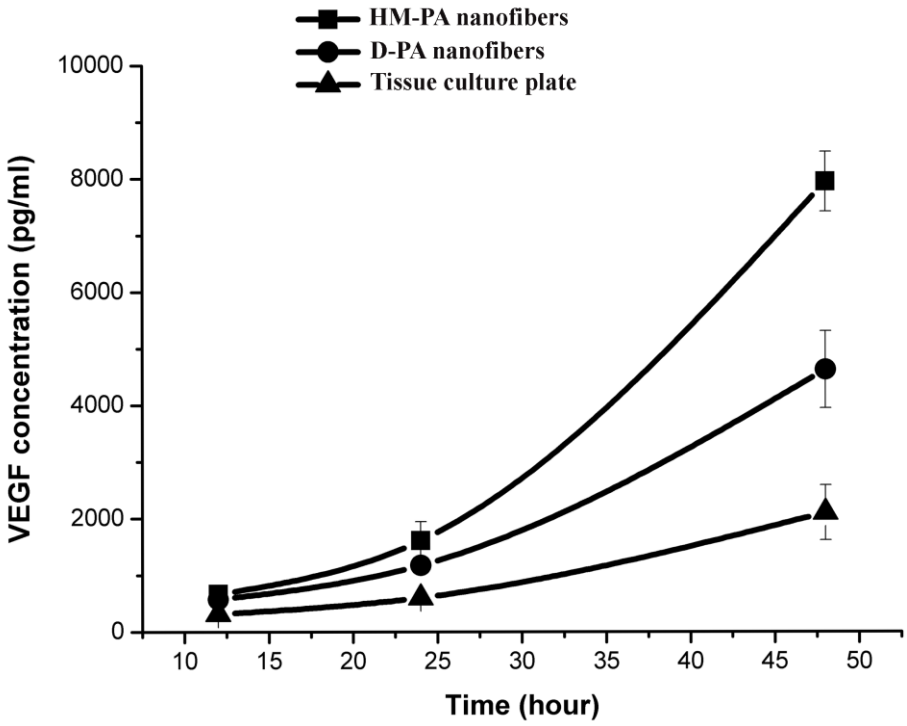

Figure 2.30. Determination of VEGF secretion from endothelial cells (HUVECs) cultured on PA nanofiber matrices or tissue culture plate. Time-dependent VEGF secretion from HUVECs cultured on different PA matrices or tissue culture plate were measured by using ELISA. $p < 0.001$ between Heparin-mimetic PA and Asp-PA or tissue culture plate at 48 h (analyzed by two-way ANOVA) ($n = 3$ for all conditions). Error bars indicate standard deviation.

2.3.5. *In vivo* neovascularization assay

The construction of robust vessels integrated into the circulatory system is crucial for functional tissue formation. To investigate *in vivo* efficacy of Heparin-mimetic PA (HM-PA) nanofibers, a rat corneal micropocket neovascularization assay was used.

Because the cornea is devoid of blood vessels, neo-vascularization in response to treatment condition can be easily detected.[81] Our treatment groups included HM-PA gel with growth factors (VEGF/FGF-2 combination) and growth factor solution only. Although the growth factor amount used was several times lower than the ones that were used in the literature,[82] it was sufficient to induce neo-vascularization when used in combination with HM-PA gel (Figure 2.31a). Moreover, vascularization after growth factor treatment without PA gel was limited and significantly lower than that induced by growth factors in combination with HM-PA gel (Figure 2.31 and 2.32).

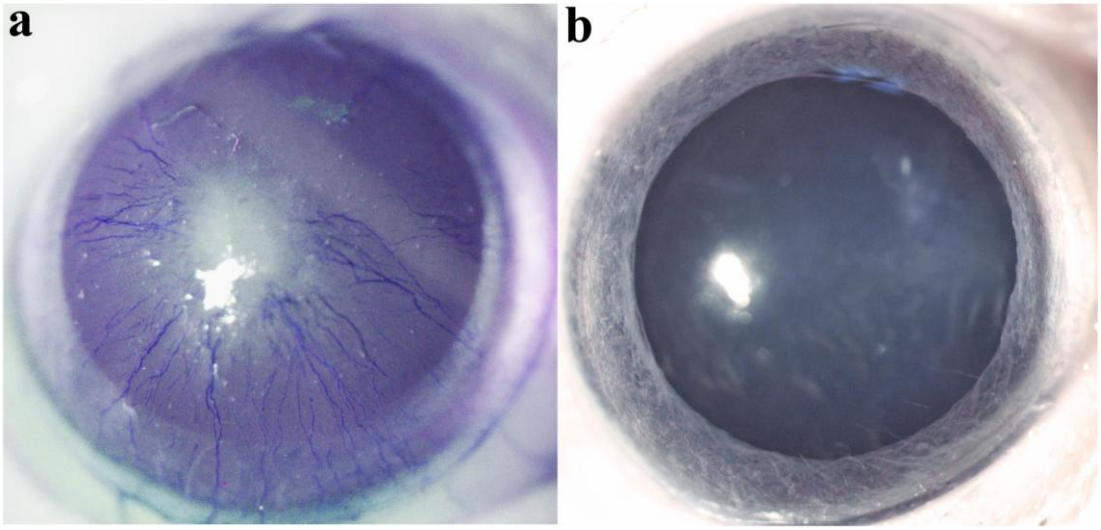

Figure 2.31. Evaluation of *in vivo* bioactivity of HM-PA nanofibers by corneal angiogenesis assay. **a.** Injection of 1 wt% HM-PA gel with 10 ng of VEGF and bFGF induced robust vascularization in cornea. **b.** Application of growth factor solution (10 ng of VEGF and bFGF) in physiological saline (without PA gel) did not induce vascularization. Photos were taken after perfusing animals with Indian ink.

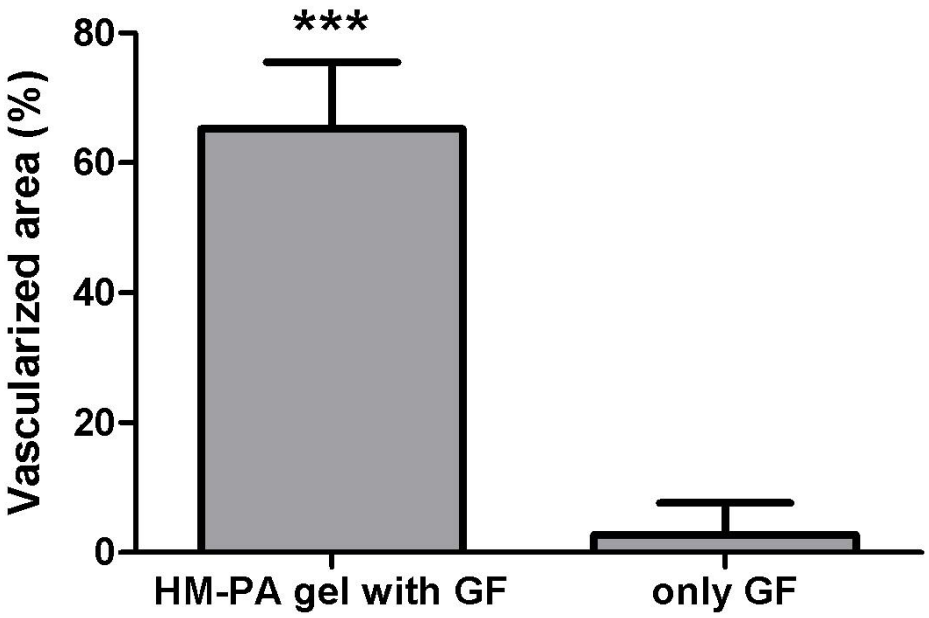

Figure 2.32. Quantification of vascularized area in corneal angiogenesis assay. Ratio of vascularized area to total area was calculated for both groups (n = 3 for each group). Heparin-mimetic PA gel with growth factor (Gel + GF) was significantly higher than growth factor alone (GF) solution treatment as compared with Student's t test (***$p < 0.001$) (n = 3 for both treatments). Error bars are standard deviations.

In the corneal angiogenesis assay, the samples were introduced to the center of cornea, which is located far from the endothelial cells, therefore there are no detectable angiogenic growth factors in this area in healthy animals. Likely due to mentioned reasons, no significant vessel formation was observed in animals injected with Heparin-mimetic PA gel without growth factor (Figure 2.33b). This observation also shows that angiogenic activity observed in Figure 2.31a and 2.33a is not caused by inflammatory response against PA nanofibers but is because of slow release of growth factors from Heparin-mimetic PA gels. Moreover, Indian ink, which was used for perfusing the animals, entered and stayed in the newly formed capillaries, confirming that new vessels are robust and integrated to the circulatory system (2.31a).

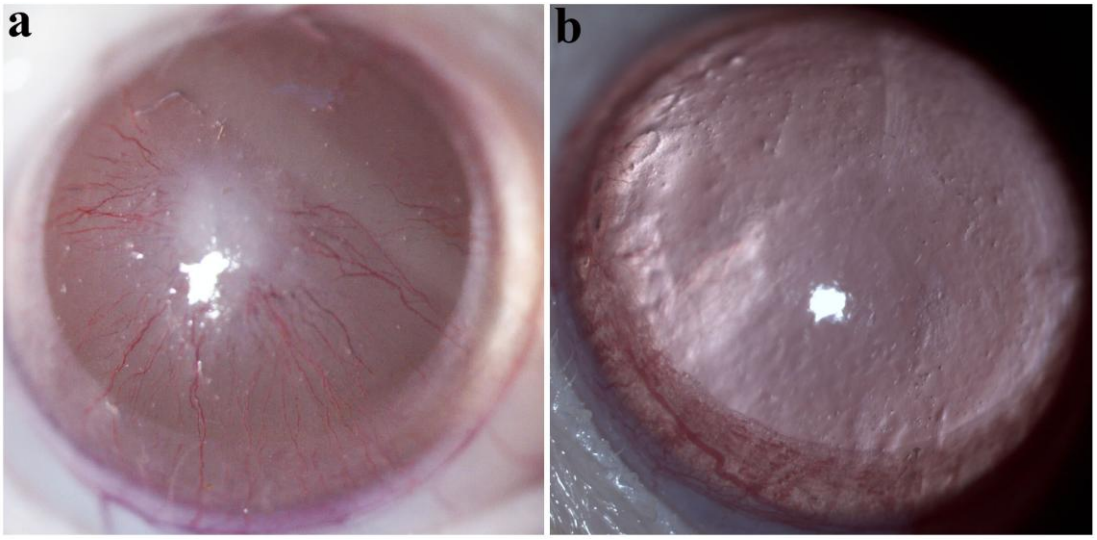

Figure 2.33. Effect of HM-PA gel alone or with growth factors on corneal angiogenesis. Treatments: **a.** HM-PA gel with growth factors (10 ng VEGF/FGF2) **b.** HM-PA gel alone (n=3 for each treatment). While robust vascularization is observed with HM-PA gel with growth factors, no detectable vascularization is observed with HM-PA gel alone.

2.4. Experimental Details

2.4.1. Materials.

9-Fluorenylmethoxycarbonyl (Fmoc) and tert-butoxycarbonyl (Boc) protected amino acids, [4-[α(20, 40 dimethoxyphenyl) Fmocaminomethyl] phenoxy] acetamidonorleucyl-MBHA resin (Rink amide MBHA resin), Fmoc-Asp(OtBu)-Wang resin, and 2-(1H-Benzotriazol-1-yl)-1,1,3,3-tetramethyluronium hexafluorophosphate (HBTU) were purchased from NovaBiochem and ABCR. Heparin was purchased from Sigma-Aldrich. The other chemicals were purchased from Fisher, Merck, Alfa Aesar, or Aldrich. All chemicals were used as provided. VEGF (vascular endothelial growth factor) used in angiogenesis assays were purchased from Sigma-Aldrich (mouse) and Invitrogen (human). Both mouse and human bFGFs (fibroblast growth factor) (FGF-2) were purchased from e-Biosciences.

2.4.2. Synthesis of Peptide Amphiphiles

PAs were constructed on Rink Amide MBHA resin or Fmoc-Asp(OtBu)-Wang resin. Amino acid couplings were performed with 2 equiv of Fmoc-protected amino acid, 1.95 equiv of HBTU, and 3 equiv of N,N-diisopropylethylamine (DIEA) for 2 h. Fmoc removal was performed with 20% piperidine/dimethylformamide solution (DMF) for 20 min. We used 10% acetic anhydride solution in DMF to block remaining free amine groups after amino acid coupling. After each step, resin was washed by using three times DMF, three times DCM, and three times DMF, respectively. Sulfobenzoic acid was added to the side chain of lysine to synthesize sulfonated PAs. A lysine residue with 4-methytrityl (Mtt) side-chain protection was used for selective deprotection of amine groups. Mtt removal was performed by shaking resins for 5 min with TFA/TIS/H_2O/DCM in the ratio of 5:2.5:2.5:90. Cleavage of the PAs from the resin was carried out with a mixture of TFA/TIS/H_2O in the ratio of 95:2.5:2.5 for 2 h. Excess TFA was removed by rotary evaporation. The remaining viscous PA solution was triturated with ice-cold ether, and the resulting white precipitate was dried under vacuum. PAs were characterized by liquid chromatography-mass spectrometry (LC-MS). Mass spectrum was obtained with Agilent 1200 LC-MS equipped with Agilent 6530 Q-TOF with an ESI source and Zorbax Extend-C18 2.1 x 50 mm column for basic conditions and Zorbax SB-C8 4.6 mm x 100 mm column for acidic conditions. A gradient of (a) water (0.1% formic acid or 0.1% NH_4OH) and (b) acetonitrile (0.1% formic acid or 0.1% NH_4OH) was used. Agilent 1200 preparative reverse-phase HPLC system equipped with a Zorbax Extend-C18 21.2 x 150 mm column for basic conditions and a Zorbax SB-C8 21.2 x 150 mm column for acidic conditions was used to purify the peptides. A gradient of (a) water (0.1% TFA or 0.1% NH_4OH) and (b) acetonitrile (0.1% TFA or 0.1% NH_4OH) was used.

2.4.3. Peptide Amphiphile Nanofiber Formation.

To investigate angiogenic potentials of PA nanofibers presenting heparin-mimicking functional groups, we designed and synthesized several PA molecules. Functional group content varied for each molecule: Heparin-mimetic PA (HM-PA) was synthesized with sulfonate, hydroxyl, and carboxylic acid groups, SO_3-PA with sulfonate and carboxylic acid groups, and D-PA with only carboxylic acid groups (Figure 2.2). To induce gel and nanofiber formation, we prepared PA formulations by mixing HM-PA PA, D-PA, and SO_3-PA molecules with K-PA at 1:2, 1:1, and 1:1 molar ratios, respectively. H-PA solution was adjusted to pH 7.4, and heparin was mixed with K-PA at ~1:8 molar ratios.

2.4.4. AFM Imaging of PA Nanofibers

AFM sample solutions were dropped on the silicon wafer surface and mixed by pipetting up and down. We mixed 25 μL of 0.02 wt% Heparin-mimetic PA or equimolar concentrations of SO_3-PA and D-PA with 25 μL of 0.02 wt% positively charged K-PA. Heparin was mixed with K-PA, and H-PA solution was adjusted to pH=7 for nanofiber formation. After 30 s, solvent on the wafer was removed by using dust-free tissue paper, and the rest was air dried. Contact mode atomic force microscopy (AFM) was performed by using model MFP-30 from Asylum Research. All images were taken with 0.5 Hz scan rate. Tips with resonance frequency of 13 kHz and spring constant of 0.2 N/m were used in all experiments.

2.4.5. SEM Imaging of PA Gels

PA gels (1 wt% Heparin-mimetic PA gel and equimolar amount for the rest) were transferred onto a metal mesh, and network dehydration was performed by incubating gels for 30 s in 20, 40, 60, 80, and 100% ethanol sequentially. Then, gels were critical-point dried by using Autosamdri-815B (Tousimis). Dried gels were

coated with 6 nm of Pt. SEM (FEI Quanta 200 FEG) images were taken by using ETD detector at high vacuum mode with 30 keV beam energy.

2.4.6. TEM Imaging of PA Nanofibers and Nanofiber Size Measurements

PA nanofiber size measurements were made according to TEM images for each nanofiber type.[83] TEM sample was prepared by mixing HM-PA, SO_3-PA, and D-PA (1 wt%) with K-PA (1 wt%). Gel was diluted 10 times, and 30 μL from this solution was drop casted onto a hydrophobic surface. TEM grid was placed onto droplet and incubated for 3 min. Staining was performed with 2% uranyl acetate. Nanofiber diameters were measured by Image J software (NIH).

2.4.7. SEM Imaging of Cells on the PA Gels

In vitro tube formation experiment was performed (as described above) on round glass coverslips located in 24-well plates. After 48 h, media on cells were aspirated, and cells were washed with 1x PBS twice. Cells were fixed with 2% glutaraldehyde 1 h prior to fixation with 1% osmium tetroxide (OsO4). After network dehydration, critical-point drying was performed as described above for SEM imaging of PA gels. Samples were coated with 6 nm Au-Pd coating, and SEM imaging was performed as described above.

2.4.8. Isothermal Titration Calorimetry

To investigate the interaction between VEGF and PAs, we used the iTC200 system (MicroCal, GE Healthcare). VEGF titration (6.25 μM) into four different PA solutions (0.08 mM) was performed on HM-PA (solution form), HM-PA/K-PA (nanofiber form), D-PA (solution form), and D-PA/K-PA (nanofiber form). VEGF into H_2O and H_2O into HM-PA with K-PA titrations were performed as control to

eliminate dilution heats. Reaction was performed at 30 °C with 400 rpm stirring speed. Twenty-five injections were performed, where the injection period was 4 s and space between injections was 200 s. The data were integrated and fit to a curve with MicroCal Origin software to calculate the binding constant. For VEGF to PA solution titrations, best-fitting was obtained with one set of sites model, whereas for VEGF to PA nanofiber titrations, best-fitting was obtained with sequential binding sites model, and binding constants were calculated accordingly. To determine supramolecular heparin-mimetic system concentration, we performed calculations based on approximations made by Silva et al.[6] (average diameter of fiber disk = 6 nm; circumference of nanofiber (Πd) = 18.8 nm, number of PA molecules/radial disk = 50). Width of radial disk ≈ size of 1 molecule = 18.8 nm/50 = 0.376 nm. A 100 nm length PA nanofiber can contain ~13,300 PA molecules with 50 PA molecules per radial disk and 0.376 nm width. HM-PA and K-PA were mixed at 1:2 molar ratio. Therefore, the number of HM-PA molecules per 100 nm nanofiber was calculated to be 13,300/3 = 4433 molecules. By assuming that the average nanofiber length was 100 nm, nanofiber concentration = 0.08 mM/4433 = 1.8 x 10^{-5} mM. D-PA and K-PA were mixed with 1:1 molar ratio. The number of D-PA per 100 nm nanofiber was calculated to be 13,300/2 = 6650 molecules. By assuming that average nanofiber length was 100 nm, nanofiber concentration = 0.08 mM/6650 = 1.2x10^{-5} mM. The nanofiber dimensions were also measured by using TEM imaging, as described above. All solutions that were used in ITC experiments were at pH=7. To investigate the interaction between heparin and K-PA, heparin (100 μg/mL) was titrated into K-PA solution (40 μg/mL). Reaction was performed at 30 ^{o}C with 400 rpm stirring speed. Twenty-five injections were performed, where injection period was 4 s and space between injections was 150 s. The data were integrated and fit to a curve with MicroCal Origin software to calculate the binding constant. Best fitting was obtained with one set of sites model.

2.4.9. Oscillatory Rheology

Oscillatory rheology measurements were performed with an Anton Paar Physica RM301 rheometer operating with a 25 mm parallel plate configuration at 25 ^{o}C. Each sample of 180 μL total volume with a final PA concentration of 1 wt% HM-PA or equimolar concentrations for other PA molecules was carefully loaded on the center of the lower plate and incubated for 15 min before measurement. After equilibration, the upper plate was lowered to a gap distance of 0.5 mm. Storage moduli (G`) and loss moduli (G``) values were scanned from 100 to 0.1 rad/s of angular frequency, with a 0.5% shear strain.

2.4.10. Circular Dichroism

JASCO J815 CD spectrometer was used at room temperature. We measured 2 x 10^{-4} M peptide solutions from 300 to 190 nm, data interval and data pitch were 0.1 nm, scanning speed was 100 nm/min, and all measurements were performed with three accumulations. DIT was selected as 1 s, bandwidth as 1 nm, and the sensitivity was standard. Molar ellipticity was calculated using the equation: $[\theta] = 100 \times \theta/(C \times l)$, where C is the concentration in molar, and l is the cell path length in centimeters. $[\theta] = \theta/(Cx\ l) = deg/(mol/1000\ cm^3) \times 0.1\ cm = 10\ cm\ 10^{-3}\ deg\ 1000\ cm^3\ mol^{-1} = 100\ deg\ cm^2\ dmol^{-1}$.

2.4.11. Zeta Potential Measurement

The zeta potential of equimolar PA solutions (0.16 mM) and heparin (0.5 mg/mL) was measured by Nano-ZS Zetasizer (Malvern). Zeta potential converts measured mobility to zeta potential by using Smoluchowski equation. After measuring zeta potential of each PA solution, K-PA was mixed with HM-PA (2:1 molar ratio), SO_3-PA (1:1 molar ratio), D-PA (1:1 ratio), or heparin and the zeta potential of the solution was measured again. Molar ratios were the same as those used for cell culture and other experiments (net theoretical -1 charge for each combination).

2.4.12. Cell Lines and Cell Culture Reagents

H5V mouse endothelial cells[72] were a kind gift from Dr. Annunciata Vecchi, Instituto Clinico Humanitas, IRCCS, Rozzano, Milano, Italy. Human umbilical vein endothelial cells (HUVECs) were donated by Yeditepe University, Istanbul, Turkey. HUVECs were purified as described[84] and were characterized by staining with CD34, CD31, and CD90 surface markers. These cells were found to be positive for CD31 and CD34 but negative for CD90. All media, sera, and other cell culture reagents were purchased from Invitrogen. Matrigel was purchased from BD Biosciences.

2.4.13. *In Vitro* Angiogenesis Assay

Equimolar concentrations of PAs (0.2 wt % for Heparin-mimetic PA and equimolar amount for the rest) were used to form gels in 96-well plates. Coated plates were incubated at 37 ^{o}C for 30 min, prior to overnight incubation in laminar flow hood at room temperature for solvent evaporation. The next day, PA matrix formed on 96-well plates was UV-sterilized, and endothelial cells were cultured on these matrices or Matrigel, which was used as a positive control. HUVECs cultured in DMEM with 10% FBS (growth medium) were collected at 80-90% confluency and resuspended in DMEM with 5% FBS for angiogenesis assay. Cell number was adjusted to 2 x 10^5 cells/mL, and 200 μL of this suspension was added to each well either alone or mixed with low (10 ng/mL) or high (50 ng/mL) dose of VEGF/bFGF combination. After 48 h, cells were imaged by using bright-field microscopy at 100x magnification. For fluorescence imaging, media over cells were aspirated, and cells were washed with PBS. Calcein solution (2 μM, 100 μL) was added to cells and incubated for 30 min at 37 °C. Cells were imaged with fluorescence microscopy. Mouse endothelial cells (H5V) were also grown in DMEM with 10% FBS until 80-90% confluency. Cells were collected and resuspended in minimal essential media (MEM) with 2% FBS during angiogenesis assay. Cell numbers were adjusted to 3 x 10^5 cells/mL. We added 100 μL from this suspension (3 x 10^4 cells) to each PA

matrix. Cells were incubated for 48 h, and imaging was performed by using bright field microscopy. All of the *in vitro* experiments and other measurements were performed at least three times.

2.4.14. Cell Proliferation Assay

96-well plates were coated with PA matrices, as described above for *in vitro* angiogenesis assay, or left uncoated (TCP). HUVEC (1 x10^4) were added to each well in DMEM with 10% FBS. BrdU-based kit (Roche) was used to evaluate cell proliferation at the end of 54 h. In brief, 16 h before ending an experiment, BrdU was added to each well. After 16 h, cells were fixed and stained by using labeled antibody against BrdU. Cells were washed three times with PBS, and substrate solution was added. After 5, 10, and 20 min, color development was measured at 370 nm by using microplate reader (Molecular Devices) and subtracted from reference wavelength (492 nm) values.

2.4.15. Quantification of *in vitro* tube formation

In total, 12 images (100x magnification) were taken for each treatment group (four different images per well). Quantification of endothelial tube lengths on each image was performed by using NIH Image J software according to previously published criteria.[85] Tube length values obtained for each well (three wells per treatment group) were summed, and mean value of data obtained from three wells was calculated. Two-way ANOVA was used for statistical analysis.

2.4.16. Growth Factor Release from PA Gels

Heparin-mimetic PA, D-PA, and heparin solutions (25 μl) were combined with K-PA (25 μl; premixed with 100 ng of VEGF) to induce gel formation (1 wt% for

Heparin-mimetic PA gel and equimolar amount for the rest). After 1 h of incubation at 37 °C, 250 μL of 1x PBS was added to each gel. Buffer over gels was collected and replaced with fresh buffer at four different time points (2, 24, 72, and 168 h). VEGF released in the buffer solutions was quantified by ELISA method. VEGF incubated in same buffer solution (without gel) was accepted as 100% release.

2.4.17. Real-Time Gene Expression Study

HUVECs (3 x 10^5 cells/ well) were cultured on bare tissue culture plate (NC), HM-PA, or D-PA nanofiber matrices (as described in the *In Vitro* Angiogenesis Assay section) for three different durations (6, 24, and 48 h). Total RNAs were extracted from cells by using TRIzol (Invitrogen) according to the manufacturer's instructions. Concentration and purity of isolated RNAs were measured by Nanodrop. Samples were diluted to a concentration of 50 ng/μL prior to their use. RNAs were converted to cDNA and amplified by using SuperScript III Platinum SYBR green one step qRT-PCR Kit (Invitrogen). Primer sequences for each gene are given at Table 2.5. Specificity of amplifications was determined by the presence of single peaks/gene in melting curve analysis and detection of the product size by running PCR products in 1.5% agarose gel. Gene expression levels were normalized with GAPDH expressions for each sample, and relative expressions were calculated by $2^{-\Delta\Delta Ct}$ method according to the below formula: ΔCt (NC) $=(Ct_{gene}-Ct_{reference})$; ΔCt (PA-coated) $= (Ct_{gene}-Ct_{reference})$; $\Delta\Delta Ct = \Delta Ct$ (PA nanofiber-coated) - ΔCt (NC); fold expression $=2^{-\Delta\Delta Ct}$; % change in expression: 100 x $2^{-\Delta\Delta Ct}$.

Table 2.5. Investigated genes taking role in angiogenesis process.

Genes	Angiogenic stage	Primer sequences
VEGF	Endothelial cell activation	5′-ATCTTCAAGCCATCCTGTGTGC-3′ 5′-CAAGGCCCACAGGGATTTTC-3′ [86]
FGF-2	Endothelial cell activation	5′-ACGGCGTCCGGGAGAA-3′ 5′-ACACTCCCTTGATGGACACAACT-3′ [87]
Integrin α5 (IA5)	Cell migration	5'-TGCAGTGTGAGGCTGTGTACA-3' 5'-GTGGCCACCTGACGCTCT-3' [88]
Integrin αv (IAV)	Cell migration	5'-AATCTTCCAATTGAGGATATCAC-3' 5'-AAAACAGCCAGTAGCAACAAT-3' [88]
Integrin β3 (IB3)	Cell migration	5'-CCGTGACGAGATTGAGTCA-3' 5'-AGGATGGACTTTCCACTAGAA-3' [88]
Angiopoietin -1 (Ang1)	Vascular maturation, stabilization	5'-ACCCGAGCCTATTCACAGTA-3' 5'-CATTCAGTTTTCCATGGTTT-3' [89]

2.4.18. Detection of VEGF Secretion by Endothelial Cells

HUVECs were cultured at a density of 4 x 10^4 cells/well on different PA matrices and bare tissue culture plates, as described above (*In Vitro* Angiogenesis Assay section). Supernatants were collected at three different time points (12, 24, and 48 h). Concentration of VEGF in these supernatants was quantified by ELISA (Invitrogen). Two-way ANOVA was used to determine the significance of difference between VEGF secretion amount from cells cultured on PA matrices or tissue culture plate.

2.4.19. *In Vivo* Corneal Micropocket Angiogenesis Assay

Animal model and experimental setup were approved by the Animal Ethics Committee of Fatih University Medical School. The *in vivo* assay was carried out with 200-220 g female Sprague-Dawley rats. A surgical micropocket was opened in

the cornea ~1.5 mm from the limbus under anesthesia, as described.[5] Three conditions were tested with this model: 1 wt% HM-PA gel with 10 ng bFGF and VEGF; growth factor solution including 10 ng bFGF and VEGF; and 1 wt% HM-PA gel without growth factors. Gels were made *in situ* by mixing HM-PA and K-PA. Eleven days after injection, rats were anesthetized with xylazine/ketamine solution and perfused through injection of India ink to the left ventricular region of their hearts to observe integration of newly formed vessels into the circulatory system. Quantification of vascularization as a response to each treatment (n = 3 per group) was done with NIH Image J software according to previous work.[5] Student's t test was used for statistical analysis of difference between treatment groups. DC-1 digital camera (Topcon Europe, Ijssel, The Netherlands) was used for imaging the cornea.

2.5. Conclusion

In this chapter, requirement for heparin for growth factor activity was eliminated by using peptide nanofibers decorated with bioactive chemical groups from heparin (sulfonate, carboxylic acid, and hydroxyl). The *in vitro* angiogenesis assays revealed that sulfonate group itself is not sufficient for an optimal angiogenic outcome. By using other biologically active chemical groups along with the sulfonate group, we were able to induce in vitro formation of capillary-like structures by mouse and human endothelial cells on bioactive peptide scaffold without further addition of growth factors and other angiogenic supplements (e.g. heparin). Endogenous angiogenic growth factors that bind to the bioactive PA nanofibers were sufficient for vessel formation. In addition, heparins induce more robust signaling when they are presented to the cells in a special conformation,[52, 90] and Heparin-mimetic PA nanofibers mimic this structure by presenting critical functional groups of heparin appropriately and induce more sustained growth factor signaling (Figure 2.34). Proper distribution of heparin-mimetic functional groups on the peptide nanofibers allows specific binding to endogenous growth factors released from cells and maintain their interaction with receptors on same cells. Potentially, Heparin-mimetic PA nanofibers bind to heparin-binding growth factors with a specific affinity, present

them effectively to target receptors for the formation of active growth factor-receptor complex, and achieve sustained angiogenic signaling (Figure 2.34). Materials presented here provide new opportunities for angiogenesis and tissue regeneration by avoiding the use of heparin and exogenous growth factors. The synthetic scaffolds enriched with proper chemical functional groups shown here can induce the desired physiological response for tissue regeneration.

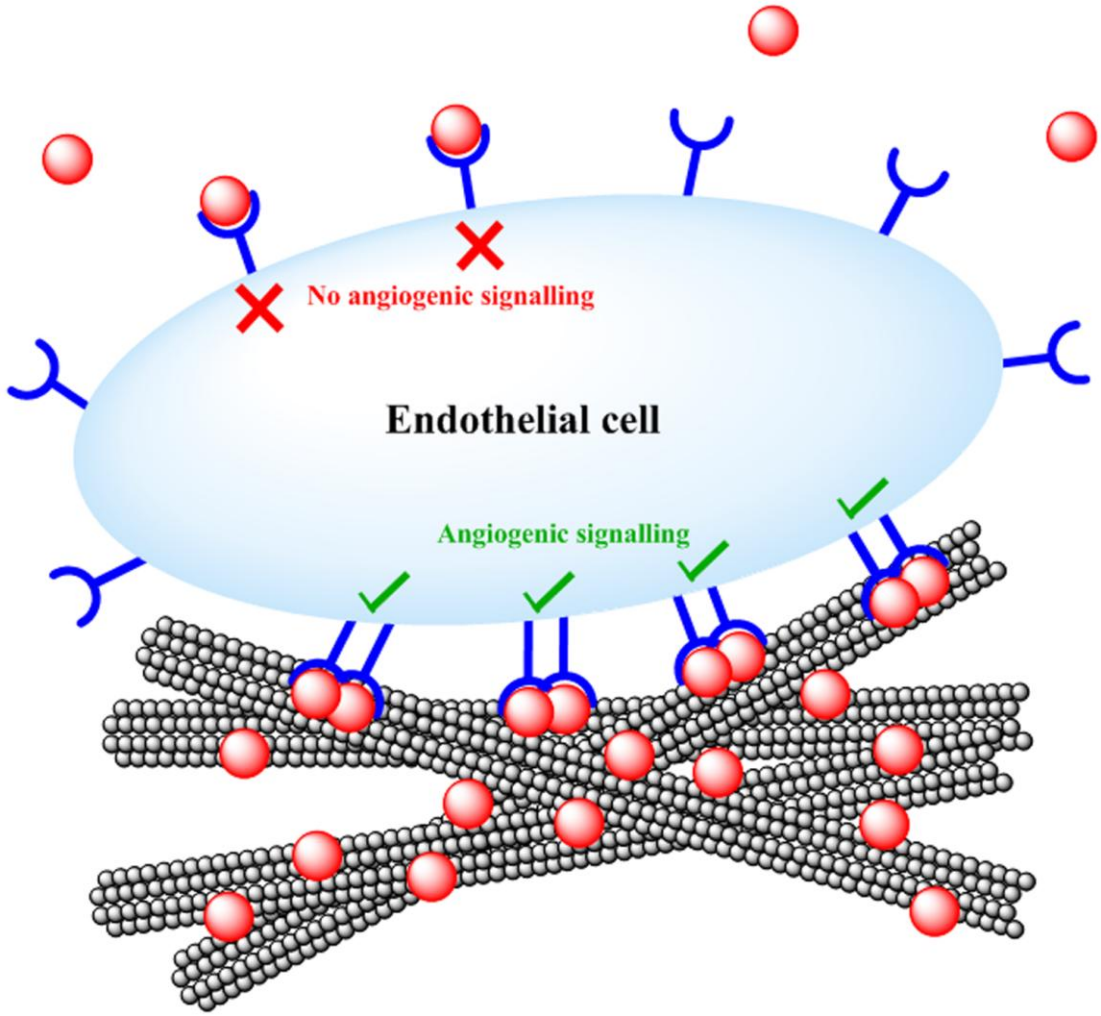

Figure 2.34. Suggested mechanism for the induction of angiogenesis by bioactive HM-PA nanofibers. HM-PA nanofibers bind to growth factors (red balls) and present them to endothelial cells appropriately, which activate the angiogenic process. However, growth factors alone do not induce angiogenic signaling as shown previously.

CHAPTER 3

3. SELECTIVE GROWTH FACTOR BINDING BY HEPARIN-MIMETIC PEPTIDE NANOFIBERS.

This work is partially described in the following publication:

Mammadov R., Mammadov B., Guler M. O., Tekinay A.B. *Biomacromolecules*, 2012, *13* (10), pp 3311–3319.[91]

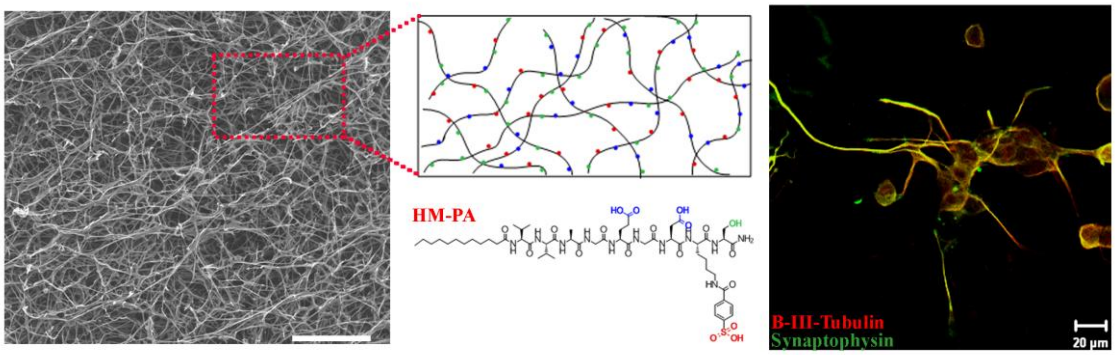

3.1. Objective

Growth factors bind to receptors on cells and induce signaling pathways, which are critical for healing of damaged tissues. Heparan sulfates are extracellular elements, which bind to growth factors and through maintaining their local accumulation, protecting them from degradation and assisting in their interaction with cellular receptors, enhance their functioning. Materials mimicking chemical structure of heparan sulfates would be beneficial for tissue engineering and regenerative medicine purposes. In this work, our aim was to understand interaction affinity of peptide nanofibers carrying chemical functional groups from heparan sulfates to various growth factors used in tissue engineering. We also asked whether this interaction happens through same domains of growth factors that binds to heparan sulfates and whether interaction between peptide nanofibers and growth factors is translated into cellular activity.

3.2. Introduction

Functional biomaterials can improve efforts to control cell behavior and promote tissue regeneration. New-generation biomaterials differ from conventional ones in terms of controlling dose and bioactivity of delivered molecules (e.g. growth factors) more precisely besides acting as mere scaffolds.[92] Immobilization of growth factors either covalently or noncovalently to a scaffold provides spatial distribution of growth factors inside the scaffold. Although covalent immobilization enables prolonged release of growth factors, specificity of coupling site on the growth factors is difficult to achieve and proteins may lose their bioactivity during coupling process.[93] Materials can also be programmed to interact with growth factors through decoration of specific binding sites that interact with growth factors noncovalently. This type of interaction is predominant in nature. For example, heparan sulfate proteoglycans in extracellular matrix bind to heparin binding growth factors mainly through electrostatic interactions.[8] Binding to heparan sulfates is critical for growth

factor signaling, protection from degradation and local accumulation of growth factors in the vicinity of cells.

Maximal dose of growth factors that can be loaded onto materials correlates with the amount of growth factor binding epitopes on the scaffolds. Designing bioactive scaffolds that can present maximum number of epitopes while enabling control over epitope number would be beneficial for regenerative medicine applications. Several strategies for designing growth factor binding scaffolds were proposed previously. Sulfated alginate hydrogels, inspired from sulfated characteristics of glycosaminoglycans (e.g. heparan sulfate), showed superior affinity to heparin binding growth factors, than bare alginate hydrogels.[24] Fibrin matrices functionalized with 12-14 type three repeats of fibronectin, which non-selectively interact with various growth factors, performed as an efficient growth factor delivery system, intensifying growth factor bioactivity *in vitro*.[94] However, the relatively larger meshwork size of these polymeric scaffolds limits the density of epitope presentation. Moreover, epitope concentration on a polymer chain should be determined before synthesis. On the other hand, peptide amphiphiles (PA), which are small building blocks, can be triggered to form supramolecular assemblies such as high-aspect-ratio nanofibers in a controlled manner.[1] Nanoscale properties maximize epitope density, while epitope concentration can be controlled via epitope dilution before inducing nanofiber formation.[7] Previously, heparin-binding PAs were reported to form nanofiber scaffolds when mixed with heparin, where heparin was used to bind to growth factors inside the scaffold.[5] This system induced *in vivo* angiogenesis more efficiently than standard scaffolds. However, since heparin long chain was used as growth factor binding ligand, epitope dilution was limited. Moreover, contaminants in heparin batches have been reported to induce side effects in humans.[56]

Considering these issues, we designed a heparin mimetic PA (HM-PA) molecule, which bears key functional groups present in heparin and can be readily induced to form nanofiber scaffolds for regenerative medicine applications.[43] In chapter 2, we have shown that these nanofibers bind VEGF and induce *in vitro* and *in vivo* angiogenesis, efficiently. The arrangement of functional groups on HM-PA/K-PA

nanofibers might be sufficient to bind other heparin binding growth factors and in a manner that would elevate the bioactivity of these growth factors. In this work, we studied the interactions of heparin mimetic peptide nanofibers with various growth factors and the bioactivity of nanofiber - growth factor complexes. This part of thesis presents the high potential of heparin mimetic peptide nanofibers in binding various heparin binding growth factors, which are widely used in regenerative medicine and in directing cellular activity.

3.3. Results and Discussion

In this chapter, binding of various heparin-binding growth factors, that are widely used in regenerative medicine studies, to peptide nanofibers was studied. (Table 3.1). Peptide molecules forming the nanofibers are depicted in Figure 3.1, and nanofiber formation mechanisms are explained in the Materials and Methods section. E-PA nanofibers are used as control of peptide nanofibers carrying negative charge. While forming nanofibers, the ratio of negatively charged PAs (HM-PA and E-PA) to positively charged K-PA in nanofibers is critical as it determines the net charge on nanofibers. Molar ratios of 1:2 and 1:1 for HM-PA/K-PA and E-PA/K-PA were chosen, respectively, in order to make both nanofibers to have (theoretically) net one negative charge. Also, heparin carrying nanofibers are used as positive control and to understand that to what extent functional groups on HM-PA mimic functionality of heparin in terms of growth factor binding. Heparin carrying nanofibers are prepared by mixing K-PA with heparin (2:1 weight ratio) to render them to have (theoretically) net one negative charge.

Table 3.1. Growth factors used in this study.

Growth Factor	Physiological Function*	Heparin affinity	Dissociation constant (Kd)**
VEGF	Angiogenesis, vasculogenesis, endothelial cell growth and migration	High ($VEGF_{165}$) None ($VEGF_{121}$)	165 nM [95]
HGF	Cell motility, mitogenesis and matrix invasion	High	12 nM [95]
FGF-2	Migration, proliferation and survival of endothelial cells, inhibition of differentiation of embryonic stem cells	High	23 nM [95] 39 nM [96]
BMP-2	Differentiation and migration of osteoblasts	High	20 nM [97]
NGF	Survival and differentiation of neural cells	Moderate	Not determined

* Functions were reproduced from Lee et al.[93] and NCBI.
** Dissociation constant of heparin – growth factor interaction.

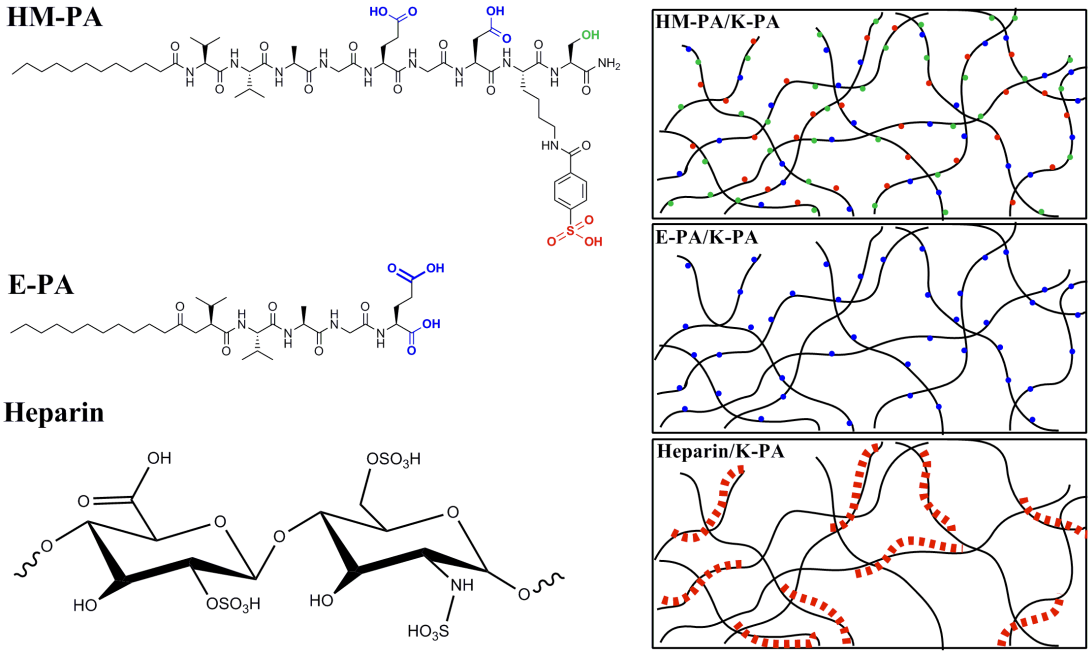

Figure 3.1. Chemical structure of PA molecules and heparin; illustration of nanofibers investigated for growth factor binding. Negatively charged HM-PA, E-PA or Heparin were mixed with positively charged K-PA to form respective nanofibers. Tiny spheres on nanofibers depict functional groups (Red - sulfonate, Green - hydroxyl, Blue - carboxylate). Dashed line in red indicates heparin. After nanofiber formation, heparin and functional groups of PAs are assumed to be presented by nanofibers into surrounding aqueous media. Density of heparin and functional groups of HM-PA on PA nanofibers does not reflect actual density.

3.3.1. Analysis of interaction of PA nanofibers with heparin-binding growth factors.

Growth factor-peptide nanofiber interaction was investigated in-depth by several methods to understand the effect of heparin mimicking functional groups (carboxylate, hydroxyl, and sulfonate) on nanofibers in growth factor binding. Firstly, we used ELISA-based growth factor binding assay to study the binding mechanism. All three types of peptide nanofibers were coated onto an ELISA plate as revealed by AFM imaging, which were clearly distinguishable in terms of roughness when compared to bare ELISA plate (Figure 3.2).

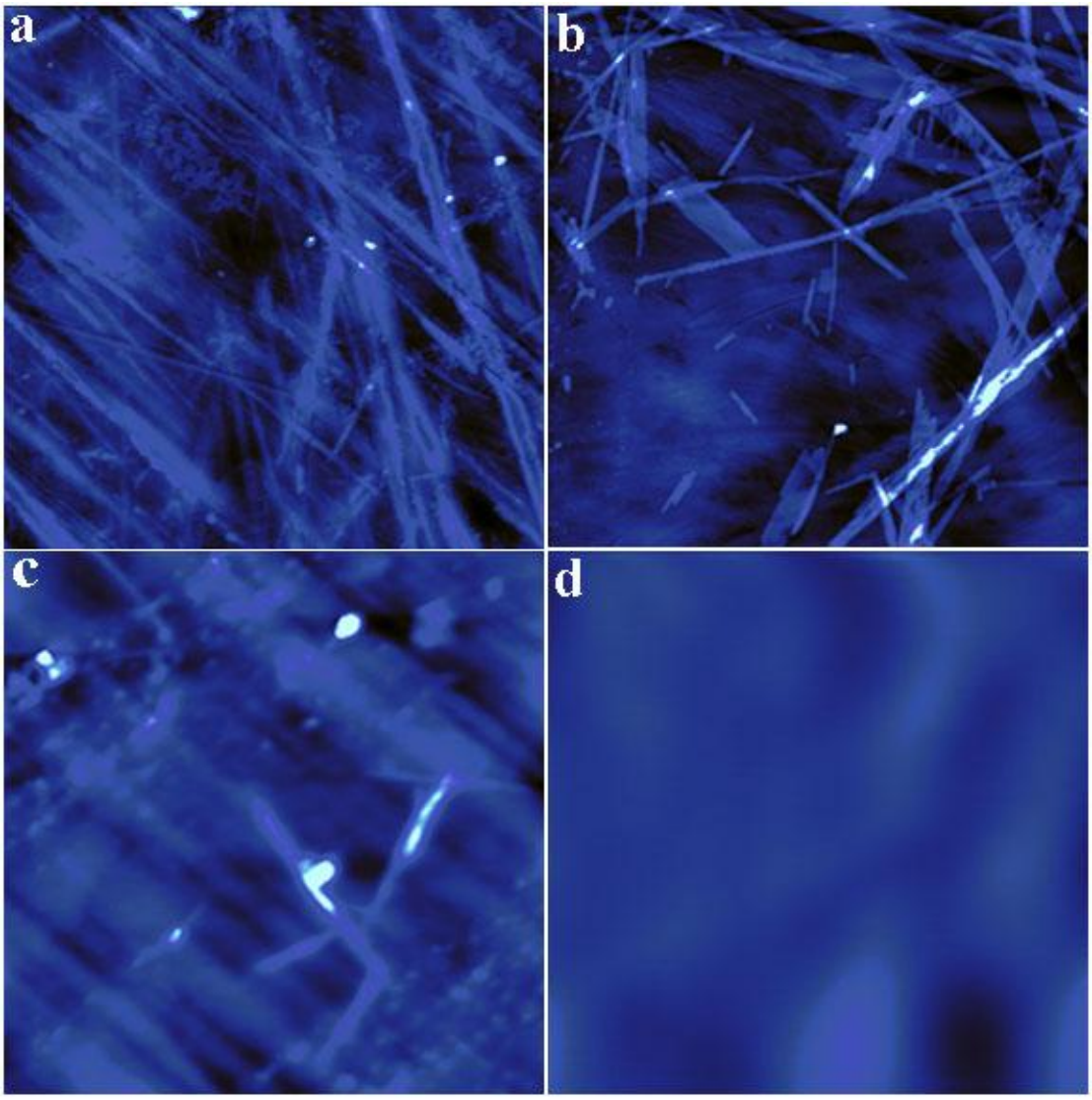

Figure 3.2. AFM images (5 μm x 5 μm) of PA nanofibers coated onto ELISA plates. After extensive washing of ELISA plate, coverage of surface with nanofibers can be observed for HM-PA/K-PA (a) E-PA/K-PA (b) and K-PA/Heparin (c) nanofibers. Bare plate surface (d) can be clearly distinguished from nanofiber-coated surfaces.

After confirming the nanofiber coating on ELISA plates, growth factors bound to the peptide nanofibers were detected with ELISA assay. Bare plate surface, which excluded only nanofibers used in other groups and was used as the negative control, showed almost no binding signal (Figure 3.3). This indicates reliability of binding signal observed with nanofiber including samples and implies that this signal is caused by growth factor – nanofiber interaction.

Although heparin-carrying (heparin with K-PA) nanofiber gels showed weak affinity to $VEGF_{165}$ in release assay in previous chapter (Figure 2.26), here surfaces coated with K-PA/Heparin nanofibers showed the strongest binding signal (Figure 3.3). Difference between these two systems was molar ratio between K-PA and heparin. In this study, we used 2:1 weight ratio for K-PA/Heparin to make nanofibers to have theoretically net one negative charge (similar to E-PA and HM-PA nanofibers), which corresponds to approximately 60:1 molar ratio (8:1 molar ratio was used to make K-PA/Heparin nanostructures). Probably, using higher PA concentration compensate for suboptimal binding of K-PA to heparin and stabilize heparin chains on nanofibers that allows large surface area presentation of heparin chains.[4] This would allow proper interaction of heparin with growth factors which is observed in Figure 3.3.

HM-PA nanofibers showed a comparable level of binding to $VEGF_{165}$ with heparin-carrying nanofibers (Figure 3.3). At higher growth factor concentration (50 ng/mL), binding levels were similar, however this might be due to saturation of binding signal - maximal level of absorbance value is reached. At lower concentration (10 ng/mL), both HM-PA and heparin showed binding signals at measurable range and heparin showed 2.5 fold higher binding than HM-PA. Nanofiber control (E-PA/K-PA) showed significantly less binding level to $VEGF_{165}$ (more than 3-fold) than HM-PA/K-PA nanofibers (Figure 3.3). An E-PA/K-PA 2x sample containing two-folds higher control nanofiber concentration was used to eliminate the possible effect of incomplete coverage of the surface on binding. There was no significant difference between E-PA/K-PA and E-PA/K-PA 2x samples, indicating complete coverage and saturation of the surface with one-fold control nanofibers (Figure 3.3).

By using same methodology, we investigated binding affinities of PA nanofibers to other growth factors. Binding signals of PA-free surface was subtracted from PA nanofiber binding signal for all growth factors and shown at Figure 3.4. HM-PA nanofibers showed a higher binding level to three growth factors - HGF, VEGF, and FGF-2 -than control E-PA nanofibers. This difference confirms that growth factor

and nanofiber interaction is further strengthened by additional functional groups on HM-PA nanofibers (Figure 3.4).

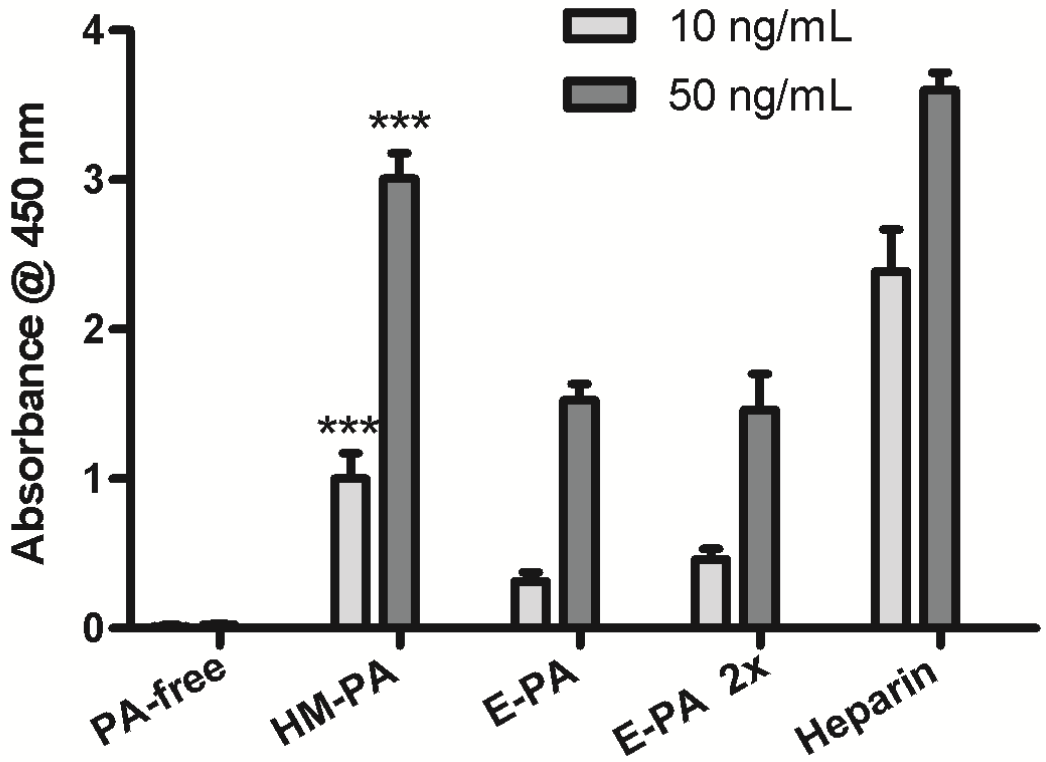

Figure 3.3. Measurement of $VEGF_{165}$ binding to nanofiber coated surfaces by using ELISA-based assay. Binding levels of 10 or 50 ng/mL of $VEGF_{165}$ with different nanofibers or PA-free surface are shown. Difference between HM-PA/K-PA and other treatments was significant for both growth factor concentrations (***$p<0.001$). Statistical analysis was performed with two-way ANOVA with Bonferroni post-hoc analysis. Experiment was performed with 3 replicates (n=3). Error bars indicate standard deviations.

Growth factor − peptide nanofiber interactions were analyzed at two different growth factor concentrations to investigate the effect of growth factor concentration on binding signal. VEGF165 and HGF showed higher level of binding to HM-PA nanofibers than control nanofibers for both 10 ng/mL and 50 ng/mL growth factor concentrations (Figure 3.4a, 3.4b). In addition, FGF-2 bound to HM-PA nanofibers significantly more than control nanofibers at higher growth factor concentration

(Figure 3.4b). In spite of its heparin-binding property, BMP-2 exhibited a strong binding pattern to both HM-PA and control nanofibers at both low and high growth factor concentrations (Figures 3.4a, 3.4b). Negative charge provided by carboxylate groups on control peptide nanofibers might be sufficient to bind to BMP-2 strongly, leading to a similar binding pattern of BMP-2 to E-PA and HM-PA nanofibers. However, the binding site of BMP-2 might differ between HM-PA and E-PA nanofibers, which could change its bioactivity. One of the weakest binding patterns was observed with NGF, where HM-PA nanofibers showed slightly better binding at higher growth factor concentration. However, it was clear that even this degree of binding makes a remarkable difference in inducing cellular activity, which will be described in more detail in the following sections. $VEGF_{121}$, which lacks heparin-binding domain, did not reveal any binding signal to HM-PA nanofibers, while it exhibited very weak binding to E-PA/K-PA nanofibers. Thus, heparin-binding domain of VEGF is critical for its binding to HM-PA nanofibers. These results indicate that HM-PA nanofibers with heparin mimicking functional groups stand to be an excellent analogue for heparin regarding growth factor binding capability.

To validate and visualize growth factor – peptide nanofiber interactions, we performed immunogold staining of growth factors bound to the nanofibers. For this experiment, we chose HGF as the model growth factor. We treated HGF bound nanofibers with specific primary antibody, which was treated with gold nanoparticle-conjugated secondary antibody. TEM was used to image the complex of heparin-mimetic peptide nanofibers and gold nanoparticle-conjugated antibody against HGF. Both individual nanofibers (Figure 3.5a, c) and nanofiber aggregates (Figure 3.5a, 3.5b) were observed to bind to growth factors (white dots in a,c; black dots in b). When primary antibody for growth factor was not used, no growth factor binding was observed, excluding the possibility of nonspecific binding of gold attached secondary antibodies to nanofibers (Figure 3.5d). Nanofiber aggregates bound to growth factors in TEM imaging were studied by energy-dispersive X-ray (EDX) analysis, and a strong sulfur signal caused by sulfonate group of HM-PA (Figure 3.6) was observed demonstrating the presence of peptide nanofibers interacting with the growth factor.

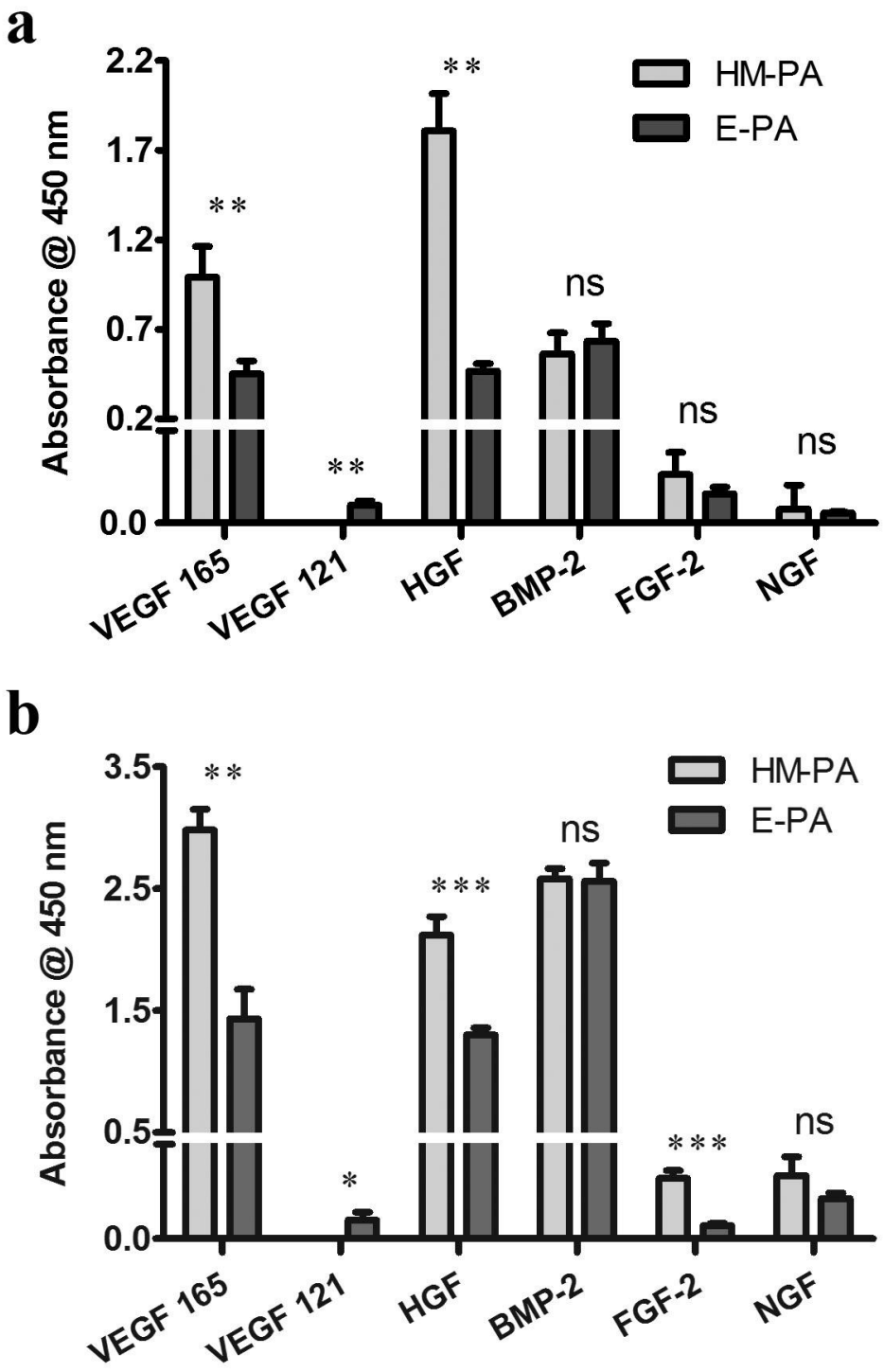

Figure 3.4. Binding levels of different growth factors to HM-PA/K-PA or E-PA/K-PA nanofibers are measured by ELISA-based assay. **a.** 10 ng/mL **b.** 50 ng/mL ***p<0.001, *p<0.01, *p<0.05, ns=not significant. Statistical analysis was performed with Student's t-test. Experiment was performed with 3 replicates (n=3). Error bars indicate standard deviations.

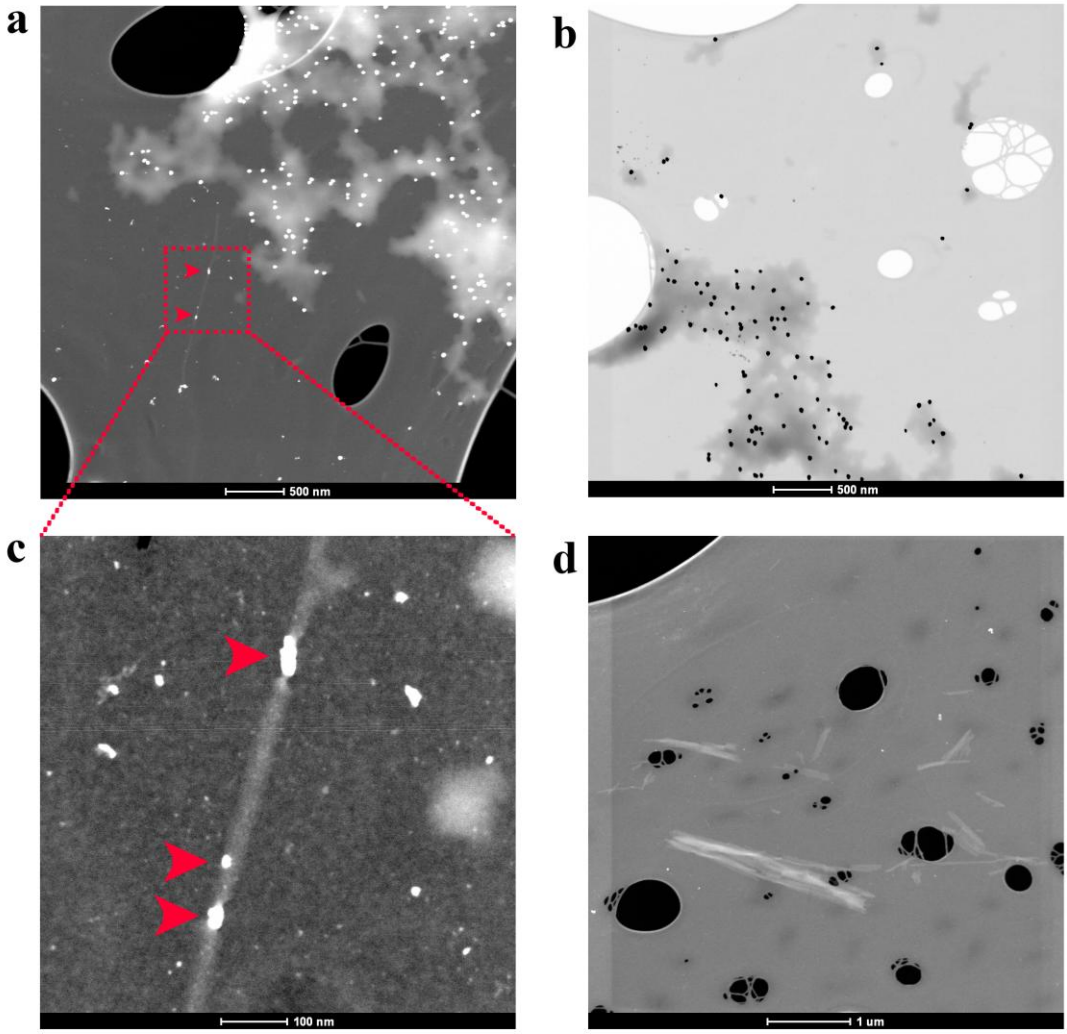

Figure 3.5. TEM images of immunogold stained HGF on HM-PA/K-PA nanofibers. a. HGFs were observed on both individual nanofibers and PA aggregates. White dots indicate gold nanoparticles. b. Inverted image, gold nanoparticles were visualized as black dots. c. Magnified version of an individual nanofiber shown in image a, presenting gold nanoparticles. d. Negative control (without primary antibody) shows no staining.

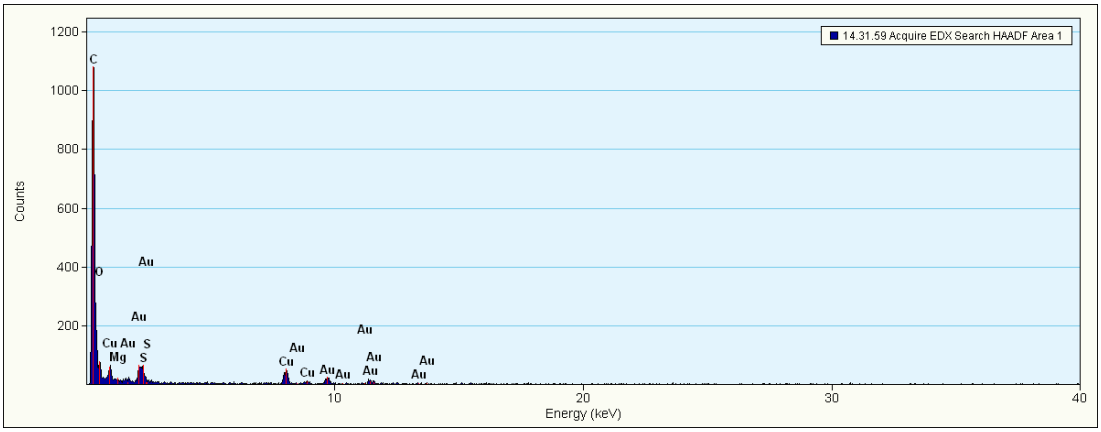

Figure 3.6. EDX analysis of nanofiber aggregates shown in TEM images at Figure 3.5. Sulfur (S) atoms indicate HM-PA, while Au indicates gold nanoparticles.

3.3.2. Role of Heparin-Binding Domains of Growth Factors in Their Interaction with HM-PA/K-PA Nanofibers.

While growth factor − nanofiber binding has been emphasized in the literature, the binding site of growth factor to material should also be taken into consideration when designing biomaterials for regenerative medicine applications. Growth factors interact with heparan sulfates through their "heparin-binding domain".[47-48, 97-101] Growth factor − heparan sulfate binding induces dimerization/oligomerization of growth factor receptors (generally tyrosine kinase receptors), which is required for autophosphorylation of receptors and subsequent activation of signaling pathways.[50, 102-103] For signaling to be effective, a threshold number of receptor-growth factor complexes should be active on the surface of cells for an appropriate period of time.[104] This requires stability of growth factor − receptor interactions, which are maintained by heparan sulfates acting as coreceptors.[104-105] Thus, a material designed to mimic heparan sulfates should bind to growth factors through their heparin-binding domains, which would prevent blocking of other sites on growth factors such as "receptor binding site" that is critical for signaling. $VEGF_{165}$ and $VEGF_{121}$ exhibited significantly different binding levels to HM-PA/K-PA nanofibers in ELISA-based binding assay. To clarify the necessity of heparin-binding domain in HM-PA nanofiber - growth factor interaction, differential affinity of $VEGF_{165}$ and

$VEGF_{121}$ to HM-PA/K-PA nanofibers was further tested by using ITC. In chapter 2, binding constant between $VEGF_{165}$ and HM-PA/K-PA nanofibers measured by using ITC technique was given (Figure 3.7, also Figure 2.25).[43] Here, interaction between $VEGF_{121}$ and HM-PA/K-PA nanofibers was investigated through a similar protocol (Figure 3.8). While the binding constant of HM-PA/K-PA−$VEGF_{165}$ was similar to the binding constant of heparin−$VEGF_{165}$, $VEGF_{121}$ revealed no binding signal with HM-PA/K-PA; further supporting the critical contribution of the heparin-binding domain in VEGF−HM-PA/K-PA nanofiber interaction.

To understand the role of heparin-binding domains of other growth factors in HM-PA/K-PA nanofiber binding, a competition assay was performed, where heparin and HMPA/K-PA nanofibers competed for binding to growth factors. In this assay, growth factors bound to heparin were expected to be washed away, while those that bound to HM-PA nanofibers were expected to stay as bound to the plate and be detected with ELISA. Thus, diminishing signal in ELISA would indicate that both heparin and HM-PA nanofibers compete for the same binding site. In total agreement with previous assays, the $VEGF_{165}$ binding signal showed a very sharp decline as heparin concentration was increased, further supporting that HM-PA/K-PA nanofibers compete for nonredundant heparin-binding domain (Figure 3.9a). Interestingly, only FGF-2 showed a similar pattern to $VEGF_{165}$ among other growth factors (Figure 3.9). The inhibitory effect was specific to heparin, since chondroitin sulfate (another sulfated glycosaminoglycan) was not able to inhibit FGF-2 binding to HM-PA/K-PA nanofibers (exhibited only limited inhibitory effect at maximal dose, Figure 3.10). Heparin was more inhibitory at its minimal dose than chondroitin sulfate at its maximal dose. Since heparan sulfate (or heparin) binding is critical for bioactivity of $VEGF_{165}$ and FGF-2,[51, 57] binding to the same site with heparin renders HM-PA/K-PA nanofibers a very efficient scaffold for delivery of these growth factors. Heparin-binding domains of HGF and BMP-2 were more redundant than those of VEGF and FGF-2 in HM-PA nanofiber binding (Figure 3.9a).

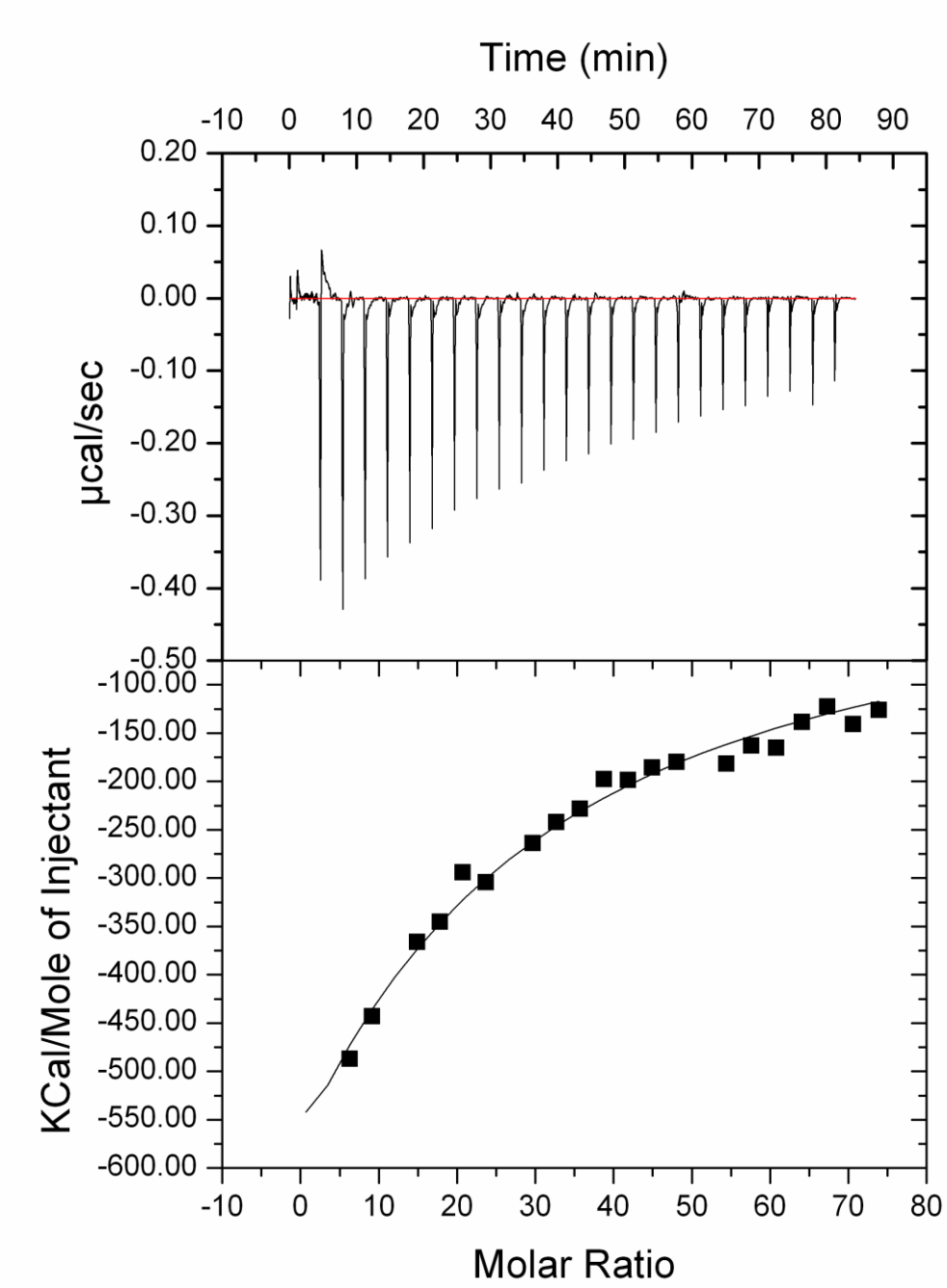

Figure 3.7. Measurement of affinity between $VEGF_{165}$ and HM-PA/K-PA nanofibers by using Isothermal Titration Calorimetry (ITC). $VEGF_{165}$, which has heparin binding domain, showed high affinity to HM-PA/K-PA nanofibers with binding constant of $7.37 \times 10^5 \pm 5.1 \times 10^4$.

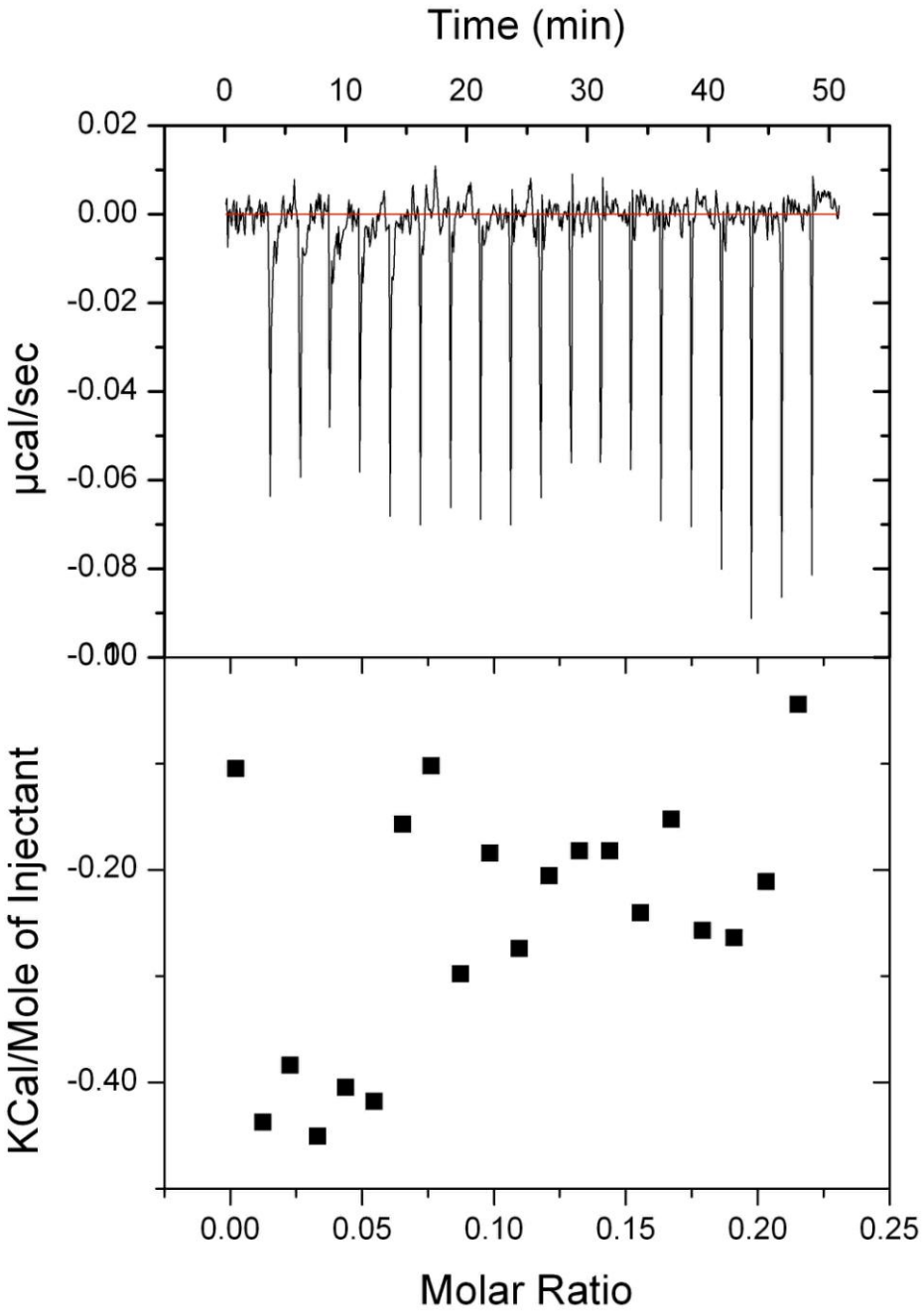

Figure 3.8. Measurement of affinity between $VEGF_{121}$ and HM-PA/K-PA nanofibers by using Isothermal Titration Calorimetry (ITC). $VEGF_{121}$, which lacks heparin-binding domain, showed no affinity to HM-PA/K-PA nanofibers.

IC_{50} for HGF and BMP-2 calculated from competitive binding curves in Figure 3.9a were nearly 10 times higher than IC_{50} of VEGF and FGF-2 (Figure 3.9b). Dissociation constants of heparin and these growth factors were shown to be similar to each other in the literature (Table 3.1). Thus, the difference between IC_{50} values of heparin between these two groups of growth factors cannot be attributed to any difference in their affinity to heparin. This difference could be caused by the existence of extra binding sites, other than the heparin-binding site, on BMP-2 and HGF for HM-PA/K-PA nanofiber binding. NGF binding to heparin is known to be moderate,[106] compared to strong binding affinities of other growth factors, which may be the reason for poor competition between heparin and HM-PA/K-PA nanofibers for binding to NGF. Nonetheless, NGF seems to have different binding sites for HM-PA/K-PA nanofibers and heparin (Figure 3.9). IC_{50} of heparin for NGF was nearly 80 times higher than IC_{50} of heparin for VEGF/FGF-2 and 7−8 times higher than IC_{50} of heparin for HGF/BMP-2 (Figure 3.9b).

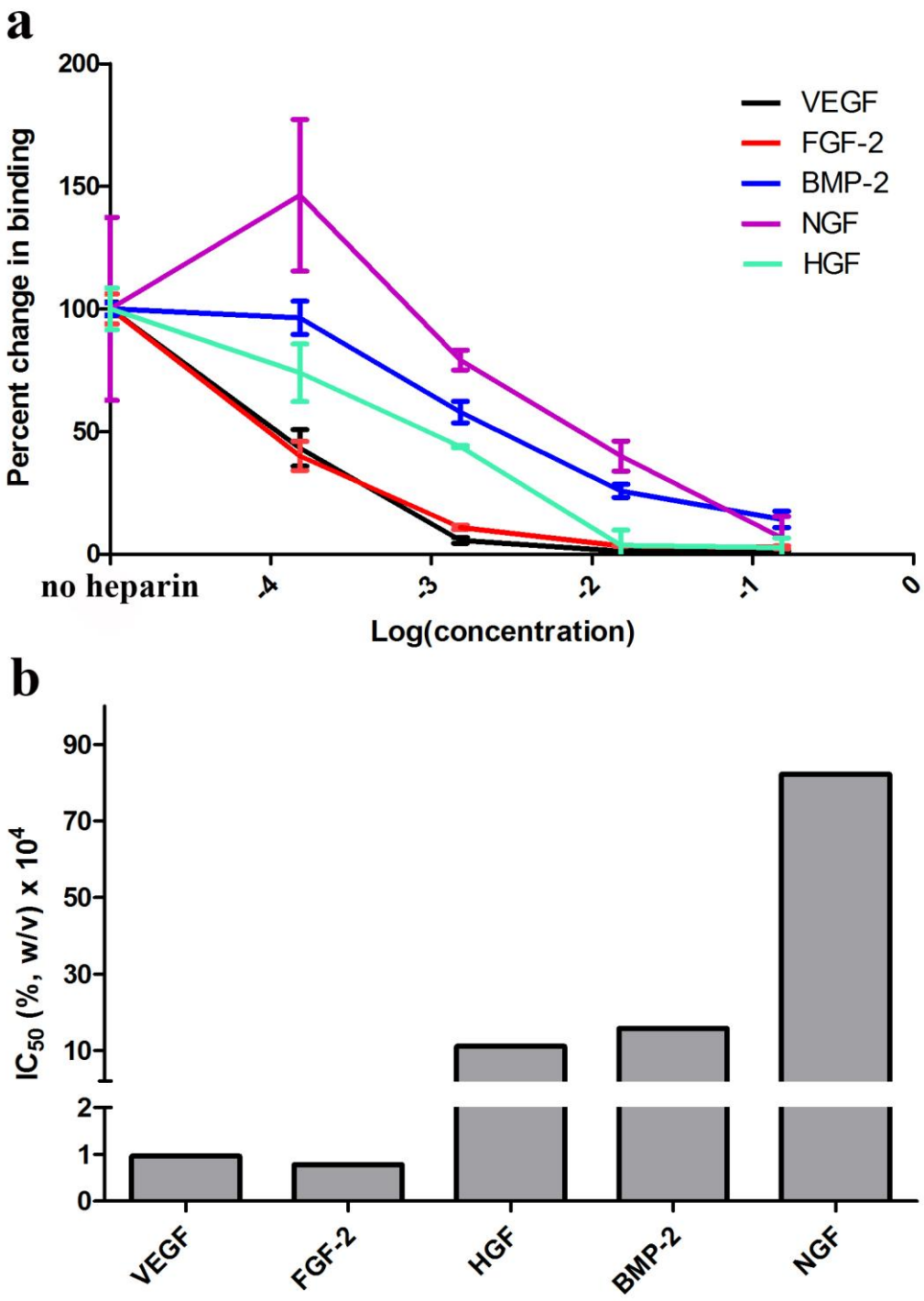

Figure 3.9. Competition assay between heparin and HM-PA/K-PA nanofibers for growth factor binding. a. Dose dependent interference of heparin with growth factor binding to HM-PA/K-PA nanofibers. For each growth factor, binding signal to HM-PA/K-PA nanofibers when there was no heparin in milieu was taken as 100%. b. IC_{50} value of heparin inhibit HM-PA/K-PA nanofiber binding of each growth factor was calculated and represented. Experiment was performed with 3 replicates (n=3). Error bars indicate standard deviations.

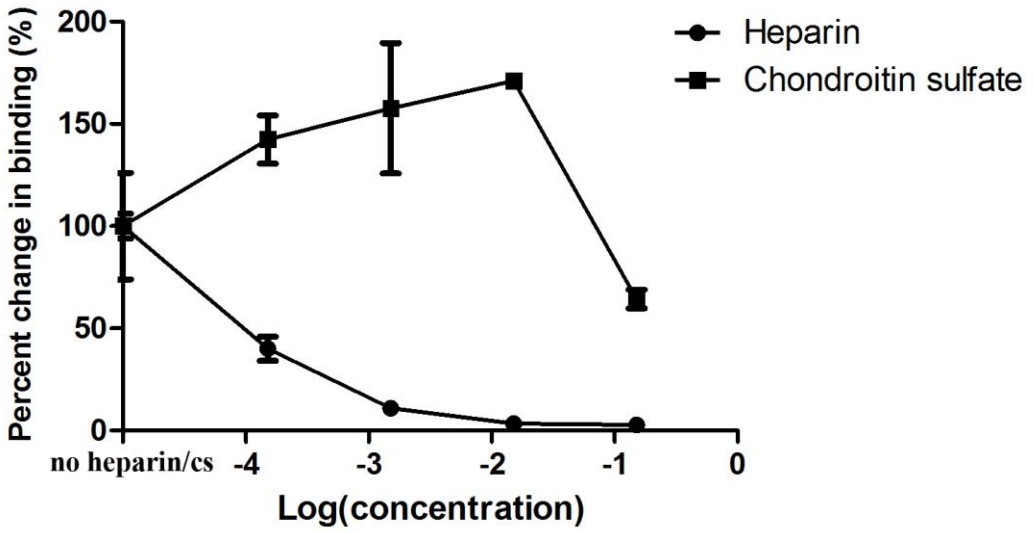

Figure 3.10. Competition assay between heparin or chondroitin sulfate (cs) and HM-PA/K-PA nanofibers for FGF-2 binding. 100% indicates (no heparin/cs) binding signal of FGF-2 to HM-PA/K-PA nanofiber when there is no heparin or cs in milieu. X-axis denotes logarithmic concentration of heparin or cs. Error bars indicate standard deviations.

3.3.3. HM-PA/K-PA nanofiber - growth factor interaction is translated to cellular activity.

As mentioned above, improper interaction of materials with growth factors (e.g., through improper binding site) can block growth factor activity unexpectedly. Hence, growth factor's biological functionality should be validated after it is tethered on the material. NGF, which had the weakest interaction with HM-PA among the growth factors that were tested in this study and whose heparin-binding domain was the least required for HM-PA/K-PA nanofiber binding, was selected for studying biological activity. In order to investigate the effect of HM-PA/K-PA nanofiber binding on NGF functionality, neurite outgrowth by PC-12 cells cultured on NGF-coated PA nanofiber surfaces was analyzed. NGF retained its ability to induce neurite outgrowth fully when it was bound to HM-PA/K-PA nanofibers. Neurite outgrowth performances of PC-12 cells did not deteriorate when NGF was presented to cells as coated on nanofibers compared to its soluble form (Figure 3.11). To exclude any possibility of bioactivity reduction due to differential amount of growth factors

between “soluble” and “coated” treatments, unbound growth factors in “coated” treatment were not removed and stayed in solution. Considering that the total growth factor amount was same in both “soluble” and “coated” treatments, HM-PA/K-PA nanofibers enhanced NGF signaling, since neurite outgrowth activity in “coated” samples was significantly higher than “soluble” samples (Figure 3.11a) in the presence of low growth factor concentration. No significant increase in bioactivity was observed at higher growth factor concentration (Figure 3.11b). This difference could be due to the fact that higher concentration of growth factors in the vicinity of cells did not necessitate their accumulation and preservation with HM-PA/K-PA nanofibers for cellular activity. Interestingly, we did not observe such a difference with E-PA/K-PA nanofibers, indicating contribution of functional groups on HM-PA/K-PA nanofibers for NGF signaling.

Moreover, higher binding of HM-PA/K-PA nanofibers to NGF, although it was statistically not significant, was translated to elevated cellular activity when compared to control nanofiber systems (Figure 3.12). Here, unbound NGFs on HM-PA/K-PA nanofiber and control surfaces were washed away, and bioactivity comparison was performed only between bound NGFs. NGF-coated and washed HM-PA/K-PA nanofibers (50 ng/mL) led to significantly longer neurites compared to E-PA/K-PA nanofiber and PDL controls (Figure 3.12). There was no such difference when 10 ng/mL NGF was used, which is in good correlation with the results of growth factor binding analysis by ELISA (Figure 3.4a).

In summary, HM-PA/K-PA nanofibers interact with NGF moderately and this interaction is translated into cellular response without any loss in bioactivity of growth factor. Promotion of the neurite length on HM-PA/K-PA nanofibers is clearly dependent on HM-PA−NGF interaction that could be translated to differentiation response.

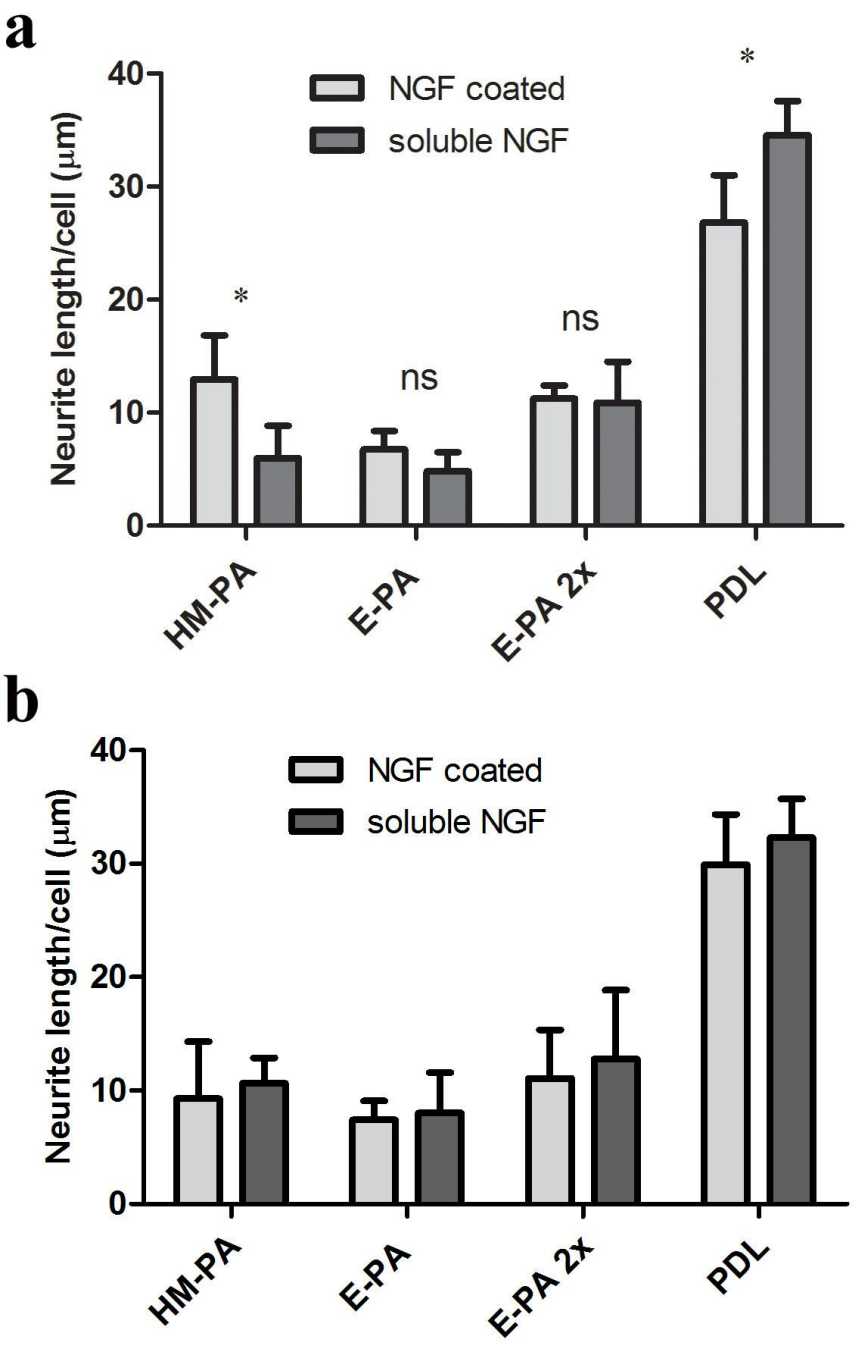

Figure 3.11. Neurite outgrowth performance of PC-12 cells on NGF treated and NGF-free substrates. NGF coated indicates that substrates were treated with NGF without removal of unbound NGF on which cells were seeded. Soluble NGF indicates that cells cultured on NGF-free substrates were induced with soluble NGF in culture media. NGF amounts used were 10 ng/mL **(a)** or 50 ng/mL **(b)**. There was no significant difference for any substrate when coated NGF is compared with soluble NGF, except for HM-PA/K-PA and PDL at 10 ng/mL (*$p<0.05$. Statistical test was performed with two-way ANOVA with Bonferroni post-hoc analysis, n=3). Error bars indicate standard deviations.

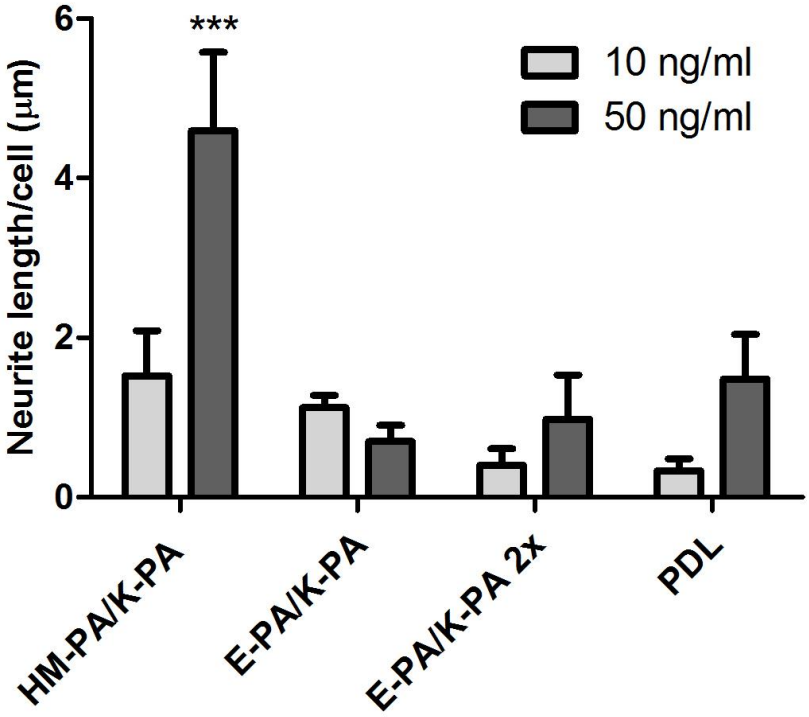

Figure 3.12. Neurite outgrowth response of PC-12 cells to washing away of unbound NGF from NGF treated substrates. PDL and PA substrates were treated with 10 ng/mL or 50 ng/mL NGF after which they were washed to remove any unbound NGF. HM-PA/K-PA interaction with NGF leaded to longer neurites on this surface when 50 ng/mL NGF was used, probably due to higher amount of NGF remained on HM-PA/K-PA nanofiber coated surface than E-PA/K-PA and PDL after washing (***$p<0.001$ between HM-PA/K-PA and other surfaces at 50 ng/mL, *$p<0.05$ between HM-PA/K-PA and E-PA/K-PA 2x or PDL, p=ns between HM-PA/K-PA and E-PA/K-PA at 10 ng/mL. Statistical test was performed with two-way ANOVA with Bonferroni post-hoc analysis, n=3). Error bars indicate standard deviations.

Immunostaining against β-III-tubulin, a neuron-abundant microtubule protein, and synaptic protein Synaptophysin 1 (Syn1) revealed higher expression of these proteins when cells were cultured on HM-PA - NGF substrates (Figure 3.13). Neural morphology was also more prominent on this surface correlating with the longer neurites (Figure 3.12). β-III-tubulin is a neuron-specific tubulin subunit that is abundantly expressed along neurites as well as cell soma.[107] Syn1 is a synaptic protein abundant in presynaptic nerve terminal, and its presence along the axonal protrusions indicates presynaptic nerve terminal development.[108-109] Expression

profiles of PC-12 cells cultured on HM-PA-NGF substrate is consistent with the expected localization of these neural marker proteins. β-III-tubulin was found to be localized in cell soma along with neurites (Figure 3.13a). Cells also expressed β-III-tubulin on E-PA/K-PA and PDL in cell soma and expression in a few short neurites was observed on E-PA/K-PA (Figure 3.13d, g). A dramatic difference in the expression profile of Syn1 was found when cells were cultured on different substrates, which can be attributed to differential interaction of these surfaces with NGF leading to differential cell responses (Figure 3.13b, e, h). Syn1 expression was heavily concentrated along neurites and nerve terminals on HM-PA/K-PA, while weak expression in cell soma was observed on other substrates. Thus, it can be concluded that higher level of binding of HM-PA to NGF induces neural differentiation of PC-12 cells more efficiently, leading to the formation of presynaptic nerve terminals, an indicator of neural maturation, on this substrate.

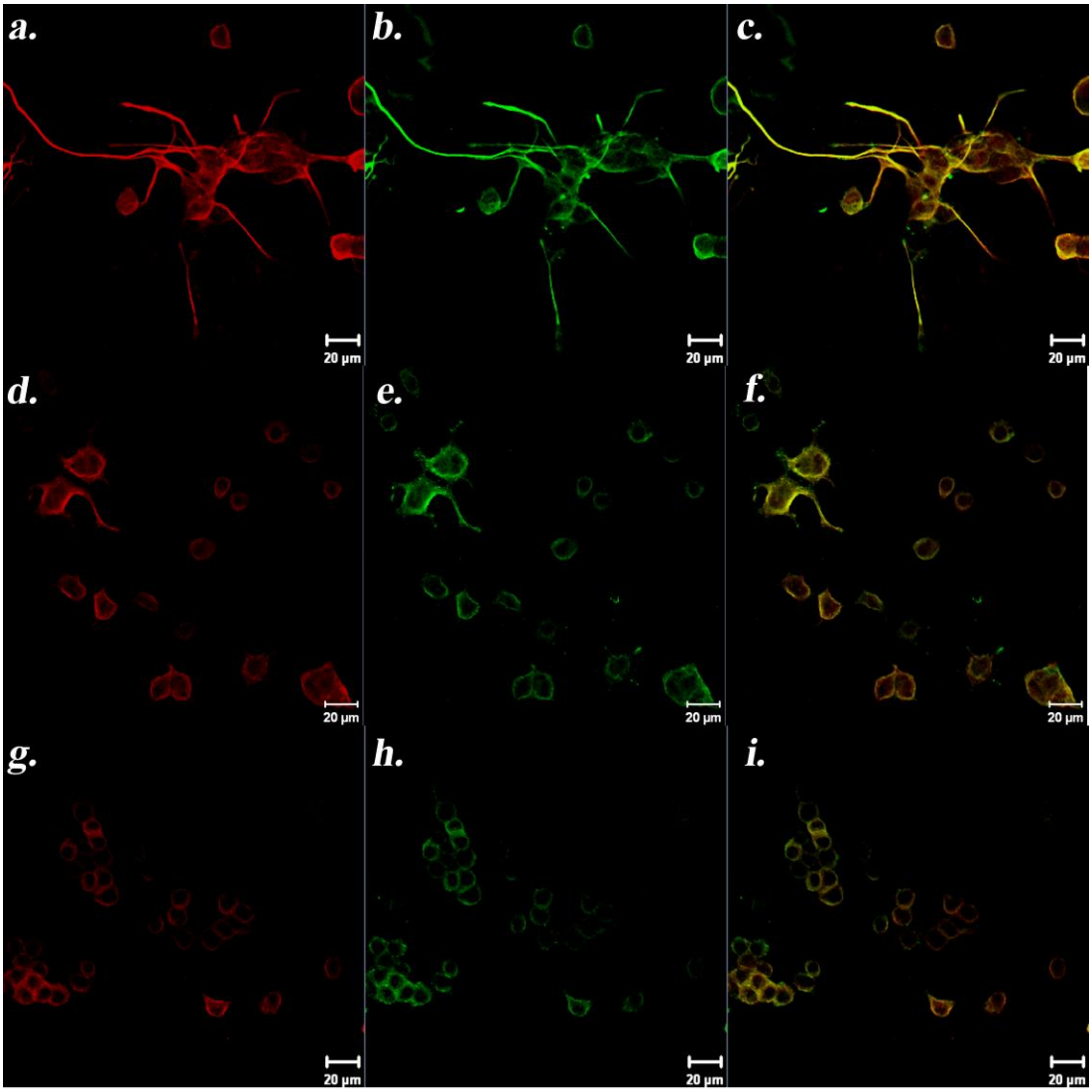

Figure 3.13. Immunostaining of PC-12 cells against β-III-Tubulin **(a, d, g)** and Synaptophysin I **(b, e, h)** on NGF treated surfaces. **a-c.** HM-PA/K-PA, **d-f.** E-PA/K-PA, **h-i**. PDL. **c, f and i** shows merged images of Syn1 staining and β-III-Tubulin on same cells. Higher expression of both neural markers along with specific localization of Synaptophysin I in nerve terminals was clear in cells cultured on HM-PA/K-PA.

3.4. Experimental details.

3.4.1. Materials

9-Fluorenylmethoxycarbonyl (Fmoc) and tert-butoxycarbonyl (Boc) protected amino acids, [4-[α-(20,40-dimethoxyphenyl) Fmoc-aminomethyl] phenoxy]

acetamidonorleucyl-MBHA resin (Rink amide MBHA resin), Fmoc-Asp(OtBu)-Wang resin, and 2-(1Hbenzotriazol-1-yl)-1,1,3,3-tetramethyluronium hexafluorophosphate (HBTU) were purchased from NovaBiochem and ABCR. The other chemicals for PA synthesis were purchased from Fisher, Merck, Alfa Aesar, or Aldrich. All chemicals were used as provided. Heparin and chondroitin sulfate were purchased from Sigma-Aldrich. ELISA reagents were obtained from Invitrogen. Paired antibodies for different growth factors were purchased from R&D, except for VEGF (Invitrogen). Gold-attached secondary antibody (Aurion Immunogold reagent) was obtained from Electron Microscopy Sciences. Growth factors were obtained from e-bioscience ($VEGF_{121}$, HGF, FGF-2, BMP-2), Invitrogen ($VEGF_{165}$), and Sigma-Aldrich (NGF).

3.4.2. Peptide Synthesis

HM-PA and Lauryl-VVAGK-Am (K-PA) were constructed on Rink Amide MBHA resin, while Lauryl-VVAGE-Am (E-PA) was constructed on Fmoc-Asp(OtBu)-Wang resin (Figure S1, Supporting Information). Amino acid couplings were performed with 2 equiv of Fmoc-protected amino acid, 1.95 equiv of HBTU, and 3 equiv of N,N-diisopropylethylamine (DIEA) for 2 h. To remove the Fmoc group, 20% (v/v) piperidine/dimethylformamide solution (DMF) was added for 20 min. To block the remaining free amine groups after amino acid coupling, 10% (v/v) acetic anhydride solution in DMF was used (30 min). After each step, the resin was washed by using DMF, dichloromethane (DCM), and DMF (three times each). To synthesize HM-PA, sulfobenzoic acid was added to the side chain of lysine. A lysine residue with 4-methytrityl (Mtt) side-chain protection was used for selective deprotection of amine groups. Resins were treated with a TFA/TIS/H_2O/DCM mixture (5:2.5:2.5:90 ratio; TFA = trifluoroacetic acid; TIS = triisopropyl silane) for 5 min to remove Mtt. To cleave PAs from the resin, TFA/TIS/H_2O mixture (95:2.5:2.5 ratio) was treated with resin for 2 h. Excess TFA was removed by rotary evaporation. The remaining viscous PA solution was triturated with ice-cold ether, and the resulting white precipitate was dissolved in aqueous solution and freeze-dried. PAs were

characterized by liquid chromatography and mass spectrometry (LC-MS). Mass spectrum was obtained with Agilent 1200 LC-MS equipped with Agilent 6530 Q-TOF with an ESI source and Zorbax Extend-C18 2.1 × 50 mm column for basic conditions and Zorbax SB-C8 4.6 mm × 100 mm column for acidic conditions. A gradient of (a) water (0.1% (v/v) formic acid or 0.1% (v/v) NH_4OH) and (b) acetonitrile (0.1% (v/v) formic acid or 0.1% (v/v) NH_4OH) was used. An Agilent 1200 preparative reverse-phase HPLC system equipped with a Zorbax Extend-C18 21.2 × 150 mm column for basic conditions and a Zorbax SB-C8 21.2 × 150 mm column for acidic conditions was used to purify the peptides. A gradient of (a) water (0.1% (v/v) TFA or 0.1% (v/v) NH_4OH) and (b) acetonitrile (0.1% (v/v) TFA or 0.1% (v/v) NH_4OH) was used.

3.4.3. Nanofiber Formation Mechanism

Nanofiber formation mechanisms were based on mixing oppositely charged PAs, which neutralized net charge on each other and induced self-assembly to higher-order nanofibers. Three different types of nanofibers were used in this study (Figure 3.1). Bioactive HM-PA nanofiber was prepared similar to one in previous chapter. HM-PA (−3 charge) and K-PA (+1 charge) were mixed in a 1:2 molar ratio for HM-PA/K-PA nanofibers, while E-PA (−2 charge) and K-PA (+1 charge) were mixed in a 1:1 molar ratio for control E-PA/K-PA nanofibers, to make both nanofibers to have theoretically net one negative charge. Since the K-PA amount is lower for E-PA/K-PA nanofibers than HM-PA/K-PA nanofibers in this case, we used E-PA/K-PA 2x nanofibers as a control for this issue. For E-PA/KPA 2x nanofibers, we used both E-PA and K-PA in doubled concentrations but same molar ratio (1:1). Heparin carrying nanofibers were also prepared by mixing heparin and K-PA as showed in chapter 2, however here their ratio was adjusted to make system to have net one negative charge. For this, weight ratio of heparin to K-PA was adjusted to 1:2. Heparin/K-PA nanofibers were used as a positive control. All PAs used for nanofiber formation were at pH 7.

3.4.4. ELISA-Based Binding Assay

ELISA technique was exploited to compare binding levels of growth factors to HM-PA/K-PA nanofibers and control nanofibers. MaxiSorp plates (Thermo Scientific, NUNC) were coated with PA nanofibers or blank solution overnight at 4 °C. The PA nanofiber formation was performed on plates by mixing negatively and positively charged PAs. Briefly, 0.05% HM-PA / 0.05% K-PA, 0.025% E-PA / 0.025% K-PA, 0.05% E-PA / 0.05% K-PA, or 0.05% heparin / 0.1% K-PA (all are w/v) equal volume mixtures were prepared. The next day, the solutions were removed and the wells were washed with washing buffer (Tween 20 in 0.9% (w/v) NaCl solution, pH = 7.4). These plates are high-affinity binding plates for a broad range of molecules with hydrophobic/hydrophilic character, thus, even after extensive washing, plates were observed to be coated completely with PA nanofibers (Figure 3.2). After tapping for drying, blocking buffer (Assay buffer, Invitrogen) was added. This was followed by the addition of growth factor solution, biotinylated antibody against growth factor, streptavidin-linked horseradish peroxidase (HRP) and HRP substrate (3,3′,5,5′ tetramethylbenzidine (TMB). After 15−20 min of incubation, the reaction was stopped with sulfuric acid. Absorbance change due to color formation was measured by a Spectramax M5 microplate reader (Molecular Devices) at 450 nm wavelength. This value was subtracted from the reference value (650 nm). All treatments were performed with three replicates and are shown as mean ± standard deviation. Experiments were repeated at least two times independently. For statistical analysis, two-way ANOVA with Bonferroni posthoc analysis and Student's t-test were used.

3.4.5. Atomic Force Microscopy (AFM) Imaging

AFM imaging was performed to determine the coating efficiency of PA nanofibers on ELISA plates. Coating was performed similarly to "ELISA-binding assay" procedures. After overnight incubation of plates with PA nanofiber solution, the solution was aspirated and the plate was washed 2−3 times with ELISA washing

buffer (Tween 20 in 0.9% (w/v) NaCl solution, pH = 7.4). The plates were dried by tapping, and the coated bottom part was removed for AFM imaging. Bare ELISA plates were also imaged with AFM to understand their surface roughness. Non-contact-mode AFM was performed by using model MFP-30 from Asylum Research. All images were taken with a 0.5 Hz scan rate. Tips with resonance frequency of 300 kHz and spring constant of 40 N/m were used in all experiments (BudgetSensors).

3.4.6. Isothermal Titration Calorimetry (ITC)

To investigate the interaction between HM-PA/K-PA nanofibers and VEGF121, we used the iTC200 system (MicroCal, GE Healthcare). VEGF121 (0.27 mg/mL in 1x PBS solution) was titrated into HM-PA/K-PA nanofiber solution. For HM-PA/K-PA nanofiber solution, 0.04% HM-PA and 0.04% K-PA (both in H_2O and w/v) were mixed to form nanofibers in solution, which was diluted 2-fold with 2x PBS to obtain HM-PA/KPA nanofiber solution in 1x PBS. Reaction was performed at 25 °C with 500 rpm stirring speed. Twenty injections were performed, where the injection period was 4 s and the space between injections was 150 s. All solutions that were used in ITC experiments were at pH 7.

3.4.7. Immunogold Staining and Transmission Electron Microscopy (TEM) Imaging.

Hepatocyte growth factor (HGF) binding on HM-PA/K-PA nanofibers was visualized by using immunogold staining and TEM imaging. First, HM-PA/K-PA gel was formed by mixing 20 μL of 1% HM-PA with 1% K-PA (w/v). Gel was diluted 10 times, and 30 μL of the diluted solutions was dropped onto parafin film. Cu grids were reversed onto these drops and incubated for 5 min. The tiny amount of liquid left on the grids was absorbed with dust-free paper, and the grids were dipped into 1x PBS solution two times to wash weakly bound nanofibers. Grids were reversed onto 30 μL of blocking solution (Assay buffer, Invitrogen) and incubated for 1 h at room

temperature. Drops on grids were absorbed, and HGF (500 ng/ mL in assay buffer) was added onto the grids. After 2 h of incubation, grids were washed with PBS five times. Primary antibody (25 μg/mL, R&D) against human HGF was added onto grids and incubated overnight at 4 °C. Grids were washed with PBS 5 times. Gold-attached antibody (25 nm gold particles conjugated to antimouse IgG), 1/20 diluted from stock with assay buffer, was put onto paraffin film, and grids were reversed onto this solution, to prevent precipitation of gold particles onto the grid surface due to gravitation. After 1 h, grids were washed five times with PBS and three times with double-distilled water (ddH_2O). After drying at room temperature for at least 3 h, TEM (FEI, Tecnai G2 F30) imaging was performed. All images were taken in STEM mode with an HAADF (high angle annular dark field) detector.

3.4.8. HM-PA/K-PA Nanofiber versus Heparin Competition Assay

HM-PA/K-PA nanofiber and heparin competition for the same site of growth factor was studied by increasing doses of heparin (0.0003% to 0.3%, w/v) in the presence of various growth factors just before latter ones were incubated with HM-PA/K-PA nanofibers. HM-PA/K-PA nanofiber coating and the rest of the assay was performed similarly to ELISA-based binding assay. IC_{50} (half-maximal inhibitory concentration) of heparin to inhibit growth factor and HM-PA/K-PA nanofiber binding was calculated for each growth factor by using GraphPad Prism software. Nonlinear regression analysis with robust fitting was carried out for this purpose. We performed the same experiment with chondroitin sulfate instead of heparin (only for fibroblast growth factor-2 (FGF-2) to control the effect of heparin. All treatments were performed with three replicates and are shown as mean ± standard deviation. Experiments were repeated twice, independently.

3.4.9. NGF Induced Neurite Extension Assay

To determine biological activity caused by interaction of PA nanofibers with nerve growth factor (NGF), PC-12 cells were cultured on NGF-coated PA nanofiber surfaces. PA nanofiber gel scaffolds with −1 charge were prepared as described below. For HM-PA/K-PA nanofiber gel, 1.5 mM HM-PA was mixed with 3 mM K-PA at equal volumes (40 μL for 96 well-plate). E-PA/K-PA nanofiber gel was formed in the same way by mixing 1.5 mM E-PA with 1.5 mM K-PA, while E-PA/K-PA 2x gel was prepared by mixing 3 mM EPA with 3 mM K-PA. 0.1% (w/v) Poly-D-lysine (PDL) was coated as a control since it is not expected to bind NGF due to its dense positive charge. After gel formation, plates were dried under a laminar flow hood and UV sterilized. For NGF coating on PA coated surfaces, NGF was added at concentrations of 10 ng/mL or 50 ng/mL. After 2 h of incubation at room temperature, wells were washed three times with PBS to remove any unbound NGF. PC-12 cells (5×10^3 cells/well) were then seeded and cultured on these surfaces for 4 days. In another experimental group, incubated NGF was not removed to test the effect of surface bound and soluble NGF at the same time (total concentration was the same with other groups). In this case, cells were added directly on NGF solution over PA or PDL coated surfaces. For soluble NGF groups, the same concentration of NGF was added on cells after seeding (n = 3 for all samples). At the end of 4 days, images (5 images/well) were taken at 200x magnification, and neurite lengths were quantified with Image J. For statistical analysis, two-way ANOVA with Bonferroni posthoc analysis was performed (Figures 6 and S4). For immunostaining, PA nanofiber coating was carried out by using the same protocol except that PAs were coated on glass coverslips placed in 24 well-plates (total volume: 300 μL/well). NGF coating (50 ng/mL) was performed as described above and 3×10^4 cells/well were seeded. After 4 days of culture, cells were fixed with 4% paraformaldehyde, permeabilized with 0.3% TritonX-100, and blocked with 10% goat serum. Antibodies against β-III-Tubulin (Millipore, 1:250 dilution) and synaptophysin 1 (Sigma-Aldrich, 1:400 dilution) were incubated overnight at 4 °C. After washing, cells were incubated with goat-antirabbit IgG-Cy3 (Chemicon, 1:200 dilution) and goatantimouse IgG-Cy2 (Chemicon, 1:400 dilution) for 1 h at room temperature and

washed to remove any unbound antibodies. Coverslips were then removed from wells, mounted by using Prolong gold antifade reagent (Invitrogen), and imaged with a confocal microscope (Carl Zeiss, LSM510).

3.5. Conclusion

In summary, the functionality of heparan sulfates in extracellular matrix can be achieved synthetically through presenting key functional groups of heparan sulfates on peptide nanofibers. While forming hydrogel scaffolds, these nanofibers bind to heparin-binding growth factors that are utilized commonly in regenerative medicine studies and present them to cells effectively. Interestingly, for VEGF and FGF-2, this binding specifically requires the presence of heparin-binding domain of growth factors, which may be critical for proper presentation of growth factors to cells. Growth factor binding property of HM-PA nanofibers could be advantageous for different tissue engineering applications, such as angiogenesis shown in previous chapter and neural differentiation shown here.

CHAPTER 4

4. VIRUS-LIKE NANOSTRUCTURES FOR TUNING IMMUNE RESPONSE: SHAPE DOES MATTER

4.1. Objective

Rational design of vaccines is required to drive immune response to desired context safely. Various pathogenic biochemical patterns, such as CpG DNA, has been proposed as vaccine adjuvant, to alarm immune system against co-delivered antigen. In nature, immune system sense pathogens as a whole with biochemical and biophysical signals together. In this study, we aimed to understand how immune system reacts to pathogenic biochemical signals, specifically CpG DNA, in the context of specific physical signals – shape of its carrier. Our purpose was to engineer immune response through synergistic action of biochemical and biophysical pathogenic patterns, and also delineate some basic principles about the effect of shape of vaccine complex on generated immune response.

4.2. Introduction

Developing novel vaccines is crucial as prospect of pandemic threat by infectious diseases such as flu (influenza virus) and SARS (coronavirus) looms large. Current vaccinology relies on inactivated or live attenuated viruses to introduce the characteristics of evolved virus to immune system as much as possible.[110] Widely used egg-based vaccine production depends on viral growth characteristics in eggs. Sluggish growth of virus or scarcity of egg resources might slow vaccine production during pandemic, when time is the limiting factor. Moreover, live attenuated viruses, which are known to be superior to inactivated viruses in eliciting immune response,[110-111] carry risk of becoming virulent as in the case of oral poliovirus vaccine[112] or causing side effects on immunocompromised individuals.[113] Due to above-mentioned reasons, rational design of simpler vaccines with easier production process along with robust effectiveness are vitally needed. In order to achieve this purpose, we should understand principles required to drive immune response to desired context (such as what type of cytokines and co-stimulatory molecules are expressed or what type of innate and adaptive immune cells will be activated).[33] These principles lie in how immune cells recognize and respond to different features

of pathogens, in the broader classification - biochemical and biophysical features. In this regard, pathogen-associated molecular patterns (PAMPs) stand out to be biochemical pathogenic signatures, which can be used as adjuvants to enhance immunogenicity of antigen.[113-114] PAMPs trigger innate immune cells to elevate antigen presentation and cytokine secretion, which eventually induce adaptive immune response.[115-116] In this context, DNA with unmethylated CpG motives, signature of bacterial/viral DNA, have extensively been studied and proved to boost humoral and cellular responses to vaccines (Figure 4.1).[40, 117-119]

In nature, biochemical signals act in the context of biophysical ones, such as size and shape of pathogen. This synergy play critical role in shaping immune response and should be projected onto the vaccine for robust effectiveness. For example, physical proximity of antigen and adjuvant (e.g. CpG DNA), which allows both to be internalized by the same immune cells, has been shown to be critical for inducing a strong immune response.[117, 120] Therefore, covalent conjugation of antigen with adjuvant elevates antigen-specific Th1 immune response - cytotoxic T cell activity, significantly.[120-122] However, covalent conjugation entails chemical modification to antigen and adjuvant, which depends on chemistry of antigen and might be inefficient for some antigens.[122] To overcome this problem, wide range of materials including cationic microparticles, liposomes, nanoparticles, and nanorods have been proposed for delivery of antigen and adjuvant in close proximity.[123] These micro/nanocarriers boost immune reaction to antigen/adjuvant also through enhanced cellular uptake and protection from enzymatic degradation.[123] Moreover, nanoparticle carriers can alter the nature of immune response (e.g. inducing different cytokine profile) to CpG oligodeoxynucleotides (CpG ODNs). Nanoparticles carrying CpG ODN or CpG ODNs which fold and aggregate to form nanoparticles (known as A type ODN) induce production of high amounts of interferon-alpha (IFNα) cytokine, which mediates anti-viral response from plasmacytoid dendritic cells.[124-127] Interestingly, high interferon-alpha response is similarly observed in immune reaction to viruses. On the other hand, linear (i.e. not folding and aggregating to form higher order structures) CpG ODN itself is known to be a poor interferon inducer, while being a strong inducer of IL-6 and TNFα production and

expression of maturation markers on cell surface.[118, 128] This dichotomy was linked to differing subcellular localization of nanoparticulate and linear CpG ODN in plasmacytoid dendritic cells and induction of distinct signaling pathways.[129]

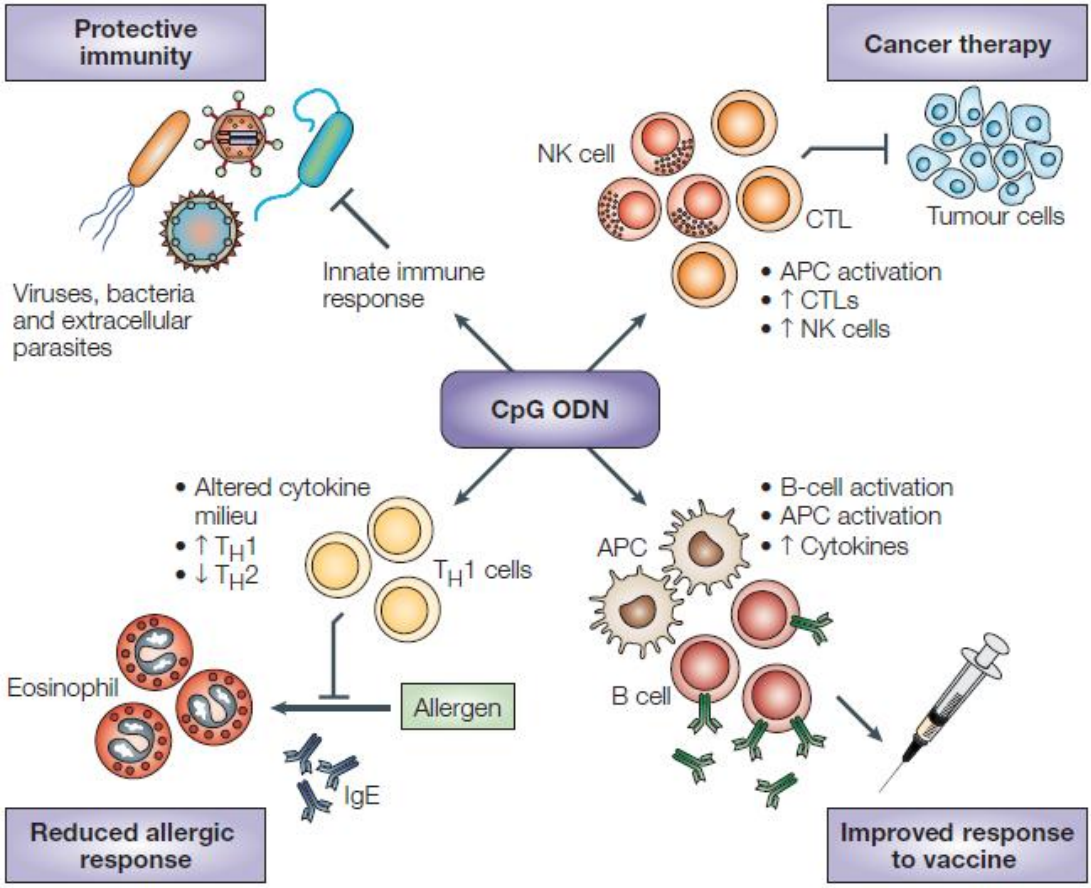

Figure 4.1. Potential therapeutic applications of CpG oligodeoxynucleotides (ODNs). CpG-induced innate immune response can protect the host from infectious pathogens. Therefore, CpG ODNs might be used as stand-alone agents to reduce susceptibility to infection. When combined with allergen, these ODNs stimulate an antigen-specific T helper 1 (Th1)-cell response that inhibits the development of Th2-cell-mediated allergic asthma. CpG ODNs also improve the function of professional antigen-presenting cells (APCs), and create a cytokine/chemokine milieu that is conducive to the development of an adaptive immune response to co-administered vaccines. Finally, the immune cascade that is elicited by CpG ODNs results in the activation of natural killer (NK) cells and cytotoxic T lymphocytes (CTLs) that facilitates (alone or in combination with other therapies) the treatment of cancer (Reproduced with permission from ref. 130 copyright © 2004 Macmillan Publishers Ltd.)[130]

All these studies suggest profound effects of physical features of the vehicles (virus or synthetic vaccine particle) carrying biochemical signals (such as viral DNA or antigen) in shaping immune response. However, a systematic investigation of how mammalian immune system responds to viral biochemical signals in the context of main viral shapes - spheres and rods - is not available. To answer this question, we compared immune response against CpG DNA, delivered by zero- and one-dimensional nanostructures formed by self-assembling peptide molecules and CpG ODNs (Figure 4.2). These nanostructures resemble viruses in several ways: i) their size and shape are comparable to viruses, where nanofibers resemble rod-like viruses and nanospheres are similar to spherical viruses; ii) they carry ODNs with motives from viral DNA (CpG), which is known to activate TLR9 during viral infection[35]; and iii) they can be engineered to carry viral antigens through peptide domain. In this chapter, virus-like nanostructures capable of potently eliciting anti-viral immune response are presented and modification of immune response against CpG DNA, through changing physical properties of the carrier vehicle it, is demonstrated (Figure 4.2).

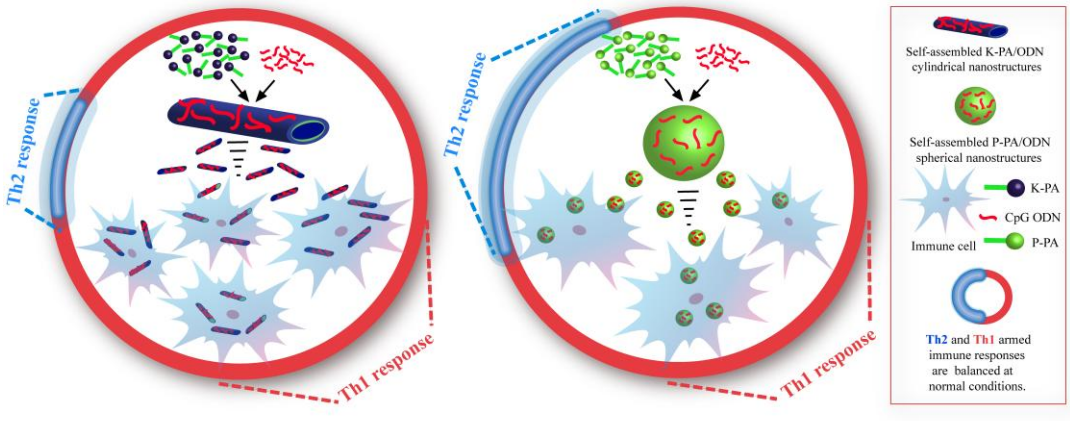

Figure 4.2. Schematic plot of designed virus-like nanostructures and tunability of immune response with these nanostructures. CpG ODNs mimick immunostimulatory CpG motives (red) of viral DNA. Mixing CpG ODNs with proline-rich peptides give rise to nanospheres with 15-20 nm diameter. While, mixing with β-sheet forming peptide leads to formation of one-dimensional nanofibers with 10-15 nm of diameter and >1 μm length. CpG ODNs are known in the literature to induce Th1-biased immune response. Delivering them on nanospheres and nanofibers elevates this effect, while nanofibers are being more potent.

4.3. Results and Discussion

Functional self-assembled architectures with varying morphologies can be developed depending on the molecular nature of building blocks.[131] The properties of amino acids guide self-assembly of peptide molecules and determine their structural properties. Valine and alanine residues in the peptide molecules, known as "β-sheet formers", favor formation of one-dimensional nanostructures, while proline residues, "β-sheet breakers", support self-assembly of zero-dimensional spherical nanostructures.[132-134] In addition, self-assembly of peptides into one or zero dimensional nanostructures can be promoted by mixing oppositely charged biomacromolecules. Non-covalent interactions such as hydrogen bonding, and electrostatic and hydrophobic interactions between the peptides and biomacromolecules enable formation of supramolecular assemblies.[2, 135-136]

In this study, we combined self-assembling peptide molecules with oppositely charged immunostimulatory oligodeoxynucleotides (CpG ODNs) to obtain one-dimensional (nanofibers) and zero-dimensional (nanospheres) virus-like nanostructures. For this purpose, we synthesized two positively charged peptide amphiphile (PA) molecules by changing backbone motifs (K-PA and P-PA; Figure 4.3) to direct self-assembled nanostructures into different morphologies. Both PA molecules include a lauryl group to drive self-assembly in aqueous solution, a glycine residue as spacer and a lysine residue to provide positive charge at the physiological pH. K-PA included valine-valine-alanine residues as a backbone to drive hydrogen bonding and β-sheet formation (Figure 4.3). While P-PA included proline-proline-proline to prevent hydrogen bonding and β-sheet formation which impairs formation of one-dimensional nanostructures (Figure 4.3).

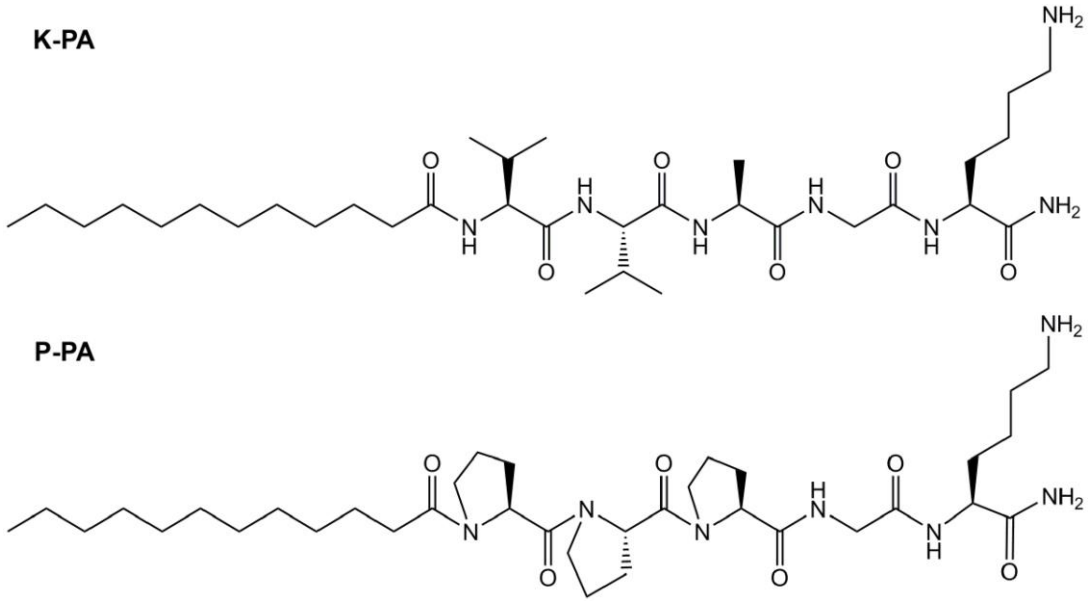

Figure 4.3. Chemical representations of K-PA (C_{12}-VVAGK) and P-PA (C_{12}-PPPGK) molecules used in this study. K-PA and P-PA are mixed with CpG ODNs to induce nanofiber and nanosphere formation, respectively.

Both K-PA and P-PA molecules were purified with High-Performance Liquid Chromatography (HPLC) and analyzed with liquid chromatography-mass spectrometry (LC-MS). As explained in Chapter 2, in LC analysis, PA molecules were eluded according to hydrophilicity and detected with UV detector (at 220 nm wavelength. Elution time points given in LC chromatograms (Figures 4.4.a – 4.5.a) were consistent with hydrophilicity of molecules. More hydrophilic P-PA (due to three proline residues) was eluded at earlier time point than K-PA (two valines and one alanine). Mass spectra of peaks obtained in LC chromatograms indicated that both synthesized PA molecules have similar masses to the expected ones (Figures 4.4.b – 4.5.b). These purified molecules were used in further studies.

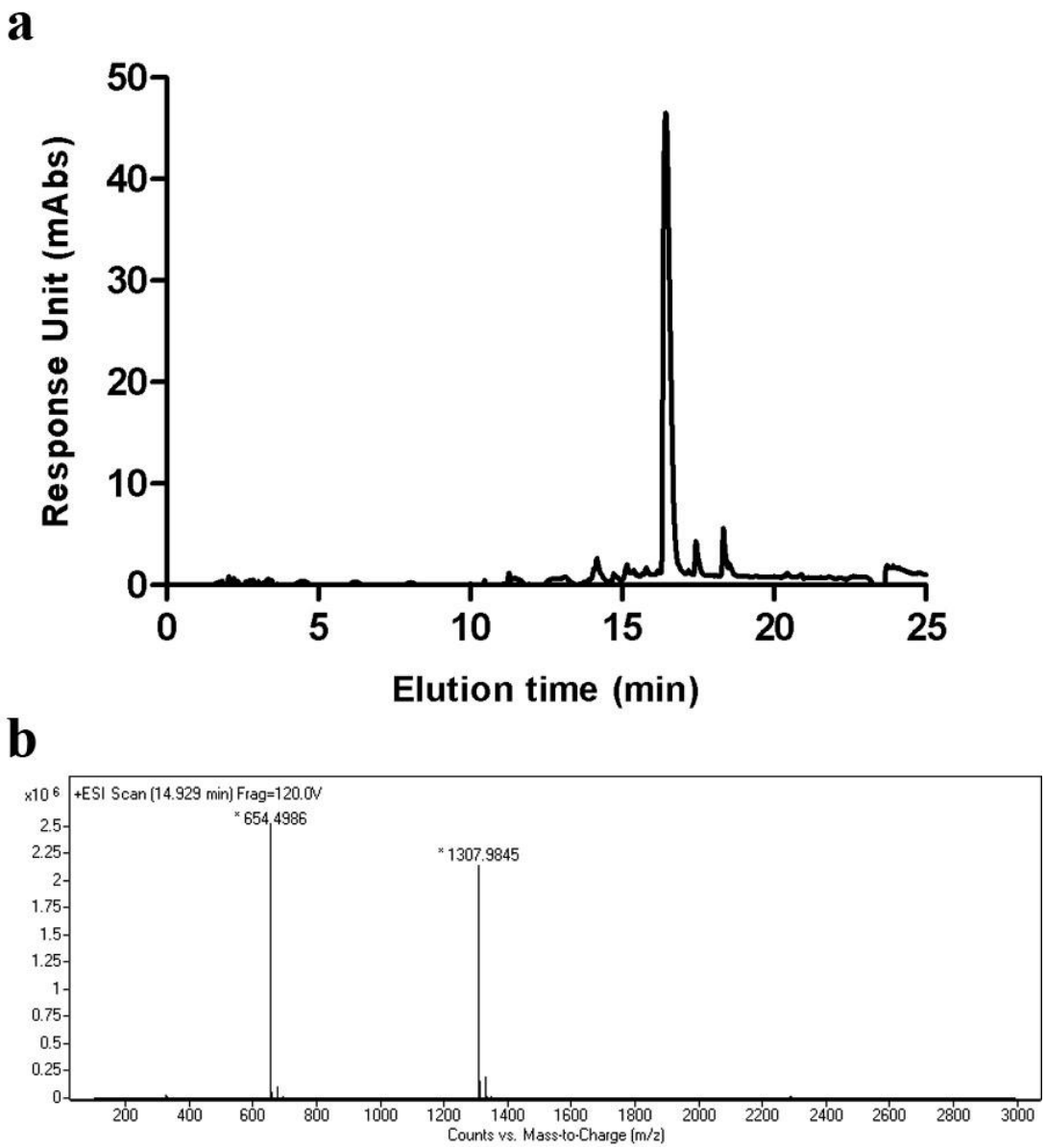

Figure 4.4. LC-MS analysis of synthesized K-PA molecule.a. LC chromatogram of purified K-PA molecules at 220 nm indicates high purity of molecule. b. Mass spectrometric analysis of peak in K-PA LC chromatogram. [M+H]+(calculated)=654.48, [M+H]+(observed)=654.50.

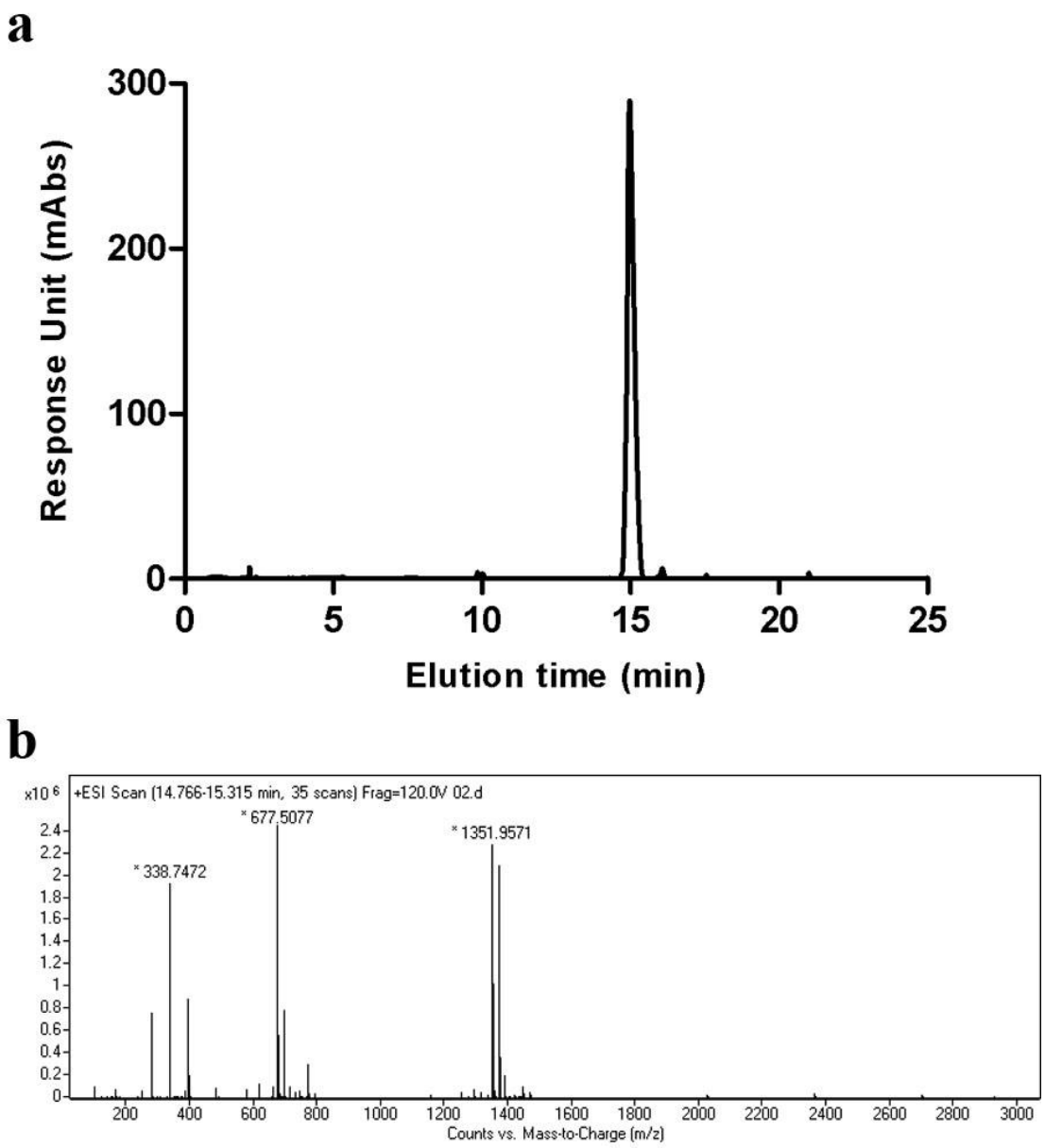

Figure 4.5. LC-MS analysis of synthesized P-PA molecule. a. LC chromatogram of purified P-PA molecules at 220 nm indicates high purity of molecule. b. Mass spectrometric analysis of peak in P-PA LC chromatogram. [M+H]+(calculated)=676.47, [M+H]+(observed)=677.51.

4.3.1. Structural characterizations of PA/ODN complexes

Since secondary structures of peptide amphiphiles play critical role in nanostructure shape, we investigated secondary structure characters of PA combinations. For this reason, we obtained circular dichroic (CD) spectra of K-PA, P-PA and their ODN complexes. The K-PA molecule has a Val-Val-Ala peptide sequence, and revealed β-sheet characteristic peaks (negative at 217 nm, positive at 197 nm) in circular dichroism (CD) spectra (Figure 4.6). While, P-PA molecule including Pro-Pro-Pro peptide sequence showed PPII helix secondary structure (a strong negative band at 203 nm and a weak positive band at 227 nm), similar to polyproline structures (Figure 4.6).[133-134, 137] PA/ODN complexes also demonstrated similar secondary structures of K-PA and P-PA and showed β-sheet and PPII helix characteristics in CD spectra, respectively.

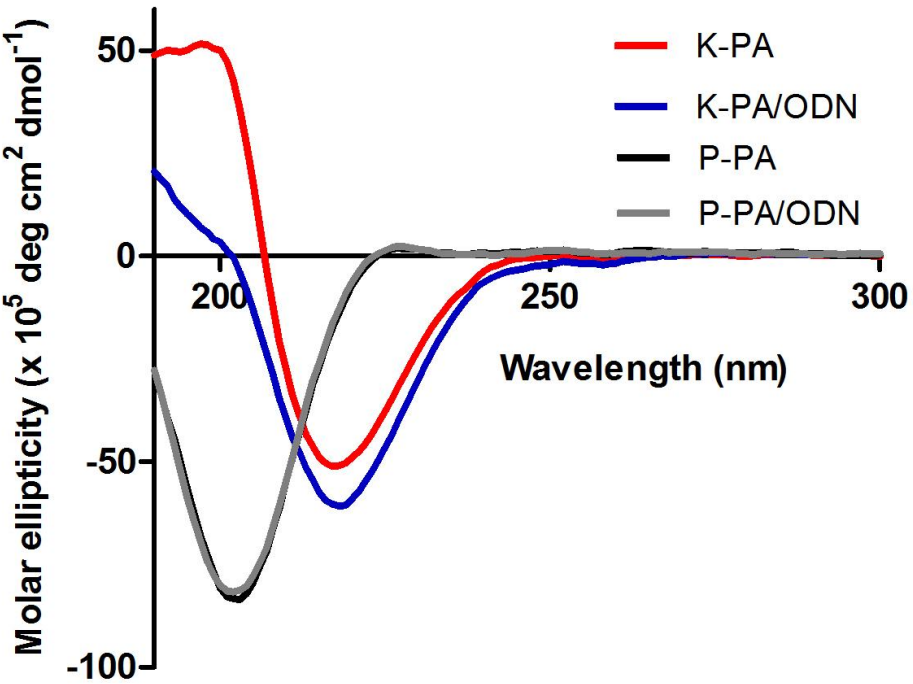

Figure 4.6. Circular dichroic (CD) spectra of K-PA and P-PA molecules alone or mixed with immunostimulatory ODN. CD spectra shows that secondary structures formed by ODN complexes of P-PA and K-PA are completely different. K-PA alone and K-PA/ODN complex shows characteristic signals for β-sheet secondary structure. However, P-PA alone and P-PA/ODN comples shows characteristic signals for PPII helix secondary structure.

Structural analyses of PA/ODN complexes were examined by using Small-angle X-ray Scattering (SAXS), which provides information on the size and shape of nanostructures, and have an advantage of studying nanostructures in aqueous environment (Figure 4.7). The low q regions of the small-angle X-ray scattering data of K-PA/ODN and P-PA/ODN complexes were best fitted to an elliptical cylinder model[138] with a major radius of 8.6±0.4 nm and oblate core shell sphere model[139-140] with a major radius of 7.2±0.3 nm, respectively. The results obtained from fitting of SAXS curve showed that K-PA/ODN complexes self-assembled into one-dimensional high-aspect-ratio cylindrical nanofibers, while P-PA/ODN complexes formed zero-dimensional oblate spherical nanostructures (Figure 4.7a, b; Table 4.1 and 4.2). The elliptical cylindrical structural properties of K-PA/ODN complexes showed similar characteristics with Tobacco Mosaic Viruses (TMVs), which can form hollow cylinders with an ellipsoidal cross-section according to SAXS measurements.[141]

For control experiments, K-PA and P-PA solutions at the same concentrations with PA/ODN complexes were prepared and SAXS analysis was performed. SAXS profiles of K-PA and P-PA nanostructures were also best fitted to an elliptical cylinder model with a major radius of 8.0±0.3 nm and oblate core shell sphere model with a major radius of 5.1±0.3 nm, respectively (Figure 4.8; Table 4.3 and 4.4).

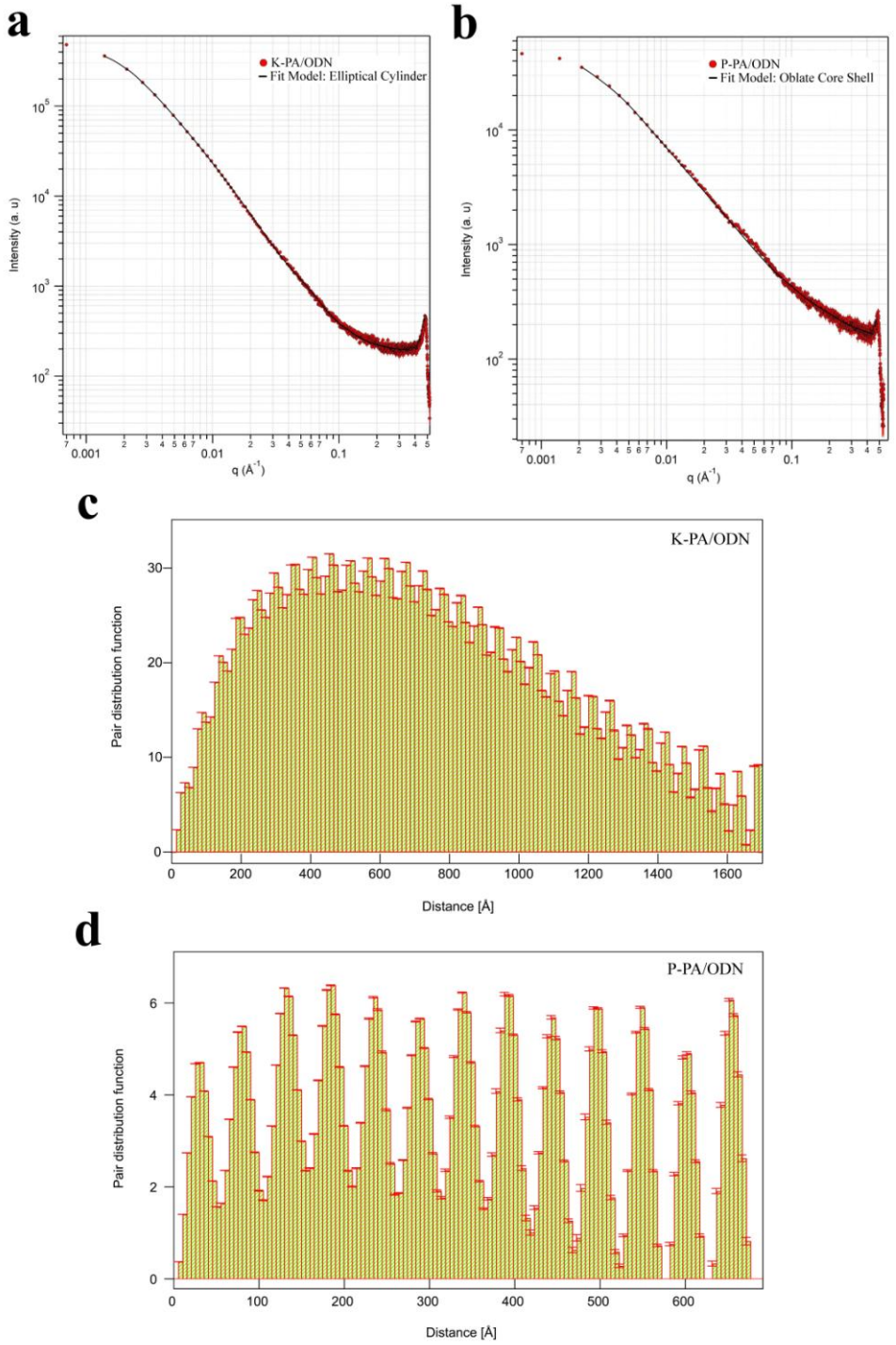

Figure 4.7. SAXS analysis and model fitting for self-assembled PA/ODN nanostructures. According to Guinier plots, radius of gyration (R_g) of (a) K-PA/ODN self-assembled nanostructures was calculated to the best fit, elliptical cylinder model and (b) P-PA/ODN self-assembled nanostructures was calculated to the best fit, oblate core shell sphere model. PDDF histograms of (c) K-PA/ODN and (d) P-PA/ODN self-assembled nanostructures also showed characteristics of elliptical cylinder and oblate core shell sphere model, respectively.

Table 4.1. Structural results obtained from fits to the SAXS data of K-PA/ODN complexes with elliptical cylinder model.

Fitting Results (Elliptical Cylinder Model)	***K-PA+ODN***
Scale	4.6
Minor radius (nm)	7.6±0.3
Major radius (nm)	8.6±0.4
Length (nm)	235.2±1.2
SLD Cylinder ($Å^{-2}$)	6.8×10^{-5}
SLD Solvent ($Å^{-2}$)	3.7×10^{-6}

Table 4.2. Structural results obtained from fits to the SAXS data of P-PA/ODN complexes with oblate core shell sphere model.

Fitting Results (Oblate Core Shell Model)	***P-PA+ODN***
Scale	2.6
Minor core (nm)	1.8±0.1
Minor shell (nm)	4.9±0.2
Major core (nm)	2.0±0.1
Major shell (nm)	5.2±0.2
SLD core ($Å^{-2}$)	1.3×10^{-6}
SLD shell ($Å^{-2}$)	3.1×10^{-5}
SLD Solvent ($Å^{-2}$)	1.4×10^{-7}

Table 4.3. Structural results obtained from fits to the SAXS data of K-PA with elliptical cylinder model.

Fitting Results (Elliptical Cylinder Model)	***K-PA***
Scale	4.6
Minor radius (nm)	7.0±0.3
Major radius (nm)	8.0±0.3
Length (nm)	235.2±1.2
SLD Cylinder ($Å^{-2}$)	4.8×10^{-5}
SLD Solvent ($Å^{-2}$)	3.7×10^{-6}

Table 4.4. Structural results obtained from fits to the SAXS data of P-PA with oblate core shell sphere model.

Fitting Results (Oblate Core Shell Model)	***P-PA***
Scale	2.6
Minor core (nm)	1.2±0.1
Minor shell (nm)	3.2±0.2
Major core (nm)	1.5±0.1
Major shell (nm)	3.6±0.2
SLD core ($Å^{-2}$)	1.3×10^{-6}
SLD shell ($Å^{-2}$)	2.0×10^{-5}
SLD Solvent ($Å^{-2}$)	1.4×10^{-7}

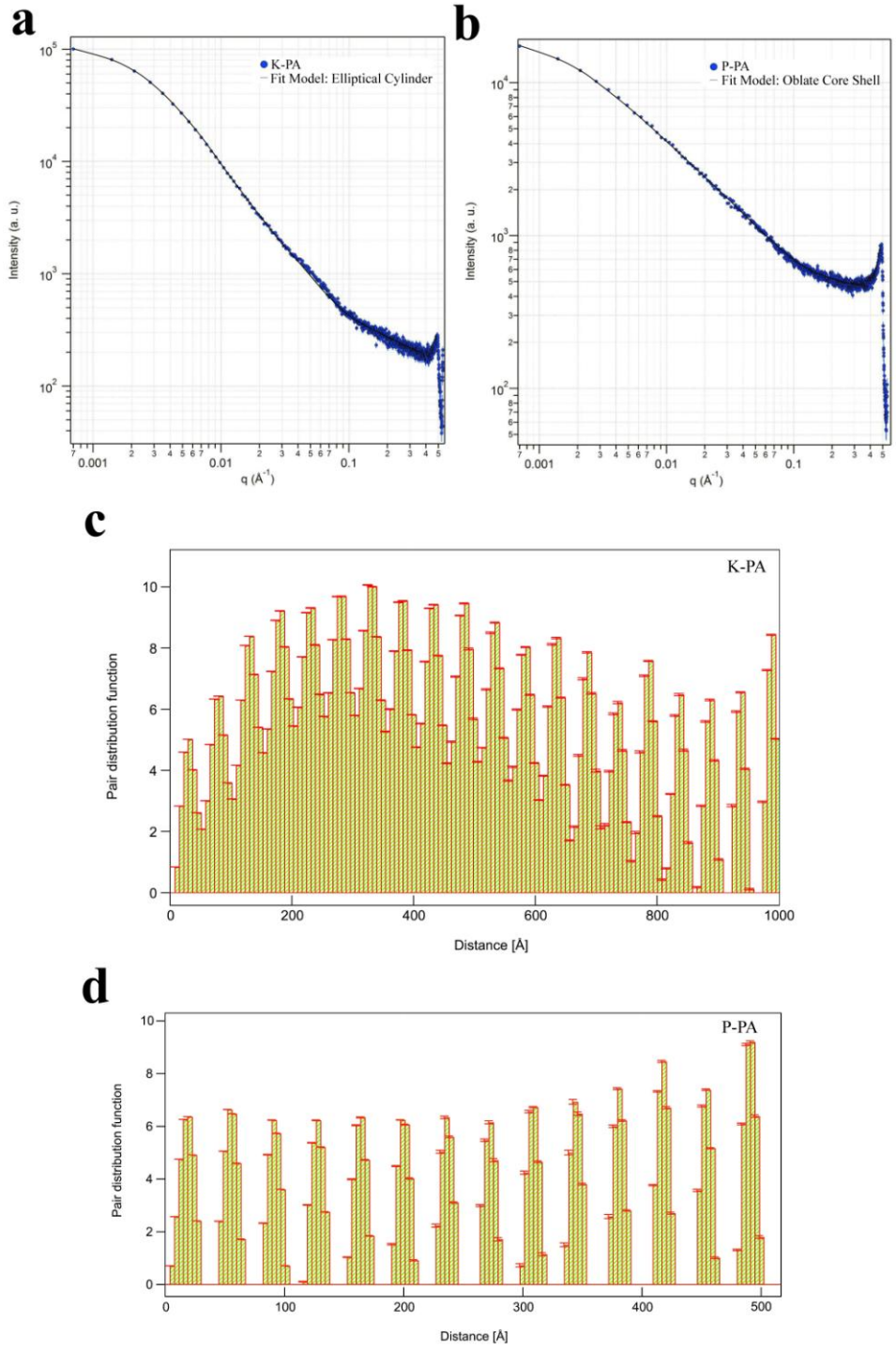

Figure 4.8. SAXS analysis and model fitting for self-assembled PA nanostructures. According to Guinier plots, radius gyration (R_g) of (a) K-PA self-assembled nanostructures was calculated to the best fit, elliptical cylinder model and (b) P-PA self-assembled nanostructures was calculated to the best fit, oblate core shell sphere model. PDDF histograms of (c) K-PA and (d) P-PA self-assembled nanostructures also showed characteristics of elliptical cylinder and oblate core shell sphere model, respectively.

In order to visualize structures formed by K-PA/ODN and P-PA/ODN complexes we performed imaging by using Scanning Transmission Electron Microscope (STEM), TEM and AFM. STEM images of the K-PA/ODN and P-PA/ODN complexes revealed cylindrical and spherical morphology, respectively, in complementary to SAXS measurements (Figure 4.9a, b, 4.10, 4.11). In addition, phosphorus signal obtained by EDX (Energy-dispersive X-ray) spectroscopic analysis on spherical nanostructures and cylindrical fibers indicated interaction of ODNs with peptide molecules, and formation of peptide/ODN complexes (Figure 4.10 and 4.11).

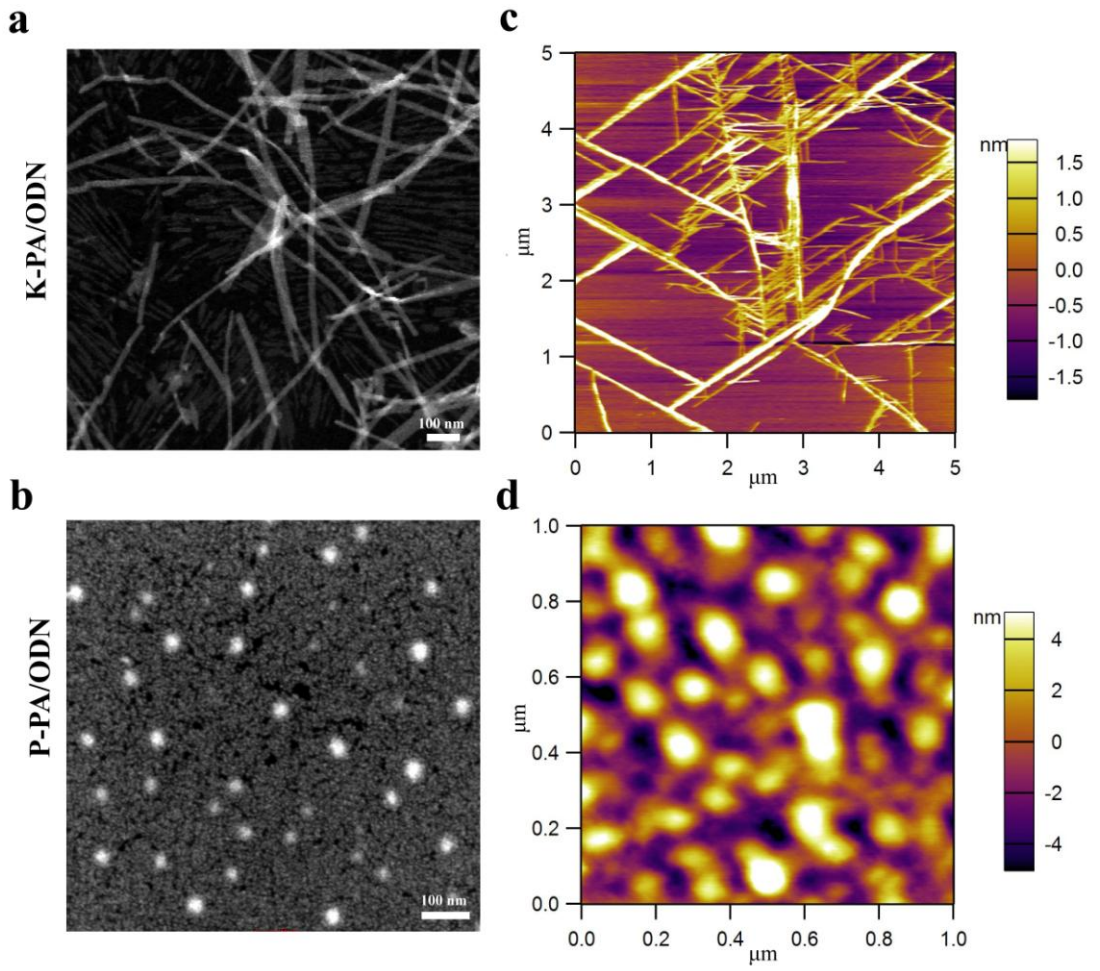

Figure 4.9. Imaging of PA/ODN nanostructures with TEM and AFM. TEM images of K-PA/ODN (a) and P-PA/ODN (b) self-assembled nanostructures and AFM images of K-PA/ODN (c) and P-PA/ODN (d) self-assembled nanostructures in aqueous environment.

AFM imaging of the peptide ODN complexes were performed to analyze these systems in aqueous environment to eliminate drying or staining effect in imaging. The peptide ODN complexes were imaged with AFM tip oscillating at the water/surface interfaces. The K-PA/ODN and P-PA/ODN complexes showed cylindrical and spherical morphologies, respectively, in complementary to SAXS measurements and TEM imaging (Figure 4.9c, d). On the other hand, K-PA/ODN self-assembled into cylindrical bundles, and larger aggregates of P-PA/ODN spherical complexes were observed in the aqueous environment. The aggregation and bundle formation on the AFM images in aqueous environment is related to the dynamic nature of peptide ODN complexes and self-assembly of the peptides.

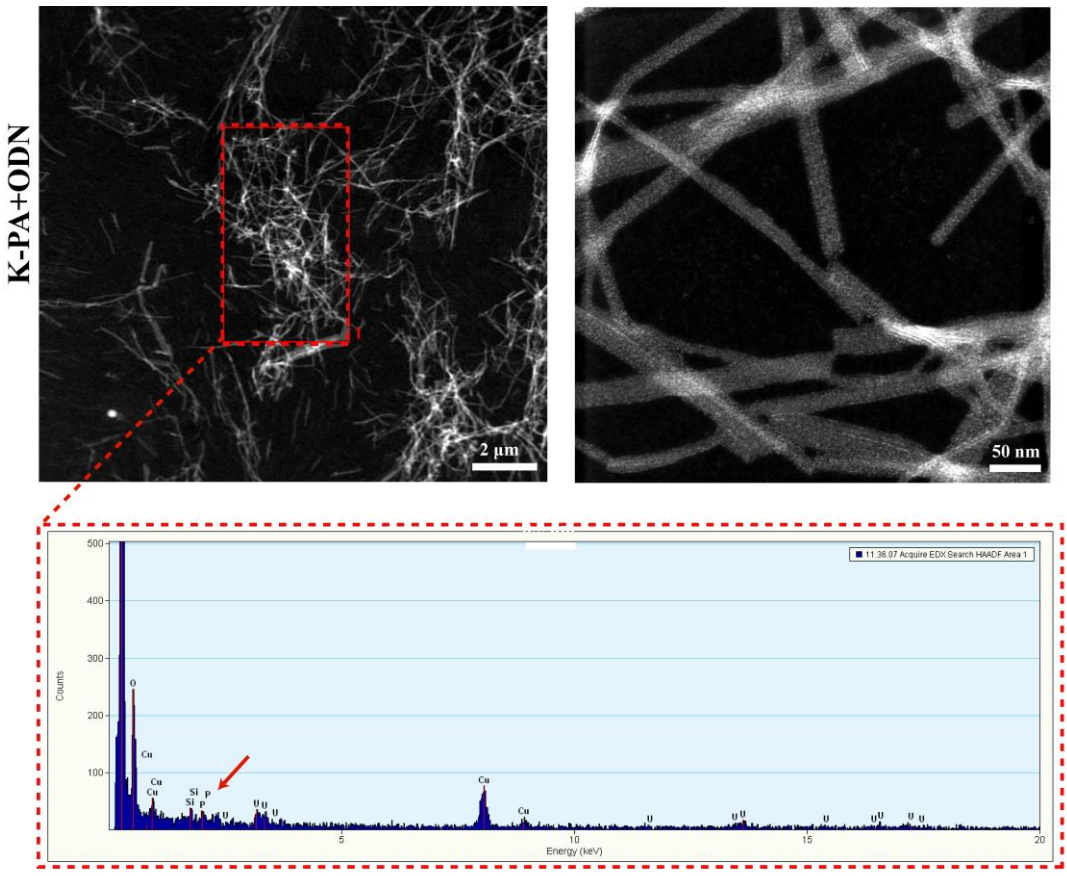

Figure 4.10. STEM images of self-assembled K-PA/ODN peptide fibers. The initial fiber formation and peptide bundles can be seen in images (scale bars: left image 2 µm, right image 50 nm). EDX analysis (from the region shown with red rectangle in left STEM image revealed P atoms on the peptide bundles and self-assembly of DNA molecules with K-PA.

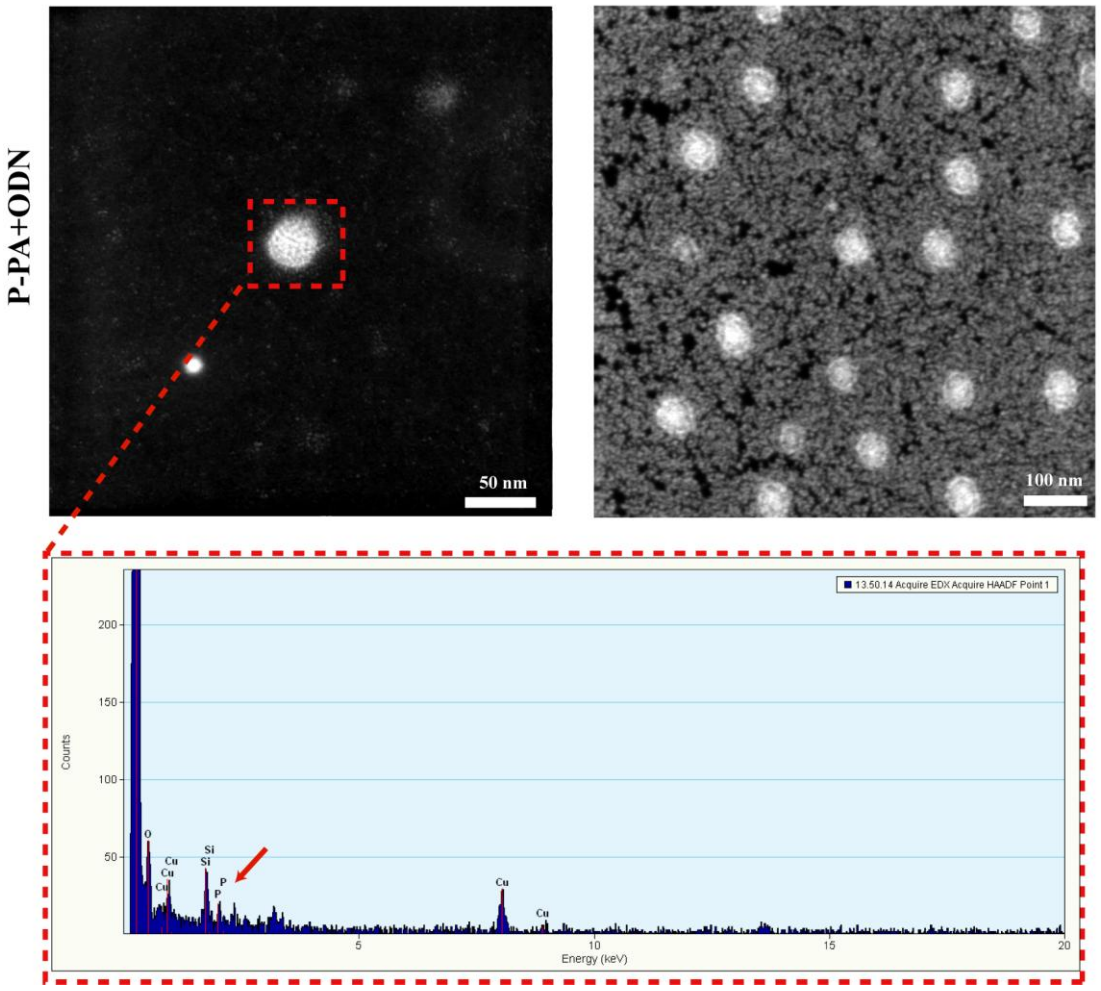

Figure 4.11. STEM images of self-assembled P-PA/ODN peptide spherical nanostructures. The spherical morphology of the nanostructures can be seen in images (scale bars: left image 50 nm, right image 100 nm). EDX analysis (from the region shown with the red rectangle in left STEM image revealed P atoms on the spherical nanostructures and self-assembly of DNA molecules with P-PA.

In addition, AFM imaging of dried peptide ODN complexes on the surfaces showed similar cylindrical and spherical morphologies of K-PA/ODN and P-PA/ODN complexes compared to aqueous environment at the same conditions (Figure 4.12). For control experiments, TEM images of K-PA and P-PA nanostructures at the same concentrations with PA/ODN complexes were taken and similar cylindrical and spherical morphologies were observed (Figure 4.13).

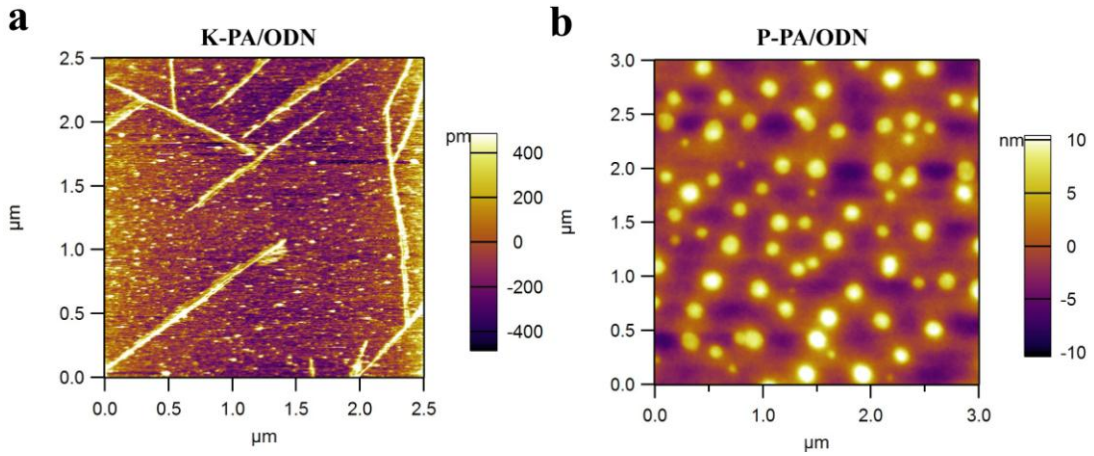

Figure 4.12. AFM images of self-assembled K-PA/ODN and P-PA/ODN nanostructures dried on mica and glass surfaces, respectively. (a) K-PA/ODN solution was dropped onto the cleaned mica surface and dried overnight; the imaging was performed on dry mica surface. (b) P-PA/ODN solution was dropped onto the glass surface and dried overnight; the imaging was performed on dry glass surface.

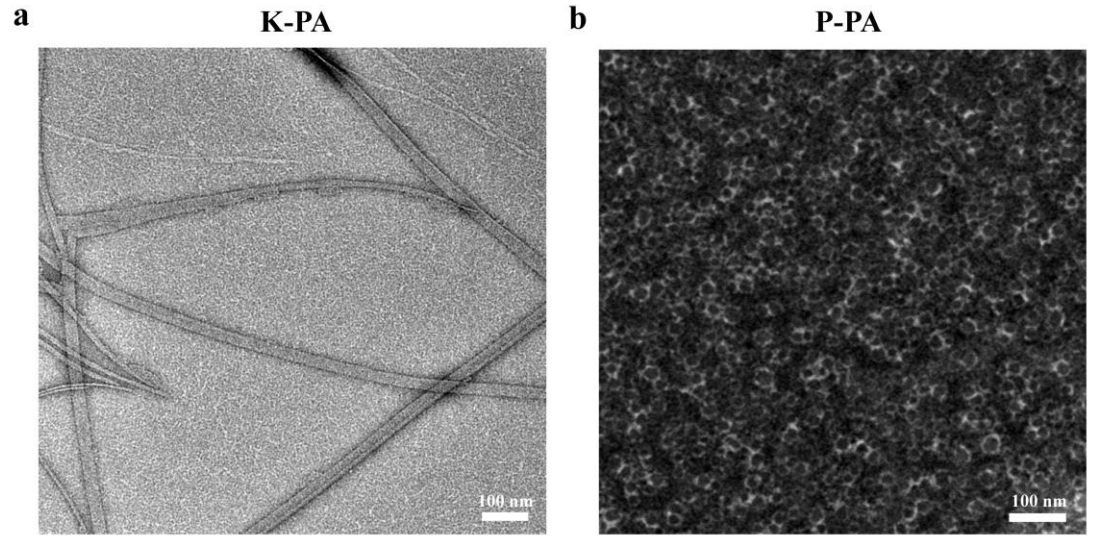

Figure 4.13. TEM and STEM images of self-assembled K-PA and P-PA nanostructures. (a) The K-PA fiber formation and peptide bundles can be seen in images. (b) The spherical morphology of the P-PA self-assembled nanostructures can be seen in images (scale bars: 100 nm).

To discern the effect of nanostructure from basal immune response to CpG motives, we prepared all groups with equal amounts of CpG ODNs (nanofiber, nanosphere and CpG ODN alone). The PA concentration was adjusted to make all ODNs in solution to bind to nanostructures. Since negatively charged ODN interacts with positively charged lysine residue on peptide molecules, the number of CpG ODNs bound to nanostructures is directly related with ODN to peptide ratio. To find critical ODN/peptide ratio, where all ODNs in solution are bound to nanostructures, we prepared formulations with varying ODN/PA ratios. All of the formulations were run on polyacrylamide gel electrophoresis (PAGE) in order to analyze the amount of ODNs, which were not bound to peptides. Molecules should have a net negative charge to be able to run in the PAGE experiment. Since the ODNs interacting with peptides would lose negative charge, they would not be able to run in polyacrylamide gel. Accordingly, any formulation not displaying an ODN band in gel suggested that all ODNs in that formulation would be bound to nanostructures. As a result of PAGE analysis, we found that 1:70 and 1:2500 ratios were critical for ODN/K-PA and ODN/P-PA complexes, respectively (Figure 4.14a, b).

Zeta potential measurements were also consistent with PAGE results and indicated that similar ratios of ODN/peptide are critical for binding of all ODNs to nanostructures (Fig. 4.15). ODN solution with no PA molecules revealed -33 mV zeta potential due to high negative charge of ODN molecule (Figure 4.15). As PA amount increased in ODN solution, zeta potential values increased, expectedly. For ODN/K-PA solution, we observed a positive potential (+6 mV) at 1:100 ratio, indicating total neutralization of ODN with PA. For ODN/P-PA, 1:2500 ratio was critical (+21 mV), similar to PAGE experiment (Figure 4.15). In summary, these two sets of data revealed the critical ODN/PA ratios to incorporate all ODNs in solution onto nanostructures. Interestingly, full neutralization of ODNs requires more of P-PA than K-PA. This might be due to concealment of positive charges on P-PA molecules during further aggregation of individual micelles mentioned above, which makes accessible charges of P-PA lower than K-PA.[142-143] Indeed, zeta potential of the P-PA was several folds lower than equimolar K-PA (Figure 4.16). Zeta potential for K-PA showed linear dependency from concentration, indicating that all of lysine molecules

are presented to aqueous media and accessible for zeta potential measurement. Although both carries single lysine amino acid to make them positively charged at pH 7, K-PA showed similar zeta potential to P-PA with 25 fold higher concentration (Figure 4.16). This suggests that at least some of the positive charges provided by lysine molecules in P-PA are buried in aggregates or nanospheres (Figure 4.13b) and concealed from zeta potential measurement and probably negatively charged molecules in aqueous media (Figure 4.15). Positive zeta potential observed for P-PA probably comes from lysine molecules on the surface of nanospheres.

Based on these findings, we prepared ODN/K-PA complexes with 1:100 ratio and ODN/P-PA complexes with 1:2500 ratio.

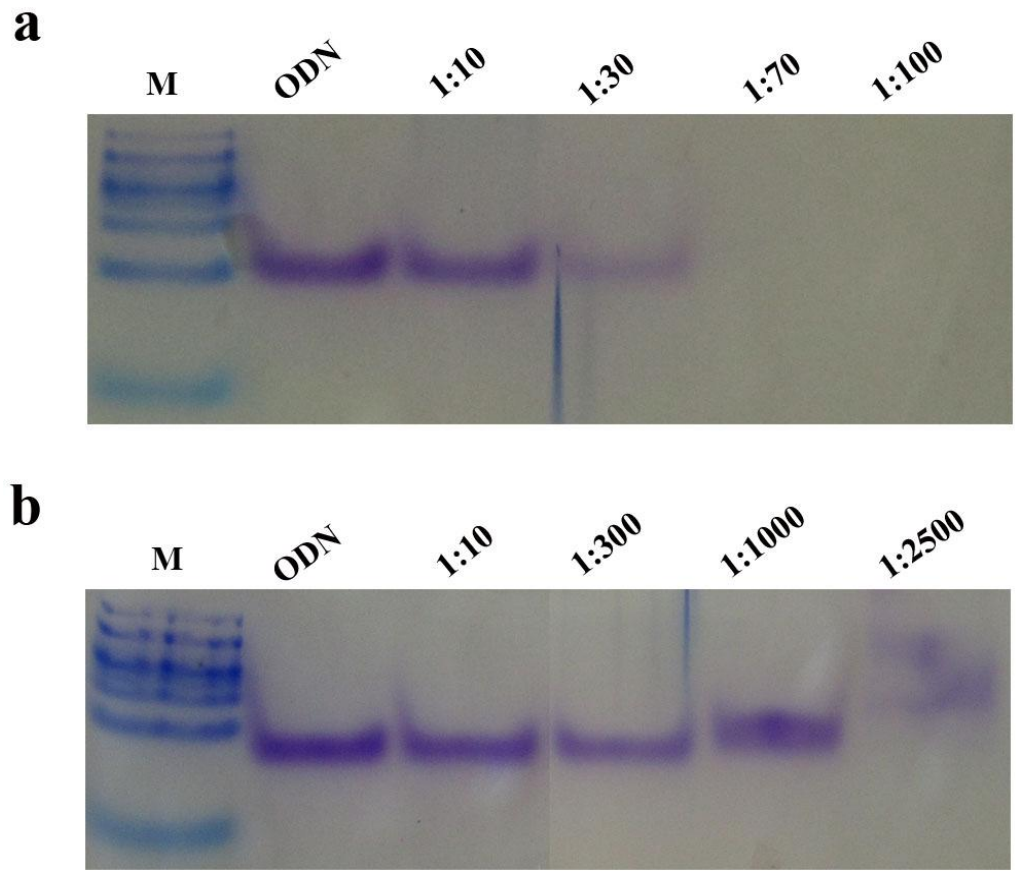

Figure 4.14. Determination of critical ODN/Peptide ratio by using polyacrylamide gel electrophoresis (PAGE). ODN/Peptide (a.K-PA, b.P-PA) formulations with varying ratios were prepared and subjected to PAGE. ODN band (verified by 20 bp marker band) dwindles away as PA amount in the mixture increases. ODN is not detectable after 1:70 ratio for K-PA, while 1:2500 ratio for P-PA, indicating binding of all ODNs in medium to PA nanostructures (ODN is ODN alone; M denotes marker, which is mixture of known ODN molecules from 10bp to 100bp).

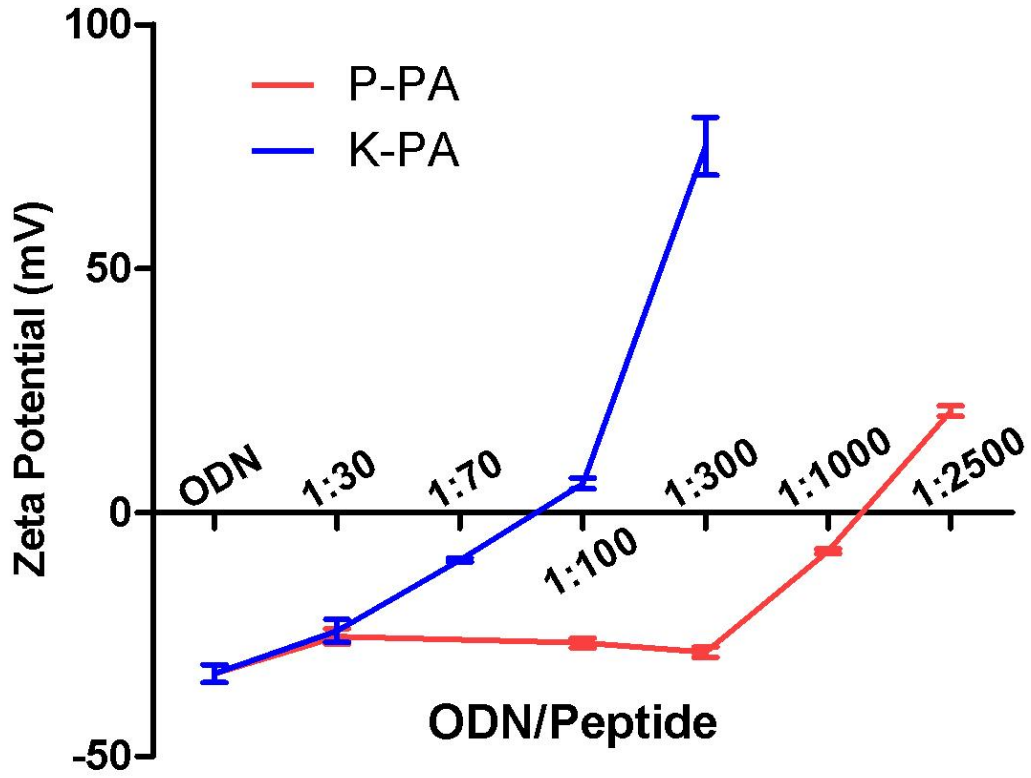

Figure 4.15. Zeta Potential measurements of PA/ODN complexes for determination of critical ODN/Peptide ratio. ODN/Peptide formulations with varying ratios were prepared and subjected to zeta potential measurement. Highly negatively charged ODN molecule shows negative zeta potential, which increases as concentration of PA molecule in the complex increases. Zeta potential of above zero was accepted as an indicator of total neutralization of ODN molecule, that also suggests binding of all ODNs in solution to PA nanostructures. For K-PA, zeta potential appeared above zero at 1:100 ODN/PA ratio, while for P-PA, this ratio was observed to be 1:2500. Sharp increase of zeta potential in K-PA samples at 1:300 also implies that K-PA molecules added to 1:100 sample didn`t bind to ODN molecules since all of them had already bound to PA nanostructures.

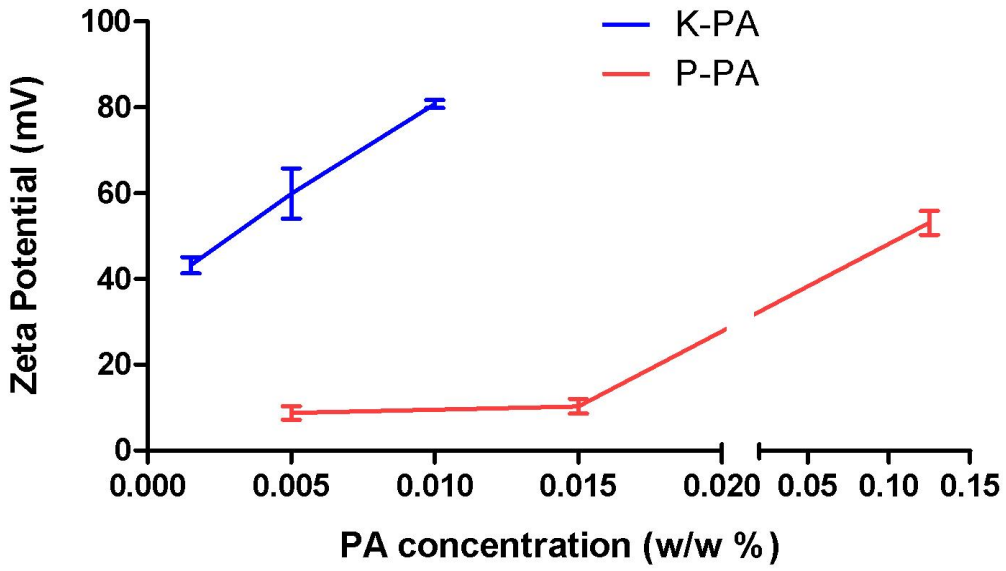

Figure 4.16. Zeta potential values of PA molecules at various concentrations. K-PA shows higher zeta potential values than P-PA at similar concentrations. Moreover, zeta potential of K-PA shows linear increase with its concentration, indicating total presentation of lysine of K-PA into aqueous media. While P-PA requires to be concentrated nearly 25 fold to show comparable zeta potential value to K-PA. This suggests that at least some of the lysine molecules in P-PA are concealed in aggreagates/nanospheres formed by P-PA.

4.3.2. Characterization of immune response to ODN nanostructure complexes

Cytokine production profiles of mouse spleen cells indicated that direction of immune response to CpG ODN was shifted by nanostructures. Spleen carries panoply of immune cells and can give insights into how interplay between immune cells would react to virus-like nanostructures. To delineate the reaction of spleen cells to virus-like shapes of the ODN delivery agents, we treated cultured splenocytes with various doses of ODN prepared as K-PA/ODN, P-PA/ODN and ODN alone (with same amount of CpG ODN between groups). To exclude any CpG-free effect, we also treated cells with similar experimental groups with control ODN instead of CpG ODN (with reverted CpG motif, see Methods section). Supernatants were collected after 48 h of culture and analyzed for cytokine (IFN-γ, IL-12 and IL-6) profiles with ELISA. These cytokines were chosen to reflect the immediate

proinflammatory response (IL-6) and Th1 response (IL-12 and IFN-γ), which fights against intracellular pathogens. IFNγ is also a critical mediator of anti-viral response and is extensively involved in anti-tumor response. Cytokine measurements showed that dose-dependent CpG-specific response saturates at higher concentrations and even become sub-optimal, as reported in literature (Figure 4.17, 4.18 and 4.19).[144]

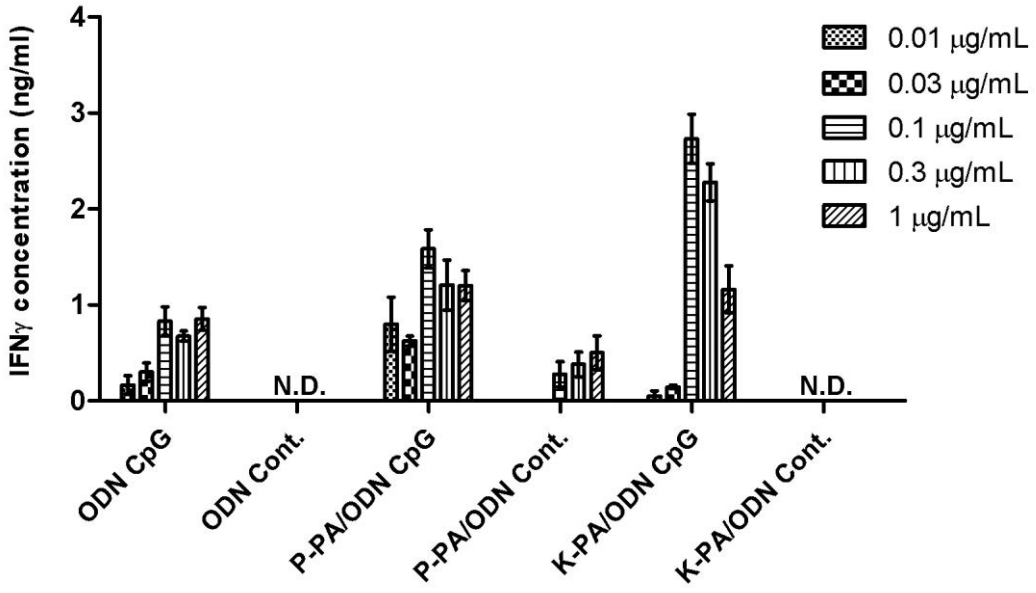

Figure 4.17. Effect of nanostructures on (CpG ODN) dose-dependent IFNγ cytokine production by splenocytes. After treating splenocytes with various doses of ODN alone or ODN bound to nanostructures, IFNγ secreted to culture media were detected with ELISA. ODN-dependent secretion of IFNγ saturates at 0.1 μg/ml of ODN and then becomes suboptimal. At optimal concentrations, ODN bound to nanostructures seem to be more potent than ODN alone, while nanofibers are more potent than nanospheres. IFNγ secretion is still CpG-specific when nanostructures are used as nanofibers and nanospheres with control ODN induced non-detectable and low amount of IFNγ, respectively (N.D is not detectable).

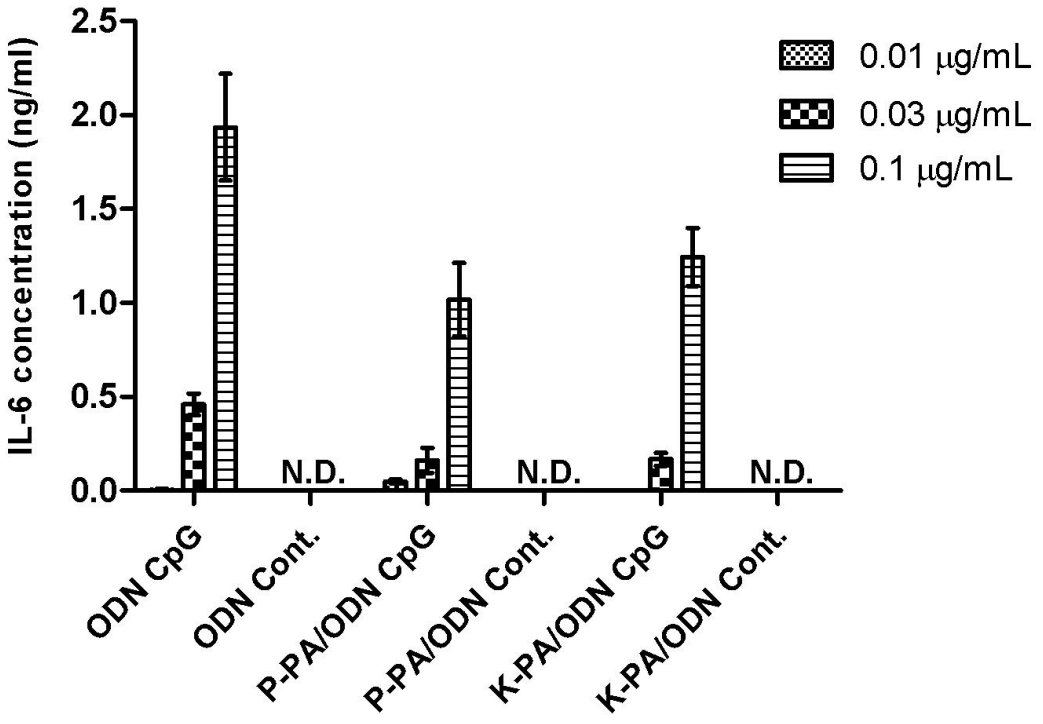

Figure 4.18. Effect of nanostructures on (CpG ODN) dose-dependent IL-6 cytokine production by splenocytes. After treating splenocytes with various doses of ODN alone or ODN bound to nanostructures, IL-6 cytokine secreted to culture media were detected with ELISA. Nanostructures impaired CpG ODN-induced IL-6 secretion at doses of 0.03 and 0.1 μg/ml, at which IL-6 is detectable in culture media. IL-6 secretion is still CpG-specific when nanostructures are used as nanofibers and nanospheres with control ODN induced non detectable (N.D.) amount of IL-6 secretion (N.D is not detectable).

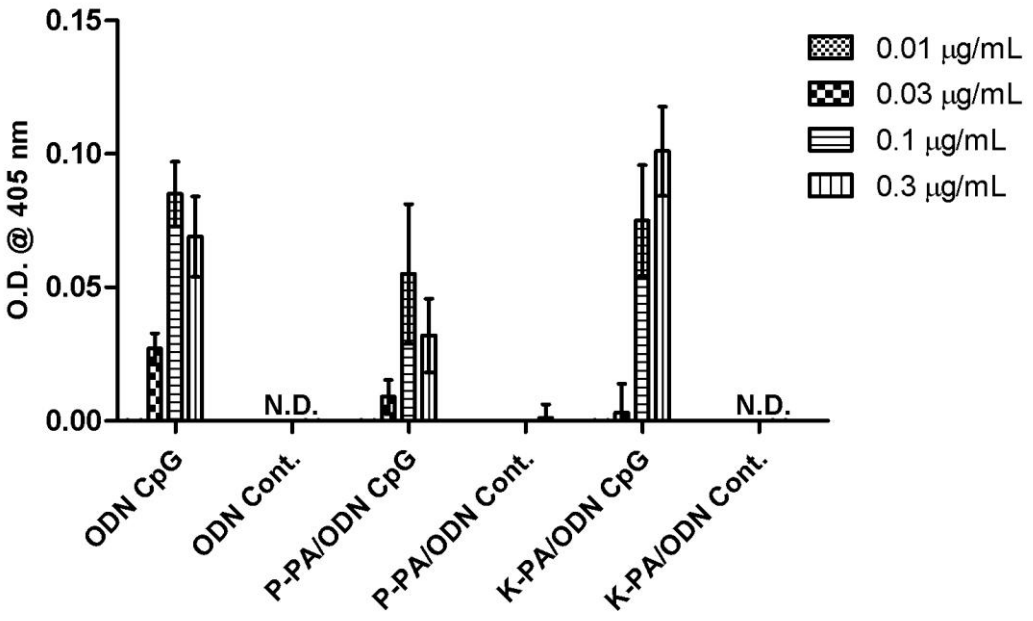

Figure 4.19. Effect of nanostructures on (CpG ODN) dose-dependent IL-12 cytokine production by splenocytes. After treating splenocytes with various doses of ODN alone or ODN bound to nanostructures, IL-12 secreted to culture media were detected with ELISA. ODN-dependent secretion of IL-12 saturates at 0.1 μg/ml of ODN and then becomes suboptimal for ODN and P-PA/ODN. At 0.1 μg/ml, IL-12 secretion was similar between ODN bound to nanostructures and ODN alone, while nanostructures seem slightly less potent. IL-12 secretion is still CpG-specific when nanostructures are used as nanofibers and nanospheres with control ODN induced non-detectable or low amount of IL-12, respectively (N.D is not detectable).

0.1 μg/ml of CpG ODN was optimal concentration for each formulation regarding induction of cytokine production. Cytokine production by different formulations at this concentration are shown at Fig. 5. Interestingly, nanostructures shifted cytokine response to CpG from a high IL-6 and low IFN-γ profile to a low IL-6 and high IFN-γ (Figure 4.17, 4.18 and 4.20). This shift in immune response was even more pronounced for nanofibers when compared to nanospheres. NF-ODN induced IFN-γ response 3-4 times higher than CpG ODN alone and nearly two times higher than NS-ODN (Figure 4.17, 4.20a). However, IL-6 production was diminished nearly two-folds in response to both K-PA/ODN and P-PA/ODN when compared to CpG ODN alone (Figure 4.20b). IL-12 induction with K-PA/ODN or P-PA/ODN was not significantly different from ODN alone, indicating that higher IFN-γ induction with

K-PA/ODN and P-PA/ODN was not IL-12 dependent (Figure 4.19). High IFN-γ production from PBMCs (peripheral blood mononuclear cells) by CpG ODNs with nanoparticulate structure (A-type ODN) were shown to be IFN-α dependent.[145] ODNs lacking CpG motives were not effective generally, even when supplied on nanostructures, which indicates that altered immune response with nanostructures was still CpG-dependent (Figure 4.17-4.20). At lower concentrations than 0.1 μg/ml, P-PA/ODN preserved its potency of IFN-γ production better than K-PA/ODN and ODN alone (Figure 4.17). Possibly at very low concentrations, K-PA/ODN complexes do not form full-fledged nanofibers, causing a sharp drop in activity.

Linear ODNs (such as ODN1826 used in this study), which do not form any higher order structures, are known for their ability to induce production of high amounts of IL-6, but low amounts of IFN-α from immune cells.[144] On the other hand, nanoparticle-forming A-ODNs, with polyG sequences at both end, or linear ODNs bound to nanoparticles were shown to induce several folds higher IFN-α /IFN-γ and lower IL-6 production than linear B-ODNs, with no polyG sequence.[124-125, 144] This change in immune profile was explained by retention of nanoparticulate ODNs in early endosomes of plasmacytoid dendritic cells much longer than linear ODNs and inducing a different signaling pathway - MyD88–IRF-7.[129]

While B-ODNs rapidly localize to lysosomes and induce MyD88– NF-κB pathway. Our spherical particles with CpG ODN resemble morphologically to nanoparticles used in these studies (both can be called as zero-dimensional) and similarly induced higher IFNγ and lower IL-6 response than CpG ODN. Remarkably, our findings reveal that one-dimensional nanofibers synergize with CpG ODN better than nanospheres in terms of IFNγ production, which indicates that immune response is driven further to Th1 direction. To the best of our knowledge, this is the first report showing thetunable nature of immune response to pathogenic DNA motives by changing shape of carrier nanostructures. Difference between immune profiles of ODN alone, K-PA/ODN and P-PA/ODN might also be caused by different retention time in early endosomes and differential induction of sıgnallng pathways like MyD88–IRF7.

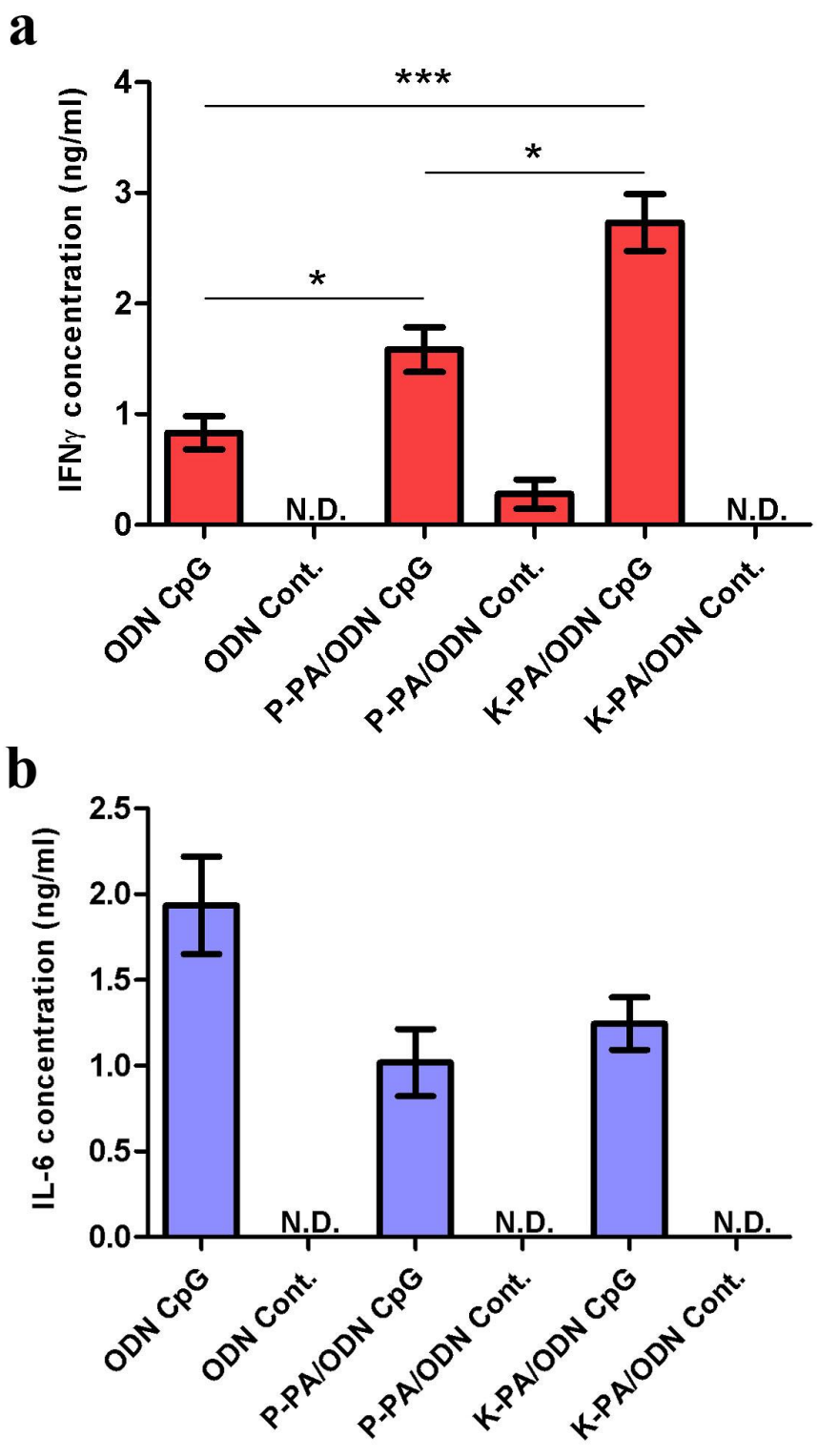

Figure 4.20. Nanostructures shift CpG-induced cytokine secretion profile of splenocytes. Mouse splenocytes were treated with indicated formulations and cytokine concentrations in culture media were detected with ELISA (a.IFNγ, b.IL-6). ODN concentration in all groups is 0.1 μg/mL. Statistical significance between groups was measured by Student's t-test. N.D. means "not detected".

Upregulation of co-stimulatory molecules on the surfaces of immune cells is another mechanism of immune activation induced by infection signals such as CpG DNA. To understand effect of nanostructures to this process, we cultured splenocytes with ODN, K-PA/ODN and P-PA/ODN similar to cytokine assay and checked expression of cell surface markers CD86 (also known as B7.2) and CD40 by flow cytometry. These molecules are expressed by antigen presenting cells (APC) upon sensing infection and important in development of adaptive immune response to foreign antigen. Interaction of CD86 molecule with CD28 on T-cell surfaces is required for recognition of antigen as foreign and activation of T-cells during antigen presentation to T-cell receptors. CD40 binding to target cells induces B-cells and number of CD86 expressing cells in splenocytes is further upregulated by NF-ODN from 17% with ODN alone to 22%, while effect is strictly CpG signal specific that nanofibers with control ODNs were similar to non-treated sample (~1%, Figure 4.21a). The P-PA/ODN treatment induced CD86 expression in 19% of cells, which did not have a statistically significant difference from ODN alone (Figure 4.21a). On the other hand, CD40 expression profiles were different. While, all CpG-containing formulations induced CD40 expression (30-40%) in splenocyte population better than the control ODN (~10%), P-PA/ODN showed the highest signal in this context (48%) (Figure 4.21b). In addition, ODN induced more cells (44%) to express CD40 than K-PA/ODN (37%). Overall, nanostructures seem to synergize with ODN in the induction of expression of co-stimulatory molecules. The shapes of the nanostructures made a difference: the nanofibers induce more CD86 expression than nanospheres, which induce CD40 expression better than nanofibers.

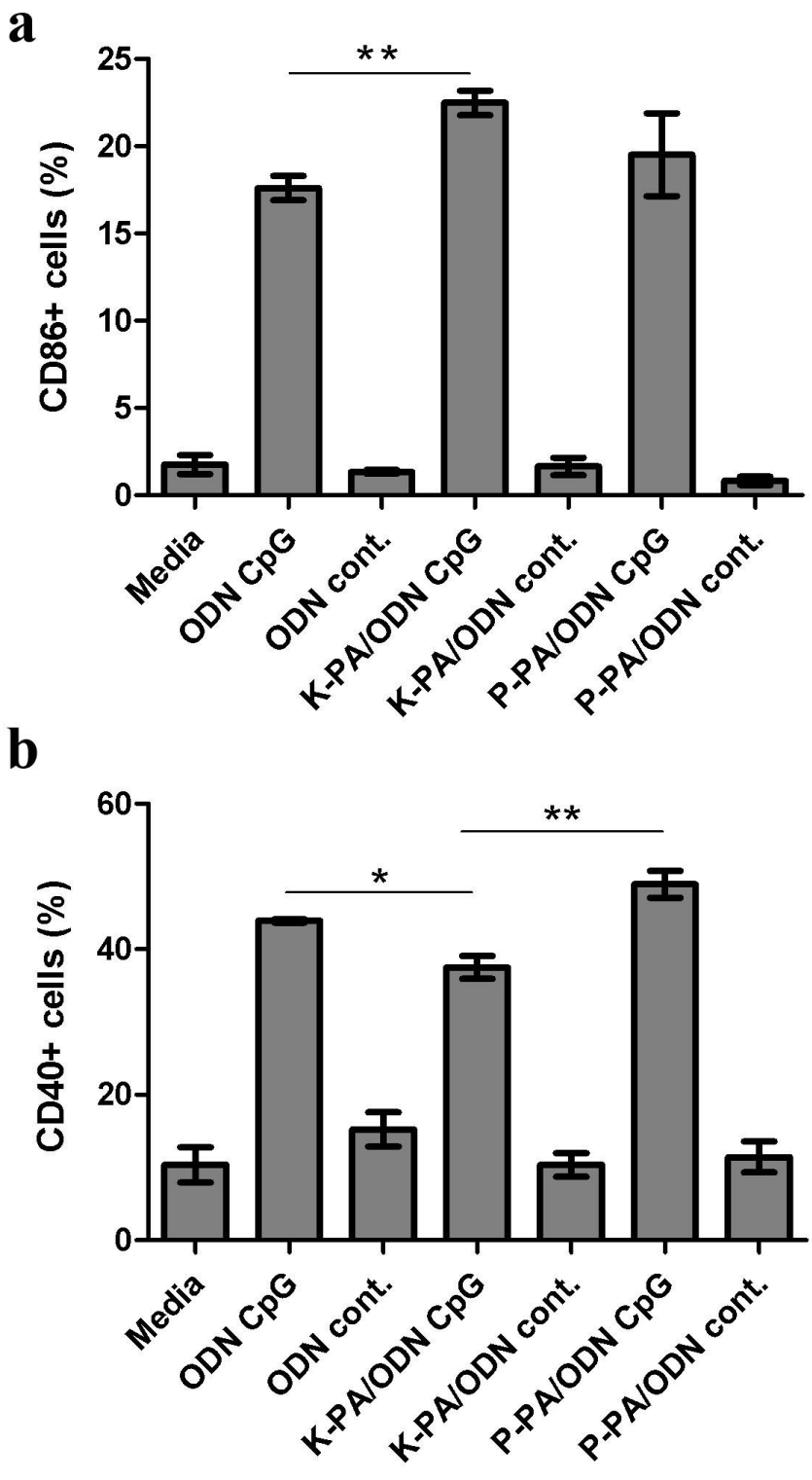

Figure 4.21. Effect of nanostructures on CpG-induced surface expression of co-stimulatory molecules. Mouse splenocytes were treated with indicated formulations for 24 h and percentage of cells expressing CD86 (a) or CD40 (b) in total population were detected by flow cytometry. Statistical significance between groups was analyzed by Student's t-test.

Besides inducing alterations in the cytokine profile of splenocytes, nanostructures also stimulated morphological changes in cellular behavior. Depending on the magnitude of CpG signal, cells formed granular structures through aggregation among a number of individual cells (Figure 4.22). Increase in the CpG ODN concentration caused increase in number and size of granules (Figure 4.16a-c, e-g, i-k). Remarkably, we couldn't find any report regarding this observation in the literature. Even more interesting observation was the correlation between formation of granules and induction of IFNγ from splenocytes. Splenocytes treated with K-PA/ODN complex induced a higher number and size of granules than P-PA/ODN and ODN alone (Figure 4.22a-c). Granulation was strictly dependent on CpG signal, since non-treated groups (Figure 4.22l) and nanostructures obtained with control ODN didn't induce this type of structures (Figure 4.22d, h). This indicates that formation of granules is not due to the toxic effect of nanostructures or ODNs, but due to the existence of infection signal in the environment. These cellular aggregations resemble granuloma – a clinical pathological pattern observed during diseases such as tuberculosis. In these cases, immune system walls off foreign signal, which cannot be destroyed by normal activities of immune cells. Macrophages fuse and aggregate together in the center of these granulomas surrounded by lymphocytes. *In vivo* IFNγ depletion by monoclonal antibodies was found to suppress both number and size of granulomas in mice.[146] Thus, high IFNγ production by K-PA/ODN nanostructures might be acting as a perpetuating infection signal on splenocytes, which coalesce to form granules with a higher number and size.

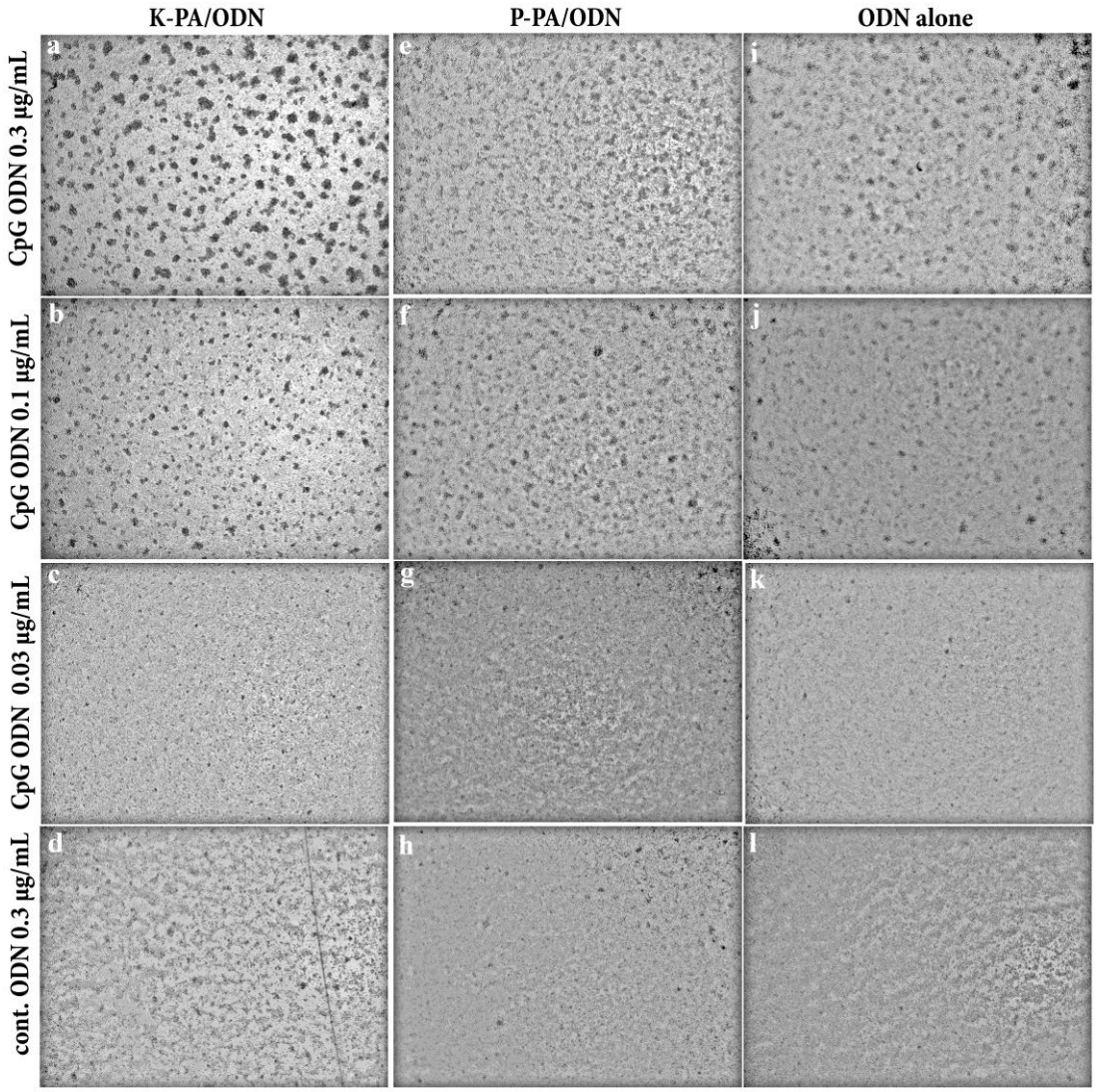

Figure 4.22. Morphological changes in splenocytes upon stimulation with K-PA/ODN (a-0.3 µg/mL, b-0.1 µg/mL, c-0.03 µg/mL), K-PA/cont.ODN (d-0.3 µg/mL), P-PA/ODN (e-0.3 µg/mL, f-0.1 µg/mL, g-0.03 µg/mL), P-PA/cont.ODN (h-0.3 µg/mL), ODN alone (i-0.3 µg/mL, j-0.1 µg/mL, k-0.03 µg/mL), media alone (l).

4.3.3. Uptake of nanostructure ODN complexes into immune cells

Recent studies have shown that the shape of the particle significantly modifies its cellular uptake. High-aspect-ratio PEG particles were internalized into HeLa cells 4 times faster than low-aspect-ratio particles and were rapidly translocated into nuclear membrane.[147] In another work, shape of the surface of particle at the point of initial contact with macrophages was shown to determine whether it will be phagocytosed

or not.[148] Polystyrene particles with oblate ellipsoid shape displayed higher internalization and phagocytosis into macrophages than prolate ellipsoid and spherical particles,[149] while prolate ellipsoid particles were better in cellular binding. Barua *et al.* showed that polystyrene nanorods coated with antibodies specific to cellular receptors exhibit higher cellular (HER2-expressing breast cancer cell line) binding, uptake and bioactivity than polystyrene nanospheres.[150] However, regarding non-specific uptake (no specific antibody on nanostucture to bind to cellular receptors), rods were inferior than spheres. This might be due to the fact that rods have larger contact area with cellular surface, which cause higher adhesion to surface through receptor-ligand interactions.[150] Considering these studies, we hypothesized that differential responsiveness of immune cells to K-PA/ODN, P-PA/ODN and naked ODN might be caused by differential uptake into immune cells.

To analyze uptake of K-PA/ODN, P-PA/ODN and ODN into different immune cells, we prepared these complexes by using FITC-conjugated CpG ODNs. Mouse splenocytes were cultured with FITC-ODN alone or FITC-ODN bound to nanostructures for two different durations (2 and 12 h) prior to staining cells with labeled antibodies against B220 and CD11c or F4/80 - surface markers of various types of TLR9+ positive cells in mice. Internalization of ODN-FITC into cells was measured by flow cytometer. In all types of cells investigated, uptake of ODN alone or bound to nanostructures increased as a function of time, except K-PA/ODN uptake into dendritic (CD11c+) and plasmacytoid dendritic (CD11c+B220+) cells (Figure 4.23). These results indicate that 2 h is not sufficient for maximal uptake of CpG ODNs into relevant immune cells. However, nanofiber-bound ODNs achieved maximal uptake into dendritic cells (DC) and plasmacytoid dendritic cells (pDC) at 2 h (Figure 4.23a, b). At both 2 h and 12 h, K-PA/ODN positive cells in DC and pDC populations were about 65% and 85-90%, respectively. ODN alone or bound to nanospheres achieved this level of uptake at 12 h. At 2 h, ODNs were internalized by 44% and 50% of DCs and pDCs, while P-PA/ODN was internalized by 34% and 42% of DCs and pDCs, respectively. Previously, removal of CpG ODNs from cellular culture media before 8 h of culture was reported to reduce its immune activating potential[151], which suggests that time is a determinant factor for entry of

CpG ODNs into TLR9-positive endosomes. Nanofibrous structure accelerated uptake of CpG ODNs into DCs. This result also correlates well with higher potential of K-PA/ODN than ODN and P-PA/ODN to induce IFNγ secretion from splenocytes and upregulate maturation marker – CD86.

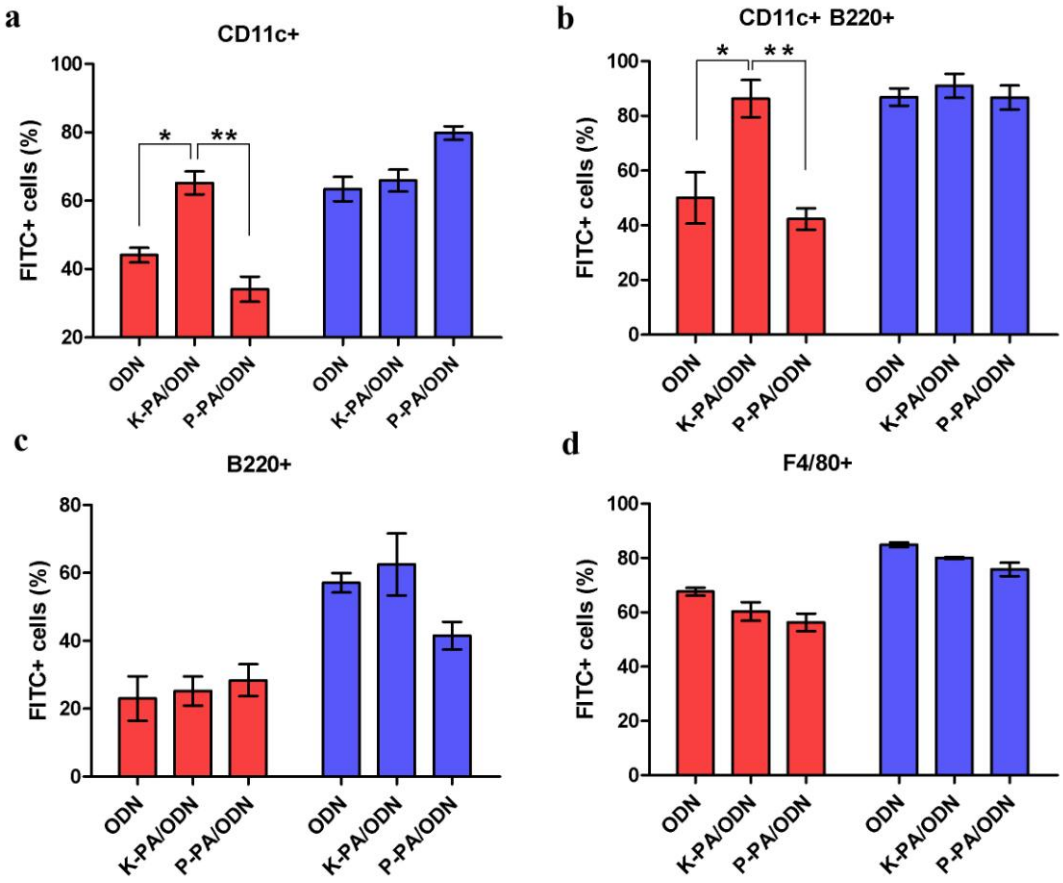

Figure 4.23. Uptake profile of FITC-ODN alone or bound with nanostructures into TLR9-expressing cell subsets in splenocytes. Percentage of FITC (ODN)+ cells in CD11c+ (dendritic cells), CD11c+B220+ (plasmacytoid dendritic cells), B220+ (B cells) and F4/80+ (macrophages) populations. Red and blue bars indicate 2 h and 12 h culture with ODN formulations, respectively. *$p<0.05$, **$p<0.01$ according to Student's t-test.

Increased uptake of K-PA/ODN to pDCs might be an explanation for their capability to induce IFNγ. As mentioned above, IFNγ production can be induced by IFNα released from pDCs upon stimulation with nanoparticulate CpG ODNs.[145] Higher

uptake of nanospherical ODN complex at 12 h than ODN also might contribute to its potential of inducing IFNγ better than ODN. Previously, scavenger receptor CXCL16 on plasmacytoid dendritic cells was charged with binding to nanoparticle forming D-ODN (analogue of A-ODN, with polyG sequences at ends) and facilitating its cellular uptake and modifying resulting immune response, such as IFNα response.[152] Similar receptors might be functioning for recognition of nanofiber structure and its preferential uptake into DCs and pDCs.

All groups were internalized similarly to B-cells (B220+) and macrophages (F4/80+). Uptake of ODN and K-PA/ODN (57% and 63%, respectively) to B-cells were higher at 12 h than P-PA/ODN (42%), while only difference between ODN and P-PA/ODN was statistically significant (Figure 4.23c). This might contribute to higher IL-6 induction by ODN alone, since CpG ODN is known induce B-cells to secrete IL-6 (Figure 4.23d). Overall, these results strongly suggest that K-PA/ODN system was better internalized by DCs and their subset – pDCs than their counterparts. These cells are critical to contain viral/intracellular bacterial infections and present processed antigens to T cells. Thus, better uptake of nanofibrous ODNs to these cells might be related to its unexpectedly high Th1-biased immune activating potential.

4.3.4. Characterization of protection provided by nanostructures to ODN against enzymatic degradation

K-PA/ODN and P-PA/ODN induced Th-1-biased immune stimulation better than ODN-alone at *in vitro* experiments, which make them promising candidates for *in vivo* applications. However, enzymatic degradation and short half-life is an important problem with CpG ODNs` *in vivo* application. To understand whether nanostructures provide any protection from enzymatic degradation, we performed DNAse assay. ODN, NF-ODN and NS-ODN were treated with DNAse I for different time periods. SDS detergent was used to remove ODNs bound to nanostructures for further investigation. All samples were run on polyacrylamide gel for visualizing remaining

ODNs after DNAse treatment. As it is shown in Figure 4.24a, ODN-alone was rapidly chopped off resulting in no visible bands in gel after 30 min of DNAse treatment. Calculation of band intensities also revealed that ODN was almost completely degraded after 24 h of treatment – 6% remained according to average of three samples (Figure 4.25). However, ODNs detached from K-PA/ODN or P-PA/ODN complexes were clearly observable even after 24 h of DNAse treatment (Figure 4.24b, c). The P-PA/ODN system protected ODN better than K-PA/ODN: 56% of ODNs remained after 24 h with P-PA/ODN, while 39% of ODNs remained with K-PA/ODN (Figure 4.25). These results indicate that nanostructures protect ODN from degradation, while nanospheres were more potent than nanofibers. Nanostructure binding possibly makes ODNs less accessible to enzymes, which might be serving as a mechanism for protection.

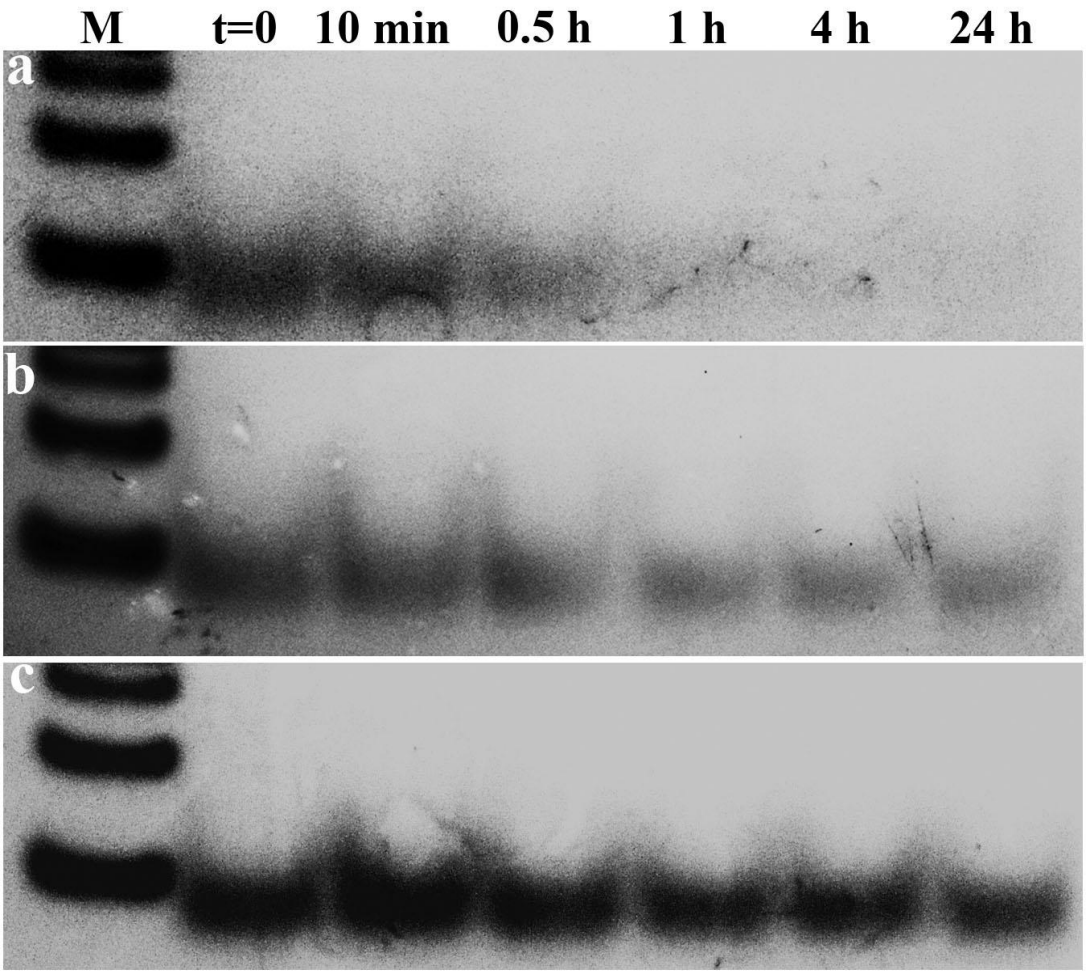

Figure 4.24. Resistance of ODNs to DNAse were investigated with polyacrylamide gel electrophoresis (PAGE). ODN alone (a), K-PA/ODN (b) and P-PA/ODN (c), which had been treated with DNAse I for different time periods, were subjected to PAGE. Lane 1 is Marker, Lane 2 is non-treated ODN, Lane3-Lane7= 10 min, 30 min, 1 h, 4 h, 24 h treatment with DNAse. d. Time-dependent degradation of ODN in different formulations, plotted according to calculated band intensities.

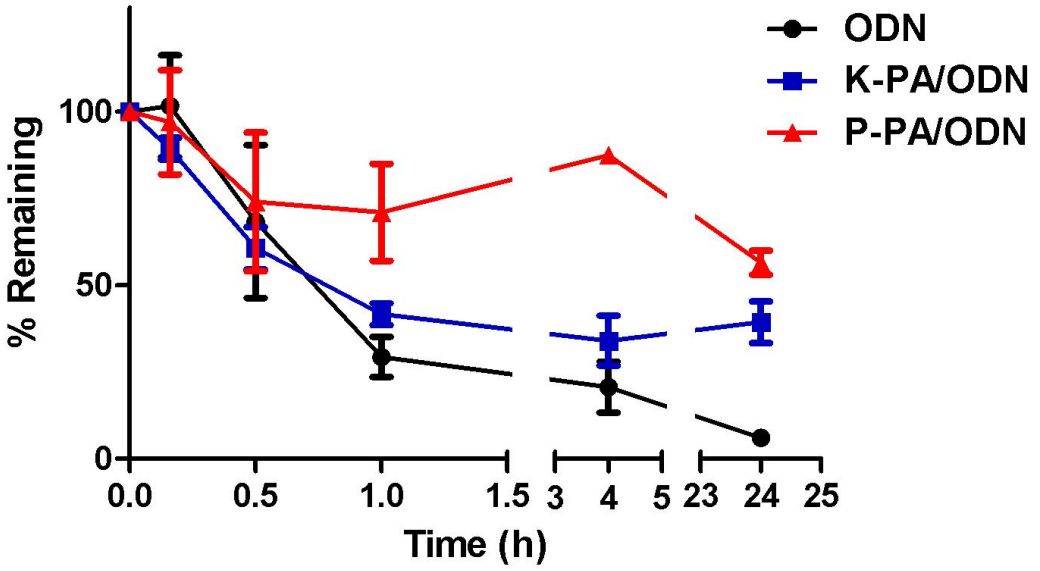

Figure 4.25. Time-dependent degradation of ODN in different formulations, plotted according to calculated band intensities. ODN alone is almost completely degraded by DNAse I at the end of 24h, while ODN bound to nanostructures retain considerable amount of ODN intact.

4.4. Experimental details

4.4.1. Materials

9-Fluorenylmethoxycarbonyl (Fmoc) and tert-butoxycarbonyl (Boc) protected amino acids, [4-[α-(20,40-dimethoxyphenyl) Fmoc-aminomethyl] phenoxy] acetamidonorleucyl-MBHA resin (Rink amide MBHA resin), and 2-(1Hbenzotriazol-1-yl)-1,1,3,3-tetramethyluronium hexafluorophosphate (HBTU) were purchased from NovaBiochem and ABCR. The other chemicals for peptide synthesis were purchased from Fisher, Merck, AlfaAesar, or Aldrich. All chemicals were used as provided. CpG and control ODNs were purchased from Invivogen. Paired antibodies and recombinant proteins of IFNγ and IL-12 were obtained from R&D systems, that of IL-6 from eBioscience. All cell culture and ELISA reagents were purchased from Invitrogen, except non-essential amino acid solution (Sigma Aldrich). Reagents for polyacrylamide gel electrophoresis were obtained from Sigma

Aldrich. Labeled antibodies were obtained from BD Pharmingen (B220 and CD11c) and eBioscience (F4/80, CD40, CD86).

4.4.2. Peptide synthesis

Lauryl-VVAGK-Am (K-PA) and Lauryl-PPPGK-Am (P-PA) were constructed on Rink Amide MBHA resin. Amino acid couplings were performed with 2 equivalents (equiv) of Fmoc-protected amino acid, 1.95 equiv of HBTU, and 3 equivalents of N,N-diisopropylethylamine (DIEA) for 2 h. To remove the Fmoc group, 20% (v/v) piperidine/dimethylformamide solution (DMF) was added and incubated for 20 min. To block the remaining free amine groups after amino acid coupling, 10% (v/v) acetic anhydride solution in DMF was used (30 min). After each step, the resin was washed by using DMF, dichloromethane (DCM), and DMF. Trifluoroacetic acid (TFA)/triisopropyl silane (TIS)/H_2O/DCM mixture (5:2.5:2.5:90 ratio) was used to cleave the peptide from the resins.

4.4.3. Preparation of virus-like nanostructures

Virus-like nanostructures were prepared by using self-assembly of peptide molecules upon mixing with oligonucleotides. To form one-dimensional nanofibrous and zero-dimensional nanosphere structures, positively charged K-PA and P-PA (Figure 4.3) molecules were mixed with CpG (ODN1826) or control ODNs, respectively. Two CpG motives in ODN1826 were reverted in control sequence: ODN1826: 5'-tccatga**cg**ttcctga**cg**tt-3'; ODN1826 control: 5'- tccatga**gc**ttcctga**gc**tt -3'. Exact molar ratio for making all ODNs in solution to interact with nanostructures was determined to be 100:1 for K-PA/ODN and 2500:1 for P-PA/ODN (Figure 4.14, 4.15). Nanostructures were prepared with these ratios for all experiments and named as nanofibrous ODN (K-PA/ODN) and nanospherical ODN (P-PA/ODN). In all experiments at least 3 independent nanofiber and nanosphere ODN formulations were prepared and tested.

4.4.4. Small Angle X-Ray Scattering (SAXS) analysis of self-assembled nanostructures

The PA/ODN complexes for SAXS analysis was prepared as; ODN1826 solution (15 μg/mL) was mixed with same volume of 0.375% (w/v) P-PA solution (2500:1 ratio) or 0.015 % (w/v) K-PA solution (100:1 ratio). The final ODN concentration in each PA/ODN complexes was equal. For control experiments, 0.008% (w/v) K-PA and 0.188% (w/v) P-PA solutions were prepared. Each PA/ODN, K-PA and P-PA solutions were loaded into a quartz capillary cell for SAXS measurement. The SAXS measurements were performed with a Kratky compact HECUS (Hecus X-ray systems, Graz, Austria) system equipped with a linear collimation system and X-ray tube Cu target (λ=1.54 Å). The generator was operated at a power of 2 kW (50 kV and 40 mA). Simultaneous measurements of SAXS and WAXS range are possible in the system with a linear-position sensitive detector used with 1024 channel resolution. Distance between channels and the sample-detector are 54 μm and 31.5 cm respectively. Scattering curves were monitored in q ranges of 0.004-0.55 $Å^{-1}$ for SAXS and 1.03-2.15 $Å^{-1}$ for WAXS. All PA/ODN complexes, K-PA and P-PA solutions were measured for 900 s at room temperature (23 °C).

4.4.5. Transmission Electron Microscopy (TEM) imaging

Nanostructures were imaged by TEM. 30 μL of PA/ODN complexes was prepared on parafilm sample by mixing 15 μL of 15 μg/mL ODN1826 with either 15 μL of 0.375% (w/v) P-PA (2500:1 ratio) or 15 μL 0.015% (w/v) K-PA (100:1 ratio). For PA only samples, same concentrations of PAs were mixed with ddH_2O instead of ODN. TEM grids were reverted onto these solutions. Grids were removed after 5 min and remaining solution on grid was absorbed by a lint-free paper. Staining was performed with 2% (w/v) uranyl acetate solution (Ted Pella, Inc) for 1 min. Grids were then immersed into ddH_2O once and dried overnight at room temperature. TEM

imaging was performed next day by a FEI, Tecnai G2 F30 instrument. All images were taken in STEM mode with a high angle annular dark field (HAADF) detector.

4.4.6. Atomic Force Microscopy (AFM) imaging

The PA/ODN complexes for AFM imaging were prepared in liquid or dried conditions. ODN1826 solution at 15 μg/mL concentrations was mixed with same volume of 0.375% (w/v) P-PA solution (2500:1 ratio) or 0.015% (w/v) K-PA solution (100:1 ratio). The final ODN concentration in each PA/ODN complexes was equal. For K-PA/ODN complexes, the prepared solution was diluted 50 times and dropped onto the cleaned mica surface and imaged directly in liquid environment or dried overnight, then imaged on the mica surface. SiN soft contact tip was used for contact mode imaging of K-PA/ODN complexes. For P-PA/ODN complexes, the solution was diluted 100 times and dropped onto the cleaned glass surface and imaged directly in liquid environment or dried overnight, then imaged on the glass surface. Si tip (150 kHz, 5 N/m) was used for soft-tapping mode imaging of P-PA/ODN complexes. The dilutions of PA/ODN complexes were necessary because initial concentrations were high for high quality AFM imaging in liquid environment. During the imaging, MFP3D Asylum microscope was used.

4.4.7. Circular Dichroism Spectroscopy

Circular dichroism (CD) spectroscopy was performed with a JASCO J815 CD spectrometer at room temperature. 0.2 mM solutions of both K-PA and P-PA and their mixtures with ODN1826 (100:1 and 2500:1, respectively) were measured from 300 to 190 nm. Data pitch was 1 nm, scanning speed was 100 nm/min, and all measurements were performed with three accumulations. DIT was selected as 4 s, bandwidth as 1 nm, and the sensitivity was standard. Molar ellipticity was calculated using the equation: $[\theta] = 100 \times \theta/(C \times l)$, where C is the molar concentration, and l is

the cell path length in centimeters. $[\theta] = \theta/(C \times l) = deg/(mol/1000\ cm^3) \times 0.1\ cm = 100\ deg\ cm^2\ dmol^{-1}$.

4.4.8. Polyacrylamide Gel Electrophoresis (PAGE)

To identify critical ODN/PA ratio required to conjugate all ODNs in solution to nanostructure, PAGE was performed. 20 μg/mL ODN1826 solution (15 μL) was mixed with varying concentrations of PA solutions (15 μL) to prepare different ODN/PA ratios (from 1:10 to 1:2500). These solutions were mixed with Orange DNA loading dye (Fermentas) and loaded into 20% polyacrylamide gels. 10 μL of 10 bp DNA ladder (O`range ruler^{TM}, Fermentas) was used as marker. Gels were run at 75 V for 1 h and subsequently at 50 V for 2.5 h (in 1x TAE). Stains-all dye working solution (0.005%, w/v) was prepared freshly from stock solution (0.1% w/v) as suggested by manufacturer (Sigma Aldrich). Gels were incubated in Stains-all overnight (dark conditions and room temperature). Next day, destaining of gels was performed under sunlight and images were taken by a Nikon camera.

4.4.9. Zeta Potential

Zeta potential measurements were performed to find critical ratio of ODN/PA, where all ODNs in solution were neutralized (and bound) with PAs. 400 μL of 5 μg/mL ODN1826 solution was mixed with varying concentrations of PA solutions (400 μL) to prepare different ODN/PA ratios (from 1:10 to 1:2500). Zeta potentials of these solutions were measured with Nano-ZS Zetasizer (Malvern). Measured mobility was converted to zeta potential by using Smoluchowski equation. The measurements were performed in triplicate – by using 3 independently generated formulations.

4.4.10. Animals

All experimental procedures have been approved by the Animal Ethics Committee of Ankara Diskapi Yildirim Beyazit Training and Research Hospital (Protocol # 2013/25). Primary spleen cells were obtained from adult BALB/c (8-12 weeks old) mice, which were maintained under controlled conditions and fed *ad libitum*.

4.4.11. Splenocyte culture and stimulation experiment

Spleens were removed aseptically and grinded between petri plate surface and plunger end of syringe in culture media (2% FBS in RPMI-1640) in order to dissociate single cells from bulk tissue. Single cell suspension was collected carefully to exclude tissue debris. Cell suspension was centrifuged at 800 g for 10 min. Supernatant was discarded and cell pellet was resuspended in culture medium (this step was performed twice). Cells were adjusted to 2 x 10^6 cells/mL cell density and cultured in 96-well plates as 200 µL/well (4 x 10^5 cells/well). Culture media was composed of RPMI-1640 with 5% FBS (Pen/Strep, L-Glu, non-essential amino acids and HEPES (20 mM) were also added). Cell stimulation was performed immediately after distributing cells to wells. K-PA/ODN (nanofiber-ODN) and P-PA/ODN (nanosphere-ODN) were prepared as described above by different doses of ODN1826 or control ODN. Nanostructure and ODN alone solutions were further diluted with media and final concentration of ODN in cell suspension was from 1 µg/mL to 0.01 µg/mL. For cytokine analysis, cells were cultured at 37 °C and 5% CO_2 for 48 h and supernatants were collected at the end of the experiment. For analysis of surface markers (co-stimulatory molecules), cells were treated with same formulations (ODN dose - 0.3 µg/ml) for 24 h. Cells were collected at the end of experiment for further staining and for analysis by flow cytometry. Also, morphological changes were followed by using a light microscope. Experiments were performed in triplicate. Also, representative result of 3 independent experiments is shown.

4.4.12. ELISA

Cytokine concentration in supernatants collected from cultures at the end of splenocyte stimulation experiment was measured by ELISA. MaxiSorp^{TM} plates (Thermo Scientific, NUNC) were coated with IL-6, IL-12 or IFN-γ primary antibodies (overnight incubation at 4 °C). Next day, plates were blocked with 0.5% BSA (2 h), incubated with supernatants of cell culture experiment or standard recombinant proteins (2 h), biotin-labeled secondary antibody (2 h) and HRP (horse radish peroxidase)-conjugated streptavidin (1 h) consecutively at room temperature. Plates were washed 5 times with (in first two steps, washing was performed once for each step) washing buffer and dried by tapping between each consecutive steps. TMB (3, 3', 5, 5'-Tetramethylbenzidine) substrate was added at the last step and reaction was stopped after 15-20 min by 1.8 N H_2SO_4. Color formation was measured by microplate reader (Spectramax M5, Molecular Devices) as absorbance at 450 nm wavelength. This value was subtracted from reference value (650 nm). All treatments were performed with at least three replicates and shown as mean +/- standard deviation.

4.4.13. Internalization of ODNs into immune cells

Internalization of ODNs into various immune cells expressing TLR9 in total splenocytes was analyzed by flow cytometry. For this purpose, FITC-conjugated ODN was used for preparing NF-ODN and NS-ODN. Freshly prepared mouse splenocytes were cultured in 96-well plates (4 x 10^5 cells/well). Cells were treated with NF-ODN, NS-ODN and ODN alone for 2 h or 12 h before flow cytometry experiment. Cells were collected into 1.5 mL Eppendorf tubes by pipetting, and were precipitated by centrifugation. Supernatants were discarded, cells were washed with 1x PBS and cell pellet was obtained again by centrifugation for further staining and analysis by flow cytometry.

4.4.14. Staining of surface markers and flow cytometry

For uptake study, cells were stained with anti-B220-PE and anti-CD11c-APC or anti-F480-PE. While, for analysis of expression of co-stimulatory molecules, cells were stained with CD40 and CD86. Cells were washed with 1X PBS and centrifuged twice and resuspended in 1x PBS. Flow cytometry was performed with BD FACSAria^{TM} III equipment with BD FACSDiva^{TM} software. Number of events was at least 10,000 for all samples. The experiment was performed in triplicate and representative results of 2 independent experiments are shown.

4.4.15. DNAse assay

In order to understand whether nanostructure binding protects ODN from enzymatic degradation, we performed DNAse assay. Briefly, NF-ODN, NS-ODN and ODN alone were treated with DNAse I for different time periods and ODN digestion was analyzed with polyacrylamide gel electrophoresis. Reaction mixtures for each experimental group are shown in Table S1. Each sample was treated with DNAse I for 10 min, 30 min, 1 h, 4 h and 24 h at 37 °C. At t=0, samples had 3 µL of ddH_2O instead of 3 µL of DNAse I. After incubation period, samples were loaded onto 10% polyacrylamide gel. Before loading, all samples were incubated with 3 µL of 1% SDS to disrupt electrostatic interaction between ODNs and PAs for 5 min at room temperature. Samples were run for 60 min at 75 V and subsequently 80 min at 50 V (in 1x TAE). All other conditions were same with PAGE experiment mentioned above. Band intensities were measured by Image J software. Representative gel images of 3 independent experiments are shown.

4.5. Conclusion

We demonstrated that immune response against viral/bacterial DNA patterns depends on shape of the carrier nanostructure. Nanofibers were more effective than

nanospheres in promoting CpG-induced immune response to Th1 phenotype, alarming immune system against intracellular pathogens. Conferring resistance to enzymatic degradation of ODNs makes nanofibrous ODN and nanospherical ODN complexes promising formulations for *in vivo* applications. Diversity of the peptide nanosystems can enable designing complex nanostructures to carry viral, bacterial or tumoral antigenic peptides. Delivering antigenic peptide and CpG ODN adjuvant in close proximity is also necessary for robust antigen-specific immune response. Considering high IFNγ production and CD86 expression, we think that nanofiber system might be beneficial to induce antigen-specific T-cell response, which is generally formidable task for vaccines. Investigation of whether increased innate immune activation by nanostructures can be translated into increased antigen-specific T and B-cell activity is necessary towards realization of this system as a vaccine model.

CHAPTER 5

EPILOGUE

5. EPILOGUE

As nanotechnology research expands and diversifies, we can engineer materials at nanoscale better. Chemical functional groups, and small peptide fragments relevant for cellular processes can be conjugated to nanosized fibers or spheres. These achievements urge researchers to develop functional materials through mimicking biological structures with an aim of influencing cellular behaviour for therapeutic purposes. However, signals controlling biological processes are complex, so mimicking all of them is not feasible. We need simpler strategies to manipulate this network of signals to induce regenerative processes in cells. In this thesis, new materials, carrying critical biochemical and biophysical signals for cells, are proposed for tissue engineering and vaccinology applications.

First is peptide nanofibers decorated with chemical functional groups from heparan sulfates – an extracellular matrix component that bind to growth factors and regulate their functionality. We showed that heparin-mimetic peptide nanofibers bind to growth factors such as VEGF, HGF, BMP-2 and FGF-2 with comparable affinity to heparin, and a significantly higher affinity than control peptide nanofibers. Moreover, they bind to heparin-binding domains of growth factors, especially for VEGF and FGF-2. Binding to heparan sulfates is critical for bioactivity of these growth factors. Heparin-mimetic peptide nanofibers can be used for delivery of these growth factors into damaged area or to bind endogenous growth factors in damaged area and induce regenerative pathway. VEGF and FGF-2 are extensively involved in induction of angiogenesis, so heparin-mimetic PA scaffolds are potent to induce angiogenesis. Indeed, this is what we observed at *in vitro* and *in vivo* experiments – HM-PA scaffolds induced angiogenesis. At *in vitro* experiments, we observed capillary formation by endothelial cells even in the absence of exogenous growth factors. HM-PA nanofibers probably bind to endogenous growth factors and synergize with them. Considering side effects of growth factors due to misdose in clinical applications, exploiting endogenous factors would be beneficial for tissue engineering applications. Functions of these growth factors hint us about applications where HM-PA nanofiber scaffolds might perform better. As mentioned above,

VEGF/FGF-2 binding might be exploited to induce angiogenesis in cases such as treatment of chronic wounds and bone, cardiac or neural regeneration. HGF is an inducer of cell motility, such as promoting migration of keratinocytes to cover damaged area with epithelial tissue. This makes HM-PA nanofiber gels suitable for wound healing applications. Also, BMP-2 has roles in osteoblast differentiation and migration indicating that this material might be used for bone regeneration. Recent work from our group indicated that HM-PA nanofibers (both with BMP-2 or alone) were better than control PA nanofibers in upregulating osteogenic activity and mineralization by osteoblast cells.[153] This shows that HM-PA nanofibers bind and present BMP-2 relevant bone regeneration. Also binding potential of these nanofibers to other growth factors important in regeneration of cartilage or wound like TGFβ, PDGF should be investigated. In another recent study of our group, HM-PA including scaffold induced chondrogenic (cartilage) differentiation better than control PA scaffolds.[154] Dose of growth factors bound to nanofibers can be controlled with changing concentration/ratio of functional groups on nanofibers. To achieve this, dose of HM-PA can be diluted with control PA molecules. Gels obtained by this way would allow also controlling release rate of growth factors encapsulated in gel. Weak NGF binding observed by HM-PA nanofibers is really matter for bioactivity. In chapter 3, we observed significant differences between HM-PA nanofibers and control nanofibers. Also, our group reported recently that HM-PA synergize with laminin-derived PA to induce neurite outgrowth, as well as slow NGF release better than control PA in laminin-derived PA gels.[155]

Besides presenting functional groups for growth factor binding, nanoscale size of fibers have several advantages. Nanoscale size allows presentation of functional groups and concomitantly growth factors with high density. Also the size of these fibers is similar to collagen fibers of ECM, making them suitable for cell attachment and survival. Indeed, this was what we observed in proliferation assay where all fibers (even with no functional groups on them) induced similar levels of proliferation and viability. It seems that peptide nanofibers themselves are sufficient to maintain cell survival. This renders HM-PA gels beneficial as a filler for damaged area, where neighboring cells will migrate and survive. Nanoscale size of fibers

synergize with functional groups in the induction of bioactivity by HM-PA gels. To further induce cell adhesion to fibers, peptide amphiphiles with integrin-binding epitopes (e.g. RGD) can be used, and they can be mixed with HM-PA.

Stiffness of scaffolds is critical for determination of cell behaviour. Stiffness of these gels is about 500 Pa, so they can be mechanically supported for applications such as bone regeneration or wound healing. Also for better handling of these gels at *in vivo* applications, they can be co-delivered with polymeric materials which have better mechanical tunability, but poor bioactivity. Peptide segments derived from proteins such as elastin can be incorporated into HM-PA peptides or into accompanying peptides to gel system to increase elasticity.

Second material proposed in this thesis is peptide nanofibers decorated with pathogenic DNA motives, known as CpG motives. Antigen itself in vaccines doesn't generate immune response, since antigen presenting cells require additional signal from pathogens like CpG DNA to activate adaptive immune cells. These additional cues determine the fate and character of adaptive immune response generated against antigen. For example, CpG ODNs trigger innate immune system to release a number of pro-inflammatory cytokines and express co-stimulatory molecules on antigen-presenting cells which eventually activates adaptive immune system. Character of this immune response is similar to that against intracellular pathogens such as viruses and mycobacterium. This type of immune response is called as Th1 immune response, which is characterized by activation of phagocytic macrophages and cytotoxic T cells. When we delivered CpG ODNs on nanofibrous and nanospherical peptidic structures immune response became more Th1-sided, while nanofibers being more potent. Therefore, nanofiber bound CpG ODNs are more useful as adjuvants for vaccines to shape immune response against intracellular pathogens and cancer. Cytotoxic T cells recognize peptidic fragments presented by cancer cells and induce cell death pathway. These nanofibrous ODNs can be given directly to tumorigenic area, which will induce local antigen-presenting cells to educate cytotoxic T cells with antigens from tumorigenic area. Nanofibrous CpG ODNs can be given together with antigen to direct immune response against antigen. CpG ODN and antigen

presented on the same particle has been shown to be more effective than freely floating in solution regarding immune response against antigen. So, nanofibers can be engineered to carry antigenic proteins through edc/nhs, biotin-avidin or s-s linkages. Also, small antigenic peptide fragments can be conjugated into nanofibers very easily. Overall, nanofibers carrying CpG DNA is promising for generating antigen specific immune response against intracellular pathogens and tumors.

To conclude, this thesis claimed how simple chemical and physical signals synergize to generate otherwise unachievable outcome. Heparin-mimetic peptide nanofibers showed that right composition of simple chemical functional groups on nanofibers is very potent in terms of growth factor binding and inducing angiogenesis. CpG DNA carrying nanofibers and nanospheres demonstrated that simple physical shapes shift immune response against pathogenic biochemical signal – CpG DNA. We should search for such synergies in nature for designing simple and effective materials.

BIBLIOGRAPHY

1. Hartgerink J.D., Beniash E., Stupp S.I. Self-assembly and mineralization of peptide-amphiphile nanofibers. *Science* 2001, 294(5547)**:** 1684-1688.

2. Hartgerink J.D., Beniash E., Stupp S.I. Peptide-amphiphile nanofibers: a versatile scaffold for the preparation of self-assembling materials. *Proc Natl Acad Sci U S A* 2002, 99(8)**:** 5133-5138.

3. Cui H., Webber M.J., Stupp S.I. Self-assembly of peptide amphiphiles: from molecules to nanostructures to biomaterials. *Biopolymers* 2010, 94(1)**:** 1-18.

4. Rajangam K., Arnold M.S., Rocco M.A., Stupp S.I. Peptide amphiphile nanostructure-heparin interactions and their relationship to bioactivity. *Biomaterials* 2008, 29(23)**:** 3298-3305.

5. Rajangam K., Behanna H.A., Hui M.J., Han X., Hulvat J.F., Lomasney J.W., Stupp S.I. Heparin binding nanostructures to promote growth of blood vessels. *Nano Lett* 2006, 6(9)**:** 2086-2090.

6. Silva G.A., Czeisler C., Niece K.L., Beniash E., Harrington D.A., Kessler J.A., Stupp S.I. Selective differentiation of neural progenitor cells by high-epitope density nanofibers. *Science* 2004, 303(5662)**:** 1352-1355.

7. Shah R.N., Shah N.A., Del Rosario Lim M.M., Hsieh C., Nuber G., Stupp S.I. Supramolecular design of self-assembling nanofibers for cartilage regeneration. *Proc Natl Acad Sci U S A* 2010, 107(8)**:** 3293-3298.

8. Dvir T., Timko B.P., Kohane D.S., Langer R. Nanotechnological strategies for engineering complex tissues. *Nat Nanotechnol* 2011, 6(1)**:** 13-22.

9. Hench L.L., Polak J.M. Third-generation biomedical materials. *Science* 2002, 295(5557)**:** 1014-1017.

10. Lutolf M.P., Hubbell J.A. Synthetic biomaterials as instructive extracellular microenvironments for morphogenesis in tissue engineering. *Nat Biotechnol* 2005, 23(1)**:** 47-55.

11. Place E.S., Evans N.D., Stevens M.M. Complexity in biomaterials for tissue engineering. *Nat Mater* 2009, 8(6)**:** 457-470.

12. Engler A.J., Sen S., Sweeney H.L., Discher D.E. Matrix elasticity directs stem cell lineage specification. *Cell* 2006, 126(4)**:** 677-689.

13. Heim M., Romer L., Scheibel T. Hierarchical structures made of proteins. The complex architecture of spider webs and their constituent silk proteins. *Chem Soc Rev* 2010, 39(1)**:** 156-164.

14. Barnes C.P., Sell S.A., Boland E.D., Simpson D.G., Bowlin G.L. Nanofiber technology: designing the next generation of tissue engineering scaffolds. *Adv Drug Deliv Rev* 2007, 59(14)**:** 1413-1433.

15. Santos M.I., Tuzlakoglu K., Fuchs S., Gomes M.E., Peters K., Unger R.E., Piskin E., Reis R.L., Kirkpatrick C.J. Endothelial cell colonization and angiogenic potential of combined nano- and micro-fibrous scaffolds for bone tissue engineering. *Biomaterials* 2008, 29(32)**:** 4306-4313.

16. Christopherson G.T., Song H., Mao H.Q. The influence of fiber diameter of electrospun substrates on neural stem cell differentiation and proliferation. *Biomaterials* 2009, 30(4)**:** 556-564.

17. Hersel U., Dahmen C., Kessler H. RGD modified polymers: biomaterials for stimulated cell adhesion and beyond. *Biomaterials* 2003, 24(24)**:** 4385-4415.

18. Shin H., Jo S., Mikos A.G. Modulation of marrow stromal osteoblast adhesion on biomimetic oligo[poly(ethylene glycol) fumarate] hydrogels modified with Arg-Gly-Asp peptides and a poly(ethyleneglycol) spacer. *J Biomed Mater Res* 2002, 61(2)**:** 169-179.

19. Ranieri J.P., Bellamkonda R., Bekos E.J., Vargo T.G., Gardella J.A., Jr., Aebischer P. Neuronal cell attachment to fluorinated ethylene propylene films with covalently immobilized laminin oligopeptides YIGSR and IKVAV. II. *J Biomed Mater Res* 1995, 29(6)**:** 779-785.

20. Shin H., Jo S., Mikos A.G. Biomimetic materials for tissue engineering. *Biomaterials* 2003, 24(24)**:** 4353-4364.

21. Ozawa C.R., Banfi A., Glazer N.L., Thurston G., Springer M.L., Kraft P.E., McDonald D.M., Blau H.M. Microenvironmental VEGF concentration, not total dose, determines a threshold between normal and aberrant angiogenesis. *J Clin Invest* 2004, 113(4)**:** 516-527.

22. Tanihara M., Suzuki Y., Yamamoto E., Noguchi A., Mizushima Y. Sustained release of basic fibroblast growth factor and angiogenesis in a novel covalently crosslinked gel of heparin and alginate. *J Biomed Mater Res* 2001, 56(2)**:** 216-221.

23. Steffens G.C., Yao C., Prevel P., Markowicz M., Schenck P., Noah E.M., Pallua N. Modulation of angiogenic potential of collagen matrices by covalent incorporation of heparin and loading with vascular endothelial growth factor. *Tissue Eng* 2004, 10(9-10)**:** 1502-1509.

24. Freeman I., Kedem A., Cohen S. The effect of sulfation of alginate hydrogels on the specific binding and controlled release of heparin-binding proteins. *Biomaterials* 2008, 29(22)**:** 3260-3268.

25. Ruvinov E., Leor J., Cohen S. The effects of controlled HGF delivery from an affinity-binding alginate biomaterial on angiogenesis and blood perfusion in a hindlimb ischemia model. *Biomaterials* 2010, 31(16)**:** 4573-4582.

26. Christman K.L., Vazquez-Dorbatt V., Schopf E., Kolodziej C.M., Li R.C., Broyer R.M., Chen Y., Maynard H.D. Nanoscale growth factor patterns by immobilization on a heparin-mimicking polymer. *J Am Chem Soc* 2008, 130(49)**:** 16585-16591.

27. Lin C.C., Anseth K.S. Controlling Affinity Binding with Peptide-Functionalized Poly(ethylene glycol) Hydrogels. *Adv Funct Mater* 2009, 19(14)**:** 2325.

28. Benoit D.S., Schwartz M.P., Durney A.R., Anseth K.S. Small functional groups for controlled differentiation of hydrogel-encapsulated human mesenchymal stem cells. *Nat Mater* 2008, 7(10)**:** 816-823.

29. Huebsch N., Arany P.R., Mao A.S., Shvartsman D., Ali O.A., Bencherif S.A., Rivera-Feliciano J., Mooney D.J. Harnessing traction-mediated manipulation of the cell/matrix interface to control stem-cell fate. *Nat Mater* 2010, 9(6)**:** 518-526.

30. Hileman R.E., Fromm J.R., Weiler J.M., Linhardt R.J. Glycosaminoglycan-protein interactions: definition of consensus sites in glycosaminoglycan binding proteins. *Bioessays* 1998, 20(2)**:** 156-167.

31. Capila I., Linhardt R.J. Heparin-protein interactions. *Angew Chem Int Ed Engl* 2002, 41(3)**:** 391-412.

32. Bachmann M.F., Jennings G.T. Vaccine delivery: a matter of size, geometry, kinetics and molecular patterns. *Nat Rev Immunol* 2010, 10(11)**:** 787-796.

33. Irvine D.J., Swartz M.A., Szeto G.L. Engineering synthetic vaccines using cues from natural immunity. *Nat Mater* 2013, 12(11)**:** 978-990.

34. Palm N.W., Medzhitov R. Pattern recognition receptors and control of adaptive immunity. *Immunol Rev* 2009, 227(1)**:** 221-233.

35. Kawai T., Akira S. The role of pattern-recognition receptors in innate immunity: update on Toll-like receptors. *Nat Immunol* 2010, 11(5)**:** 373-384.

36. Schenten D., Medzhitov R. The control of adaptive immune responses by the innate immune system. *Adv Immunol* 2011, 109**:** 87-124.

37. Moon J.J., Huang B., Irvine D.J. Engineering nano- and microparticles to tune immunity. *Adv Mater* 2012, 24(28)**:** 3724-3746.

38. Steinman R.M., Banchereau J. Taking dendritic cells into medicine. *Nature* 2007, 449(7161)**:** 419-426.

39. Blander J.M., Medzhitov R. Toll-dependent selection of microbial antigens for presentation by dendritic cells. *Nature* 2006, 440(7085)**:** 808-812.

40. Krieg A.M., Yi A.K., Matson S., Waldschmidt T.J., Bishop G.A., Teasdale R., Koretzky G.A., Klinman D.M. CpG motifs in bacterial DNA trigger direct B-cell activation. *Nature* 1995, 374(6522)**:** 546-549.

41. Hemmi H., Takeuchi O., Kawai T., Kaisho T., Sato S., Sanjo H., Matsumoto M., Hoshino K., Wagner H., Takeda K., Akira S. A Toll-like receptor recognizes bacterial DNA. *Nature* 2000, 408(6813)**:** 740-745.

42. Klinman D.M., Klaschik S., Sato T., Tross D. CpG oligonucleotides as adjuvants for vaccines targeting infectious diseases. *Adv Drug Deliv Rev* 2009, 61(3)**:** 248-255.

43. Mammadov R., Mammadov B., Toksoz S., Aydin B., Yagci R., Tekinay A.B., Guler M.O. Heparin mimetic peptide nanofibers promote angiogenesis. *Biomacromolecules* 2011, 12(10)**:** 3508-3519.

44. Kaully T., Kaufman-Francis K., Lesman A., Levenberg S. Vascularization--the conduit to viable engineered tissues. *Tissue Eng Part B Rev* 2009, 15(2)**:** 159-169.

45. Davis G.E., Senger D.R. Endothelial extracellular matrix: biosynthesis, remodeling, and functions during vascular morphogenesis and neovessel stabilization. *Circ Res* 2005, 97(11)**:** 1093-1107.

46. Phelps E.A., Garcia A.J. Engineering more than a cell: vascularization strategies in tissue engineering. *Curr Opin Biotechnol* 2010, 21(5)**:** 704-709.

47. Schlessinger J., Plotnikov A.N., Ibrahimi O.A., Eliseenkova A.V., Yeh B.K., Yayon A., Linhardt R.J., Mohammadi M. Crystal structure of a ternary FGF-FGFR-heparin complex reveals a dual role for heparin in FGFR binding and dimerization. *Mol Cell* 2000, 6(3)**:** 743-750.

48. Fairbrother W.J., Champe M.A., Christinger H.W., Keyt B.A., Starovasnik M.A. Solution structure of the heparin-binding domain of vascular endothelial growth factor. *Structure* 1998, 6(5)**:** 637-648.

49. Dougher A.M., Wasserstrom H., Torley L., Shridaran L., Westdock P., Hileman R.E., Fromm J.R., Anderberg R., Lyman S., Linhardt R.J., Kaplan J., Terman B.I. Identification of a heparin binding peptide on the extracellular domain of the KDR VEGF receptor. *Growth Factors* 1997, 14(4)**:** 257-268.

50. Simons M., Rubanyi G.M. *Modern concepts in angiogenesis*. Imperial College Press: London, 2007.

51. Zhou Z., Wang J., Cao R., Morita H., Soininen R., Chan K.M., Liu B., Cao Y., Tryggvason K. Impaired angiogenesis, delayed wound healing and retarded tumor growth in perlecan heparan sulfate-deficient mice. *Cancer Res* 2004, 64(14)**:** 4699-4702.

52. *Angiogenesis : an integrative approach from science to medicine*, 1st edn. Springer: New York, 2008.

53. Hynes R.O. The extracellular matrix: not just pretty fibrils. *Science* 2009, 326(5957)**:** 1216-1219.

54. Chow L.W., Bitton R., Webber M.J., Carvajal D., Shull K.R., Sharma A.K., Stupp S.I. A bioactive self-assembled membrane to promote angiogenesis. *Biomaterials* 2011, 32(6)**:** 1574-1582.

55. Chow L.W., Wang L.J., Kaufman D.B., Stupp S.I. Self-assembling nanostructures to deliver angiogenic factors to pancreatic islets. *Biomaterials* 2010, 31(24)**:** 6154-6161.

56. Guerrini M., Beccati D., Shriver Z., Naggi A., Viswanathan K., Bisio A., Capila I., Lansing J.C., Guglieri S., Fraser B., Al-Hakim A., Gunay N.S., Zhang Z., Robinson L., Buhse L., Nasr M., Woodcock J., Langer R., Venkataraman G., Linhardt R.J., Casu B., Torri G., Sasisekharan R. Oversulfated chondroitin sulfate is a contaminant in heparin associated with adverse clinical events. *Nat Biotechnol* 2008, 26(6)**:** 669-675.

57. Figg W.D.F., J. *Angiogenesis : an integrative approach from science to medicine*, 1st edn. Springer: New York, 2008.

58. Maynard H.D., Hubbell J.A. Discovery of a sulfated tetrapeptide that binds to vascular endothelial growth factor. *Acta Biomater* 2005, 1(4)**:** 451-459.

59. Dvir T., Timko B.P., Kohane D.S., Langer R. Nanotechnological strategies for engineering complex tissues. *Nat Nanotechnol* 2010.

60. Kim S.H., Kiick K.L. Heparin-mimetic sulfated peptides with modulated affinities for heparin-binding peptides and growth factors. *Peptides* 2007, 28(11)**:** 2125-2136.

61. Nishida T., Yasumoto K., Otori T., Desaki J. The network structure of corneal fibroblasts in the rat as revealed by scanning electron microscopy. *Invest Ophthalmol Vis Sci* 1988, 29(12)**:** 1887-1890.

62. Poincloux R., Lizarraga F., Chavrier P. Matrix invasion by tumour cells: a focus on MT1-MMP trafficking to invadopodia. *J Cell Sci* 2009, 122(Pt 17)**:** 3015-3024.

63. Niece K.L., Hartgerink J.D., Donners J.J., Stupp S.I. Self-assembly combining two bioactive peptide-amphiphile molecules into nanofibers by electrostatic attraction. *J Am Chem Soc* 2003, 125(24)**:** 7146-7147.

64. Guler M.O., Soukasene S., Hulvat J.F., Stupp S.I. Presentation and recognition of biotin on nanofibers formed by branched peptide amphiphiles. *Nano Lett* 2005, 5(2)**:** 249-252.

65. Engler A.J., Griffin M.A., Sen S., Bonnemann C.G., Sweeney H.L., Discher D.E. Myotubes differentiate optimally on substrates with tissue-like stiffness: pathological implications for soft or stiff microenvironments. *J Cell Biol* 2004, 166(6)**:** 877-887.

66. Stendahl J.C., Rao M.S., Guler M.O., Stupp S.I. Intermolecular Forces in the Self-Assembly of Peptide Amphiphile Nanofibers. *Advanced Functional Materials* 2006, 16(4)**:** 499-508.

67. Anderson J.M., Andukuri A., Lim D.J., Jun H.W. Modulating the gelation properties of self-assembling peptide amphiphiles. *ACS Nano* 2009, 3(11)**:** 3447-3454.

68. Folkman J., Haudenschild C. Angiogenesis in vitro. *Nature* 1980, 288(5791)**:** 551-556.

69. Lafleur M.A., Handsley M.M., Knauper V., Murphy G., Edwards D.R. Endothelial tubulogenesis within fibrin gels specifically requires the activity of membrane-type-matrix metalloproteinases (MT-MMPs). *J Cell Sci* 2002, 115(Pt 17)**:** 3427-3438.

70. Montesano R., Orci L., Vassalli P. In vitro rapid organization of endothelial cells into capillary-like networks is promoted by collagen matrices. *J Cell Biol* 1983, 97(5 Pt 1)**:** 1648-1652.

71. Hiraoka N., Allen E., Apel I.J., Gyetko M.R., Weiss S.J. Matrix metalloproteinases regulate neovascularization by acting as pericellular fibrinolysins. *Cell* 1998, 95(3)**:** 365-377.

72. Garlanda C., Parravicini C., Sironi M., De Rossi M., Wainstok de Calmanovici R., Carozzi F., Bussolino F., Colotta F., Mantovani A., Vecchi

A. Progressive growth in immunodeficient mice and host cell recruitment by mouse endothelial cells transformed by polyoma middle-sized T antigen: implications for the pathogenesis of opportunistic vascular tumors. *Proc Natl Acad Sci U S A* 1994, 91(15)**:** 7291-7295.

73. Potente M., Gerhardt H., Carmeliet P. Basic and therapeutic aspects of angiogenesis. *Cell* 2011, 146(6)**:** 873-887.

74. Arnaoutova I., Kleinman H.K. In vitro angiogenesis: endothelial cell tube formation on gelled basement membrane extract. *Nat Protoc* 2010, 5(4)**:** 628-635.

75. Aranda E., Owen G.I. A semi-quantitative assay to screen for angiogenic compounds and compounds with angiogenic potential using the EA.hy926 endothelial cell line. *Biol Res* 2009, 42(3)**:** 377-389.

76. Brandner B., Kurkela R., Vihko P., Kungl A.J. Investigating the effect of VEGF glycosylation on glycosaminoglycan binding and protein unfolding. *Biochem Biophys Res Commun* 2006, 340(3)**:** 836-839.

77. Brown A. Analysis of cooperativity by isothermal titration calorimetry. *Int J Mol Sci* 2009, 10(8)**:** 3457-3477.

78. Brockhaus M., Ganz P., Huber W., Bohrmann B., Loetscher H.R., Seelig J. Thermodynamic studies on the interaction of antibodies with beta-amyloid peptide. *J Phys Chem B* 2007, 111(5)**:** 1238-1243.

79. von Degenfeld G., Banfi A., Springer M.L., Wagner R.A., Jacobi J., Ozawa C.R., Merchant M.J., Cooke J.P., Blau H.M. Microenvironmental VEGF distribution is critical for stable and functional vessel growth in ischemia. *Faseb Journal* 2006, 20(14)**:** 2657-2659.

80. Claffey K.P. Molecular profiling of angiogenic markers: a step towards interpretive analysis of a complex biological function. *Am J Pathol* 2002, 161(1)**:** 7-11.

81. Martin S., Murray J.C. *Angiogenesis protocols*, 2nd edn. Humana; Springer distributor: New York London, 2009.

82. Cao R., Brakenhielm E., Pawliuk R., Wariaro D., Post M.J., Wahlberg E., Leboulch P., Cao Y. Angiogenic synergism, vascular stability and improvement of hind-limb ischemia by a combination of PDGF-BB and FGF-2. *Nat Med* 2003, 9(5)**:** 604-613.

83. Toksoz S., Mammadov R., Tekinay A.B., Guler M.O. Electrostatic effects on nanofiber formation of self-assembling peptide amphiphiles. *J Colloid Interface Sci* 2011, 356(1)**:** 131-137.

84. Baudin B., Bruneel A., Bosselut N., Vaubourdolle M. A protocol for isolation and culture of human umbilical vein endothelial cells. *Nat Protoc* 2007, 2(3)**:** 481-485.

85. Nakatsu M.N., Hughes C.C. An optimized three-dimensional in vitro model for the analysis of angiogenesis. *Methods Enzymol* 2008, 443**:** 65-82.

86. Zygalaki E., Stathopoulou A., Kroupis C., Kaklamanis L., Kyriakides Z., Kremastinos D., Lianidou E.S. Real-time reverse transcription-PCR quantification of vascular endothelial growth factor splice variants. *Clin Chem* 2005, 51(8)**:** 1518-1520.

87. Izikki M., Guignabert C., Fadel E., Humbert M., Tu L., Zadigue P., Dartevelle P., Simonneau G., Adnot S., Maitre B., Raffestin B., Eddahibi S. Endothelial-derived FGF2 contributes to the progression of pulmonary hypertension in humans and rodents. *J Clin Invest* 2009, 119(3)**:** 512-523.

88. Dingemans A.M., van den Boogaart V., Vosse B.A., van Suylen R.J., Griffioen A.W., Thijssen V.L. Integrin expression profiling identifies integrin alpha5 and beta1 as prognostic factors in early stage non-small cell lung cancer. *Mol Cancer* 2010, 9**:** 152.

89. Hwang J.Y., Park J.W., Hong S.Y., Park H.S. Reduced expression of angiopoietin-1 in Hantaan virus-infected human umbilical vein endothelial cell increases their permeability. *Acta Virol* 2009, 53(1)**:** 7-13.

90. Jakobsson L., Kreuger J., Holmborn K., Lundin L., Eriksson I., Kjellen L., Claesson-Welsh L. Heparan sulfate in trans potentiates VEGFR-mediated angiogenesis. *Dev Cell* 2006, 10(5)**:** 625-634.

91. Mammadov R., Mammadov B., Guler M.O., Tekinay A.B. Growth factor binding on heparin mimetic peptide nanofibers. *Biomacromolecules* 2012, 13(10)**:** 3311-3319.

92. Mieszawska A.J., Kaplan D.L. Smart biomaterials - regulating cell behavior through signaling molecules. *BMC Biol* 2010, 8**:** 59.

93. Lee K., Silva E.A., Mooney D.J. Growth factor delivery-based tissue engineering: general approaches and a review of recent developments. *J R Soc Interface* 2011, 8(55)**:** 153-170.

94. Martino M.M., Hubbell J.A. The 12th-14th type III repeats of fibronectin function as a highly promiscuous growth factor-binding domain. *FASEB J* 2010, 24(12)**:** 4711-4721.

95. Ashikari-Hada S., Habuchi H., Kariya Y., Itoh N., Reddi A.H., Kimata K. Characterization of growth factor-binding structures in heparin/heparan sulfate using an octasaccharide library. *J Biol Chem* 2004, 279(13)**:** 12346-12354.

96. Ibrahimi O.A., Zhang F., Hrstka S.C., Mohammadi M., Linhardt R.J. Kinetic model for FGF, FGFR, and proteoglycan signal transduction complex assembly. *Biochemistry* 2004, 43(16)**:** 4724-4730.

97. Ruppert R., Hoffmann E., Sebald W. Human bone morphogenetic protein 2 contains a heparin-binding site which modifies its biological activity. *Eur J Biochem* 1996, 237(1)**:** 295-302.

98. Stauffer M.E., Skelton N.J., Fairbrothe W.J. Refinement of the solution structure of the heparin-binding domain of vascular endothelial growth factor using residual dipolar couplings. *J Biomol NMR* 2002, 23(1)**:** 57-61.

99. Mizuno K., Inoue H., Hagiya M., Shimizu S., Nose T., Shimohigashi Y., Nakamura T. Hairpin loop and second kringle domain are essential sites for heparin binding and biological activity of hepatocyte growth factor. *J Biol Chem* 1994, 269(2)**:** 1131-1136.

100. Zhou H., Mazzulla M.J., Kaufman J.D., Stahl S.J., Wingfield P.T., Rubin J.S., Bottaro D.P., Byrd R.A. The solution structure of the N-terminal domain of hepatocyte growth factor reveals a potential heparin-binding site. *Structure* 1998, 6(1)**:** 109-116.

101. Thompson L.D., Pantoliano M.W., Springer B.A. Energetic characterization of the basic fibroblast growth factor-heparin interaction: identification of the heparin binding domain. *Biochemistry* 1994, 33(13)**:** 3831-3840.

102. Alberts B. *Molecular biology of the cell*, 4th edn. Garland Science: New York, 2002.

103. Kwan C.P., Venkataraman G., Shriver Z., Raman R., Liu D., Qi Y., Varticovski L., Sasisekharan R. Probing fibroblast growth factor dimerization and role of heparin-like glycosaminoglycans in modulating dimerization and signaling. *J Biol Chem* 2001, 276(26)**:** 23421-23429.

104. Iozzo R.V., San Antonio J.D. Heparan sulfate proteoglycans: heavy hitters in the angiogenesis arena. *J Clin Invest* 2001, 108(3)**:** 349-355.

105. Pellegrini L. Role of heparan sulfate in fibroblast growth factor signalling: a structural view. *Curr Opin Struct Biol* 2001, 11(5)**:** 629-634.

106. Chu H., Johnson N.R., Mason N.S., Wang Y. A [polycation:heparin] complex releases growth factors with enhanced bioactivity. *J Control Release* 2011, 150(2)**:** 157-163.

107. Spooner B.S., Holladay C.R. Distribution of tubulin and actin in neurites and growth cones of differentiating nerve cells. *Cell Motil* 1981, 1(2)**:** 167-178.

108. Kwon S.E., Chapman E.R. Synaptophysin regulates the kinetics of synaptic vesicle endocytosis in central neurons. *Neuron* 2011, 70(5)**:** 847-854.

109. Liebau S., Vaida B., Storch A., Boeckers T.M. Maturation of synaptic contacts in differentiating neural stem cells. *Stem Cells* 2007, 25(7)**:** 1720-1729.

110. Neumann G., Noda T., Kawaoka Y. Emergence and pandemic potential of swine-origin H1N1 influenza virus. *Nature* 2009, 459(7249)**:** 931-939.

111. Demento S.L., Siefert A.L., Bandyopadhyay A., Sharp F.A., Fahmy T.M. Pathogen-associated molecular patterns on biomaterials: a paradigm for engineering new vaccines. *Trends Biotechnol* 2011, 29(6)**:** 294-306.

112. Yakovenko M.L., Cherkasova E.A., Rezapkin G.V., Ivanova O.E., Ivanov A.P., Eremeeva T.P., Baykova O.Y., Chumakov K.M., Agol V.I. Antigenic evolution of vaccine-derived polioviruses: changes in individual epitopes and relative stability of the overall immunological properties. *J Virol* 2006, 80(6)**:** 2641-2653.

113. Kotton C.N. Vaccination and immunization against travel-related diseases in immunocompromised hosts. *Expert Rev Vaccines* 2008, 7(5)**:** 663-672.

114. Ishii K.J., Akira S. Toll or toll-free adjuvant path toward the optimal vaccine development. *J Clin Immunol* 2007, 27(4)**:** 363-371.

115. Janeway C.A., Jr., Medzhitov R. Innate immune recognition. *Annu Rev Immunol* 2002, 20**:** 197-216.

116. Iwasaki A., Medzhitov R. Regulation of adaptive immunity by the innate immune system. *Science* 2010, 327(5963)**:** 291-295.

117. Bode C., Zhao G., Steinhagen F., Kinjo T., Klinman D.M. CpG DNA as a vaccine adjuvant. *Expert Rev Vaccines* 2011, 10(4)**:** 499-511.

118. Klinman D.M., Klaschik S., Sato T., Tross D. CpG oligonucleotides as adjuvants for vaccines targeting infectious diseases. *Advanced Drug Delivery Reviews* 2009, 61(3)**:** 248-255.

119. Akira S. Innate immunity and adjuvants. *Philos Trans R Soc Lond B Biol Sci* 2011, 366(1579)**:** 2748-2755.

120. Shirota H., Sano K., Hirasawa N., Terui T., Ohuchi K., Hattori T., Shirato K., Tamura G. Novel roles of CpG oligodeoxynucleotides as a leader for the sampling and presentation of CpG-tagged antigen by dendritic cells. *J Immunol* 2001, 167(1)**:** 66-74.

121. Cho H.J., Takabayashi K., Cheng P.M., Nguyen M.D., Corr M., Tuck S., Raz E. Immunostimulatory DNA-based vaccines induce cytotoxic lymphocyte activity by a T-helper cell-independent mechanism. *Nat Biotechnol* 2000, 18(5)**:** 509-514.

122. Wagner H. The immunogenicity of CpG-antigen conjugates. *Adv Drug Deliv Rev* 2009, 61(3)**:** 243-247.

123. Krishnamachari Y., Salem A.K. Innovative strategies for co-delivering antigens and CpG oligonucleotides. *Adv Drug Deliv Rev* 2009, 61(3)**:** 205-217.

124. Kerkmann M., Lochmann D., Weyermann J., Marschner A., Poeck H., Wagner M., Battiany J., Zimmer A., Endres S., Hartmann G. Immunostimulatory properties of CpG-oligonucleotides are enhanced by the use of protamine nanoparticles. *Oligonucleotides* 2006, 16(4)**:** 313-322.

125. Kerkmann M., Costa L.T., Richter C., Rothenfusser S., Battiany J., Hornung V., Johnson J., Englert S., Ketterer T., Heckl W., Thalhammer S., Endres S., Hartmann G. Spontaneous formation of nucleic acid-based nanoparticles is responsible for high interferon-alpha induction by CpG-A in plasmacytoid dendritic cells. *J Biol Chem* 2005, 280(9)**:** 8086-8093.

126. Chinnathambi S., Chen S., Ganesan S., Hanagata N. Binding mode of CpG oligodeoxynucleotides to nanoparticles regulates bifurcated cytokine induction via Toll-like receptor 9. *Sci Rep* 2012, 2**:** 534.

127. Gilliet M., Cao W., Liu Y.J. Plasmacytoid dendritic cells: sensing nucleic acids in viral infection and autoimmune diseases. *Nat Rev Immunol* 2008, 8(8)**:** 594-606.

128. Kerkmann M., Rothenfusser S., Hornung V., Towarowski A., Wagner M., Sarris A., Giese T., Endres S., Hartmann G. Activation with CpG-A and CpG-B oligonucleotides reveals two distinct regulatory pathways of type I IFN synthesis in human plasmacytoid dendritic cells. *J Immunol* 2003, 170(9)**:** 4465-4474.

129. Honda K., Ohba Y., Yanai H., Negishi H., Mizutani T., Takaoka A., Taya C., Taniguchi T. Spatiotemporal regulation of MyD88-IRF-7 signalling for robust type-I interferon induction. *Nature* 2005, 434(7036)**:** 1035-1040.

130. Klinman D.M. Immunotherapeutic uses of CpG oligodeoxynucleotides. *Nat Rev Immunol* 2004, 4(4)**:** 249-258.

131. Lim Y.-b., Moon K.-S., Lee M. Rod–coil block molecules: their aqueous self-assembly and biomaterials applications. *Journal of Materials Chemistry* 2008, 18(25)**:** 2909-2918.

132. Cui H., Webber M.J., Stupp S.I. Self-assembly of peptide amphiphiles: From molecules to nanostructures to biomaterials. *Peptide Science* 2010, 94(1)**:** 1-18.

133. Guler M.O., Claussen R.C., Stupp S.I. Encapsulation of pyrene within self-assembled peptide amphiphile nanofibers. *J Mater Chem* 2005, 15(42)**:** 4507-4512.

134. Yoon Y.R., Lim Y.B., Lee E., Lee M. Self-assembly of a peptide rod-coil: a polyproline rod and a cell-penetrating peptide Tat coil. *Chem Commun (Camb)* 2008(16)**:** 1892-1894.

135. Toksoz S., Mammadov R., Tekinay A.B., Guler M.O. Electrostatic effects on nanofiber formation of self-assembling peptide amphiphiles. *Journal of Colloid and Interface Science* 2011, 356(1)**:** 131-137.

136. Chakrabarti R., Klibanov A.M. Nanocrystals modified with peptide nucleic acids (PNAs) for selective self-assembly and DNA detection. *Journal of the American Chemical Society* 2003, 125(41)**:** 12531-12540.

137. Crespo L., Sanclimens G., Montaner B., Perez-Tomas R., Royo M., Pons M., Albericio F., Giralt E. Peptide dendrimers based on polyproline helices. *J Am Chem Soc* 2002, 124(30)**:** 8876-8883.

138. Feigin L.A., Svergun D.I., Taylor G. Determination of the Integral Parameters of Particles. In: Taylor G (ed). *Structure Analysis by Small-Angle X-Ray and Neutron Scattering*. Springer US, 1987, pp 59-105.

139. Kotlarchyk M., Chen S.H. Analysis of small angle neutron scattering spectra from polydisperse interacting colloids. *The Journal of chemical physics* 1983, 79**:** 2461.

140. Berr S.S. Solvent isotope effects on alkytrimethylammonium bromide micelles as a function of alkyl chain length. *The Journal of Physical Chemistry* 1987, 91(18)**:** 4760-4765.

141. Lee B., Lo C.-T., Thiyagarajan P., Winans R.E., Li X., Niu Z., Wang Q. Effect of interfacial interaction on the cross-sectional morphology of tobacco mosaic virus using GISAXS. *Langmuir* 2007, 23(22)**:** 11157-11163.

142. Pujals S., Fernandez-Carneado J., Lopez-Iglesias C., Kogan M.J., Giralt E. Mechanistic aspects of CPP-mediated intracellular drug delivery: relevance of CPP self-assembly. *Biochim Biophys Acta* 2006, 1758(3)**:** 264-279.

143. Kogan M.J., Dalcol I., Gorostiza P., Lopez-Iglesias C., Pons M., Sanz F., Ludevid D., Giralt E. Self-assembly of the amphipathic helix (VHLPPP)8. A mechanism for zein protein body formation. *J Mol Biol* 2001, 312(5)**:** 907-913.

144. Vollmer J., Weeratna R., Payette P., Jurk M., Schetter C., Laucht M., Wader T., Tluk S., Liu M., Davis H.L., Krieg A.M. Characterization of three CpG oligodeoxynucleotide classes with distinct immunostimulatory activities. *Eur J Immunol* 2004, 34(1)**:** 251-262.

145. Krug A., Rothenfusser S., Hornung V., Jahrsdorfer B., Blackwell S., Ballas Z.K., Endres S., Krieg A.M., Hartmann G. Identification of CpG oligonucleotide sequences with high induction of IFN-alpha/beta in plasmacytoid dendritic cells. *Eur J Immunol* 2001, 31(7)**:** 2154-2163.

146. Asano M., Nakane A., Minagawa T. Endogenous gamma interferon is essential in granuloma formation induced by glycolipid-containing mycolic acid in mice. *Infect Immun* 1993, 61(7)**:** 2872-2878.

147. Gratton S.E., Ropp P.A., Pohlhaus P.D., Luft J.C., Madden V.J., Napier M.E., DeSimone J.M. The effect of particle design on cellular internalization pathways. *Proc Natl Acad Sci U S A* 2008, 105(33)**:** 11613-11618.

148. Champion J.A., Mitragotri S. Role of target geometry in phagocytosis. *Proc Natl Acad Sci U S A* 2006, 103(13)**:** 4930-4934.

149. Sharma G., Valenta D.T., Altman Y., Harvey S., Xie H., Mitragotri S., Smith J.W. Polymer particle shape independently influences binding and internalization by macrophages. *J Control Release* 2010, 147(3)**:** 408-412.

150. Barua S., Yoo J.W., Kolhar P., Wakankar A., Gokarn Y.R., Mitragotri S. Particle shape enhances specificity of antibody-displaying nanoparticles. *Proc Natl Acad Sci U S A* 2013, 110(9)**:** 3270-3275.

151. Yamada H., Gursel I., Takeshita F., Conover J., Ishii K.J., Gursel M., Takeshita S., Klinman D.M. Effect of suppressive DNA on CpG-induced immune activation. *J Immunol* 2002, 169(10)**:** 5590-5594.

152. Gursel M., Gursel I., Mostowski H.S., Klinman D.M. CXCL16 influences the nature and specificity of CpG-induced immune activation. *J Immunol* 2006, 177(3)**:** 1575-1580.

153. Kocabey S., Ceylan H., Tekinay A.B., Guler M.O. Glycosaminoglycan mimetic peptide nanofibers promote mineralization by osteogenic cells. *Acta Biomater* 2013, 9(11)**:** 9075-9085.

154. Ustun S., Tombuloglu A., Kilinc M., Guler M.O., Tekinay A.B. Growth and differentiation of prechondrogenic cells on bioactive self-assembled peptide nanofibers. *Biomacromolecules* 2013, 14(1)**:** 17-26.

155. Mammadov B., Mammadov R., Guler M.O., Tekinay A.B. Cooperative effect of heparan sulfate and laminin mimetic peptide nanofibers on the promotion of neurite outgrowth. *Acta Biomater* 2012, 8(6)**:** 2077-2086.